



# **Computational and Mathematical Modeling of Medical Images: Advanced Methods and Applications in Translational Myology and Surgical Planning**

**Kyle Edmunds**

Doctor of Philosophy

June 2017

Biomedical Engineering

Reykjavík University

**Ph.D. Dissertation**





# **Computational and Mathematical Modeling of Medical Images: Advanced Methods and Applications in Translational Myology and Surgical Planning**

Dissertation submitted to the School of Science and Engineering  
at Reykjavík University in partial fulfillment of  
the requirements for the degree of  
**Doctor of Philosophy (Ph.D.) in Biomedical Engineering**

June 2017

Thesis Committee:

Paolo Gargiulo, Supervisor and Associate Professor  
Reykjavík University, Reykjavík, Iceland

Þórður Helgason, Associate Professor  
Reykjavík University, Reykjavík, Iceland

Hannes Petersen, Head of the Dept. of Anatomy and Professor  
University of Iceland, Reykjavík, Iceland

Sigurður Brynjólfsson, Professor  
University of Iceland, Reykjavík, Iceland

Thesis Examiner:

Antonio Fratini, Lecturer and Biomedical Engineering Program Coordinator  
Aston University, Birmingham, United Kingdom



Copyright  
Kyle Edmunds  
June 2017



# **Computational and Mathematical Modeling of Medical Images: Advanced Methods and Applications in Translational Myology and Surgical Planning**

Kyle Edmunds

June 2017

## **Abstract**

The growing field of translational myology continually seeks to define and promote the generalizability of muscle research to clinical practice via optimizing the transition of a wide variety of investigative muscle assessment modalities. There are distinct challenges in all facets of this research, but understanding the physiological importance of mobility currently presents a strategic priority. The severe physiological consequences from the loss of mobility are experienced by all of us: whether induced by normative ambulatory challenges as we age or as sequela of lower extremity pathology. Indeed, a growing wealth of literature clearly implicates mobility loss with a plethora of comorbidities, leading to an increasingly deleterious quality of life and ultimately resulting in early mortality. The loss of mobility is concomitantly evidenced by the progressive decline of skeletal muscle size and quality – phenomena which altogether define muscle degeneration. Nonetheless, complete etiological definitions and methodological comparisons for the precise, non-invasive quantification of muscle degeneration remains disparately described in literature.

This thesis focuses on the development, application, and assessment of novel methods in computational and mathematical modeling of medical images to quantify muscle degeneration and optimize our understanding of two mobility-restorative procedures: Functional Electrical Stimulation and Total Hip Arthroplasty. Additional impacts of these methods are further explored in defining multimodal metrics for mobility analysis, characterizing the utility of 3D printing for surgical planning, modeling craniofacial electromyography, and computing pre-surgical periprosthetic fracture risk. Results from these investigations altogether present the efficacies and limitations of available image processing modalities, and introduce novel methodologies, such as nonlinear trimodal regression analysis of radiodensitometric distributions and computational interference fitting for periprosthetic femoral fracture analysis. Such analyses and perspectives are herein presented in both a theoretical and practical context. Standardizing computational modeling methodologies for medical image assessment in these contexts would allow for the generalizability of such research to the indication of respective compensatory targets for clinical intervention.





# **Tölfræði og Stærðfræðileg Líkanagerð Byggð á Læknisfræðilegum Upplýsingum, Framsækinni Nýtingu á Famförum í Vöðvafræði Nýting þessa við Undirbúning Skurðaðgerða**

Kyle Edmunds

Júní 2017

## **Útdráttur**

Vöðvafræði er vaxandi svið sem sækist að því að skilgreina og upphefja rannsóknir á vöðvakerfinu svo hægt sé að nýta þekkinguna í klínísku umhverfi. Þessu er náð fram með því að nýta þær rannsóknaraðferðir við höfum nú þegar, til hins ýtrasta. Það eru fjölbreytilegar áskoranir og erfiðleikar framundan en það má ekki aftra okkur. Mikilvægi þess að skilja þörf líkamans fyrir hreyfingu er mikið forgangsatriði. Við höfum öll orðið vitni að því hvað gerist við fólk þegar hreyfigetan hverfur, hvort sem það er ellin sem kippir undan okkur eða afleiðingar sjúkdóma, þá benda rannsóknir til þess að takmarkanir á hreyfigetu dragi verulega úr lífsgæðum fólks og stuðlað að hærri dánartíðni. Minnkuð hreyfigeta er bókfærð með mælingum á stærð og gæðum beinagrindarvöðva - Hlutir sem skilgreina vöðvarýrnun. Engu að síður eru læknisfræðilegar skilgreiningar og óáreitandi aðferðum við öflun gagna ekki einhvað sem er vanalega lýst í greinargerðum

Þessi ritgerð einblínir á þróun, nýtingu og mat á nýjum aðferðum sem hægt er að nota við öflun gagna og nýtingu þeirra við þær tvær aðferðir sem við höfum til að hjálpa fólki með minnkaða hreyfigetu: rafstuðsméðferð og gerfiliðaraðgerð á mjöðm. Áframhaldandi afleiðingar þessara aðferða er kannað enn frekar í: skilgreiningar á fjölpátta tölfræði greiningu á hreyfanleika, skilgreiningar á nýtingu þrívíddarprentunar við undirbúning skurðaðgerða, modeling craniofacial electromyography og tölfræðilegir útreikningar á brotlíkum beinstoðtækja fyrir aðgerð. Niðurstöður þessara aðgerða hafa leitt í ljós möguleika og hindranir tækninnar sem nú er notuð og hjálpað til við að auðga flórana m.a. með nýstárlegum leiðum til að greina brotlíkur þegar beinagrindarstoðtækjum er komið fyrir við lærlegg sem er brotinn eða í brothættu. Að koma upp staðli fyrir aðferðir sem beitt er við módelgerð myndi flýta mikið fyrir því að þessar aðferðir finni praktísk hlutverk innan heilbrigðisstofnana.



The undersigned hereby certify that they recommend to the School of Science and Engineering at Reykjavík University for acceptance this Dissertation entitled **Computational and Mathematical Modeling of Medical Images: Advanced Methods and Applications in Translational Myology and Surgical Planning** submitted by **Kyle Edmunds** in partial fulfillment of the requirements for the degree of **Doctor of Philosophy (Ph.D.) in Biomedical Engineering**

**Date**

**07.06.2017**



Paolo Gargiulo, Supervisor and Associate Professor Reykjavík University, Reykjavík, Iceland

**Thesis Committee:**



Þórður Helgason, Associate Professor Reykjavík University, Reykjavík, Iceland



Hannes Petersen, Head of the Dept. of Anatomy and Professor University of Iceland, Reykjavík, Iceland



Sigurður Brynjólfsson, Professor University of Iceland, Reykjavík, Iceland



Antonio Fratini, Examiner

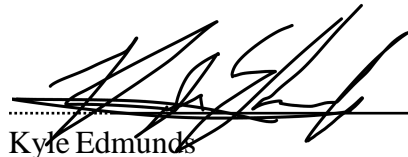


The undersigned hereby grants permission to the Reykjavík University Library to reproduce single copies of this Dissertation entitled **Computational and Mathematical Modeling of Medical Images: Advanced Methods and Applications in Translational Myology and Surgical Planning** and to lend or sell such copies for private, scholarly or scientific research purposes only.

The author reserves all other publication and other rights in association with the copyright in the Dissertation, and except as herein before provided, neither the Dissertation nor any substantial portion thereof may be printed or otherwise reproduced in any material form whatsoever without the author's prior written permission.

7.6.2017

7.6.2017

A handwritten signature in black ink, appearing to read 'K. Edmunds', is written over a horizontal dotted line.

Kyle Edmunds

Doctor of Philosophy



*I dedicate this to my family, for all the years of support, patience, and inspiration – I truly can never thank you enough.*





# Acknowledgements

It is impossible to fully describe my gratitude for Dr. Paolo Gargiulo, my doctoral advisor. Over the last three years, since I moved from Boston to Iceland, he has shown me nothing but the sincerest support with his genuine positive energy and contagious passion for research, mentorship, and education. His perspective on biomedical engineering as a field (and life, in-general) has been truly inspirational – perhaps the greatest lesson he has taught me over the years was how to “keep one foot in the future, and one foot in the present, with a respect for what’s behind you”. His ability to keep his focus on what needs to be done now, in the context of planning for a growing department at Háskólinn í Reykjavík, has inspired me to continue my own personal pursuit of establishing myself as a professor whose focus revolves around the clinical translational applications of biomedical engineering.

My personal transition to a new life as an immigrant in Iceland was always full of challenges, but as I felt from my first moments in the country, no matter where you go in this world, you will always find love and friendship to guide you through life. However, it is equally important for me to recognize all of my dearest friends back in the States who I truly can never thank enough for inspiring me to become who I am today: Dan, Layne, Rob, Harrison, Ben, Aaron, Sean, Morgan, Becky, Adam, Patrick, P-Ham, Steve, Tara, Nish, and so many others – I cannot express the depth of my personal gratitude enough, and I can’t wait for our paths to cross again.

For my friends and colleagues I have had the distinct pleasure of getting to know here, I would also like to express my deepest thanks: Raggi, Christian, Laura, Sölvi, Siggi, Orri, Villi, Fribbi, Óli, Jósef, Þóroldur, and so many other amazing people – and last, but *certainly* not least, my amazing, beautiful, and inspirational girlfriend, Sarah. All of the love and support that you all have provided me when I absolutely needed to decompress, reinvent, and redefine, together with all the crazy adventures, have truly made life amazing and helped to shape who I have come to be. Likewise, my sincerest thanks to my colleagues in the biomedical technology center at Háskólinn í Reykjavík, for your inspiration, advice, and willingness to involve me in collaboration.

Finally, none of us could have gotten anywhere without the trust and support from Háskólinn í Reykjavík and agencies around the world who provided our team with our main means of financial support:

- Landspítali Scientific Fund, PI: Paolo Gargiulo, “Bone Modeling in patients undergoing THA”, A-2014-072
- Rannís Icelandic Research Fund (Rannsóknasjodur), PI: Paolo Gargiulo, “Clinical evaluation score for Total Hip Arthroplasty planning and postoperative assessment”, 152368-051
- Rannís Innovation Fund (Nyskopunarsjodur), PI: Paolo Gargiulo, “Clinical assessment for patients undergoing total hip replacement”
- The IRCCS Fondazione Ospedale San Camillo, Venezia, Italia

- The European Regional Development Fund - Cross Border Cooperation Programme Slovakia – Austria 2007–2013 (Interreg-IVa), project Mobilität im Alter, MOBIL, N\_00033 (partners: Ludwig Boltzmann Institute of Electrical Stimulation and Physical Rehabilitation, Austria, Center for Medical Physics and Biomedical Engineering, Medical University of Vienna, Austria, and Faculty of Physical Education and Sports, Comenius University in Bratislava, Slovakia)
- Austrian national co-financing of the Austrian Federal Ministry of Science and Research
- Ludwig Boltzmann Society (Vienna, Austria) to CH, SL, HK
- The EU Commission Shared Cost Project RISE (Contract n. QLG5-CT-2001-02191) and The Austrian Ministry of Science funds to Prof. DDr. H. Kern Vienna (Austria) covered the clinical costs, the production of customized devices and the international management of the project
- The Italian MIUR funds to UC and FC, the Laboratory of Translational Myology, and the Italian C.N.R. funds to the Institute of Neuroscience, University of Padova, Italy, supported light microscopy, morphometry, and costs of data analyses;

Some of the research reported herein was additionally supported by the National Institute of Arthritis and Musculoskeletal and Skin Diseases of the National Institutes of Health, under award number NIH NIAMS 1R03AR053706-01A2 to ALP. It should be noted that the respective content presented here is solely the responsibility of us, the authors, and does not necessarily represent the official views of the National Institutes of Health.

I would also like to thank Sigurður I. Erlingsson for chairing my doctoral defense, as well as Þórður Helgason, Antonio Fratini, Sigurður Brynjólfsson, and Hannes Petersen for serving on my dissertation committee and providing me with additional support and scholarship during my time here at Háskólinn í Reykjavík. Finally, I would not have been where I am today without the endless love and inspiration from parents, John and Denise, and two amazing sisters, Jackie and Patty, back where it all began in Wisconsin, and all the amazing people in my crazy huge, loving family.

Thank you and much love to everyone!

# Publications

Much of the text of this thesis has been adapted from the following 13 publications, of which I, Kyle Joseph Edmunds, am an author; a list of these works is depicted herein, along with, primarily, their respective chapters. All publications were submitted for peer review to their respective journals during the duration of my doctoral studies.

1. Edmunds, K. J., & Gargiulo, P. (2015). Imaging Approaches in Functional Assessment of Implantable Myogenic Biomaterials and Engineered Muscle Tissue. *European Journal of Translational Myology*, 25(2), 4847. <https://doi.org/10.4081/ejtm.2015.4847> (Chapter 2, Section 2.6)
2. Edmunds, K. J., Gíslason, M. K., Arnadóttir, I. D., Marcante, A., Piccione, F., & Gargiulo, P. (2016). Quantitative Computed Tomography and Image Analysis for Advanced Muscle Assessment. *European Journal of Translational Myology*, 26(2), 6015. <https://doi.org/10.4081/ejtm.2016.6015>
3. Edmunds K.J., Árnadóttir Í., Gíslason M.K., Carraro U., Gargiulo P. (2016). Nonlinear Trimodal Regression Analysis of Radiodensitometric Distributions to Quantify Sarcopenic and Sequelae Muscle Degeneration. *Computational and Mathematical Methods in Medicine*. 2016;2016:8932950.
4. Magnússon B, Pétursson Þ, Edmunds K, et al. Improving Planning and Post-Operative Assessment for Total Hip Arthroplasty. *European Journal of Translational Myology*. 2015;25(2):4913. doi:10.4081/ejtm.2015.4913.
5. Edmunds, K. J., Hermannsson, Þ., Barbato, M., Árnadóttir, I., Gíslason, M. K., Jónsson, H., ... Gargiulo, P. (2016). Multimodal Quantitative Assessment for Pre-operative Prosthesis Selection in Total Hip Arthroplasty. In E. Kyriacou, S. Christofides, & C. S. Pattichis (Eds.), *XIV Mediterranean Conference on Medical and Biological Engineering and Computing 2016: MEDICON 2016, March 31st-April 2nd 2016, Paphos, Cyprus* (pp. 709–714). Cham: Springer International Publishing. [https://doi.org/10.1007/978-3-319-32703-7\\_136](https://doi.org/10.1007/978-3-319-32703-7_136)
6. Pétursson, Þ., Edmunds, K. J., Gíslason, M. K., Magnússon, B., Magnúsdóttir, G., Halldórsson, G., ... Gargiulo, P. (2015). Bone Mineral Density and Fracture Risk Assessment to Optimize Prosthesis Selection in Total Hip Replacement. *Computational and Mathematical Methods in Medicine*, 2015, 1–7. <https://doi.org/10.1155/2015/162481>
7. Wiedemann L, Chaberova J, Edmunds K, Einarsdóttir G, Ramon C, Gargiulo P. Low-Amplitude Craniofacial EMG Power Spectral Density and 3D Muscle Reconstruction from MRI. *European Journal of Translational Myology*. 2015;25(2):4886. doi:10.4081/ejtm.2015.4886.
8. Carraro, U., Edmunds, K. J., Gargiulo, P. (2015). 3D False Color Computed Tomography for Diagnosis and Follow-Up of Permanent Denervated Human Muscles Submitted to Home-Based Functional Electrical Stimulation. *European Journal of Translational Myology*, 25(2), 5133. <https://doi.org/10.4081/ejtm.2015.5133>
9. Edmunds, K. J., Hermannsson, Þ., Barbato, M., Árnadóttir, I., Gíslason, M. K., Jónsson, H., ... Gargiulo, P. (2017). Multimodal Pre and Postsurgical Biometrics for Patient-Specific Assessment in Total Hip Arthroplasty. (*Under Review*)

10. Edmunds, K.J., Gíslason, M.K., Sigurðsson, S., Guðnason, V., Harris, T.B., Carraro, U., Gargiulo, P. (2017). Advanced quantitative methods in correlating sarcopenic muscle degeneration with lower extremity function biometrics and comorbidities. (*Under Review*).
11. Carraro, U., Kern, H., Gava, P., Hofer, C., Loeffler, S., Gargiulo, P., ... Mosole, S. (2016). Recovery from muscle weakness by exercise and FES: lessons from Masters, active or sedentary seniors and SCI patients. *Aging Clinical and Experimental Research*. <https://doi.org/10.1007/s40520-016-0619-1>
12. Gislason, M. K., Menichetti, A., Edmunds, K.J., Hermannsson, T., Jonsson, H., Esposito, L., ... Garigiulo, P. (2017). BIOMECHANICAL ASSESSMENT AND MODELLING OF TOTAL HIP ARTHROPLASTY PATIENTS. *Bone & Joint Journal Orthopaedic Proceedings Supplement*, 99–B(SUPP 1), 3 LP-3. Retrieved from [http://www.bjjprocs.boneandjoint.org.uk/content/99-B/SUPP\\_1/3.abstract](http://www.bjjprocs.boneandjoint.org.uk/content/99-B/SUPP_1/3.abstract)
  - a. Gargiulo, P., Árnadóttir, Í., Gíslason, M.K., Edmunds, K.J., Ólafsson, I. (2017). New Directions in 3D Medical Modeling: 3D-Printing Anatomy and Functions in Neurosurgical Planning. *Journal of Healthcare Engineering*, ID:1439643 (*In Press*)

It should likewise be noted that portions of the text presented here in the background chapter, Chapter 2, have been adapted from the abovementioned publications for their respective, relevant sections. I fully acknowledge that these papers are written in collaboration with my co-authors and that this thesis therefore contains significant text and concepts that were conceived in collaboration. I hereby confirm that the inclusion of all previously published text was written either by myself and/or included here with the permission of both my co-authors and the journals to which these manuscripts were submitted for publication.

While the bulk of the published work in this thesis was collaborative in origin, all of the publication manuscripts were either prepared or drafted by me, along with a vast majority of the present literature review, as both the first and/or corresponding author. In addition, I orchestrated and/or participated in all of the analyses presented by experiments described in this thesis, although several notable contributions were made primarily by other coauthors:

- The interference fit analysis reported in Section 6.3.1.1 was performed in collaboration with Þ. Hermannsson and M.K. Gíslason.
- The gait and EMG analyses presented in Chapter 6 and the FEA analyses presented in Section 8.3 were performed by our coauthors in each respective work from the University of Naples Federico II in Napoli, Italy (L. Esposito, A. Cutolo, P. Bifulco, M. Cesarelli, and M. Fraldi).
- The FRI analyses in Chapter 7 were performed by Þ. Petursson and B. Magnússon.

In addition, some of the text has been adapted, with permission, from the following two textbook chapters, of which I am likewise an author:

13. Edmunds, K.J., Gíslason, M.K., Gargiulo, P. “*CT BASED BONE AND MUSCLE ASSESSMENT IN NORMAL AND PATHOLOGICAL CONDITIONS*”. **Encyclopedia of Biomedical Engineering**. John Wiley & Sons, Inc. (*Under Review*).
14. Gargiulo, P., Edmunds, K.J., Árnadóttir Í., Carraro, U., Gíslason, M.K. “*Muscle Assessment Using 3D Modeling & Soft Tissue CT Profiling*”. **Rehabilitation Medicine for Elderly Patients**. Springer Publishing. doi:10.1007/978-3-319-57406-6



# Contents

<b>Acknowledgements</b>	<b>xvii</b>
<b>Publications</b>	<b>xix</b>
<b>Contents</b>	<b>xii</b>
<b>List of Figures</b>	<b>xxvii</b>
<b>List of Tables</b>	<b>xxxii</b>
<b>1 Introduction</b>	<b>1</b>
<b>2 Background</b>	<b>4</b>
2.1 The Biological Importance of Skeletal Muscle Quality and its Impact on Mobility and Mortality . . . . .	4
2.2 Mechanisms of Skeletal Muscle Degeneration. . . . .	6
2.2.1 Size and Myofiber Contractility . . . . .	6
2.2.2 Architecture and Fibrosis . . . . .	7
2.2.3 Aerobic Capacity. . . . .	8
2.2.4 Myosteatorsis . . . . .	9
2.2.5 Neuromuscular Activation. . . . .	9
2.3 The Effects of Volitional Exercise of Recovery from Muscle Degeneration . . . . .	10
2.3.1 Exercise and Sarcopenia . . . . .	11
2.3.2 Decline in Muscle Power Evidenced from Aging Elite Athletes . . . . .	12
2.3.3 Degeneration and Reinnervation in Average Individuals . . . . .	13
2.4 Reviewing a Potential Restorative Muscle Therapy: Home-Based Functional Electrical Stimulation. . . . .	16
2.4.1 H-bFES: Materials and Methods. . . . .	16
2.4.2 The Effects of h-bFES on Recovery from Sarcopenia . . . . .	17
2.4.3 The Effects of h-bFES on Recovery from Spinal Cord Injury . . . . .	18
2.5 Advanced Techniques in X-Ray Computed Tomography Image Analysis . . . . .	20
2.5.1 Radiodensitometric Attenuation: Distribution Matrices. . . . .	21

2.5.2	Soft Tissue Segmentation and 3D Modeling . . . . .	22
2.5.3	CT-Based Finite Element Modeling . . . . .	23
2.6	Noninvasive Functional Assessment of Engineered Muscle Tissue and Implantable Myogenic Biomaterials: A Review of Imaging Modalities . . . . .	25
2.6.1	Extant Functional Assessment Methods and the Expanding Role of Imaging. . . . .	26
2.6.2	Two-Photon Excited Fluorescence . . . . .	29
2.6.3	Photoacoustic Microscopy. . . . .	29
2.6.4	Fluorescence-Lifetime Imaging Microscopy . . . . .	30
2.6.5	Optical Coherence Tomography . . . . .	31
2.6.6	Positron Emission Tomography . . . . .	32
2.6.7	Bioluminescent Imaging . . . . .	33
2.6.8	Micro X-ray Computed Tomography . . . . .	34
2.7	Applications of 3D Medical Image Modeling . . . . .	35
2.7.1	Total Hip Arthroplasty: Modeling Periprosthetic Muscle and Femoral Biomechanics. . . . .	35
2.7.2	Source Localization and Electroencephalography. . . . .	37
2.7.3	False-Color CT: Clinical Impact of Modeling Segmented Tissue Morphologies. . . . .	38
2.7.4	3D Printing of Segmented Tissues: Methods and Impacts . . . . .	40
<b>3</b>	<b>A First Look: Preliminary Impacts of Modern Methods for CT Image Analyses in Translational Myology and THA</b>	<b>41</b>
3.1	Implicating Muscle Quality as a Clinical Comorbidity Index . . . . .	41
3.2	Monitoring Trophism Decay of LMN-Denervated Muscle and its Restoration by h-b FES Compliance . . . . .	42
3.3	Utility of 3D Muscle Segmentation in Monitoring Incomplete Denervation from Spinal Cord Injury . . . . .	43
3.4	3D Muscle Segmentation and HU Distribution Analysis: Improving Patient Assessment in THA . . . . .	45
3.4.1	Introduction. . . . .	45
3.4.2	Material and Methods. . . . .	46
3.4.2.1	CT Data Acquisition. . . . .	46
3.4.2.2	CT Data Processing . . . . .	47
3.4.2.3	Hounsfield Unit Distribution Modeling . . . . .	47
3.4.2.4	Statistical Analyses. . . . .	48
3.4.3	Results . . . . .	48
3.4.4	Discussion and Conclusions. . . . .	52
<b>4</b>	<b>Nonlinear Trimodal Regression Analysis of Radiodensitometric Distributions to Quantify Sarcopenic and Sequelae Muscle Degeneration</b>	<b>53</b>
4.1	Introduction. . . . .	53
4.2	Materials and Methods . . . . .	54
4.2.1	Subject Details and Recruitment. . . . .	54
4.2.2	CT Acquisition and Soft Tissue Voxel Segmentation . . . . .	54
4.2.3	Voxel Distribution Binning . . . . .	55
4.2.4	Statistical Analyses. . . . .	55

4.2.5	The Method: Nonlinear Trimodal Regression Analysis . . . . .	56
4.3	Results and Discussion . . . . .	57
4.3.1	Initial Case Studies: A Comparison of Degeneration Pathways . . . . .	57
4.3.2	Assessing Changes in Muscle Following Total Hip Arthroplasty. . . . .	60
4.3.3	Exploring the Partial Volume Effect. . . . .	62
4.4	Conclusions. . . . .	63
<b>5</b>	<b>Advanced Quantitative Methods in Correlating Sarcopenic Muscle Degeneration with Lower Extremity Function Biometrics and Comorbidities</b>	<b>65</b>
5.1	Introduction. . . . .	65
5.2	Materials and Methods . . . . .	66
5.2.1	Subject Recruitment. . . . .	66
5.2.2	CT Acquisition and Segmentation. . . . .	66
5.2.3	LEF Biometrics and Sarcopenic Comorbidity Measurements . . . . .	67
5.2.4	Pixel Distribution Binning and Smoothing . . . . .	67
5.2.5	Nonlinear Trimodal Regression Analysis (NTRA) Method . . . . .	67
5.2.6	1-D K-means Clustering Discretization of LEF Biometrics and Sarcopenic Comorbidities. . . . .	69
5.2.7	Statistical Analyses . . . . .	70
5.3	Results and Discussion. . . . .	70
5.3.1	Gold Standard Analyses on LEF Biometrics and Sarcopenic Comorbidities. . . . .	70
5.3.2	NTRA Analyses on LEF Biometrics and Sarcopenic Comorbidities. . . . .	72
5.3.3	NTRA and Gold Standard Analyses on Age and Sex . . . . .	78
5.4	Conclusions. . . . .	80
<b>6</b>	<b>Multimodal Patient-Specific Pre- and Post-Surgical Assessment in Total Hip Arthroplasty</b>	<b>81</b>
6.1	Introduction. . . . .	81
6.2	Methods. . . . .	82
6.2.1	Cohort Recruitment and Representative Patients . . . . .	82
6.2.2	CT Data Acquisition . . . . .	82
6.2.3	Soft Tissue Segmentation for Volumetric and Density Assessment . . . . .	82
6.2.4	3D Fracture Risk Analysis via Interference Fit Modeling . . . . .	83
6.2.5	Soft Tissue Radiodensitometric Distribution Profiling. . . . .	84
6.2.6	Quantitative Gait Assessment . . . . .	84
6.2.7	Muscle Contraction Computation and Indexing via EMG . . . . .	85
6.3	Results and Discussion. . . . .	86
6.3.1	Multimodal Biometrics for Presurgical THA Assessment . . . . .	86
6.3.1.1	3D Fracture Risk Analysis via Interference Fit Modeling . . . . .	86
6.3.1.2	3D Segmentation and Volumetric Assessment . . . . .	87
6.3.1.3	Presurgical Gait Parameter Assembly. . . . .	88
6.3.2	Multimodal Biometrics for Postsurgical THA Assessment . . . . .	89
6.3.2.1	Changes in Soft Tissue Radiodensitometric Amplitudes . . . . .	89
6.3.2.2	Postsurgical Gait Parameter Assembly . . . . .	91
6.3.2.3	Electromyographic Activity Analyses. . . . .	92
6.4	Conclusions. . . . .	92



<b>7</b>	<b>Bone Mineral Density and Fracture Risk Assessment to Optimize Prosthesis Selection</b>	<b>94</b>
7.1	Introduction . . . . .	94
7.2	Materials and Methods. . . . .	96
7.2.1	Patient Recruitment. . . . .	96
7.2.2	CT Data Acquisition . . . . .	96
7.2.3	Segmentation and Finite Element Modeling. . . . .	97
7.2.4	Fracture Risk Index Computation . . . . .	98
7.2.5	Bone Mineral Density Computation. . . . .	99
7.3	Results . . . . .	99
7.4	Discussion and Conclusions . . . . .	102
7.4.1	Bone Mineral Density as a Potential Computational Tool in THA . . . . .	103
7.4.2	Fracture Risk as a Potential Computational Tool in THA . . . . .	103
7.4.3	Limitations and Future Directions. . . . .	103
<b>8</b>	<b>Additional Applications of Computational Modeling of Medical Images</b>	<b>105</b>
8.1	Low-Amplitude Craniofacial EMG Power Spectral Density and 3D Muscular Reconstruction from MRI . . . . .	105
8.1.1	Introduction . . . . .	105
8.1.2	Material and Methods . . . . .	106
8.1.2.1	EMG Data Acquisition . . . . .	106
8.1.2.2	Frequency Analyses . . . . .	106
8.1.2.3	Craniofacial Muscle Modeling from MRI. . . . .	107
8.1.2.4	Statistical Analyses . . . . .	108
8.1.3	Results . . . . .	108
8.1.4	Discussion and Conclusions . . . . .	111
8.2	New Directions in 3D Medical Modeling: 3D-Printing Anatomy and Functions in Neurosurgical Planning . . . . .	112
8.2.1	Introduction . . . . .	112
8.2.2	Material and Methods . . . . .	114
8.2.2.1	CT and MRI Acquisition . . . . .	114
8.2.2.2	DTI: Fiber Tract Extrapolation . . . . .	114
8.2.2.3	Quality Assessment: Anatomical Accuracy and Incorrectly Displayed Fibers. . . . .	116
8.2.2.4	Segmentation and Registration . . . . .	117
8.2.2.5	Navigation System and Rapid Prototyping . . . . .	118
8.2.3	Results . . . . .	118
8.2.4	Conclusion . . . . .	121
<b>9</b>	<b>Conclusions and Future Directions</b>	<b>122</b>
	<b>Bibliography</b>	<b>126</b>
<b>A</b>	<b>Code: NTRA</b>	<b>159</b>



# List of Figures

2.1	Age-related decline of skeletal muscle power derived from world records of running, jumping and throwing events of elite athletes within different age classes. . . . .	12
2.2	Denervation/reinnervation process starts with a checkerboard cluster of muscle fibers. . . . .	14
2.3	Permanent long-term denervation simulates premature aging in muscle. . . . .	18
2.4	2D Color CT evidence of recovery from permanent denervation (i.e., premature muscle aging) by home-based Functional Electrical Stimulation (h-bFES) . . . . .	19
2.5	Example of 3D soft tissue segmentation utility. . . . .	23
2.6	Types of functional assessment metrics for various tissue engineering studies. . . . .	27
2.7	Standard destructive methods for the functional analysis of engineered tissue. . . . .	28
2.8	The potential function of a portable simultaneous PET/MR scanner. . . . .	33
2.9	$\mu$ CT image and its corresponding 3D model of an implantable biomaterial scaffold. . . . .	35
2.10	3D false-color CT reconstruction of a <i>Rectus femoris</i> muscle from a healthy patient, including the epimysium at the cortical level in A) gray and B) false colors, along with C) the corresponding cross-section at mid belly. . . . .	39
3.1	Example of a patient with irreversible <i>Conus</i> and <i>Cauda Equina</i> syndrome who underwent five years of compliance with h-bFES treatment, followed by another five years of non-compliance to h-bFES. . . . .	43
3.2	3D soft tissue segmentation to compare the compositional changes between the calf muscles in both legs (A, before and B, after h-bFES rehabilitation). . . . .	44

3.3	HU distribution comparison between left and right legs, as assessed at the mid-thigh. . . . .	45
3.4	Representative subject's CT scanning region, showing A) a CT slice in a coronal view showing the quadriceps muscles, B) the same slice after segmentation of the quadriceps muscles, and C) the quadriceps muscles and the femur in a 3D view after segmentation. . . . .	47
3.5	The average composition of the quadriceps muscles for each of the specific patient groups and healthy versus operative legs. . . . .	48
3.6	Hounsfield unit (HU) distribution from -135 to 200, divided into 20 bins. . . . .	49
3.7	Binned Hounsfield unit (HU) distribution for patients grouped by sex. . . . .	50
3.8	Binned Hounsfield unit (HU) distribution for patients grouped by age. . . . .	51
4.1	Segmented soft tissues and compositions within the <i>Tibialis anterioris</i> from A) the healthy control subject, B) the elderly subject, and C) the pathological subject. . . . .	55
4.2	Diagram depicting the three components of the trimodal radiodensitometric distribution utilized in this study. . . . .	57
4.3	Radiodensitometric distributions showing their respective nonlinear regression curves and average HU values. . . . .	58
4.4	Results from the three representative subjects' nonlinear trimodal regression analyses. . . . .	59
4.5	Results from the nonlinear trimodal regression analyses of the n=15 THA cohort. . . . .	61
4.6	Results from Partial Volume Effect pixel removal using the healthy control subject. . . . .	63
5.1	Diagram depicting the three components of the trimodal radiodensitometric distribution utilized in this study. . . . .	69
5.2	Gold standard analyses against A) LEF biometrics and B) sarcopenic comorbidities. . . . .	71
5.3	NTRA parameters against gait speed LEF biometrics. . . . .	73

5.4	NTRA parameters against timed up-and-go and isometric leg strength LEF biometrics. . . . .	74
5.5	NTRA parameters against sarcopenic comorbidities. . . . .	77
5.6	Assembly of NTRA parameters whose LEF and comorbidity parameters yielded linear correlation coefficients greater than 0.85. . . . .	78
5.7	A) NTRA parameters along with B and C) gold standard analyses assessment against age and sex. . . . .	79
6.1	Representative 3D soft tissue segmentation of the <i>Rectus femoris</i> , <i>Vastus lateralis</i> , and the <i>Vastus medialis</i> . . . . .	83
6.2	3D Fracture Risk Analysis via Interference Fit Modeling. . . . .	87
6.3	3D Muscle Segmentation and Soft Tissue Volumetric Assessment. . . . .	88
6.4	Presurgical Gait Parameter Assembly. . . . .	89
6.5	Postsurgical Changes in Soft Tissue Radiodensitometric Profile Amplitudes. . . . .	90
6.6	Postsurgical Changes in Patient Gait Parameters. . . . .	91
6.7	Postsurgical Changes in Periprosthetic Segmented Muscle EMG Activities. . . . .	92
7.1	Bone Mineral Density and Fracture Risk Assessment to Optimize Prosthesis Selection: Study Workflow. . . . .	95
7.2	CT scanning protocol range on the femoral head. . . . .	96
7.3	A finite element model of the femur consisting of more than 100,000 elements. The elements are given material properties: namely, Poisson's ratio and Young's modulus. Red colors indicate higher density bone. . . . .	97
7.4	The 9.25 kN cementless prosthesis forces applied on the model where the highest stress can be expected during the press-fitting of the tapered stem. . . . .	98
7.5	A) Axial view of one slice of the CT-data from a patient, and B) the 3D view of the region of interest for BMD calculations. . . . .	99

7.6	Examples of calculated FRI from A) a 71 year old female patient and B) a 46 year old female. . . . .	100
7.7	Elements plotted in their three-dimensional coordinates. . . . .	100
7.8	Results from FRI and BMD assessment for each patient grouped by sex and prosthesis type. . . . .	102
8.1	Sample raw EMG data depicting the results of the clustering methodology utilized to separate active and inactive chewing conditions (Red is active, and blue is inactive). . . . .	107
8.2	Example thresholding method using MIMICS software to identify and segment the frontal (A) and temporal (B) muscles. . . . .	108
8.3	Results from EMG signal FFT analysis and mean signal amplitude assessment. . . . .	109
8.4	Comparison of mean signal amplitudes across all measured conditions. . . . .	110
8.5	MRI segmentation and 3D reconstruction of temporal and frontal craniofacial muscles. . . . .	111
8.6	Clinical areas associated to the 200 surgeries assisted with 3D-printed models. . . . .	113
8.7	TRACTS superimposed on MRI structural data. . . . .	118
8.8	Tractography planning from StealthViz (a-b) and nordicBrainEx (c-d). . . . .	119
8.9	Comparison between the corpus callosum tracts obtained with different software: nordicBrainEx (a) and StealthViz (b). . . . .	120
8.10	3D computer model made in mimics with fiber tracts result from nordicBrainEx (a) and when it has been 3D printed and painted (b). . . . .	121



## List of Tables

2.1	Target pathophysiology of various <sup>18</sup> F-containing radiopharmaceuticals. . . . .	32
6.1	Gait Parameter definitions and measurement methods. . . . .	84
7.1	FRI and BMD results from the ten cemented and cementless THR subjects. . . .	101
8.1	Grades for incorrectly displayed fibers. . . . .	116
8.2	Grades for anatomical accuracy. . . . .	117
8.3	The grading results for anatomic accuracy and for incorrectly displayed fibers both for StealthViz (SV) and nordicBrainEx (BE). . . . .	120







# Chapter 1

## Introduction

The growing field of translational myology continually seeks to define and promote the generalizability of muscle research to clinical practice via optimizing the transition of a wide variety of investigative muscle assessment modalities. There are distinct challenges in all facets of this research, but understanding the physiological importance of skeletal muscle and its relationship with mobility presents a current strategic priority. Alterations in our mobility are experienced by all of us: whether induced by normative ambulatory challenges as we age or as sequela of increasingly-common pathology impacting lower extremity function. A growing wealth of literature clearly indicates that the loss of mobility presents severe physiological consequences – not only in deleterious changes to overall quality of life, but with a plethora of comorbidities that ultimately result in early mortality. Indeed, these effects of mobility loss are considerably evidenced by the progressive, deleterious changes in both skeletal muscle size and quality – phenomena which altogether define muscle degeneration. Whether diagnosed as sarcopenia, cachexia, or muscle degeneration from sequela of trauma, complete etiological definitions and methodological comparisons for the precise, non-invasive quantification of these phenomena remain disparately described in literature.

In the clinical context, medical imaging remains a vital tool for diagnostic and clinical investigations. For the purposes of mobility assessment, though both the lenses of translational myology and surgical planning, the optimization and standardization of soft tissue assessment methodology has been of particular importance. Indeed, visually simplistic medical imaging methods that can enable the noninvasive, high-resolution assessment of diseased or damaged tissues have implicated a wide variety of extant computational and mathematical modeling methods as preferential for investigation in this regard. However, the optimal employment of such methods remains debated, and reported techniques may not be sufficient for various avenues of research in translational myology or surgical planning.

This thesis focuses on the development, application, and assessment of novel methods in computational and mathematical modeling of medical images to quantify muscle degeneration and optimize our understanding of mobility-restorative procedures, such as

Functional Electrical Stimulation and Total Hip Arthroplasty. Additional impacts of these methods are further explored in characterizing the utility of 3D printing for surgical planning, modeling craniofacial electromyography, and computing pre-surgical periprosthetic fracture risk. These investigations altogether present the efficacies and limitations of available image processing modalities, and results and perspectives are herein presented in both a theoretical and practical context. Standardizing computational modeling methodologies for medical image assessment in these contexts would allow for the generalizability of such research to the indication of respective compensatory targets for clinical intervention.

### ***Contributions:***

The remainder of this thesis is organized into eight chapters. Chapter 2 outlines the state of the art in translational myology and medical image analyses by computational and mathematical modeling, highlighting the scope and implications of current research. The main contributions of this thesis are then presented in Chapters 3 to 8, before concluding and outlining future directions in Chapter 6. The bulk of the main contributions in this thesis are derived from a series of publications in their respective topics; it is important to note that many of these results represent a cumulative and procedural line of investigation and some preliminary results are therefore further expanded in later, related chapters. It is to our belief that this representation does not invalidate the reported findings; rather, organization in this regard serves to inspire a thorough discussion of each topic, defining branching points for commensurate iteration in future or parallel works. The main contributions of Chapters 3 to 8 are hereby summarized as follows:

- ***Chapter 3:*** The focus of this chapter is on the introduction of the impacts of modern methods for X-Ray Computed Tomography image analyses in the contexts of investigating muscle degeneration, functional electrical stimulation, and total hip arthroplasty. The intent of the collection of these works is to inspire a discussion of extant assessment methods and therapeutic interventions currently investigated by the fields of translational myology and surgical planning.
- ***Chapter 4:*** The focus of this chapter is on the definition and utility of our novel method for quantifying muscle quality by radiodensitometric attenuation distribution analysis using a combinatorial methodology involving nonlinear trimodal regression analysis and histogram iteration via a generalized reduced gradient algorithm. This method was tested first with three subjects with varying degrees of muscle quality defined by their respective conditions as a proof-of-concept. Following this, the utility of the method was demonstrated with a cohort of total hip arthroplasty patients to investigate changes in periprosthetic muscle quality according to implant procedure and post-surgical normalization of ambulation.
- ***Chapter 5:*** This chapter continues the investigation on the utility of the abovementioned nonlinear trimodal regression analysis method by assembling computed tomography radiodensitometric distributions, cross-sectional areas, average Hounsfield unit values, lower extremity function biometrics, and sarcopenic comorbidities in the AGES-II database of 3,162 aging subjects. This investigation highlights the specificities of each muscle quality metric as quantitative indicators

for sarcopenia.

- **Chapter 6:** This chapter describes the novel assembly of biometric assessment and computational modeling modalities from a 100-patient total hip arthroplasty cohort as a first step towards creating patient-specific applications that rehabilitators and orthopedic surgeons can utilize for prescribing their respective surgical procedures. Along with outlining further utility of the previously-described nonlinear trimodal regression analysis method for muscle quality assessment, this investigation reports notable aspects of each patient's dataset and compares these results across available subgroups of the cohort, highlighting the combinatorial utilities of each reported modality.
- **Chapter 7:** The objective of the research presented in this chapter was to continue computational modeling discussion in the context of surgical support by describing a novel finite elements analysis methodology for patient bone mineral density and fracture risk evaluation before total hip arthroplasty surgery. The presented results highlight the feasibility of the methodology as a foundation to develop a clinical database for correlating bone mineral density obtained from computed tomography images with computational methods for assuming fracture risk and predicting patient outcomes.
- **Chapter 8:** This chapter contains two additional computation and mathematical modeling applications across the aforementioned fields of translational myology and surgical planning. The first of these studies describes the recapitulation of craniofacial morphology as a crucial first step in developing an anatomical model for the isolation and removal of confounding low-amplitude craniofacial electromyographic signals from electroencephalography datasets. The second study reports the integration of 3D-printing process with diffusion tensor imaging for neurosurgical planning, in association with surgical navigation systems.

**Chapter 9** is a conclusion of the contributions made to this thesis.

## Chapter 2

### Background

#### 2.1 The Biological Importance of Skeletal Muscle Quality and its Impact on Mobility and Mortality

Muscle degeneration, characterized by the progressive loss of muscle mass, strength, and function, has been consistently identified as an independent risk factor for high mortality in both aging populations and individuals suffering from neuromuscular pathology or injury [1-7]. When associated with aging, this phenomenon is defined as sarcopenia, and while its prevalence has been readily linked with profound decreases in both physical activity and vitality, a precise, quantitative method for defining its diagnosis and etiology remains unknown [8-10]. However, despite the absence of a universally accepted definition, extant clinical literature commonly acknowledges the association of sarcopenia with the loss of both skeletal muscle structure and function, and many mechanisms have been implicated to govern these changes [11-20]. Regardless of origin, the loss of skeletal muscle mass, quality, and strength have all been directly correlated to eventual mortality in middle-aged and elderly adults [25, 26]. With a suggested prevalence of over 50% in individuals aged over 80 years, it is clear that identifying a normative clinical definition for sarcopenia is of considerable importance in an increasingly aging world [7].

Regardless of the cause for muscle degeneration, it is clear that one of the key, deleterious impacts of the loss of muscle form and function is on personal mobility. Mobility is not only critical for maintaining one's physical independence, but also for establishing normative biological function. Indeed, studying how changes in muscle mass and quality affect mobility is the prime motive for the field of investigative lower extremity function (LEF), which cites LEF as the main indicator for mobility as a clinical screening tool [27]. LEF is generally assessed by measuring both walking capacity (gait speed) and leg strength [28], and in the context of sarcopenia research, a growing wealth of literature cites regular physical activity in early life as being associated with increased mobility and delayed onset of sarcopenic muscle degeneration in old age [24, 27-31]. Many such studies additionally cite the association of diagnosed sarcopenia with decreasing LEF performance and induced mobility impairment, incident disability, and eventual mortality [24-26, 32, 33]. Such investigations solidify the critical importance of mobility and sarcopenia research to the

field of translational myology, as an intimate understanding muscle would further sharpen the potential biological mechanisms of muscle degeneration that govern changes in LEF biometrics. This chapter serves to outline many of such mechanisms and are herein discussed in detail; to begin, we will discuss these mechanisms in the context of sarcopenia.

Sarcopenia was originally described only decades ago as the age-related loss of skeletal muscle mass, in association with decreases in both muscle strength and impaired mobility [34, 35]. Despite its prevalence being characterized by both high mortality and profound decreases in physical activity and overall quality of life, a normative quantitative definition for its diagnosis and etiology remains debated around the world [8-10, 34-36]. Nonetheless, investigations into the decline of muscle mass across the adult lifespan generally agree that the onset of sarcopenia typically occurs in the third to fourth decade of life [37, 38]. However, the rates of loss in these metrics have likewise been shown to be highly variate: the loss of muscle strength being as high as 1-3% per year, whereas the loss of muscle mass seems to be comparatively less, at 0.4%–2.6% per year [39, 40]. While muscle biopsy remains the investigative gold standard for assessing these changes, the procedure remains highly invasive and thereby impractical for consistent, non-essential lifecourse assessment in aging individuals. Instead, a host of non-invasive biometric assessment modalities have been implicated for their comparative utility in this regard: from more clinically “exotic” modalities like dual X-ray absorptiometry (DXA) or bioelectrical impedance (BIA) [41] to traditional medical imaging modalities such as magnetic resonance imaging (MRI) or X-Ray Computed Tomography (CT) [13, 23, 36, 42-47]. Sections 2.5 through 2.7 further explore the respective utilities of mycological assessment with a host of such medical imaging modalities – notions which are further supported by publications embodying several chapters in this thesis.

Aside from highly evident mycological assessment metrics, such as cross-sectional area and mass, additional changes to muscle occur that may be somewhat obfuscated. The most challenging of these phenomena to model is the non-contractile tissue infiltration of muscle volumes, known as myosteatosis, which has been consistently associated with muscle degeneration. Myosteatosis, in accordance with the loss of muscle size and mass, has been shown to be a direct metric for increased risk for frailty, disability, and eventual hospitalization [24, 29-31, 36]. Many investigations define a commensurate metric for myosteatosis as “muscle quality” – or the degree to which inter- and intramuscular fat tissue is present in a given muscle. While theoretically simplistic in definition, a standardized methodology for robust, quantitative muscle quality assessment remains undefined in literature; although, many mechanisms have been shown to influence muscle quality, including muscle architecture, fiber type, aerobic metabolism capacity, fibrosis and myoneural activation. Section 2.2 discusses these underpinning mechanisms in detail and highlights their potential for serving as metrics for muscle quality.

In addition, the potential mechanisms that govern muscle degeneration in sarcopenia have likewise been identified within the context of neuromuscular pathology (cachexia) or injury. Indeed, the dramatic deleterious changes in muscle composition and function exhibited in these patients have been implicated as accelerated analogues to the changes evidenced in sarcopenia. This notion is especially evident in patients with spinal cord injury (SCI), as paralysis from lower motor neuron denervation drastically reduces skeletal muscle mass and increase local muscle adiposity and fibrosis [44, 45]. One extreme sequela of SCI is irreversible *Conus* and *Cauda Equina* syndrome. In this syndrome, ischemic and/or

infective complications may extend the traumatic damage of the spinal cord, thus inducing the permanent disconnection of leg muscles from the nervous system. Soon after SCI, leg muscle fibers below the spinal cord lesion become inactive (flaccid) and atrophic, and within only a few years they are progressively replaced by fat and fibrous connective tissues [44, 47-56]. Sections 2.3, 2.7, and 3.2 in this thesis delve into further details in this regard, detailing several representative case studies and applied myological assessment methods.

## **2.2 Mechanisms of Skeletal Muscle Degeneration**

Whether by sarcopenia, cachexia, or sequela of trauma, methodological comparisons for the precise, non-invasive quantification of the progressive reduction of muscle quality remain disparately described in literature. Standardizing a quantitative methodology for myological assessment in this regard would allow for the generalizability of sarcopenia research to the indication of compensatory targets for clinical intervention. In the following sections, we discuss the mechanisms underpinning changes in muscle quality and highlight the potential ways to utilize them as quantitative metrics for myological assessment.

### **2.2.1 Size and Myofiber Contractility**

The overall size of a particular muscle is largely determined by both the number and type of myofibers present within the tissue volume [36, 49]. A common metric for overall muscle size involves the segmentation of medical image cross-sections to compute cross-sectional area: a technique further explored throughout this thesis (procedural details and impacts are discussed primarily in Section 2.5.2). It may be somewhat apparent, but it is nonetheless important to note that muscle cross-sectional area has a proven direct correlation with overall muscle strength [50]. However, as a note of caution: increases in cross-sectional area do not always imply an increase in muscle quality: indeed, increases in overall muscle size is obfuscated by increased body mass index (BMI) in normal to obese men and women [51]. As previously mentioned, this type of hypertrophy may be induced by the phenomenon known as myosteatosis: more commonly referred to the infiltration of inter and intra-muscular adipose tissue [49]. However, if myosteatosis is not apparent from medical image analysis, and one observes hypertrophy due to the increased presence of lean muscle tissue (e.g., a recapitulate normalization of muscle quality), a commensurate rescue of muscle strength is observed: Sections 2.3 and 2.4 discuss the recovery of muscle strength via increased myofiber number from volitional exercise and a home-based therapy known as functional electrical stimulation.

Aside from myofiber number, as previously mentioned, myofiber type is likewise an important defining characteristic of overall muscle strength. However, myological assessment in this regard is distinctly challenging, as the only reliable extant method for myofiber analysis is that of invasive muscle biopsy. Nonetheless, analysis in this regard remains of key interest and importance to the field of translational myology – especially in the investigation of muscle degeneration. Myofiber type can be broadly categorized based on the metabolic capacities of the muscle in-question, and three of such types are generally identified: types I, IIa, and IIb. Type I myofibers predominately generate energy via oxidative mechanisms dictating long, low-amplitude force generation, whereas both type II myofibers, type IIa and IIb, induce high-force, quick force production via non-oxidative pathways [52]. Indeed, observation of athletes whose muscle utilization is purposefully



stratified is an effectual method for understanding the broad impacts of having more or less of each fiber type. Elite endurance athletes' muscles are comprised primarily of type I fibers, as long-twitch activation gives rise to specialized muscles capable of withstanding long-duration contractile activities; whereas, conversely, type IIa and IIb fibers facilitate short-duration, high-twitch force activities in elite strength/power athletes [53]. Regarding the relative size of each fiber type, type I fibers exhibit relatively small cross-sectional areas compared to type II fibers, but their oxidative capacity is significantly higher – a predictable notion, given their relative physiological roles [54]. In advanced age, there is still much debate as to whether observable shifts in myofiber type composition occur: some investigations suggest a reduced presence of type IIb fibers with age [55], while others report no significant changes, when controlling for other age-related changes in muscle utility [56]. Indeed, since type I fibers predominantly govern low-impact activities such as general ambulation and ordinary mobility tasks in daily life, it is reasonable to expect that shifts in fiber type towards predominantly type I fibers would follow from general disuse atrophy and denervation observed in aging populations. Likewise, skeletal muscle with a significantly-reduced proportion of glycolytic type II muscle fibers in-turn directly elicits diminished myofibril contractility – a phenomenon likewise observed in aging muscle [11, 12, 52-56]. Unfortunately, longitudinal changes in myofiber composition in aging humans remain disparately present in literature – most likely due to the expense and aforementioned invasiveness of muscle biopsy [60-63]. Likewise, whether this shift has any impact on overall mobility and lower extremity function remains contested and limited by the availability of such investigations [12, 57-59]. If, in fact, myofiber contractile properties are indeed preserved with age, this would imply that such differences in skeletal muscle function are related to muscle fibre size or number rather than the more quasi-quantitative changes observed in studying myofibril contractile characteristics.

While human research in these topics remains generally underperformed, many studies utilizing animal models report intriguing findings. As an example, the  $Ku80^{+/-}$  knockout mouse, an animal displaying accelerated muscle aging while in the presence of normal postnatal growth, has shown an increased proportion of slow type I fibers with a decreased proportion of faster type II fibers in the soleus muscle, highlighting many of the aforementioned human sarcopenia studies involving muscle biopsy [60-63]. Conversely, however, a follow-up study identified that rhesus monkeys with characteristic sarcopenia exhibited shifts in both oxidative phosphorylation (a marker for mitochondrial metabolism) and fiber type composition away from type I fibers towards myosin heavy chain (MHC)-rich type II fibers [64]. This oppositional shift has been likewise identified in human patients, but these changes were evidenced in generalized disuse atrophy rather than sarcopenia, wherein fiber size was shown to decrease in the transition from type I to type II fibers, yet with the maintenance of overall fiber number [60, 65-67]. With these studies in complete contrast, it remains clear that additional mechanisms in muscle degeneration may exist that encourage either type of fiber type transition.

### **2.2.2 Architecture and Fibrosis**

In addition to observations regarding changes in myofiber type and contractility with age, the overall muscle architecture has likewise shown intriguing changes. Muscle architecture, broadly defined, is dictated by the overall arrangement of myofibers within the muscle volume, which may be evidenced by either parallel or pennated patterning. The degree to

which myofiber pennation is present, as well as the magnitude of relative pennation angles, has been shown to impact both fascicle length and total lean cross-sectional area [36, 68]. In aging, ultrasonography has been utilized to assess these effects in the *gastrocnemius medialis* muscle in elderly adults, showing decreases in both fascicle length and pennation angle with advanced age [69]. However, once again this notion seems to be different in relative disuse atrophy, as muscle degeneration from long-term bedrest has not shown significant changes in pennation angle [70]. Such contradiction in literature again reinforces the need for further longitudinal investigation in aging individuals with cachexia and sarcopenia.

Alongside changes in muscle architecture, muscle fibrosis has been observed due to the relative impairment of muscle repair processes in both individuals with sarcopenia or muscle degeneration as a sequela of traumatic injury. Fibrosis, on a biological level, is characterized by the deposition of structural extracellular matrix (ECM) proteins (most predominantly collagen) instead of more functionalized proteins involved in the various complex signaling pathways of muscle repair, restoration, and normative function [71, 72]. The process of pathological fibrosis can be thought of as the final step in the biological procedure of injury repair, first involving inflammation, muscle degeneration, and ECM-depositing fibroblast proliferation [71, 72]. Furthermore, in the context of the aforementioned presence of myosteatosis in aging muscle, the commensurate presence of fibrosis has been observed [73, 74]. Likewise, stem cells in the pre-myocyte lineage have been shown to transition from myogenic to fibrogenic lineage in aging mice [75]. While precise analysis of this transition requires tissue resection and intensive labwork, tissue fibrosis is detectable using traditional medical imaging modalities, such as CT, MRI, or ultrasound, to a degree; however, their traditional employment methods aiming to detect and diagnose pathological hepatic fibrosis may not be optimized for detecting minute changes associated with the onset of sarcopenia or cachexia. Indeed, the contribution of fibrosis to traditional metrics of muscle quality remains an essential target for further investigation.

### 2.2.3 Aerobic Capacity

As is true with the aforementioned characteristics of muscle, shifts in aerobic metabolic capacity are likewise key determinants of muscle quality and function. Myological aerobic capacity is defined as the maximal ability of muscle to utilize oxygen to meet the demands of the physical activity being performed. In this regard, aerobic capacity reflects not only the degree to which cardiovascular adaptation for the transport of oxygen is exhibited, but also specific adaptations within muscle to utilize delivered oxygen. Many of these adaptations, such as mitochondrial DNA content, mRNA abundance, and adenosine triphosphate (ATP) production, have been shown to decrease along with increasing age in older adults [76, 77]. Evidently, aerobic capacity, as measured by skeletal muscle mitochondrial capacity and efficiency, has also been implicated as a strong predictor for general mobility, as measured by average gait speed in advanced age [78, 79]. For the purposes of further discussion, the effects of volitional exercise in early age and how this affects the onset of sarcopenia in older adults is further explored in Section 2.3 of this thesis.

While many mechanisms have been identified for their utility in measuring skeletal muscle metabolism, whole-body glucose uptake presents a particularly useful metric. Due to skeletal muscle's significant overall demand for glucose, even subtle decreases in muscle mass and consumption can lead to pronounced insulin resistance and equivocal reduction in

insulin-mediated glucose uptake [80, 81]. However, as in aforementioned metrics, evidence for the singular utility of insulin resistance as a direct metric for the onset and progression of sarcopenic or cachectic muscle degeneration remains contradictory, as many potentially-obfuscating factors exist that could confound results, such as volitional physical fitness, BMI, and myosteatorsis [19, 36, 81-84].

#### **2.2.4 Myosteatorsis**

In recent years, myosteatorsis, or the aforementioned presence of inter- and intramuscular adipose tissue, has emerged as a primary target for muscle quality research. The increased muscle adiposity and decreased contractility associated with myosteatorsis has been linked to mitochondrial dysfunction and impaired oxidative metabolism, which has been shown to secondarily induce metabolic insulin resistance and Type 2 diabetes mellitus in patients [29, 85]. In general, non-contractile tissue infiltration, in accordance with a loss of muscle mass, confers an increased risk for frailty, disability, reduced mobility, and eventual hospitalization [30]. In addition to muscle infiltration, much of the detrimental consequences in myosteatorsis additionally arise from the migration of subcutaneous adipose tissue to intermuscular barriers near or within vital organs [49, 86]. Indeed, a direct link between aging and increasing degrees of non-contractile tissue infiltration in thigh muscle has been observed [30, 31]. However, a precise definition for the onset of myosteatorsis contains a number of often-interchangeable parameters, such as the direct measurement of ectopic adipose tissue under the muscle fascia, or the presence of low radiodensitometric attenuation values in muscle morphology measured by CT [36, 43]. MRI has likewise shown feasibility in correlating the direct measurement of muscle lipid droplet content, which has likewise been implicated as the most robust predictor of mobility in sarcopenia patients, compared to strength and quadriceps lean muscle cross-sectional area [87]. However, despite the superior soft tissue contrast in MRI and non-dependence on the use of ionizing radiation, CT has higher spatial resolution and is comparatively less obfuscated by technical variations in machine preparation and acquisition protocols [71, 88]. These notions are critical when attempting to discern diagnostically-relevant information from cross-sectional images of soft tissue, and further discussion on the comparative utility of CT can be found throughout this thesis, but primarily in Section 3.1.

#### **2.2.5 Neuromuscular Activation**

In addition to alterations in muscle composition and form, components of the neuromuscular system and its activation are likewise commensurate with the degeneration of muscle. Skeletal muscle fibers are organized into bundles known as motor units. Each motor unit is innervated by its own respective motoneuron which is activated by the translation of volitional motor cortex depolarization events transmitted through alpha motoneurons connected to the central nervous system (CNS) via the spinal cord. Throughout out lifespan, motor units naturally undergo phases of remodeling, denervation, and reinnervation. However, investigations estimating the number of motor units, measured by both surface electromyography (EMG) and isometric muscle strength, indicate that there is some degree of progressive denervation in advanced age [89, 90]. However, surface EMG signals are sensitive to the presence of adipose tissue; thus, changes in myosteatorsis, which clearly follow the onset of sarcopenia as previously mentioned, could hamper the interpretation of EMG signals. For this reason, the general efficacy of EMG to discern these changes remains

debated. It likewise remains unclear whether the loss of motoneurons or the degradation of motoneuronal axons leads directly to the loss of overall muscle strength, as oftentimes adjacent motoneurons respond to the phenomenon by adjacent remodeling via terminal axonal sprouting, which in-turn rescues the innervation ratio of downstream motor units [91, 92]. It has likewise been shown that improvements in neuromuscular activation precede complimentary increases in muscle mass following resistance training, suggesting the importance of including neuromuscular activation as an essential metric for muscle quality [89]. Section 2.3 discusses further evidence from the positive, recapitulative effects of exercise on overall muscle health.

In contrast, long-lasting, complete denervation of skeletal muscles has been shown to result in permanent lower motoneuron (LMN) death in patients with either acute damage, such as spinal cord injury (SCI), or pathological conditions, such as peripheral nerve lesions that result in severe muscular atrophy, apoptosis, and eventual myosteatosis in muscle tissue [93-104]. In either case, the progression of denervation in muscle fibers begins with spontaneous activation, i.e. fibrillation, and eventually leads to myocyte hypertrophy, ultrastructural changes of excitation-contraction coupling, and the gradual loss of excitability via external electrical stimulation using standard commercial electrical stimulators [104]. Finally, muscles enter severe conditional atrophy, wherein myofibers undergo internalization of coil subsarcolemmal myonuclei, resulting in the regrouping of tens of myonuclei at a time within the center of myofibers and the complete disappearance of long segments' contractile apparatuses [105]. Eventually, muscle fibers all but completely disappear, while fibrous and adipose tissue accumulates [106]. Additionally, based on recent results from the CIR-myo-Bank of human muscle biopsies depicting LMN-denervation, the time course of human skeletal muscle atrophy and degeneration has been shown to be longer than what was previously accepted in previous literature [106-108]. The mid and late phases in such degeneration present two very contrasting myofiber populations: beside those which are severely atrophic with internalized groups of myonuclei, large type II myofibers continue to be present four to six years following SCI [109]. With such a window of opportunity for designing methods for clinical intervention, it is key to continue developing robust, non-invasive quantitative methods for myological assessment.

### **2.3 The Effects of Volitional Exercise on Recovery from Muscle Degeneration**

Regular, volitional physical activity is a powerful natural stimulus to help retain or recapitulate aerobic muscle capacity, which can in-turn facilitate the maintenance of muscle function and mobility as we age [110]. Indeed, exercise has shown significant protective effects against the onset of sarcopenia in individuals who are aerobically active in their youth and middle years, as studies have elicited higher muscle strength in these individuals compared to their sedentary peers [36, 93, 106, 111, 112]. The focus of this section is to outline several recent investigations into the mechanisms and impacts of exercise on both the protection and recovery from muscle degeneration. These studies altogether highlight evidence from elite athletes and aging cohorts alike and further reinforce the importance of aerobic physical activity throughout one's lifespan.

### 2.3.1 Exercise and Sarcopenia

As previously outlined in this thesis, sarcopenia is a clinically-diagnosable phenomenon used to describe the loss of muscle mass and function as well as the reduction in force generation and mobility that occurs in elderly persons. Contributing factors include decreased nutrition and muscle disuse which can result in a severe decrease in both myofiber size and number, in particular a loss of the most powerful fast type muscle fibers. Concomitant effects in motor neurons are accompanied with reinnervation by surviving slow type motor neurons [95, 96]. Reduced mobility and functional limitations promote a sedentary lifestyle, leading to a cycle of worsening muscle performance, decreased quality of life, and a predisposition to increased risks of disabilities and mortality. In addition to a progressive loss of muscle mass, aging skeletal muscle also presents with a conspicuous reduction in myofiber plasticity and alterations in muscle-specific transcriptional mechanisms [105, 113, 114]. During the aging process, protein synthesis rates decrease and an increase in protein degradation follows [115, 116], affecting biochemical, physiological and morphological characteristics of muscle fibers [117]. It is generally accepted that a cumulative failure to repair damage is a primary cause of functional impairment in aging muscle [118-121] and that this failure to repair damage is related to an overall decrease in anabolic processes, which promotes the detrimental replacement of functional contractile muscle with fibrous tissue [117].

Volitional physical exercise can reverse these damaging processes [96, 122]. Interestingly, it has been shown that both acute and prolonged resistance exercise stimulates the proliferation of satellite cells in healthy sedentary elderly subjects [123-127], although a recent report suggests that, relative to younger people, the response is blunted in elderly people; this fact may possibly be explained by the reported increased levels of myostatin protein [128] (a negative regulator of muscle mass [129]) in the older individuals. Autophagy, a physiological process by which selected cell organelles and molecules are destroyed, is modulated by physical exercise and plays an important role in muscle homeostasis [130]. An increase in autophagy in the muscle of athletic people has been reported [131, 132], suggesting that exercise may activate an important system that detoxifies muscle cells. Another major factor that is associated with physical exercise is Insulin-like Growth factor 1 (IGF-1) [133]. IGF-1 production by muscle increases after 5–10 min of moderate to high-intensity exercise [134-136]. The evidence suggests that training and regular exercise, by modulating functional autophagy, myokines (IL-6) and IGF-1 expression, can increase muscle strength and attenuate the pathological signs of sarcopenia, thereby decreasing the risk of falls [137-139].

Volitional exercise likewise appear to reverse the effects of myosteatorsis. As previously-mentioned, myosteatorsis is characterized by the presence of inter- and intramuscular adipose tissue and has emerged as a primary target for muscle quality research. This increased muscle adiposity has been shown to directly incur decreased myofiber contractility, mitochondrial dysfunction, and impaired oxidative metabolism, which has in-turn been linked to secondarily-induced metabolic insulin resistance and Type 2 diabetes mellitus [29, 85]. However, after six months of aerobic exercise training and healthy weight loss in subjects aged 60 years, a recent investigation shows decreased intramuscular adipose tissue with concomitant improvement in fasting plasma glucose and glucose tolerances [140]. Conversely, four weeks of enforced sedentariness in healthy young adults induced by unilateral lower limb suspension resulted in a 15-20% increase in myosteatorsis and a

commensurate loss of lower limb strength, calculated after correction for the overall loss of muscle mass [141].

As discussed in previous sections, the increased presence of inter- and intramuscular adipose tissue confers fibrosis and further muscle functional impairment in advanced age. However, modest improvements in overall muscle architecture have been shown after four to five weeks of resistance training in older adults [142]. Likewise, such investigations have shown these changes to occur prior to muscle hypertrophy, suggesting the onset of a progressive recapitulative process [142, 143]. As such, the identification of non-invasive, as-home assessment techniques (a form of ultrasound, for example) for individual use would be of significant practical utility to older adults who would benefit from retaining normative muscle architecture.

### 2.3.2 Decline in Muscle Power Evidenced from Aging Elite Athletes

The rate of muscle power deterioration that occurs with aging has been studied with many different approaches [40]. A famous 1925 paper by Professor A.V. Hill stated that valuable information concerning the physiology and pathology of mobility may be found in the records of sport competitions [93]. Following this suggestion, we studied the performance of world record holding “elite” athletes in various track and field events and deduced relevant hints about the pattern of changes in muscle function from the noted decline over time [94]. Our results showed that age-related power decline typically commences after age 30 and continues to decrease toward complete dysfunction, which, according to our models, is suggested at approximately the age of 110 years (Figure 2.1).

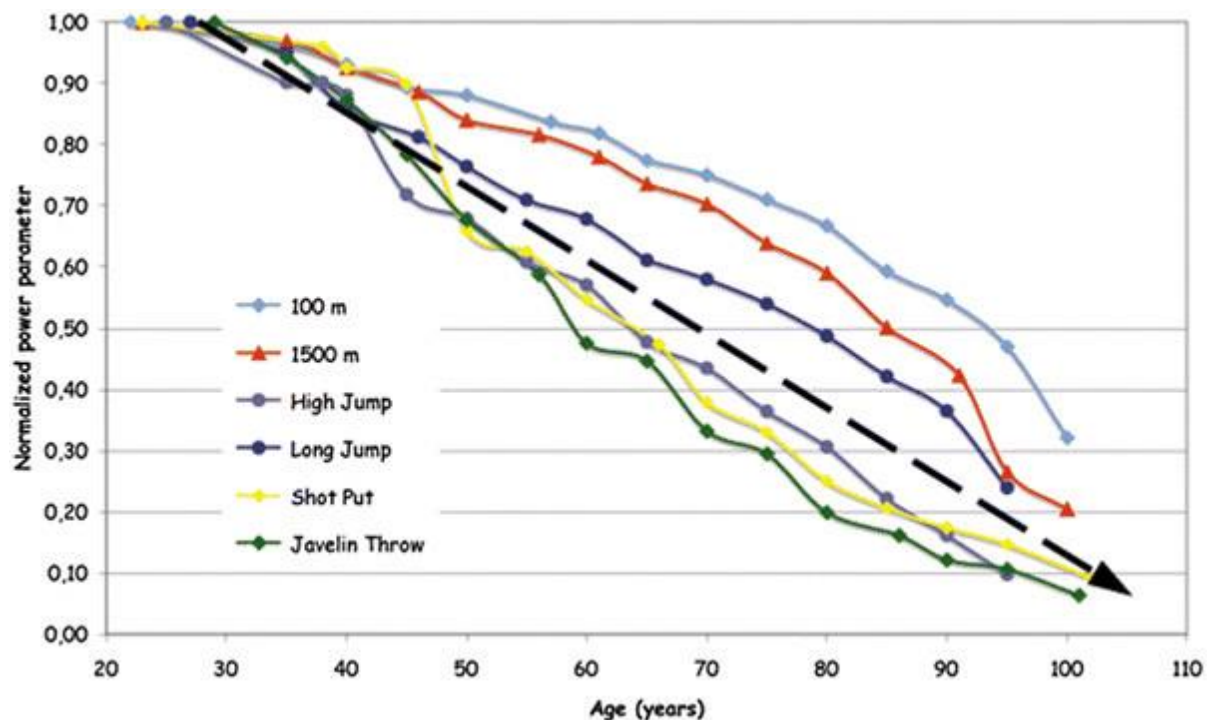


Figure 2.1: Age-related decline of skeletal muscle power derived from world records of running, jumping and throwing events of elite athletes within different age classes [94]. Each progression is detailed by the individual profession record: light blue: 100m run; red: 400m run; blue: long jump; gray: high jump; yellow: shotput, green: hammer throw.

What we believe is the most surprising finding of our investigation is that muscle power declines in a linear fashion and that this loss of power is a rather consistent 25% every 20 years [94]. It is important to note that at any fixed time, each world champion is the best in his area, representing just one out of billions of people. Even these exceptional athletes (conceivably, with optimal genetic backgrounds, focused attitudes towards training and performing, and access to the best personal trainers) lose power drastically as they age. Thus, it appears that something in our genome dictates this decline, and nothing (as of yet) has been found to fully prevent it. Of course, billions of people have performance lines which fall under those of these elite athletes, but for healthy people, the overall trends reported here will, conceivably, be very similar: they will be at their best around age 30, and their performance will analogously decline relatively linearly until their death. Luckily, at seventy years of age, we still have roughly 50% of the power we had in our youth - more than enough for a “normal” lifestyle within a typical lifespan. The size and power of our muscles can go up and down several times in our lifetime in accordance with our nutritional and activity statuses, as well as with our general lifestyle and health; however, no matter how well we may fight aging, in the end, we will lose. Elite athletes may remain stronger than average individuals for decades, but they also are fighting against the same genome-dictated life expectancy.

### **2.3.3 Degeneration and Reinnervation in Average Individuals**

Age-related changes in muscle performance occur even in exceptionally active people – as previously noted by elite athletes [94]. To address the situation for non-exceptionally athletic persons, we also collected data and compared the muscles of young sportsmen with those of two groups of seniors, who were either sedentary persons or those with a lifelong history of a high activity level. The overall evidence here suggested that age-related muscle degeneration is strongly influenced by one’s lifestyle (activity level, in particular), and that the phenomenon is also brought about by the loss of motoneurons and/or motor axons [40, 95, 96]. Electrophysiological and histological measurements of skeletal muscle in older adults have detected reductions in the number of motor units and the presence of fiber type groupings (7-10) that are suggestive of denervation; these occurrences may contribute to aging-related muscle weakness and myofiber atrophy and loss [101-10]). In sedentary seniors, the vast majority of muscle fibers appear to co-express both slow and fast Myosin Heavy Chain (MHC) proteins, and some of these fibers are peculiarly small and angulated in appearance – likely a result of being denervated [96]. In contrast, there are larger muscle fibers in the senior amateur sportsmen, and most interestingly, there is a larger number of slow fiber type groupings in these muscles [96]. The “type grouping” is strong evidence that the grouped muscle fibers were “denervated” and then “reinnervated” by different motoneuron axons [96,105]; their number and distribution, however, do not suggest a process of muscle fiber transformation related to the kind of exercise performed by these very active seniors [95, 96, 105].

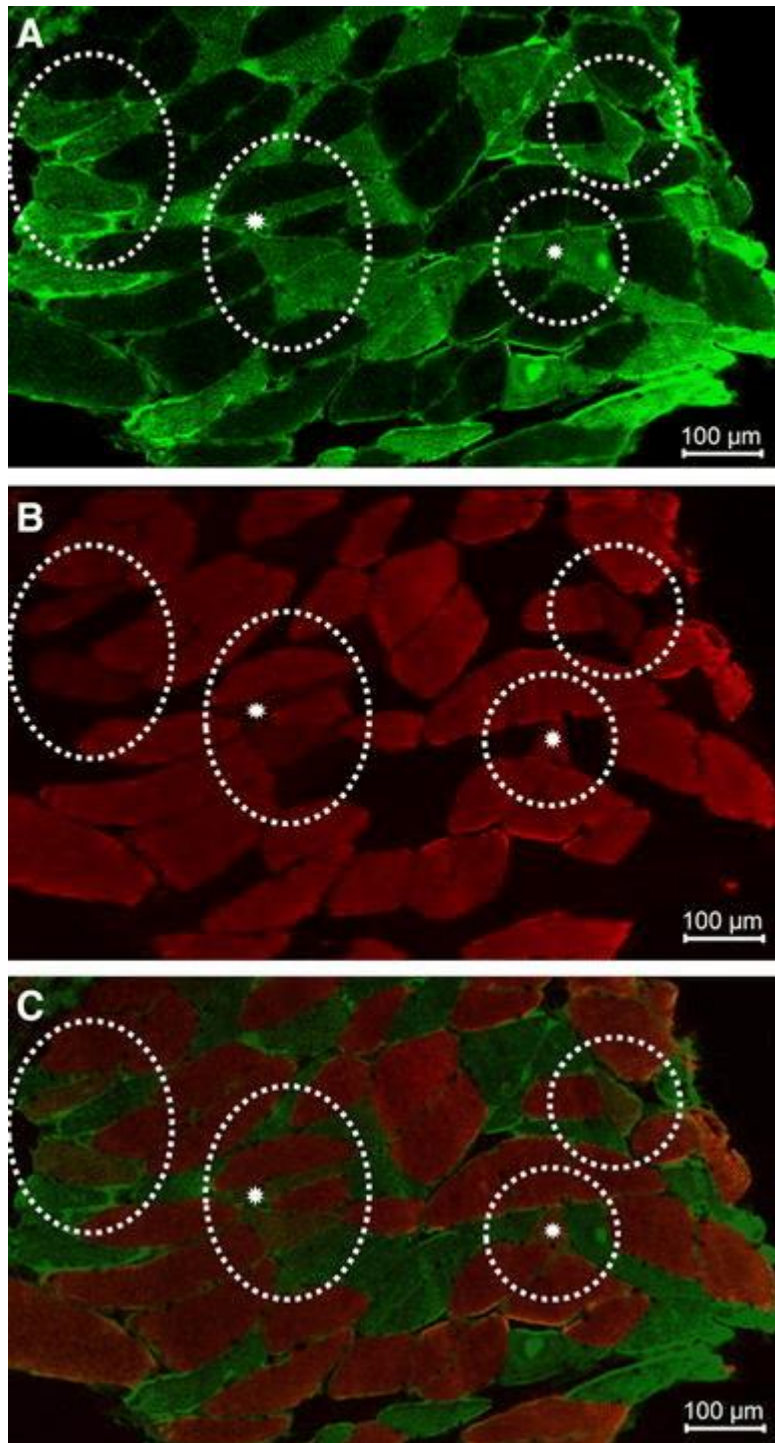


Figure 2.2: Denervation/reinnervation process starts with a checkerboard cluster of muscle fibers. a) Green fluorescence identifies fast MHC type fibers, while b) the red indicates slow MHC type fibers. Fibers that co-express both fast and slow MHC (circled in c) are either normal-sized or atrophic (white star). It is likely that these are fibers which have been denervated by axonal damage and then reinnervated by a single regenerated motor axon

Figure 2.2 shows that the denervation/reinnervation process starts with a checkerboard cluster of muscle fiber types that are denervated by axonal degeneration and then reinnervated by a single regenerating motor axon. Incremental summation of



denervation/reinnervation processes may occur to such a degree that whole muscle biopsies might exhibit very large, almost complete reinnervation of the constituting muscle fibers [96]. Furthermore, and more importantly, in the senior sportsmen, muscle fibers co-expressing both slow and fast MHC are normal in size and often fill in the gaps that occur between clusters of slow myofibers. We suggest that these fibers were once of the fast type, but have been reinnervated by axons sprouting from nearby slow motoneurons [96]. Consonant findings are reported in a recent study of older obese adults, showing that five months of resistance training enhanced skeletal muscle innervation [106]. Furthermore, indirect evidence of the occurrence of background denervation in aging was reported from the electrostimulation of leg muscles in old rats. A stimulation protocol that maintained mass and force of denervated *extensor digitorum longus* muscles of young adult rats analogously maintained these properties in old rats during a two month period of age-induced decline [107]. Contractile activity generated by the electrical stimulation eliminated age-related losses in muscle mass and reduced the deficit in force by 50%, providing support for the hypothesis that during aging, decreased contractile activity in fibers contributes to muscle atrophy and even more weakness.

Why muscle fibers are preferentially reinnervated by axons sprouting from slow motoneurons with age is a critical question. Our opinion is that this is related to the fact that slow motoneurons are activated much more often per day than fast motoneurons [108] and that their frequent firing preferentially spares them [109]. Thus, greater activity maintains the slow-type motoneurons and muscle fibers. It is possible that as much as 1% of fibers lose innervation and are almost all reinnervated every month past the age of 30 [40]. This may not seem impactful, but over a time-span of 40 years, this 1% per month results in a substantial series of denervation/reinnervation events. Furthermore, it may, at least in part, explain why older people have slower muscles. Regardless, the fact is that sedentary senior people and lifelong, highly active seniors have different distributions of both muscle fiber diameter and type. The senior sportsmen who were highly active up to the day of the muscle biopsies had been active for as much as 40 years prior. This is majorly different from participating in sport activities for only 10 years during one's youth.

The idea that denervation occurs naturally with aging is based on evidence of reinnervation, and we may say this because in the normal muscle of young sportsmen, there are few to no type-groupings [137]. In a recent review, Hepple RT and Rice CL state that “... changes ... affecting the ageing motor unit manifest structurally as a reduction in motor unit number secondary to motor neuron loss, fiber type grouping due to repeating cycles of denervation-reinnervation, and instability of the neuromuscular junction ... Regular muscle activation in postural muscles or through habitual physical activity can attenuate some of these structural and functional changes ...” [144]. We may underscore these statements because, when the type of lifelong sporting activity of seniors is correlated with the extent of type groupings detected, there is no relationship [96]. In our opinion, the key factor is the increased amount of activity, whether this is strength or endurance training. Our conclusion is that senior sportsmen have greater myofiber diameters, a lower percentage of denervated myofibers, and a higher number of type groupings because they are more physically active. It confirms that exercise has beneficial effects on age-related muscle degradation because it promotes muscle fiber reinnervation, preferentially rescuing slow type motoneurons. Indeed, opposite behavior, i.e., increased inactivity in aging, increases muscle weakness and atrophy and the percentage of fast type motor units in the disused muscles [40, 95, 96, 105]. Thus, activity not only maintains the muscle fibers, but also the motoneurons and/or their axon sprouting

potentials [40, 96, 106, 144].

## 2.4 Reviewing a Potential Restorative Muscle Therapy: Home-Based Functional Electrical Stimulation

Unfortunately, elderly people may be unable to adequately participate in physical exercise. Therefore, an at-home, alternative approach to volitional physical exercise for improving muscle function is of particular interest to the field of aging research and translational myology. The focus of this section is to introduce the procedure known as home-based functional electrical stimulation (h-bFES) and initiate a discussion regarding its potential restorative utility in this regard.

The investigation of h-bFES began with the design of a stimulator for neuromuscular electrical activation that was motivated to especially suit the requirements of elderly people with diminished motor skills [145]. As detailed in Kern et al. [115], initial h-bFES research involved exposing subjects to regular neuromuscular h-bFES training for a period of nine weeks. The outcomes reported here were threefold: subjects exhibited an increase in muscle strength, an increase in overall myofiber number, and, most importantly, an increase in percent composition of fast type-II fibers (which, as previously detailed in this thesis, are directly related to the power of skeletal muscle) [115]. Because insulin-like growth factor 1 (IGF-1) is one of the signaling molecules activated during physical exercise, whether h-bFES would induce an increase in expression of IGF-1 in these subjects, along with certain other known components of the IGF-1 downstream signaling pathways, was of prime interest. Indeed, we discovered that h-bFES increases expression of IGF-1 and markers of both satellite cell proliferation and extracellular matrix remodeling, and this increase in expression downregulated the expression of protein-degradative enzymes. These data demonstrated that h-bFES stimulates not only anabolic pathways, but downregulated muscle catabolism [115]. In this work, collagen expression was likewise explored, and it was reported that analogous myological remodeling was present during both volitional physical exercise and h-bFES. Indeed, three different forms of collagen (I, III and VI) were upregulated in electrically stimulated muscle, but these increases in collagen likely did not stimulate the process of fibrosis, as was shown by both morphological evidence and the expression of miR29, an important regulator of fibrosis [146, 147].

### 2.4.1 H-bFES: Materials and Methods

A typical protocol for h-bFES is herein reported [115, 148]. In this and analogous investigations, patients were provided with stimulators and electrodes in order to perform h-bFES independently for five days per week as described [115, 148]. Large (180 cm<sup>2</sup>) electrodes (Schuhfried GmbH, Mödling, Austria), made of conductive polyurethane, were placed on the skin surface using a wet sponge cloth (early training) and fixed via elastic textile cuffs. As soon as the skin was accustomed to the necessary high current density, gel was used under the polyurethane electrodes to achieve minimal transition impedance. The electrodes were flexible enough to maintain evenly distributed pressure to the uneven and moving skin, thus providing homogeneous current distribution throughout the entire contact area. The particular h-bFES training strategy consisted of four combined stimulation programs, as reported in the literature [148-152].

In this study, since the progression of recovery by h-bFES is inherently slow, patients were clinically evaluated every 12 weeks by physiatrists who progressively modified their training protocols according to the patient's improvements [153, 154]. At two years, 90% of h-bFES trained subjects recovered/increased tetanic contractions and 25% stood during electrical stimulation in parallel bars. Minimal functional improvements were associated with long time elapses between SCI and initiation of h-bFES and, possibly lower compliance with training. In single case reports, low compliance substantially decreased the effects of training, yet in the same subjects the mass of thigh muscles increased when the patient resumed h-bFES [155-157]. Important additional benefits for the patients were the improved cosmetic appearance of lower extremities, the enhanced cushioning effect for seating, and the reduction of leg edema. Further outcomes of our studies are new noninvasive imaging procedures designed and implemented to objectively demonstrate the improvements of muscle mass and contractility, despite permanent LMN denervation [158-160].

#### **2.4.2 The Effects of h-bFES on Recovery from Sarcopenia**

Several longitudinal studies have shown that regular exercise may extend life expectancy and reduce morbidity in aging people [40, 110, 122, 133, 144]. Thus, we sought to compare the effects of regular exercise and h-bFES on senior people. The Interreg IVa project recruited sedentary seniors with a normal life style who were trained for nine weeks with either leg press exercise [161] or h-bFES [145]. Before and after training, subjects were submitted to mobility functional tests, and muscle biopsies were harvested from the *vastus lateralis* muscles of both legs [114, 115]. Functional tests of trained subjects showed that leg press and h-bFES induced improvements of leg muscle force and of mobility [146, 162]. Morphometric and immunofluorescent analyses of muscle biopsies showed that h-bFES significantly increased the size of fast type-II muscle fibers ( $p < 0.001$ ), together with a significant increase in the number of Pax7 and NCAM positive satellite cells ( $p < 0.005$ ). However, a significant decrease in slow fiber type-I diameter was observed in the muscle of both training groups ( $p < 0.001$ ). Further, no signs of muscle damage and/or of inflammation were observed in muscle biopsies after either training. Altogether the results demonstrate that physical exercise, either voluntary (leg press) or induced by h-bFES, improves the functional performance of aging muscles; however, neither training can stop the aging process as we have learned from the Master Athletes. Further, the data show that electrical stimulation in this regard is a safe, home-based method that is able to counteract the atrophy of fast type muscle fiber, a biomarker of skeletal muscle aging [105, 114]. This is especially helpful to individuals unable to exercise adequately as a result of injury, illness, or lack of motivation and knowledge.

In conclusion, physical exercise is partly able to counteract the negative effects of aging on skeletal muscle, and h-bFES, which can be applied to people who cannot or are reluctant to carry out normal physical activity, modulates factors associated with volitional physical exercise [117]. Altogether, these data may serve to aid in the design of rehabilitation strategies that seek to counteract muscle weakness and atrophy, delaying sarcopenic muscle degeneration in advanced aging.

### 2.4.3 The Effects of h-bFES on Recovery from Spinal Cord Injury

A crucial question remains for patients suffering from these types of SCI: Is there anything that can be done in this extreme situation to prevent muscle degeneration? First, we should look at the effects of long-term denervation on human muscle (Figure 2.3). Four phases have been identified: 1) ultrastructural disorganization and loss of contraction in response to ES (within several months); 2) muscle atrophy (up to two years after SCI); 3) muscle degeneration with severe muscle atrophy (three to six years after SCI); and 4) loss of myofibers (more than three years after SCI).

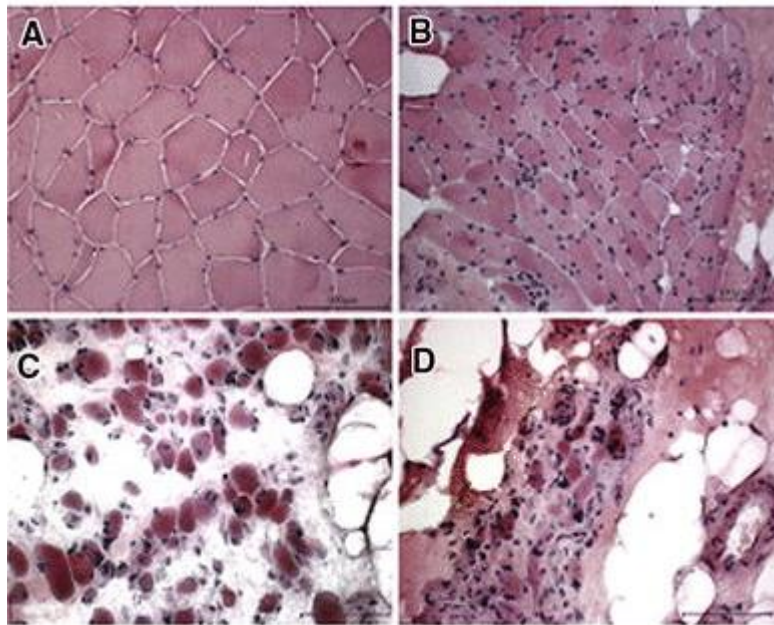


Figure 2.3: Permanent long-term denervation simulates premature aging in muscle. EU Program RISE: use of electrical stimulation to restore standing in paraplegics with long-term denervated degenerated muscles (Contract no. QLG5-CT-2001-02191) [47].

At some point, after more than ten years of permanent denervation, there are almost no muscle fibers remaining in the thighs of these patients. Obviously, the consequences of this degree of muscle loss can be devastating, resulting in increased morbidity and mortality in these patients [148]. On the other hand, in the case of SCI with only upper motor neuron lesions (i.e. below the level of damage requisite to prevent muscle reflex activity or spasticity triggered by stimulation) muscle fiber disuse induces, at most, a 50% decrease in size, which remains stable for at least 20 years post SCI. Additionally, such patients exhibit a stable histochemical ATPase checkerboard pattern, although the slow-type fibers stain more lightly [163]. We have shown that h-b FES of permanently denervated muscles stops and reverses the degeneration of skeletal muscle tissue [48-56]. 2D Muscle Color Computer Tomography scans of thigh muscles in a transverse section (Figure 2.4) demonstrate the effect of h-b FES on long term permanently denervated leg muscles.

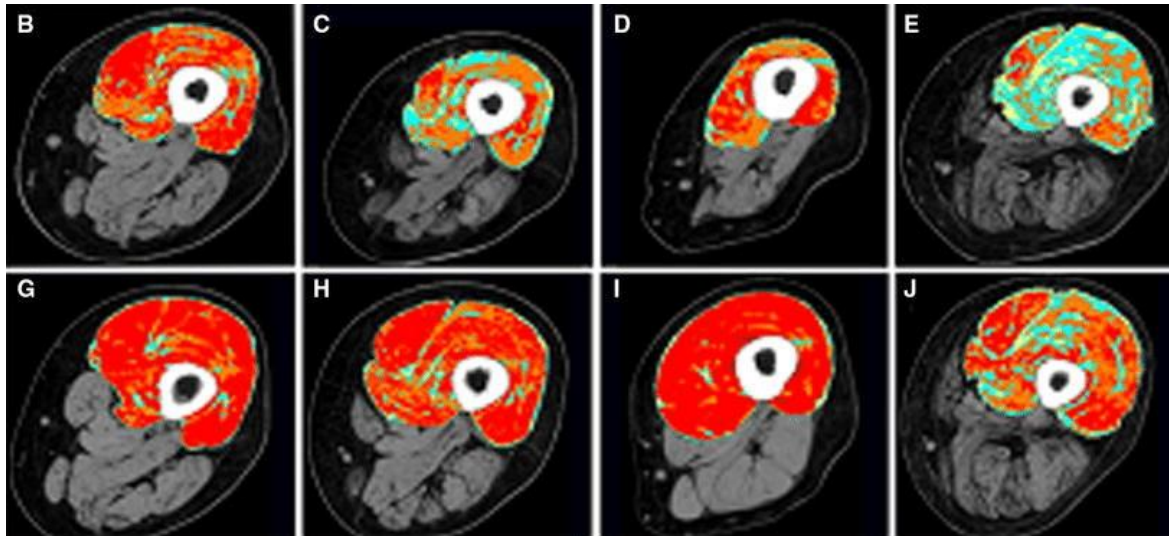


Figure 2.4: 2D Color CT evidence of recovery from permanent denervation (i.e., premature muscle aging) by home-based Functional Electrical Stimulation (h-bFES). Color scans of thigh muscles before (b–e) and after 2 years (g–j) of h-bFES. Each panel Cross-sectional area and the quality of quadriceps muscles in patients starting h-bFES at different time points after denervation (b 1.2; c 1.7; d 3.2; e 5.4 years) increased after 2 years of home training (g–j, respectively). Moreover, the interstitial tissues that increased with post-denervation time (compare yellow, green and blue areas in b–e) decreased in the respective patient after 2 years of h-bFES (g–j, respectively) [47]

Here, the relative amount of muscle increased in each patient after 2 years of h-b FES with a concomitant decrease in the abundance of interstitial tissues. Please note panels B to E (Figure 2.4), wherein we show that following SCI, there is progressive loss of muscle tissue (in red) with an increase in interstitial tissue (yellow, green, and blue represent fat, loose connective, and fibrous connective tissues, respectively). After two additional years of permanent denervation, but with FES treatment (Figure 2.4, G to J), the muscles began to resemble normal tissue. The most impressive evidence for the positive effects of FES on permanently denervated muscles is the extreme differences seen between panels E and J of Figure 2.4. Even after tissue degeneration was evident (at 5.4 years from SCI), two years of home based electrical stimulation substantially improved the percent of muscle content (red area). Indeed, the colors represent different tissues, computed on the basis of their radiodensity (i.e., the amount of attenuated x-rays, in Hounsfield Units). These results are quite astonishing, highlighting the utility of FES to greatly improve even badly degenerated muscle tissue.

Indeed, if people are compliant with the use of h-b FES, then the atrophy of completely denervated leg muscles can be reversed. Despite difficulties with obtaining a response from denervated muscle to surface electrical stimulation, there are protocols involving this technique which defer the onset of the late phases of muscle degeneration. In particular, if FES training is started within the first year following SCI, the retention of muscle is much greater – even almost complete. If one induces many contractions daily in those muscle fibers, that are otherwise destined to die, these fibers will survive and contract for up to dozens of years, but only if one stimulates them with very long, high amplitude impulses delivered by large surface electrodes designed for stimulating denervated muscles. In short, appropriate electrical stimulation coupled with progressive training against increasing load

will recover tetanic stimulation during the first year of training [49-53] and may even rescue the ability to stand up and perform “walking in place” exercises during the second year of FES [54]. Commercial devices that are designed for electrical stimulation of long term permanently denervated muscles and are capable of producing the needed stimulation patterns are currently available. Therefore, this excellent therapy should become accessible to more people for the preservation of skeletal muscle. Thus, one must ask why FES is not more widely used and why it is considered ineffective for treatment of permanently denervated muscles by many specialists in the medical field. This may be due in large part to the fact that the generic words “electrical stimulation” alone are meaningless. For FES to be effective, one has to know which kind of electrical stimulation pattern to use and how much and how often it should be administered. That is, one must know how to correlate appropriate protocols with desired clinical effects.

The RISE trial was designed to determine the effects of treatment on denervated muscle. The final report of this trial was published in the best of the neurorehabilitation journals, *Neurorehabilitation and Neural Repair* (2010) [54]. Afterward, researchers familiar with our publications ceased to criticize FES for use with denervated muscles. Indeed, research conducted over the past 50 years has demonstrated that muscle activity, not neurotrophic substances, is the most important factor in the regulation of size and of specific physiological and biochemical properties of muscle fibers. Application of this knowledge has led to considerable experimentation with chronic electrical stimulation as a possible clinical tool for the treatment of denervated muscles. Evidence accumulated from animal studies has indicated that direct electrical stimulation of denervated muscles can, to a significant extent, directly substitute reinnervation and preserve or restore the normal properties of these muscles. Appropriate stimulation parameters were critical for successful intervention, and the best results were obtained when the stimulation pattern resembled the differential firing pattern of motoneurons [109, 164, 165]. Nonetheless, even now, the vast majority of neurologists and physiatrists, who are not yet aware of those results, profess that denervated muscle cannot be maintained and certainly not regenerated [49, 56, 166]. Furthermore, based mainly on animal studies of the removal of polyneuronal innervation in developing muscle fibers [167], there is a common sentiment that FES may even hamper reinnervation despite the mounting evidence of the role of exercise in maintaining the integrity of the neuromuscular junction [168]. There are also claims that regular muscle activation may lose its efficacy with very advanced age, and that, at least in rodents, this exercise may exacerbate age-related motor neuron death [144]. Contrastingly, many pioneering and recent experiments are showing the contrary. Denervated muscles, stimulated electrically for four days prior to reinnervation, can preserve the structure of the endplate as well as accelerate recovery of normal function in reinnervated muscle fibers after eleven days of denervation [169]. Further discussion into the investigations into the utility of FES can be found in Sections 2.7.3, 3.2, and 3.3 in this thesis.

## **2.5 Advanced Techniques in X-Ray Computed Tomography Image Analysis**

In the clinical context, medical imaging remains a vital tool for diagnostic and clinical investigations. Of the many facets of the field, most current research aims to improve aspects of instrumentation design, data acquisition methodology, image processing software, and

computational modeling. Indeed, three-dimensional (3D) visualization of the internal anatomy provides valuable information for the diagnosis and surgical treatment of many pathologies, but every modality has its inherent limitations. For the purposes of clinical assessment in particular, visually simplistic imaging methods that can optimize the noninvasive, high-resolution assessment of diseased or damaged tissues have readily been identified as a strategic priority in clinical research, and extant imaging modalities have certainly been identified as preferential. However, their employment via standard methodology may not be optimal for various avenues of translational myology research. The implementation of traditional imaging modalities, in the context of a variety of novel case studies, can significantly impact this process of methodology optimization.

X-Ray Computed Tomography (CT) remains one of the most often-utilized imaging modalities in the field of muscle research, as it allows for the precise recapitulation of soft tissue morphologies. Indeed, CT images are often utilized for both diagnostic and therapeutic purposes in a wide variety of medical disciplines. 2D slices from CT scans are of particular utility in identifying key changes in both subcutaneous and intramuscular fat content, selected from defined locations identified from morphological landmarks. As many studies suggest, increased adiposity in this regard can be directly linked to decreased muscle quality and performance, which in turn has severe physiological consequences. This chapter introduces important analytical concepts in CT image analysis that will be further expanded upon in later sections of this thesis.

### 2.5.1 Radiodensitometric Attenuation: Distribution Matrices

The principal objective of medical imaging is to recapitulate morphologies of interest as a digital image consisting of matrices of pixels or voxels. This chapter will focus on X-ray Computed Tomography (CT) – a modality whose image matrices consist of linear attenuation values that are calculated from the specific x-ray absorption characteristics of present tissue. These linear attenuation coefficients may then be linearly transformed into a scale known as the Hounsfield Unit (HU) scale [45, 47].

The HU scale is defined by referencing the radiodensity of distilled water at standard temperature and pressure, thereby defining water and “water equivalent” tissue as having a zero HU value [45, 47]. In this scale, the radiodensity of air under analogous conditions is defined as -1000 HU, and a change of one HU represents a deviation of 0.1% from the attenuation coefficient of water. Equation 1 defines the computation of any image element’s HU value according to its linear attenuation coefficient,  $\mu$ .

$$HU = \frac{\mu_{material} - \mu_{water}}{\mu_{water}} \times 1000 \quad (2.1)$$

When considering CT images of soft tissue, HU distributions of pixel/voxel values typically range from around -200 HU for fat, up to 200 HU including dense connective and muscle tissues [45, 47]. Further sections of this thesis will illustrate a precise, novel method for quantifying these HU distributions, but we will first describe 2D and 3D CT image segmentation, reconstruction, and qualitative analyses. These methods are commonly utilized in both a clinical and experimental context and are important tools for establishing

a baseline for improving our understanding of the mechanisms and implications of changes in muscle.

### **2.5.2 Soft Tissue Segmentation and 3D Modeling**

The dramatic deleterious changes in muscle quality, as evidenced by qualitative CT image assessment, can be further captured by 3D image analysis and soft tissue segmentation. 3D images can be assembled in this regard by the careful slice-by-slice reassembly of a CT scan, which is typically automated by specialized algorithms in CT acquisition. Despite the procedure's utility, the segmentation of particular morphologies from CT images is still relatively uncommon in a clinical context – but indeed, the procedure receives considerable attention in current muscle research literature.

In CT, all tissue types elicit varying degrees of radiodensitometric attenuation, allowing for the precise segmentation of particular tissues of interest. The particular computational method described here is founded upon this critical HU thresholding criteria, which is used in-turn to define different tissues within the muscle. Further details and applications are well cited in literature and described further in this thesis [45, 47]. The main advantage of using this segmentation technique is that it provides the option to reconstruct and analyze entire muscles or muscle groups as a 3D model, which makes it significantly simpler for clinicians to diagnose and visualize discrete changes in any muscle architecture of interest.

The first step in this segmentation process is to establish a threshold, which discriminates tissues of interest from the rest by their grey values, more specifically defined as either CT numbers or Hounsfield Unit (HU) values via the typical CT modality. Visually, this thresholding process allows pixels to be highlighted by colorization, thereby distinguishing pixels with certain HU values from others.

The second segmentation tool which typically follows thresholding is known as region growing. Region growing is an image segmentation approach in which neighboring pixels of the current region's boundaries are examined and added to the region class if no edges are detected (or, more generally, if some inclusion criteria is met). This process is iterated for each boundary pixel in the region, and an arbitrary pixel seed is then chosen and compared with neighboring pixels. This region is then grown from the pixel seed by adding neighboring pixels that are similar, increasing the size of the region. This entire process is continued until all pixels belong to a region. Thus, if there are several compact bones not connected directly to each other in the dataset, region growing enables the display of these bones individually although they indeed have the same threshold.



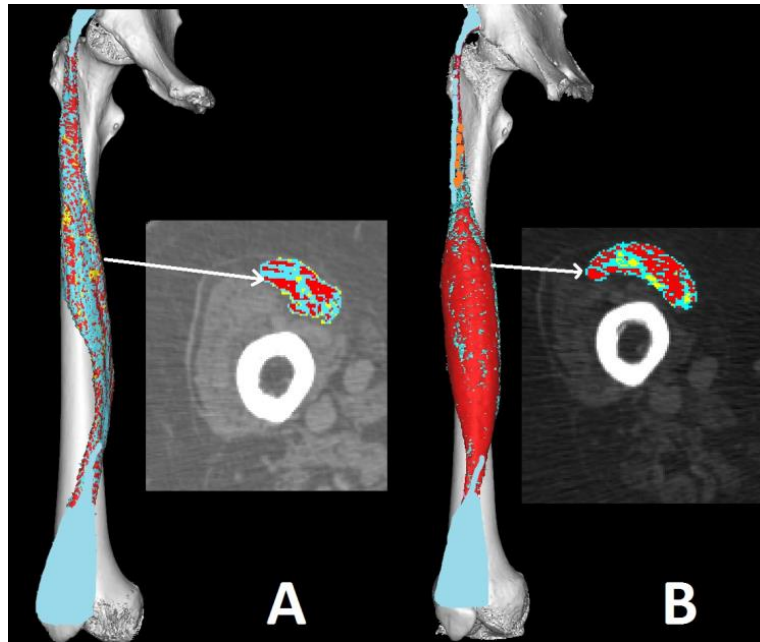


Figure 2.5: Example of 3D soft tissue segmentation utility. This patient was a 52 year old male who had suffered a right pelvic mass infiltration of the sciatic nerve, causing A) complete denervation and severe muscle degeneration of the *rectus femoris* muscle. B) Utilizing the same 3D muscle segmentation technique, clinicians were able to observe significant reinnervation and rescue of normative muscle architecture after one year of home-based functional electrical stimulation [83].

As a preliminary example of the utility of this procedure in 3D, we see in Figure 2.5 a case study with complete and total muscle degeneration. This patient was a 52 year old male who had suffered a right pelvic mass infiltration of the sciatic nerve, which had to be partially sacrificed during surgery, and despite the progressive reinnervation of the thigh and posterior leg muscles using home-based functional electrical stimulation, complete denervation of the *rectus femoris* was once again confirmed after one year post-surgery [83]. Using 3D muscle segmentation and image reconstruction, one may readily isolate the *rectus femoris* as the muscle belly of interest and observe changes in its volume as a function of treatment, as depicted. Further details from this case study and others can be found in Sections 2.7.3 and 3.2 in this thesis.

### 2.5.3 CT-Based Finite Element Modeling

As a novel method to estimate the risk of intra-operative periprosthetic proximal femur fracture in Total Hip Arthroplasty, we herein define the CT-based finite element modeling procedure. This model relies on a pre-operative, calibrated CT scan of the patient, as well as knowledge of the volumetric data and the positioning of the broach and prosthesis. A geometry-based, finite element model is constructed by processing the densitometric and geometric CT information, assuming elastic-plastic constitutive behavior of the bone as function of the local density. Expansion of the broach volume is considered to resemble actual surgery. Distributions of stress and strain inside the femur are then computed, and a strain-based fracture risk factor is estimated in early post-elastic stage.

In order to derive the mechanical properties of bone from the CT scan data, CT numbers or

HU values are first converted into bone densities. Then, bone material properties, in terms of Young's modulus and strength, may be estimated from these data. The relationship between bone density and CT numbers is obtained using a calibration phantom with known material densities. This relationship may be considered linear in the range of interest and can be described by the following equation [446]:

$$\rho_{app}(\mathbf{P}) = phrs \cdot HU + phri \quad (2.2)$$

where  $phrs$  and  $phri$  are the linear slope and rescale intercept.

Moreover, the value of ash density,  $\rho_{ash}(\mathbf{P})$ , is related to apparent density,  $\rho_{app}(\mathbf{P})$ , by means of the following equation [447]:

$$\rho_{ash}(\mathbf{P}) = \begin{cases} 0.522\rho_{app}(\mathbf{P}) + 0.007 & \text{if } \rho_{app} < 1 \\ 0.779\rho_{app}(\mathbf{P}) - 0.025 & \text{if } \rho_{app} \geq 1 \end{cases} \quad (2.3)$$

The relationship between bone density and bone elasticity has been deeply discussed [448-450]. Most investigations report modeling the human femur as isotropic, omitting the orthotropic behavior if the inhomogeneous character of the bone was considered in the model [450-454]. As a consequence, non-homogeneous and isotropic behaviors of femurs are often assumed, giving each point  $\mathbf{P}$  the following correlation between the Young's Modulus,  $E$ , and the local density,  $\rho_{ash} = \rho_{ash}(\mathbf{P})$ :

$$E(\mathbf{P}) = \begin{cases} 33900\rho_{ash}(\mathbf{P})^{2.2} & \text{if } \rho_{ash} \leq 0.27 \\ 5307\rho_{ash}(\mathbf{P}) + 469 & \text{if } 0.27 < \rho_{ash} < 0.6 \\ 10200\rho_{ash}(\mathbf{P})^{2.01} & \text{if } \rho_{ash} \leq 0.6 \end{cases} \quad (2.4)$$

where  $E$  represents the actual local stiffness (MPa) at the generic point  $\mathbf{P}$ .

The choice of a very fine mesh in the FE-model ensures that structural gradients over the Representative Volume Element (RVE) result very small, avoiding conflicts in terms of the relationship between structural gradients and elastic symmetry [455].

Since values of the ultimate tensile stress of trabecular bone are approximately 79% of the compressive yield stress, and values of the ultimate tensile stress of cortical bone are approximately equal to 76% of compressive yield stress [455], symmetrical bilinear isotropic hardening material models have been adopted, neglecting this negligible difference. The yield stress, which corresponds with the mean yield strain, can likewise be set to 0.7% [455], while the tangent modulus can be set to five hundredths of the corresponding elastic modulus [456], depending on local density. Up to four hundred different materials may be implemented in order to mechanically describe the bone tissue behavior in the entire range of density. Poisson's ratio of the bone is typically set to 0.4 [455, 456]. THA prostheses may be modeled as isotropic with Young's moduli equal to 109,000 MPa, and their Poisson's ratios may be set to 0.3. Finally, the model must be constrained in the distal part.

To simulate the actual press-fitting phenomenon (i.e. the interaction between prosthesis and femur), a volumetric expansion of the broach volume should be considered. This expansion may be obtained by applying a temperature gradient  $\Delta T$  to the broach nodes (a temperature rise corresponds to a volume expansion):

$$\Delta T = \frac{\Delta V}{3\alpha} \quad (2.5)$$

where  $\Delta V$  is the percentage difference between the broach and prosthesis volumes and  $\alpha$  is the linear coefficient of thermal expansion of the broach, which was set to  $1.2 \times 10^{-5} K^{-1}$ .

Finally, the difference between the ultimate strain and the yield strain of the bone  $\epsilon_{ult-Y}$ , expressed in terms of the ash densities, may be set equal to the following expression [447, 455, 456]:

$$\epsilon_{ult-Y}(\mathbf{P}) = \begin{cases} 0 & \text{if } \rho_{ash} < 0.433 \\ \frac{15}{3}(-0.00315 + 0.0728\rho_{ash}) & \text{if } \rho_{ash} \geq 0.433 \end{cases} \quad (2.6)$$

When the resultant value of the total mechanical Von Mises strain in a given point  $\mathbf{P}$   $\epsilon_{VM}(\mathbf{P})$  is less than the yield strain  $\epsilon_Y$ , the femoral element can be considered at a low risk of failure (i.e. safe); when  $\epsilon_{VM}(\mathbf{P})$  is between  $\epsilon_Y$  and  $\epsilon_{ult}$ , the bone tissue has to be considered prone to fracture, and finally, when  $\epsilon_{VM}(\mathbf{P})$  is greater than  $\epsilon_{ult}$ , the femoral element is at a high risk of fracture.

## 2.6 Noninvasive Functional Assessment of Engineered Muscle Tissue and Implantable Myogenic Biomaterials: Reviewing Imaging Modalities

Tissue engineering and regenerative medicine are rapidly growing fields of research that aim to use a multi-disciplinary approach to restore or replace tissues that have either been lost or damaged through trauma or disease. Although strategies for restoring function and structure typically vary considerably, most investigations involve the use of cells, biomaterial scaffolds, and various inducible factors which are either directly implanted *in vivo* or first incubated in bioreactors. The complex environments that these components and methodologies generate present unique challenges – not only in generating functional engineered tissue, but in monitoring and assessing outcomes both *in vitro* and *in vivo*.

Of the many tissue types under investigation in these fields, the creation of new muscle through tissue engineering represents a promising alternative to the replacement of tissue after either severe damage or degeneration from various myopathies [170-173]. Surgical reconstruction in patients with significant muscle tissue loss typically utilizes transferred tissue from local and/or distant sites, which often results in significant local denervation, functional loss, and/or volume deficiency [174, 175]. The engineering of lost connective,

nervous, and muscular tissue on a patient-specific basis has been suggested by many to represent the future of muscle surgical reconstruction [176-178]. Likewise, tissue engineering approaches have been suggested for treating musculoskeletal myopathies such as spinal muscular atrophy or Duchenne muscular dystrophy (DMD) [179-181]. However, a common challenge remains in either approach to muscular regeneration – how best to non-invasively assess the viability and function of engineered or extant muscular tissue, both *in vitro* and *in vivo*. This section outlines extant medical imaging modalities and their respective utilities in quantitative muscle or myogenic biomaterial analyses, as published in the European Journal of Translational Myology [71].

### **2.6.1 Extant Functional Assessment Methods and the Expanding Role of Imaging**

As is the common goal in every focus of tissue engineering, engineered muscular tissues should exhibit biomimetic functional properties and recapitulate native structure – specifically with regards to densely packed and uniformly aligned myofibers throughout the tissue volume [170]. As such, methods for assessing cellular viability, proliferation, biological integration, and/or differentiation are crucial to understanding the optimal tissue generation strategies. What is herein broadly referred to as the "functional assessment" of engineered muscular tissue and/or implantable biomaterials depends largely on the methodology employed in the particular investigation. In the case where large volumes of muscular, nervous, and connective tissue must be replaced, regeneration may not be possible by the exclusive transplantation of autologous cells – rather, a bioreactor-based approach may be prescribed, wherein large-volume tissue formation is initiated and controlled prior to implantation. In contrast, in considering general musculoskeletal degeneration due to a particular myopathy, regeneration might be optimally achieved through the injection of myocytes or relevant multipotent progenitor cells, both with or without biomaterials and/or therapeutic factors, to stimulate the release of soluble signals, the formation of extracellular matrix (ECM), and/or the incorporation of new tissues. In either approach to regeneration, functional assessment of engineered cells or large-volume tissues remains a crucial step in quantitatively and non-destructively characterizing and monitoring the dynamic and complex interactions of the host site and engineered cells and/or large-volume muscular tissue [182]. Such assessments are crucial in understanding the optimal methods for rational control of muscular tissue structure and function via complex, temporally-dependent interactions between cells, biomolecules, and engineered scaffolds.

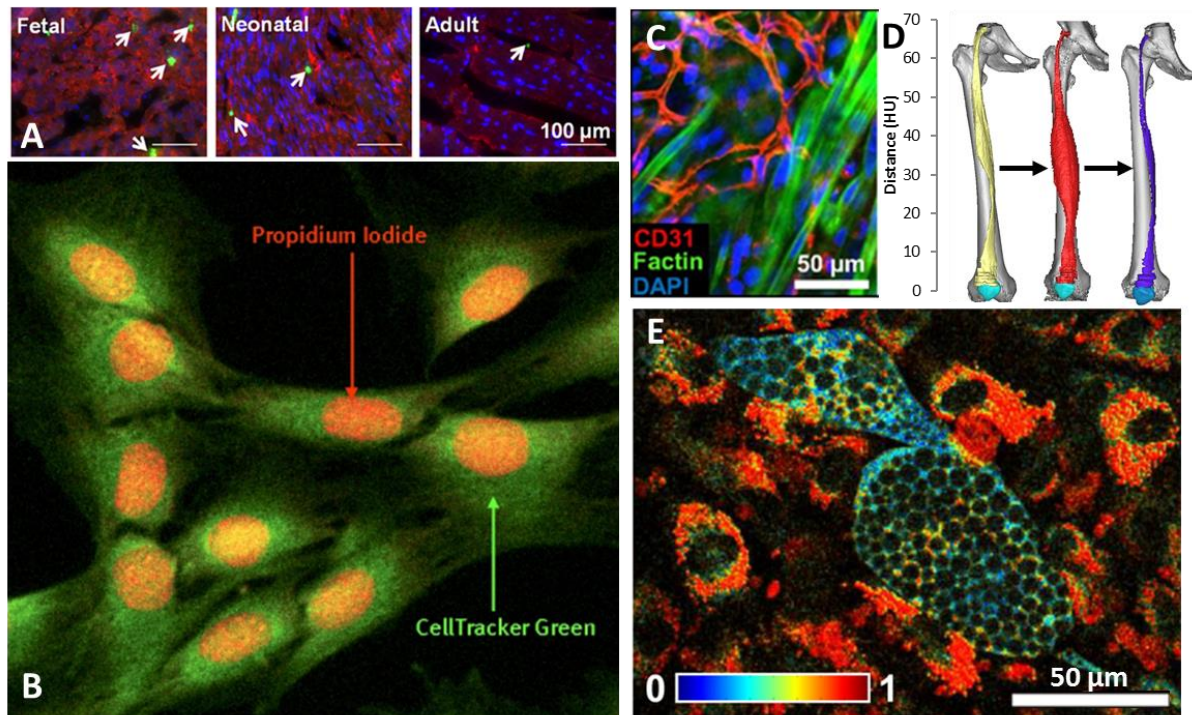


Figure 2.6: Types of functional assessment metrics for various tissue engineering studies. A) Proliferation of cardiomyocytes measured by immunohistochemical staining of phosphohistone H3 [184]. B) Muscle cells viability measured in cells stained with CellTracker™ Green and propidium iodide showing dying myocytes [305]. C) Periphery of implanted engineered muscle showing neonatal rat satellite cells and their myogenic pre-differentiation via f-actin filamentous formation and integration with extant, CD31-labeled endothelial cells [306]. D) CT reconstructions of denervated thigh muscle that was electrically stimulated for growth, highlighting a possible modality for measuring myogenesis in engineered muscular tissue [312, 313]. E) Changes in redox ratios observed in adipogenic differentiation with TPEF along with characteristic, non-autofluorescent lipid droplets [219].

There are many standard analysis methods that are currently available for tissue engineers to utilize at both the individual cell and whole-tissue level, but all of them have their innate limitations (Figure 2.6). For example, metabolomics assays offer only a temporal snapshot of tissue physiological function – an assessment that likewise kills the construct in question [173, 183, 184]. MTT assays can be used as a quick and relatively simple assay for cellular metabolic activity (and, indirectly, viability) but is limited by the use of the tetrazolium dye, as only certain cells can participate in its reduction [185]. Other methods such as fluorescent immunohistological staining or tissue biopsy are labor intensive, invasive, and destructive; thus, multiple timepoints and endpoint studies must be performed and temporal correlation inferred. Rendering engineered cells unrecoverable is of particular concern in cell therapy investigations, where cells and implantable biomaterials are introduced to their hosts and tracked over time to assess both viability and cell fate [182, 186-189].

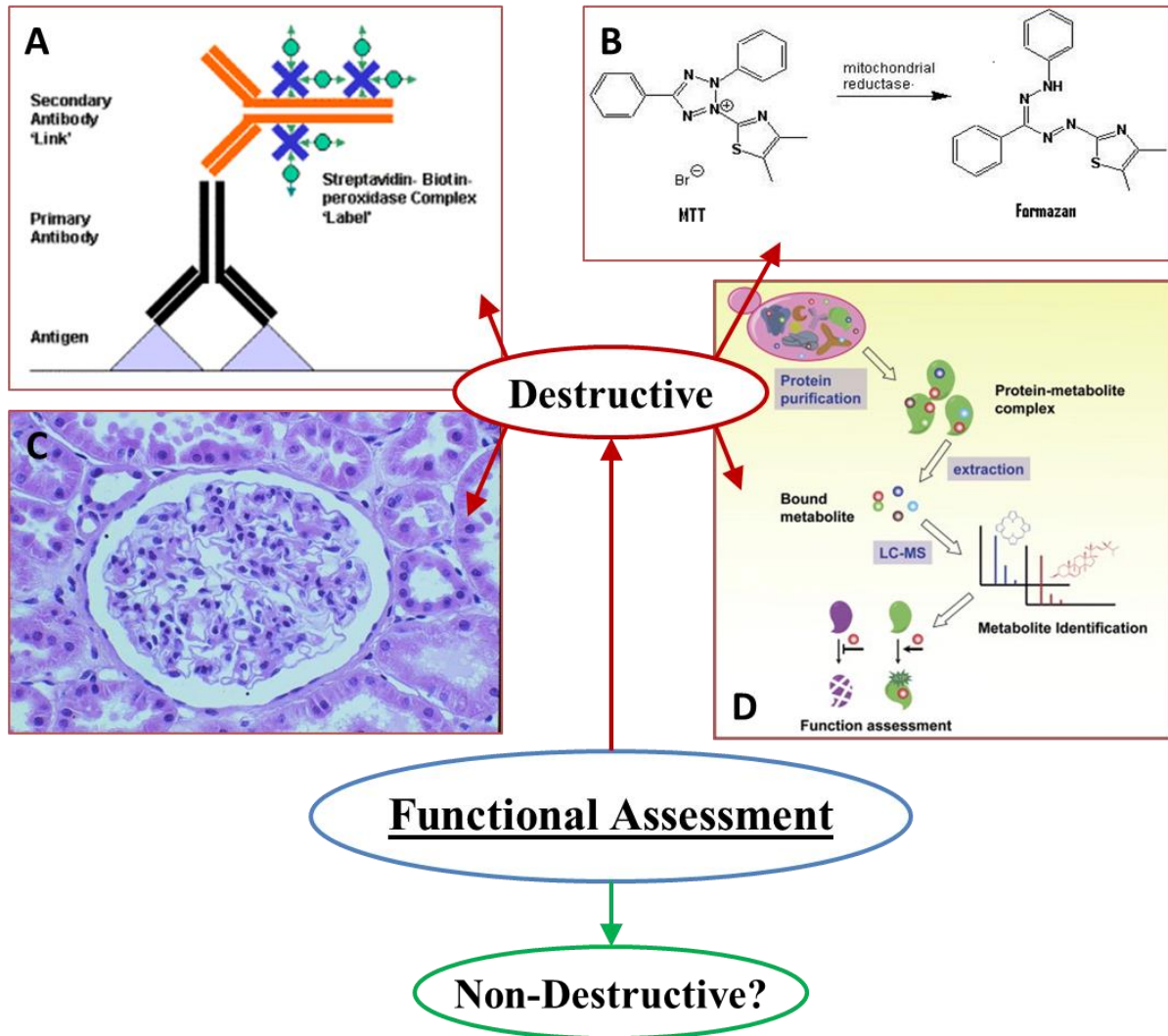


Figure 2.7: Standard destructive methods for the functional analysis of engineered tissue. A) Method outlining the theory behind quantitative immunohistochemistry [30]. B) MTT assay for measuring mitochondrial reduction by the eventual formation of insoluble formazan [308]. C) Histological H&E staining of a renal tissue sample [309]. D) Graphical abstraction of metabolomics [310].

To alleviate these concerns, several noninvasive imaging techniques have recently been developed to obtain information on both cell metabolism and fate in engineered tissues [190-198]. These methods exploit a number of intrinsic cellular phenomena, such as autofluorescence and tissue glycolysis. While many of these methods have shown considerable promise, it is important to comprehensively distill their respective benefits and limitations, as there exists a clear need for the development of an assessment platform that not only operates in real-time, but also operates at relevant tissue depths and may also be relevantly employed in vivo.

High resolution imaging methods that can allow for noninvasive, real-time assessment of cellular and tissue-level function within engineered muscle could provide significant aid to the fields of tissue engineering and regenerative medicine. These methods have readily been identified as a strategic priority in other venues of tissue engineering research, and extant applicable imaging modalities have been identified; however, their employment via standard methods may not be optimal when considering advances in myological research

[199]. While researchers continue to address many of these concerns, there is yet relatively little literature offering a comprehensive assessment of modern approaches to noninvasive functional imaging of engineered muscle and myogenic biomaterials. The following sections seek to present these modalities to guide and promote current discussion on the development and evaluation of optimal methods of their employment.

## 2.6.2 Two-Photon Excited Fluorescence

As previously mentioned, non-invasive imaging techniques that take advantage of the endogenous fluorophores of cells have been in development for decades [200-203]. Many of these modalities have investigated the quantification of cellular and tissue metabolic state through fluorescent excitation of both the primary electron donor and receptor in cellular respiration: nicotinamide adenine dinucleotide (NADH) and flavin adenine dinucleotide (FAD), respectively. In its reduced form, NADH may be fluorescently excited at 350 nm (emission maximum at 460 nm), whereas its oxidized counterpart, NAD<sup>+</sup>, is non-fluorescent [204]. Likewise, FAD has fluorescent excitation and emission maxima of 450 nm and 535 nm, respectively [205]. During high tissue metabolic demand, the ratio of mitochondrial NADH to NAD<sup>+</sup> decreases, resulting in a markedly reduced fluorescent profile which therein allows for the single-channel (350 nm) assessment of respiration within the mitochondrial matrix space [206, 207]. Alternatively, both a 350 nm and 450 nm excitation may be employed to obtain an approximation of the mitochondrial oxidation-reduction ratio, or the ratio of the fluorescent intensity of FAD to that of NADH.

Two-photon excited fluorescence (TPEF) is a promising method for the imaging of mitochondrial redox ratios *in vivo*, since it offers high resolution (approx. 400 nm) at relatively large tissue depths (approx. 1 mm) [205, 208, 209]. Two-photon excitation occurs when a fluorophore interacts with two photons whose energies are equal to half of the excitation energy of that particular fluorophore. These fluorophores can be the same target probed by single-photon fluorescence [210]. Both NADH and FAD can be readily excited by two-photon excitation at near infrared wavelengths (650-900 nm). Excitation wavelengths from 710-780 nm results in NADH excitation, whereas oxidized flavoprotein in FAD may be excited from 700-900 nm, and these wavelength ranges are both relatively safe, yet highly penetrative, due to reduced scattering and absorption as the excitation volume is inherently confined by its non-linear dependence on incident beam intensity [211-213]. As such, many recent investigations have employed TPEF of NADH and FAD to monitor metabolism of many tissue types, including cardiac, corneal, pancreatic, and brain [21, 213-221]. TPEF is a promising modality for the functional assessment of glycolysis and oxidative phosphorylation in engineered tissues due primarily to its non-destructive use of infrared light, as opposed to UV excitation otherwise inherent to single-photon excited fluorescence. However, despite TPEF being a relatively deeply-penetrating optical method, its maximum penetration depth of 1 mm is its greatest drawback when considering the assessment of deeper tissues.

## 2.6.3 Photoacoustic Microscopy

Photoacoustic Microscopy (PAM) is a hybrid modality combining principles of ultrasound detection and what is known as the photoacoustic effect. In PAM, pulses of near-infrared light are absorbed rapidly by a tissue and quickly converted to heat which leads to a transient

thermoelastic expansion. This expansion propagates as an ultrasonic wave and is eventually detected by an ultrasound transducer [222, 223]. Structural and functional information of various tissue morphologies can be readily determined, as photoacoustic absorption varies strongly with oxyhemoglobin content. As such, many recent studies have successfully resolved both the structure and oxygenation levels of complex tissues and vasculatures down to the capillary level [224, 225].

PAM has been suggested by many for its utility in tissue engineering applications. Due to its inherent ability to detect functional vasculature, PAM has already been used to resolve angiogenesis in tumors: a crucial metric in assessing the biological integration of engineered tissue [226-228]. Likewise, neovascularization and cellular distribution within implantable biomaterials, such as porous polymer foams [225-229], mesenchymal stem cell seeded hydrogels [230], and cell-free hydrogels containing the growth factor FGF-2 [231], have been monitored using PAM. Introducing contrast agents such as gold particles to engineered tissues, biomaterials, or injected cells has likewise proven successful for researchers investigating blood oxygen saturation levels and stem cell trafficking [232-234]. In general, PAM offers a number of benefits over other functional imaging methods, but its maximum depth of penetration (approx. 3 mm) and its dependency on local laser fluence might make longitudinal studies of deeper tissues prohibitively difficult to perform.

#### **2.6.4 Fluorescence-Lifetime Imaging Microscopy**

As previously mentioned, improvements in the field of multiphoton microscopy present a great opportunity for both high-resolution and long-term imaging of engineered tissues and biomaterials. Due to both its intrinsic 3D resolution and high depth of penetration, multiphoton microscopy allows for the investigation of a local environment in femtoliter volumes located deep within tissues [209, 235]. Investigations utilizing multiphoton microscopy take advantage of the autofluorescent nature of endogenous fluorophores, such as collagen, elastin, porphyrin, flavin, hemoglobin, serotonin, and as previously discussed, NADH and FAD [211, 213-221]. However, using emission wavelengths to discriminate between multiple fluorescent species within the same focal volume is majorly limited by their emission spectra overlap [211].

Fluorescence-Lifetime Imaging Microscopy (FLIM) is a promising imaging modality that has elicited many successes in monitoring the differentiation of stem cells [190, 197, 236, 237]. Additionally, FLIM has been shown to have utility in separating NADH and NADPH emission spectra, aiding greatly in the study of the photochemistry of living tissues [192, 219, 238, 239]. While FLIM has shown considerable flexibility and utility in a number of studies in the field of tissue engineering, there is still much discussion regarding the optimum FLIM analysis methodology.

One such method, known as phasor analysis, has proven its utility as a fit-free and label-free approach to probing cellular environments and identifying biologically relevant details regarding cell fate. Rather than fitting multiple lifetimes of one or multiple species, Phasor analysis represents each lifetime as a vector defined by its modulation and phase – thereby removing the need for a priori knowledge of each species' specific lifetimes [190]. This likewise means that relative concentrations of each species can readily be determined by simply ascertaining the ratio of their phasor representations. This method has recently been



employed in characterizing the different metabolic and differentiation states of both *C. Elegans* and human endothelial stem cells [190, 236]. However, for species that are close to each other on the phasor diagram, phenomena such as photo-bleaching and quenching could account for significant error in assessing relative species' concentrations. Nonetheless, as a non-invasive, non-destructive, and label-free imaging modality that can identify cellular differentiation and metabolic states, the phasor approach to FLIM is a promising imaging modality for future muscular tissue engineering applications.

### **2.6.5 Optical Coherence Tomography**

Another potential strategy for the real-time, non-invasive, and label-free assessment of the structure and function of engineered tissue is optical coherence tomography (OCT). OCT is an interferometry technique that uses broadband near-infrared light at wavelengths greater than 800 nm, allowing for deeper tissue penetration (approx. 2000 nm) than previously-mentioned near-infrared imaging modalities [239-242]. OCT has been utilized extensively to monitor cell location, migration, differentiation, and interaction with local biomaterials [243-245]. Thanks to its near-cellular level resolution, OCT has been employed in investigations that would have otherwise been prohibitively challenging with other imaging modalities, such as the study of structural changes in the retina [246], the 3D characterization of polylactate and chitosan scaffolds [247], and the kinetics of cell integration into collagen, agarose, and other hydrogels [241, 242, 244, 248, 249]. In addition, OCT has also been utilized to monitor the optical attenuation of cells that were cultured within agarose gels [250]. Other studies have utilized OCT to monitor macroscopic tissue regeneration via such processes as calcification in gelatin scaffolds and the growth of skin models [244, 248, 249, 251-254].

In many recent studies, OCT has been combined with other imaging or processing techniques to image cells and assess their deposition onto engineered tissue scaffolds *in vitro*. Additionally, the combination of OCT and Doppler velocimetry has revealed a technique that can image micron-level fluid flow, allowing for noninvasive and real-time imaging of engineered tissue rheological and elastic properties [244, 252]. Another type of OCT, known as Time Domain OCT, has likewise been utilized for the noninvasive imaging of the porosity of polymer foam scaffolds that have been seeded with aggregates of cells [255]. In this investigation, cell proliferation and extracellular matrix deposition could be monitored as a function of the allowable imaging depth and the degree to which porosity could be detected over time. In another type of OCT, whole-field OCT was employed, along with the use of magnetic beads as a contrast agent, to observe changes in cellular morphology within engineered bone tissue *in vitro* [255]. Likewise, OCT has been shown to have efficacy in combination with fluorescence imaging techniques to optimize cellular or material visibility within engineered scaffolds, enabling the investigation of how scaffold porosity and structural architecture can play a role in governing cell morphology [244, 249, 256]. The overall adaptability of OCT to many different types of investigations, in addition to its being noninvasive, non-destructive, and label-free, makes it an encouraging imaging modality for use in future tissue engineering applications.

### 2.6.6 Positron Emission Tomography

Position Emission Tomography (PET) is an extremely valuable clinical diagnostic imaging modality that aims to assess physiological function in situ in the human body in a non-invasive manner. PET relies on the emission of a positron from a radioactive pharmaceutical, or radiopharmaceutical, which then decays into two coincident photons that can be collected and traced by imaging equipment. This technique has been especially useful in the diagnosis of many types of cancer, and has likewise shown efficacy in diagnosing hyperthyroidism and detecting localized inflammation through mapping the distributions of leukocyte [257]. While many radiopharmaceuticals may be used as Fluorine-18 positron emitters (Table 2.1), the most common by far is  $^{18}\text{F}$ -fluorodeoxyglucose (FDG) which, as a functional glucose analogue, may be used as a direct metric for cellular glycolysis – even from extremely low cell concentrations [258-560].

Table 2.1: Target pathophysiology of various  $^{18}\text{F}$ -containing radiopharmaceuticals [261].

Target Pathophysiology	Radiopharmaceutical
Metabolism	$^{18}\text{F}$ -fluorodeoxyglucose ( $^{18}\text{F}$ -FDG)
Cell Proliferation	3'-deoxy-3'- $^{18}\text{F}$ -fluorothymidine ( $^{18}\text{F}$ -FLT)
Gene Expression	9-(4-fluoro- $^{18}\text{F}$ -3-hydroxymethylbutyl) guanine ( $^{18}\text{F}$ -FHBG)

PET imaging in accordance with the use of FDG could provide considerably more information when measuring the metabolic capacity of engineered tissue constructs. However, even the smallest commercially-available PET scanners, typically used in nuclear medicine departments in veterinary facilities, are excessively bulky to directly be repurposed for small tissue construct imaging. Additionally, average system resolutions for these scanners are typically on the order of 4.5- 5.0mm and would thereby be ineffectual for resolving important details in tissue engineered constructs any smaller than this size [174]. Design proposals therefore must include some method of controlling the resolution loss attributed to positron blur – the governing source blur in PET imaging.

To ameliorate the reduction of resolution from positron blur, simultaneous imaging with PET and magnetic resonance imaging (MRI) have been proposed and have recently been utilized for small animal studies [262-264]. The presence of a unidirectional magnetic field was originally theorized in combination with PET imaging [265, 266], but its effects on image resolution have only recently been characterized (Figure 2.8) [182]. However, recent advances in the electronics involved with such a system have made it possible to fabricate a working device. In order to construct the proposed device, one would have to take into account issues with function due to the interferences between the PET imaging mechanism and the magnetic field. For instance, PET detectors are typically comprised of scintillation crystals coupled with photomultiplier tubes. The sensitivity of these tubes, along with other

electrical and radiofrequency components, towards an magnetic field would be a major constraint, but recently, silicon photomultipliers have been considered for use in combination with magnetic fields present from MRI imaging [267-269]. These photomultipliers have been shown to be able to resolve most of these issues, as silicon based avalanche photodiodes utilize very short optical fiber bundles, which are not affected by the presence of external electromagnetic field fluxes up to 4.0T.

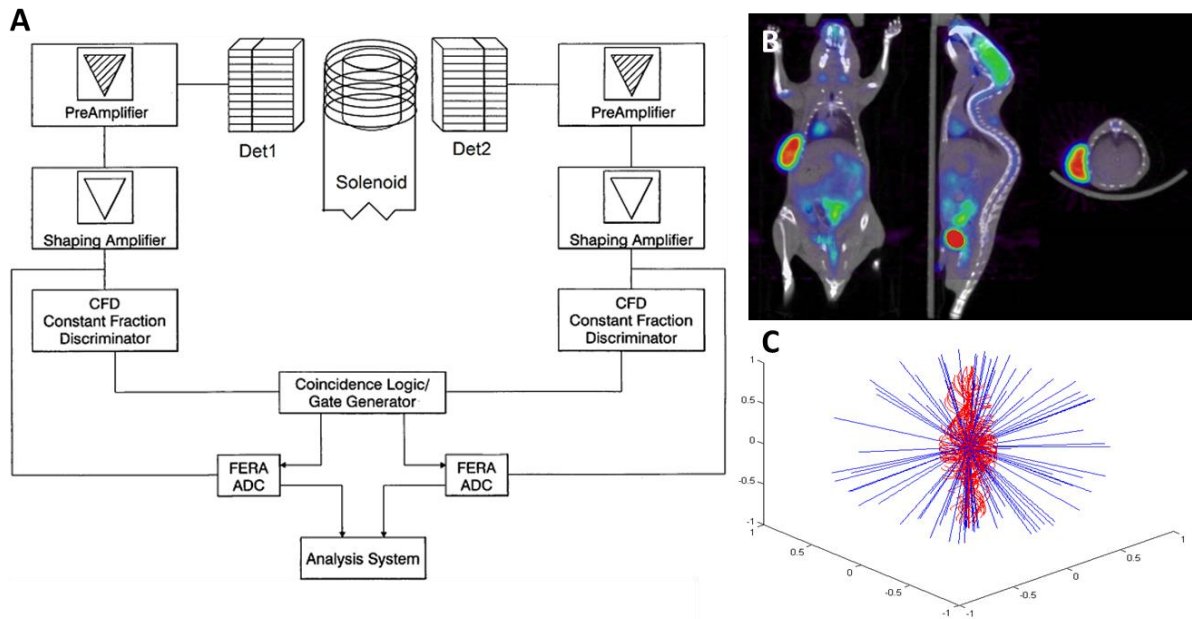


Figure 2.8: The potential function of a portable simultaneous PET/MR scanner. A) Theoretical design abstraction of a portable simultaneous PER/MR scanner. B) Example output of a small-animal PET/MR scan.142 C) Monte Carlo simulation comparing the positron pathlengths in traditional PET (blue) and simultaneous PET/MR (red), illustrating a greatly-increased resolution in PET/MR.

Simultaneous imaging with PET and MRI combined modalities may become a powerful monitoring technique for the functional assessment of engineered muscular tissue – especially in regards to the characterization of engineered muscle glycolysis versus fatty acid metabolism. However, to accurately discern its utility in this regard, further research on the miniaturization of these scanners for use on engineered tissue constructs will be necessary.

### 2.6.7 Bioluminescent Imaging

Bioluminescent Imaging (BLI) is an imaging technique that relies on emitted light from the enzymatic generation of luminescence in living organisms. BLI typically requires the introduction of the luciferase gene from *Photinus pyralis* into a receptive cell line or tissue. The luciferase and luciferin reaction results in the emission of photons from 500-620 nm (blue-green to yellow-orange) wavelengths, with peak emission at 612 nm at 37C [270, 271]. However, luciferase from the *Renilla wildtype* emits light from 460-490 nm [272, 273]. Additionally, small genetic changes in these luciferase reporters' encoding DNA can be made to adjust their emission wavelengths without significant changes to the biochemical

reaction – thereby allowing for the potential to utilize multiple luciferase reporters in the same engineered tissue to simultaneously investigate multiple biological processes [214]. Aside from transfection, luciferase may be introduced to tissue via simple diffusion – a technique employed by many investigations to characterize perfusion in vascularized tissue constructs or live animal models [270, 274].

Many studies utilize BLI to track cells following implantation, providing detailed information on cell viability, migration, differentiation, and integration with surrounding scaffolds and/or tissues [257, 275, 276]. Additionally, stem cell viability, migration, and proliferation have been monitored for months using BLI on various engineered polymer scaffolds in both bioreactor and non-bioreactor culture conditions [277-279]. The potential for lengthy investigations has given rise to many current projects aiming to monitor temporal changes in not only cytotoxicity, but also cell gene expression, the progression of infection, and the growth and angiogenesis of tumors [280]. Investigations on the formation of bone in mice *in vivo* have likewise relied on luciferase transfection to gauge the degree to which bone formation from extant bone and introduced stem cell sources occurred [257, 275, 281-283]. BLI has recently become a modality of great interest from within the tissue engineering community – primarily for its noninvasive, non-destructive, and longitudinal imaging of cells and engineered tissue, both *in vivo* and *in vitro*. However, transfection of a luciferase reporter gene is invasive and potentially destructive to target cells and tissues, and spatial information is limited to two dimensions. Current BLI research calls for the development of optimum luciferase transfection or introduction strategies, along with an imaging system that allows for simultaneous 3D spatial acquisition.

### **2.6.8 Micro X-ray Computed Tomography**

Micro X-ray Computer Tomography ( $\mu$ CT) is another promising imaging modality for the functional assessment of engineered tissue, as it allows for the non-destructive quantification of many aspects of engineered scaffolds, such as porosity, pore size, and interconnectivity [284-291]. Inferring cellular integration and interaction with its engineered scaffold is made possible in  $\mu$ CT, as images can be acquired sequentially over time with minimal negative effects to cells from X-ray dose [292, 293]. However, in order to achieve sufficient X-ray absorption (contrast), soft tissues and biomaterials oftentimes need to be freeze-dried or kept under dry conditions instead of standard culture conditions – a notion which can significantly affect certain cell or tissue types. Due to this X-ray absorption issue,  $\mu$ CT is most commonly associated with the characterization of engineered bone tissue, as the comparatively high X-ray absorption of calcium eliminates the need for freeze-drying in mineralized tissues and hydrogels (Figure 2.9) [294, 295]. In these types of studies,  $\mu$ CT can allow for the noninvasive, non-destructive, and label-free assessment of mineralization as a function of time with minimal effect to the tissue or engineered construct being imaged [296, 297].

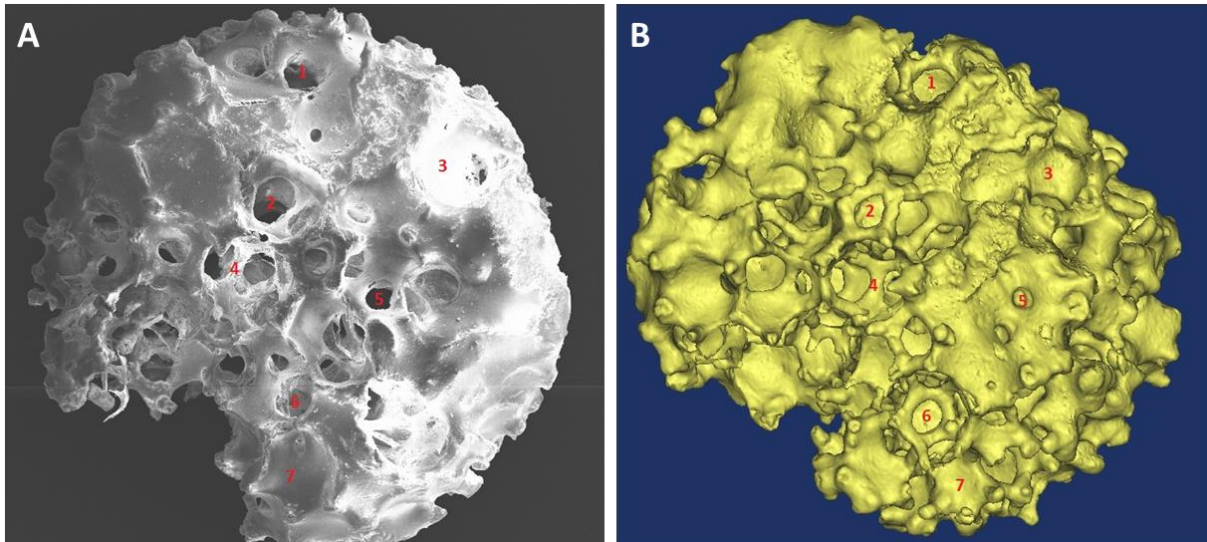


Figure 2.9:  $\mu$ CT image and its corresponding 3D model of an implantable biomaterial scaffold. A)  $\mu$ CT image of an engineered bone construct with B), its corresponding 3D model.

In studies involving  $\mu$ CT on-mineralized tissue, many techniques have otherwise been employed to minimize the aforementioned negative effects of conventional  $\mu$ CT use. For example, contrast agents such as heavy metal, barium sulfate, or Microfil may be used to image anything from 3D scaffold architectures to blood vessel or neural tissue integration and neovascularization within engineered tissues [298-303]. High resolution  $\mu$ CT has also been utilized *in vivo* to identify stem cells that were labeled with magnetic nanoparticles following an intra-arterial transplant [304]. However, the use of contrast agents, dyes, or radioactive labels always results in the destruction of engineered tissue, so functional assessment of engineered constructs or post-transplant engineered tissues is limited to longitudinal studies assessing multiple timepoints from individual subjects or constructs.

## 2.7 Applications of 3D Medical Image Modeling

### 2.7.1 Total Hip Arthroplasty: Modeling Periprosthetic Muscle and Femoral Biomechanics

As one of the most ubiquitously successful procedures in orthopedic surgery, Total Hip Arthroplasty (THA) aims to restore function and ameliorate pain in the hip by prosthetic replacement of diseased or damaged acetabula and femoral heads. The hip is a load bearing joint, constantly subjected to high loads which lead to the gradual degradation of articular surfaces. Over time, this degradation (arthrosis) can cause functional impairment and pain. Arthrosis can gradually lead to osteoarthritis of the hip or fracture-induced osteonecrosis of the femoral head or neck, necessitating the complete replacement of the joint and proximal femur. THA has been historically prevalent in countries with relatively high life spans, like the Nordic community [312-314]. With increasing life expectancies in many populations worldwide, THR rates have increased considerably over the last few decades and are projected to continue to increase in the future [315]. However, despite its increasing prevalence, annual reports from national arthroplasty registries indicate differences in choices of implant brands, fixation methods, and overall prosthetic survival [316-318].

While THA remains one of the most efficacious surgical modalities for both reducing patient pain and restoring hip function, post-operative complications and revisions are relatively common, primarily due to localized fracture or periprosthetic loosening [319, 320]. These notions altogether necessitate the development of innovative and collaborative approaches to THA planning.

About 80% of people who undergo THA report improved mobility, normalized ambulation, and an overall reduction in periprosthetic pain. However, even after full recovery, gait asymmetries may be present, typically caused by prosthetic length discrepancy, articular surface degradation (arthrosis), variability in rehabilitation protocol, or periprosthetic changes in stress distributions, as dictated by the type of implant [321]. Since there exists much inherent variance in repetitive load amplitudes subjected to each individual's hip, the degree to which these conditions may affect an individual post-THA can vary considerably.

Current surgical philosophy dictates that a non-cemented prosthesis should only be used if a patient's femur can withstand both the forces incurred by compressive stresses during the press-fitting and the functional loading after the operation. Additional consideration is given to whether eventual bone ingrowth can be both predictable and sufficient. Unfortunately, there is no straightforward approach to make this assessment, since quantitative pre-operative bone quality measurement is not performed, despite knowing that it would have a positive influence on the success of the operation. Additionally, the use of extant literature resources is problematic since large studies comparing non-cemented to cemented THA have shown contrasting outcomes [322]. Instead, orthopedic surgeons must carefully evaluate each particular patient's individual situation and choose an optimal protocol based upon acquired or shared intuition – a difficult task for novice surgeons. Initially, both the patient's age and gender are taken into account, since bone mineralization decreases with aging and differs between men and women [323, 324]. In general, cemented implants are more frequently used for older, less active people and/or people with weak bones, while non cemented implants are more frequently used for younger and/or more active people. However effective these generalizations may be in prescribing THA procedures, there may be many other relevant differences between individual patients; thus, the development of a patient-specific, quantitative methodology is needed.

After THA, patients' gaits typically exhibit improvement, but still exhibit asymmetries even after full recovery [325-329]. However, even with the continued development of gait analysis techniques there is a general lack of understanding regarding joint motion of the lower extremities in the THA population, which can make certain patient's rehabilitation challenging and lengthy. The densities of the quadriceps muscles in patients undergoing THA have been shown to correlate with femoral bone mineral density. Both bone and muscle densities tend to be lower in the operative side [330] which may be caused by the patient's shielding the involved side due to pain. However, muscular strength tends to increase substantially on this side following the first post-operative year [331].

Indeed, many recent investigations have involved a variety of assessment metrics to observe and characterize periprosthetic THA pathophysiology. Results from such studies not only identify preoperative factors that may affect surgical outcome, but likewise hold promising utility in assessing the efficacy of post-THA rehabilitation. For example, correlating bone mineral density (BMD) with factors affecting osseointegration, osteonecrosis, and primary osteoarthritis have been of particular interest in current literature [332-336]. Other

investigations report developing computational models to recapitulate forces experienced in THA fixation and postsurgical ambulation – most notably utilizing finite element analysis (FEA) [335-339]. Of these investigations, interference fitting via principal strain computational modeling has been particularly identified as a promising tool for estimating bone mineral density (BMD), computing ultimate bone strength, and predicting the propagation of proximal femoral fractures [338, 339]. Additional investigative metrics include local electromyography (EMG) to show peripheral neurogenic processes [340-342], functional gait analyses to better understand the efficacies of different rehabilitation methods [344–345], and radiodensitometric profiling to assess discrete changes in local soft tissue composition [45, 346, 347].

While many of these assessment tools may indeed characterize specific effects of THA prosthetic fixation, there is no clear indication of their utility in a clinical context. Indeed, before surgery, prosthetic fixation methods are primarily determined by an orthopedic surgeon's own experiences and quasi-qualitative generalizations of suggested indicators for bone quality (gender, age, and qualitative assessment of CT images) [348]. Likewise, postsurgical rehabilitation methods tend to follow generalized guidelines rather than operate on a quantitative, patient-specific level [345]. The prevalence of periprosthetic failure and discrepancies in patient outcome together necessitate the development of biometric gold standards for THA assessment. Chapters 6 and 7, along with Sections 3.4 and 8.3, detail investigations into complimentary methodologies for pre- and post-surgical THA assessment and offer a complete discussion on their implementation in a clinical context.

## **2.7.2 Source Localization and Electroencephalography**

Of the many obfuscating phenomena that have been identified and studied in the field of electroencephalography (EEG), craniofacial electromyographic (EMG) artifacts remain of great concern in clinical research applications [349-351]. The notion that craniofacial EMG activities contaminate EEG data is not a new concept, but its urgency has only become apparent after a study by Whitham et al. in 2007 suggested that most scalp EEG data above 20 Hz might simply be recorded EMG activity [350]. Indeed, results from many recent investigations have further contributed to this notion and thereby further necessitate the development of reliable techniques for characterizing and isolating EMG artifacts [349, 352-356].

Not all noise from EMG activity is difficult to disseminate from EEG data. Any large-amplitude muscle activity is readily visible in any EEG data set and can therefore be easily removed with the use of signal processing techniques such as filtering, spectral analysis, and/or Principle or Independent Component Analysis (ICA) [357-366]. On the contrary, the efficacy of many of these signal processing techniques is questionable and unreliable in the separation of low-amplitude EMG activity from EEG data, as these two signals may be of comparable amplitude [355, 356]. Aside from amplitude, the frequency spectra of EMG and EEG can overlap – a phenomenon which is particularly prevalent in scalp EEG, whose ripple frequency measurements are typically between 80-250 Hz may be significantly affected by high-frequency craniofacial EMG artifacts [367-369].

In order to generate an accurate and clinically-relevant model of the signal contribution of craniofacial EMG, detailed morphological information must likewise be known. The use of segmented magnetic resonance imaging (MRI) has previously been developed to model the

electrical behavior of the human brain under normal and pathological conditions [291]. This imaging modality can be utilized to accurately characterize extant coupled non-linear physical mechanisms and how they impact the propagation of EMG and EEG signals through the inhomogeneous media of the head [370]. In the generation of a 3D model from segmented MRI images, most major tissue surfaces can readily be identified in each slice [291, 371, 372].

In general, the successful application of modern EEG signal processing methods requires a detailed knowledge of both the topography and frequency spectra of low-amplitude craniofacial EMG. This information remains limited to clinical research, and as such, there is no known reliable technique for the removal of these artifacts from EEG data. Section 8.1 of this thesis outlines a preliminary investigation of both craniofacial EMG frequency spectra and 3D MRI segmentation that offers insight into the development of an anatomically-realistic model for characterizing these effects. Such a model then can be applied in a clinical setting to excise low-amplitude EMG activity and ultimately help to extend the use of EEG in various clinical roles.

### **2.7.3 False-Color CT: Clinical Impact of Modeling Segmented Tissue Morphologies**

The ever-expanding field of medical imaging utilizes a wide variety of techniques and processes to produce non-invasive images of various internal and external tissue morphologies. In the clinical context, medical imaging remains a vital tool for diagnostic and clinical investigations. Of the many facets of the field, most current research aims to improve aspects of instrumentation design, data acquisition methodology, image processing software, and computational modeling. Indeed, three-dimensional (3D) visualization of the internal anatomy provides valuable information for the diagnosis and surgical treatment of many pathologies, but every modality has its inherent limitations [373, 364]. For the purposes of clinical assessment in particular, visually simplistic imaging methods that can optimize the noninvasive, high-resolution assessment of diseased or damaged tissues have readily been identified as a strategic priority in clinical research, and extant imaging modalities have certainly been identified as preferential. However, their employment via standard methodology may not be optimal for various avenues of myological research. The implementation of traditional imaging modalities, in the context of a variety of novel case studies, can significantly impact this process of methodology optimization.

Despite being widely used as an imaging modality in cardiology, the false color approach to spiral CT is typically ignored in clinical imaging-based evaluations of skeletal muscle tissue [373, 374]. Despite this notion, the use of false-color CT in the context of clinical myology has shown great utility – indeed, many of the investigations reported in this thesis utilize this approach to visualize and quantify soft tissue compositions in a host of investigative contexts. Further details in this regard are widely available throughout the forthcoming chapters.

To illustrate the false color methodology and introduce its utility, we may begin here with an example of a typical spiral CT scanning protocol where 3D image data are gathered by scanning a patient's lower limbs with a spiral CT machine. As evidenced by Figure 2.10, a typical leg scan starts above the head of the femur and continues down to the knee joint, covering both legs with one scan. Slice increments are typically set to 0.625mm, resulting



in a total of about 750–900 CT slices, depending on the patient’s size. Each slice consists of 512x512 pixels, and each pixel has a radiodensitometric gray value in the HU scale containing up to 4096 values, meaning that pixels may be represented by a 12 bit value. This dataset is effectively a complete 3D description of the particular morphological structure, including all tissue types. The size of the volumetric element (voxel) in the dataset is about 0.7 mm<sup>3</sup>; therefore, the CT number assigned to the voxel represents, in effect, an average of different tissue elements, present within a single elementary volume. For instance, in the case of normal muscle tissue, such a voxel would contain the transverse section of 20 to 50 muscle fibers, which is approximately one tenth of the volume accessed by a typical muscle needle biopsy [55, 158].

Throughout many of the investigations discussed in this thesis, results of this microstructural analysis are presented both as the percentage of three different soft tissues (muscle, loose and fibrous connective tissue, and fat). In our example here, these tissues are depicted in the total volume of the *Rectus femoris* muscle as a 3D muscle reconstruction, displaying the first cortical layer of voxels that describes the muscle epimysium (Figure 2.10).

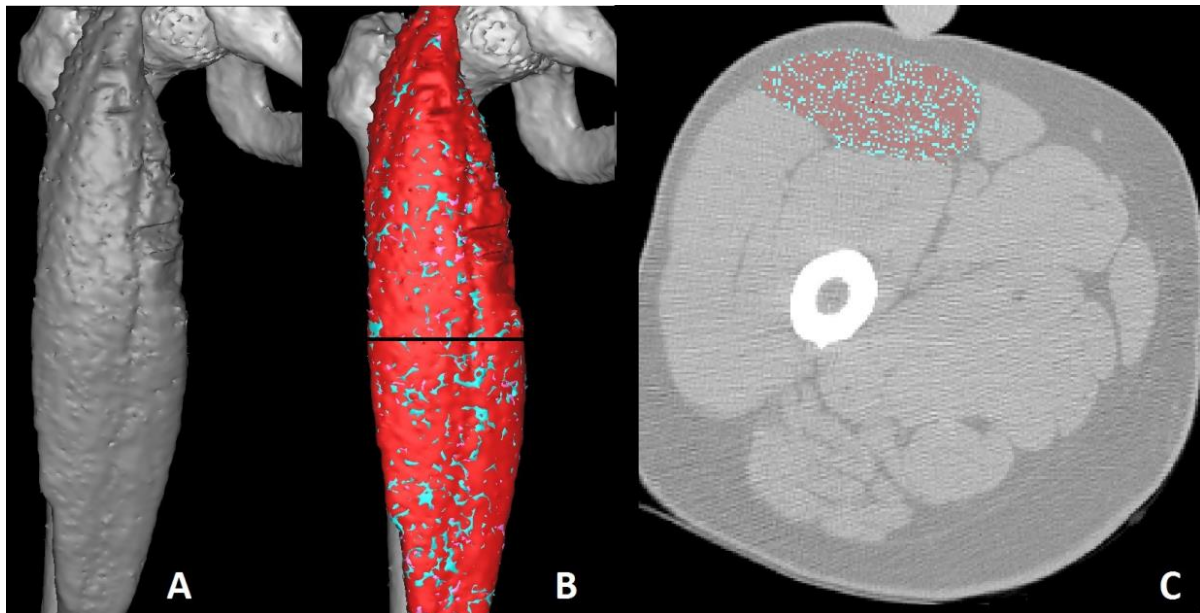


Figure 2.10: 3D false-color CT reconstruction of a *Rectus femoris* muscle from a healthy patient, including the epimysium at the cortical level in A) gray and B) false colors, along with C) the corresponding cross-section at mid-belly. The total volume is  $4.2 \times 10^5$  mm<sup>3</sup>, and from this volume, 3% is fat [-200; -10] HU, 28.7% is loose connective tissue and low-density (atrophied) muscle [-9; 40] HU, and 68.3% is normal muscle [41; 200] HU.

For the purposes of this and all segmentation investigations reported in this thesis, the imaging software MIMICS (<http://www.materialise.com>) was utilized for segmentation and 3D reconstruction. Figure 2.10 here clearly illustrates that this is possible in the *Rectus femoris* – even when severely degenerated due to long-term denervation, as the muscle remains readily recognizable despite hypotrophy.

### 2.7.4 3D Printing of Segmented Tissues: Methods and Impacts

Three-dimensional (3D) modeling and rapid prototyping technologies have recently shown great utility in a wide variety of applications in medicine and surgery [375] and [376]. In principle, the 3D recapitulation of patient-specific anatomical features provides surgeons with an immediate and intuitive understanding of even the most complex morphological geometries, enabling the accurate planning and emulation of a host of surgical procedures [377-384]. The employment of 3D anatomical models is additionally being considered for patient implantation procedures, such as dental crowning, craniofacial reconstruction, and tissue regeneration via biological scaffolds [378-380].

The first 3D rapid prototype was reported by Hideo Kodama in 1982, and the first use of the technology in support of surgical planning was reported in 1994 [385]. Since its inception, the development and use of 3D rapid prototyping in a medical context has been rapidly growing hand in hand with improvements in medical imaging modalities such as CT and MRI. Modern rapid prototyping technology allows for the construction of anatomical models with layer thicknesses as low as 250  $\mu\text{m}$ , and with concurrent advancement in medical image contrast segmentation, these models are able to recapitulate almost every external or internal morphological structure [385]. Some of the main benefits for using rapid prototyping models include improving surgical planning, enhancing diagnostic quality, decreasing patient exposure time to general anesthesia, decreasing patient blood loss, and shortening wound exposure time [378]. However, each of these benefits is distinctly relative to both the particular type of surgery involved, as well as the individual patient case itself. As such, most extant literature on the use of 3D rapid prototyping in a clinical context outlines specific impacts to individual cases or theoretical applications [378]. In order to step back and critically assess the potential for this technology as an integrated service within a hospital, it is best to assemble a detailed critique of how a long-running, successful example of such a service has been operating, in a broad surgical context.

With the aims of improving surgical outcomes, reducing future costs, and developing thorough clinical guidelines for enhancing surgical planning and assessment, the National University Hospital of Iceland, Landspítali, established an in-house service for 3D rapid prototyping. Since its inception in 2007, this service has allowed physicians and surgeons from different specialties to submit requests for a host of 3D models to be made available within 24 hours of submission. This process was simultaneously employed in research activities to study the anthropometry of human muscles [386] and the use of rapid prototyping as preparation for complex brain surgeries in combination with neurosurgical navigation systems [387]. Since then, the National University Hospital of Iceland has fabricated over 200 surgical models for patient cases in the fields of cardiac, orthopedic, and neurosurgery. The overwhelming success of the 3D rapid prototyping service has led to its solidification as an essential service within the hospital, and the rapid prototyping service continues to expand its impact on an increasing number of surgical cases.

## Chapter 3

# A First Look: Preliminary Impacts of Modern Methods for CT Image Analyses in Translational Myology and THA

### 3.1 Implicating Muscle Quality as a Clinical Comorbidity Index

Muscle biopsy is the current gold standard for the assessment of muscle, but the procedure is invasive and occasionally limited in relevance by the small size of excised tissue. However, recent investigations have realized the potential of X-ray computed Tomography (CT) and Magnetic Resonance Imaging (MRI) to describe muscle quality and composition. This is often performed either quasi-quantitatively, via the visual grading of muscle structure morphologies [346, 388-390], or quantitatively via the computation of muscle cross-sectional areas and radiodensitometric absorption values in CT, measured in Hounsfield units (HU) [44-47, 166, 392]. Despite the superior soft tissue contrast in MRI and non-dependence on the use of ionizing radiation, CT has higher spatial resolution and is comparatively less influenced by technical variations in machine preparation and acquisition protocols [71, 88]. These notions are critical when attempting to discern diagnostically-relevant information from cross-sectional images of soft tissue.

While the propensity of CT imaging literature describing sarcopenia differs largely regarding analytical methodology, one metric that remains ubiquitous is the use of average HU values to characterize muscle quality. Goodpaster et al report the utility of this methodology for quantifying skeletal muscle lipid content, highlighting the potential for the method to investigate the association between muscle composition and function [16, 43, 393]. Hicks et al likewise utilized average HU values within lower back and posterior muscle groups to illustrate the inverse relationship between these muscle qualities and the prevalence of lower back pain [394]. Additionally, Sur et al utilized average HU values weighted by total muscle area to show a correlation between muscle quality in the psoas and serious post- Pancreaticoduodenectomy complications [395]. Likewise, Lang et al utilized

average HU attenuation values within thigh muscles to predict the propensity for hip fracture in elderly, otherwise healthy subjects [13].

While average HU values might indeed describe general shifts in adiposity, it is our hypothesis that generalizing CT image matrices in this regard may risk eliminating other distribution characteristics that could elucidate additional subtle changes in muscle properties. In Chapter 4 of this thesis, we introduce the utility of computational modelling involving entire radiodensitometric distributions using our novel nonlinear trimodal regression analysis (NTRA) method [45]. This paper outlines the eleven unique regression model parameters inherent to the NTRA method and shows their utility in characterizing muscle HU distributions in a preliminary THA cohort. Furthermore, Chapter 5 explores the further utility of this method using a large subject dataset in tandem with extant gold standard muscle quantity and quality analyses (cross-sectional area and average HU value).

### **3.2 Monitoring Trophism Decay of LMN-Denervated Muscle and its Restoration by h-b FES Compliance**

Many of the tissue analyses employed to study structural changes occurring in LMN (Lower Motor Neuron) denervated muscle are usually performed with biopsies – i.e., the analysis of only a few milligrams of muscle. Complementary imaging techniques, such as CT scans, are also employed to assess and validate histological information and to study macroscopic changes. The combinatorial value of CT imaging methods, post-processing techniques, and segmentation can be demonstrated by studying the effect of h-bFES training entire muscle volumes [346, 391, 396]. An excellent example of such a case study involved the assessment of a patient with irreversible *Conus* and *Cauda Equina* syndrome who underwent five years of this stimulation treatment, followed by five years of non-compliance to h-Bfes [397]. The main novelty introduced in this work was the morphological analysis of the whole quadriceps in different pathological conditions and the quantification of the tissue compositions within the muscle volumes.

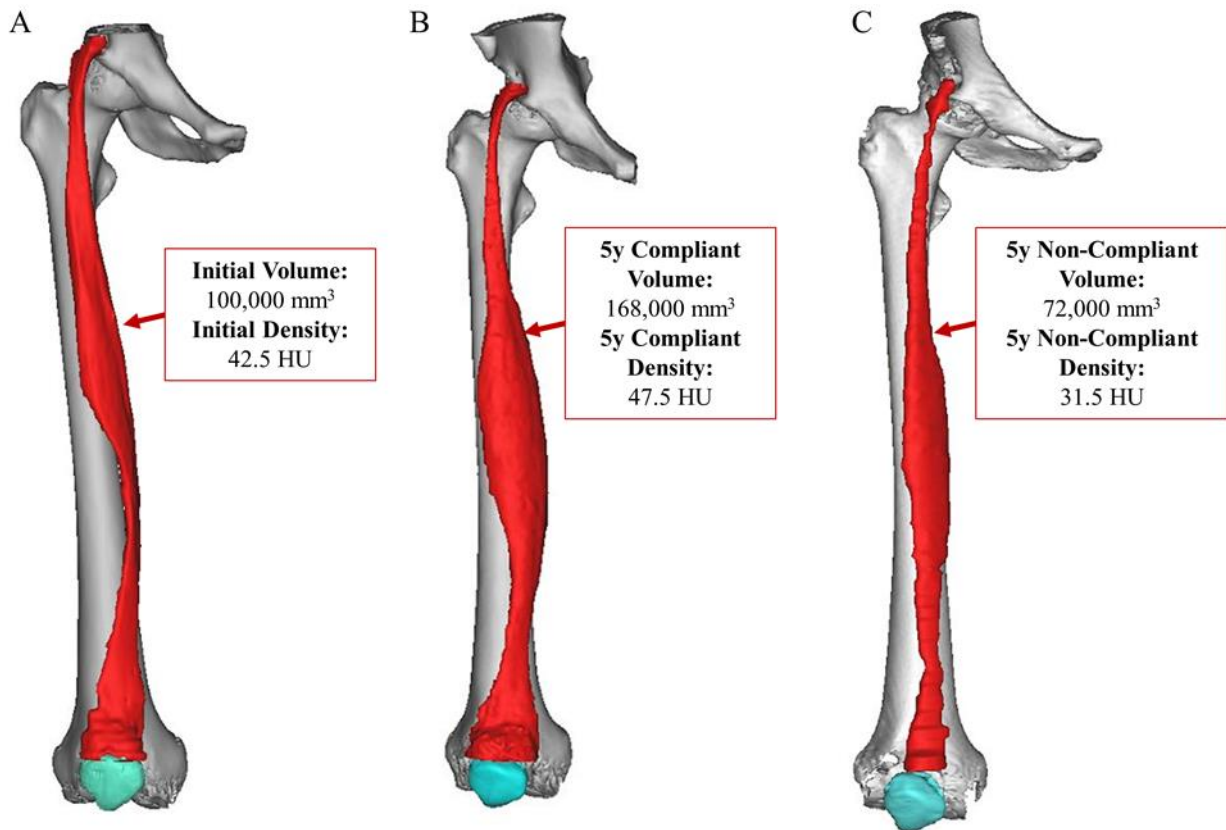


Figure 3.1: Example of a patient with irreversible *Conus* and *Cauda Equina* syndrome who underwent five years of compliance with h-bFES treatment, followed by another five years of non-compliance to h-bFES [397]. As is evident above, the 3D volume and density analyses readily identify changes in *Rectus femoris* volume and density (average HU value) over the timespan of the study [346].

Figure 3.1 presents the results for this Patient. The 3D model and voxel assessment of the *Rectus femoris* shows a clear increase in muscle volume and density during the h-bFES compliant period, and likewise shows a clear decline in these muscle characteristics after five years of non-compliance.

### 3.3 Utility of 3D Muscle Segmentation in Monitoring Incomplete Denervation from Spinal Cord Injury

In the second of these reported case studies, analogous soft tissue analyses and segmentation methods were used on CT images of a 53 year old male patient 15 years post SCI before and after h-bFES rehabilitation was performed [346]. The residual asymmetric innervation of the leg muscles and the effects of six weeks of h-bFES rehabilitation regime allowed the patient to perform short walks without crutches – a monumental improvement in function and quality of life after years of only heavily-supported walking and many daily hours of bed rest.

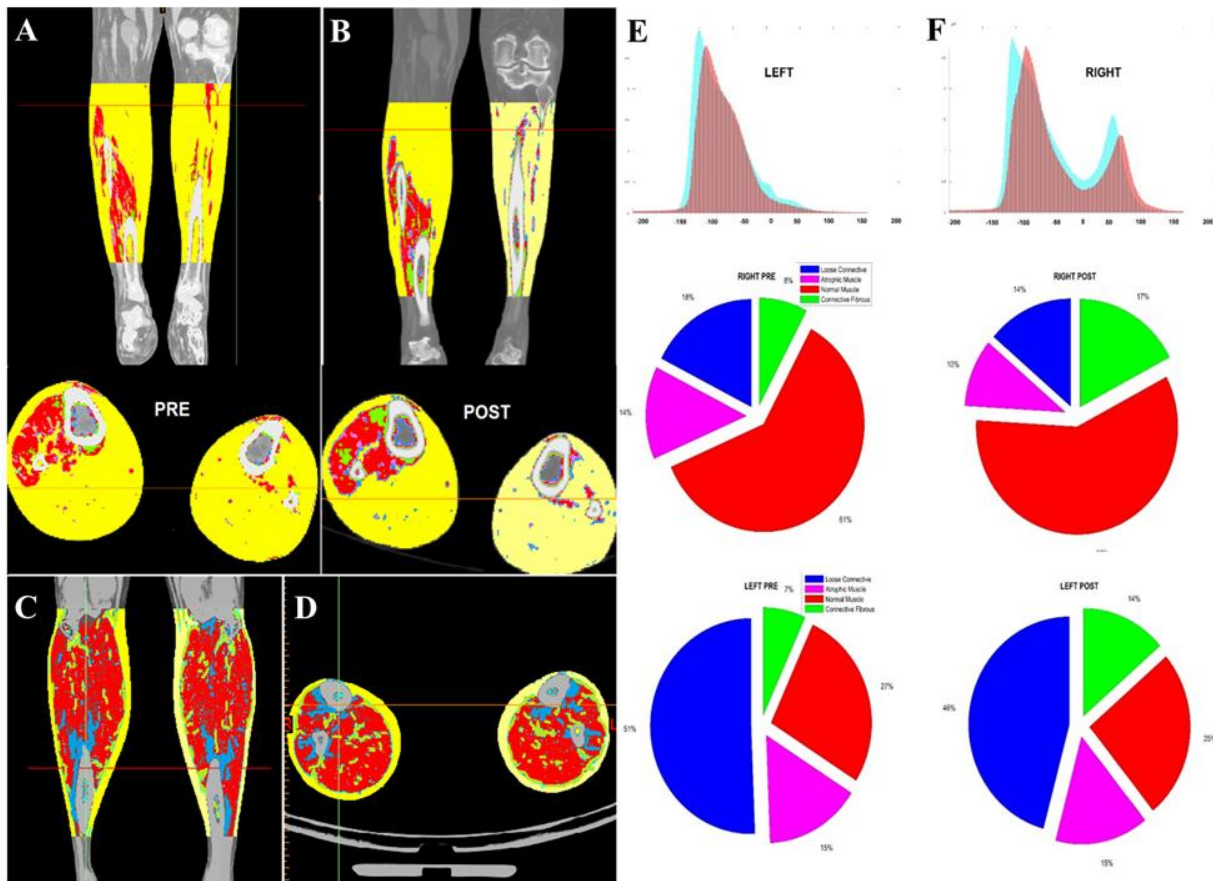


Figure 3.2: 3D soft tissue segmentation to compare the compositional changes between the calf muscles in both legs (A, before and B, after h-bFES rehabilitation). Note that soft tissue segmentation thresholds and colorizations are defined as: subcutaneous fat (yellow HU -200; -10), Intramuscular fat (orange HU -200; -10), low density muscle (cyan HU -9; 40), muscle (red HU 41; 70) and fibrous connective (gray HU 71; 150). E and F depict the HU distributions and changes within both legs (cyan: pre-rehabilitation, red; post-rehabilitation), and the pie charts contain corresponding compositional data changes. It is likewise important and useful to notice the qualitative muscle volume and quality differences between the SCI patient and a healthy subject (C+D) [346].

Figure 3.2 depicts the comparison between soft tissues before and after six weeks of h-bFES rehabilitation using the soft tissue segmentation method detailed herein [346]. The subject was treated each day for 30 minutes with electrical stimulation for denervated calf muscles – bilaterally on the anterior and lateral side of the leg. Additionally, the Histograms containing HU distributions show that fat is the dominant tissue type within the volume, especially on the left side where muscle content is almost absent. However, the distribution after the rehabilitation period (red) shows an increase in muscle density and a reduction in fat within the right leg. Furthermore, it is possible to analyze the specific soft tissue compositional changes within these muscles. The pie charts in Figure 3.2 depict these particular changes; indeed, it is evident that there was an increase of dense connective or fibrous tissue in both legs, to the detriment of loose connective tissue [346]. Finally, to compare whether there were any significant changes in the muscular composition outside of the h-bFES rehabilitation volume, analogous segmentation analyses were performed on the middle of the *Rectus femoris* thigh muscles. Figure 3.3 contains the corresponding HU histograms, showing, once again, the differences between left and right side, both pre and post h-bFES.

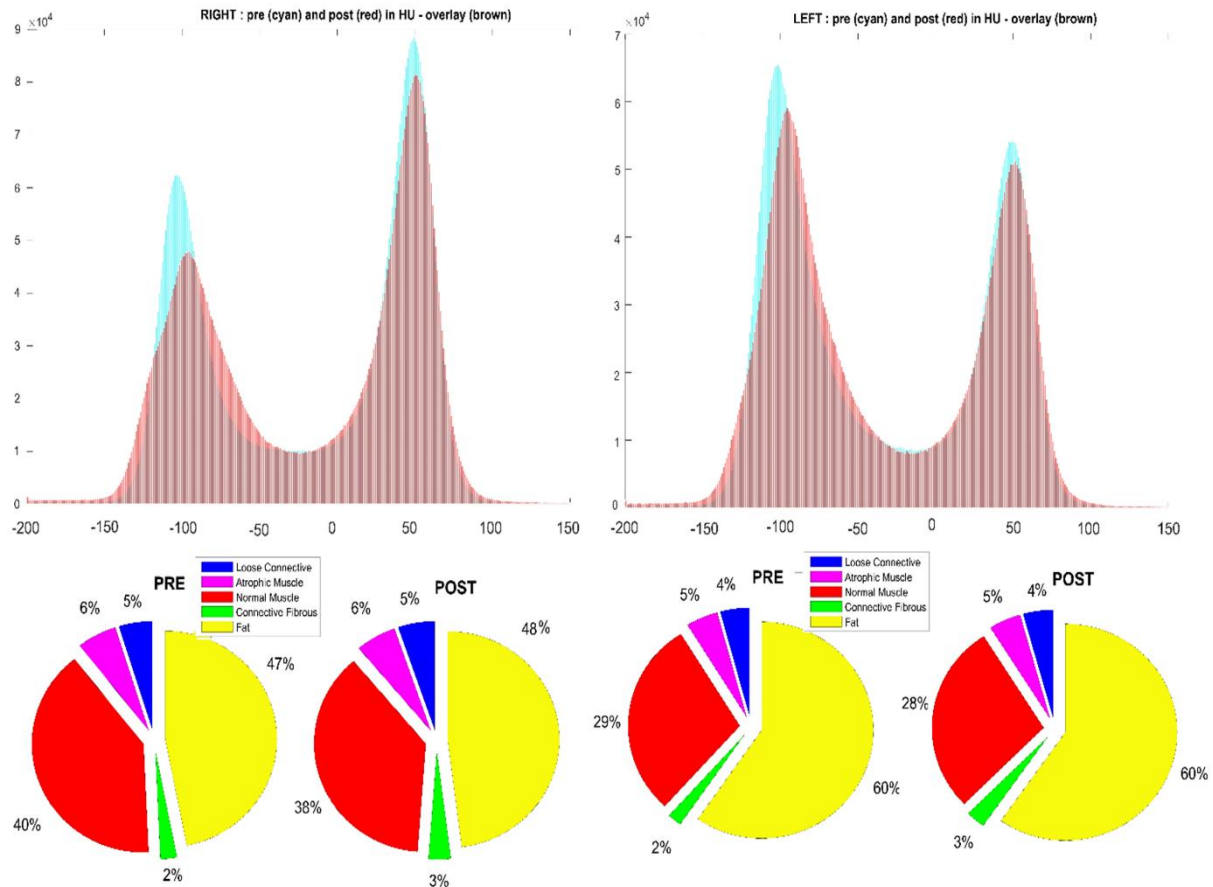


Figure 3.3: HU distribution comparison between left and right legs, as assessed at the mid-thigh. Note that compositions in the left and right *Rectus femoris* muscles changed very little in the same time span, which is to be expected due to h-bFES being withheld in this region [346].

It is evident here that there are no remarkable changes between these time points. However, intriguingly, there was a slight shift towards higher density HU values on both legs. These results altogether present a useful first look at the quantitative efficacy of h-bFES.

### 3.4 3D Muscle Segmentation and HU Distribution Analysis: Improving Patient Assessment in THA

#### 3.4.1 Introduction

Total Hip Arthroplasty remains the gold standard of treatment for patients who suffer from a variety of hip-related pathological degeneration or trauma. These patients often exhibit significantly less post-operative pain and an increase in the range of motion of the joint, but there are still relatively common instances of debilitating periprosthetic complications that call into question the method for pre-surgical implant choice. Currently, there are two principal options for THA prostheses: cemented or noncemented. Utilizing the cemented procedure ensures a faster acquisition of adequate implant stability than with the noncemented procedure, but can eventually lead to an increased intraoperative periprosthetic fracture risk. Non cemented prosthetic stems are more frequently revised

within the first few years following THA due to periprosthetic fracture, but non cemented revision surgeries generally result in fewer complications than those of cemented implants. Surgeons typically rely on experience or simple patient metrics such as age and sex to prescribe which implant procedure is optimal, and while this may work for most patients, there is a clear need to more rigorously analyze patient conditions that correlate to optimal post-THA outcomes. The results from the investigation reported herein indicate that an understanding of how the percent composition and quality of a patient's quadriceps muscle in both healthy and operative legs may be a useful indicator for prosthetic choice [347]. Additionally, these data emphasize that the traditional metrics of age and sex inadequately predict changes in quadriceps composition and quality and thereby have comparatively minor utility in determining the patient-appropriate prosthetic type.

### **3.4.2 Material and Methods**

#### **3.4.2.1 CT Data Acquisition**

This study includes data from 68 patients: 38 females (an average age 64 years) and 30 males (an average age of 56 years) who were scheduled to undergo their first total hip arthroplasty. Of the 68 patients, 40 of them received a noncemented implant, while 28 received a cemented implant. The decision regarding prosthetic suitability was in the hands of the operating surgeon of each patient, who based his implant prescription on typical general patient characteristics or conditions, such as age and sex. All patients were scanned in a 64 slice Phillips Brilliance CT scanner. The scanning area reached from the iliac crest to the middle of the femur bone (Figure 3.4) with slice thicknesses of 1 mm [347].



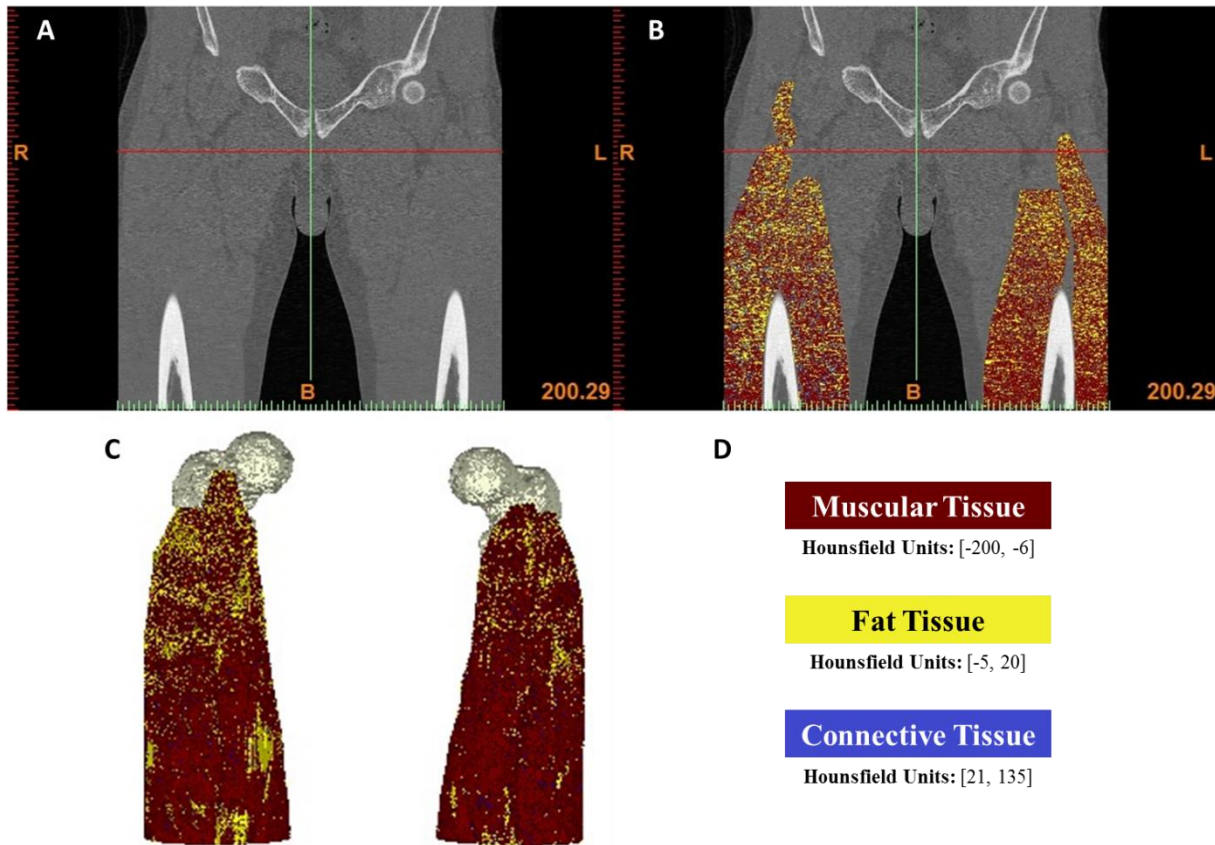


Figure 3.4: Representative subject’s CT scanning region, showing A) a CT slice in a coronal view showing the quadriceps muscles, B) the same slice after segmentation of the quadriceps muscles, and C) the quadriceps muscles and the femur in a 3D view after segmentation. D) Legend showing Hounsfield unit values and respective tissue coloring: muscles are labeled red, fat is yellow, and connective tissue is blue (none visible from this view) [347].

### 3.4.2.2 CT Dataset Processing

After the scanning, all datasets were processed in MIMICS. The processing protocol was as follows. Firstly, each of the quadriceps muscles of both legs were segmented, dividing the muscles into sections according to tissue types defined by known HU values [27] (Figure 3.4D). Finally, all Hounsfield values were exported so they could be further analyzed [347].

### 3.4.2.3 Hounsfield Unit Distribution Modeling

To discern the average Hounsfield unit values for each compared condition (prosthetic type, sex, and age), each CT scan was binned into 20 Hounsfield unit bins, generating a histogram of Hounsfield unit values. These values were normalized to obtain histogram percentages, generating a normal distribution. This normal distribution was fitted to a theoretical Gaussian curve using the Solver function of Excel (Microsoft: 2007) and a generalized reduced gradient algorithm to maximize each  $R^2$  value and obtain an optimum curve fit. These distribution averages were then exported for further analysis [347].

### 3.4.2.4 Statistical Analyses

Statistical analyses were performed using appropriately sized ANOVA with posthoc testing carried out using a student’s T-test. Differences were considered statistically significant for  $p < 0.05$ .

### 3.4.3 Results

Following segmentation and thresholding for muscular, fat, and connective tissues, it was possible to observe changes in tissue composition in both legs as a function of various patient parameters. Patients were sorted firstly according to the type of prosthesis selected by their surgeon, or cemented versus non cemented (n of 28 versus 40, respectively). Secondly, patients were sorted according to their sex (n of 38 for females and 30 for males). Lastly, sorting was performed according to patient age, where patients were divided into four age groups: younger than 50 (n of 10), between 51 and 60 (n of 11), between 61 and 70 (n of 16), and between 71 and 80 (n of 11). The results from these analyses are shown in Figure 3.5 [347].

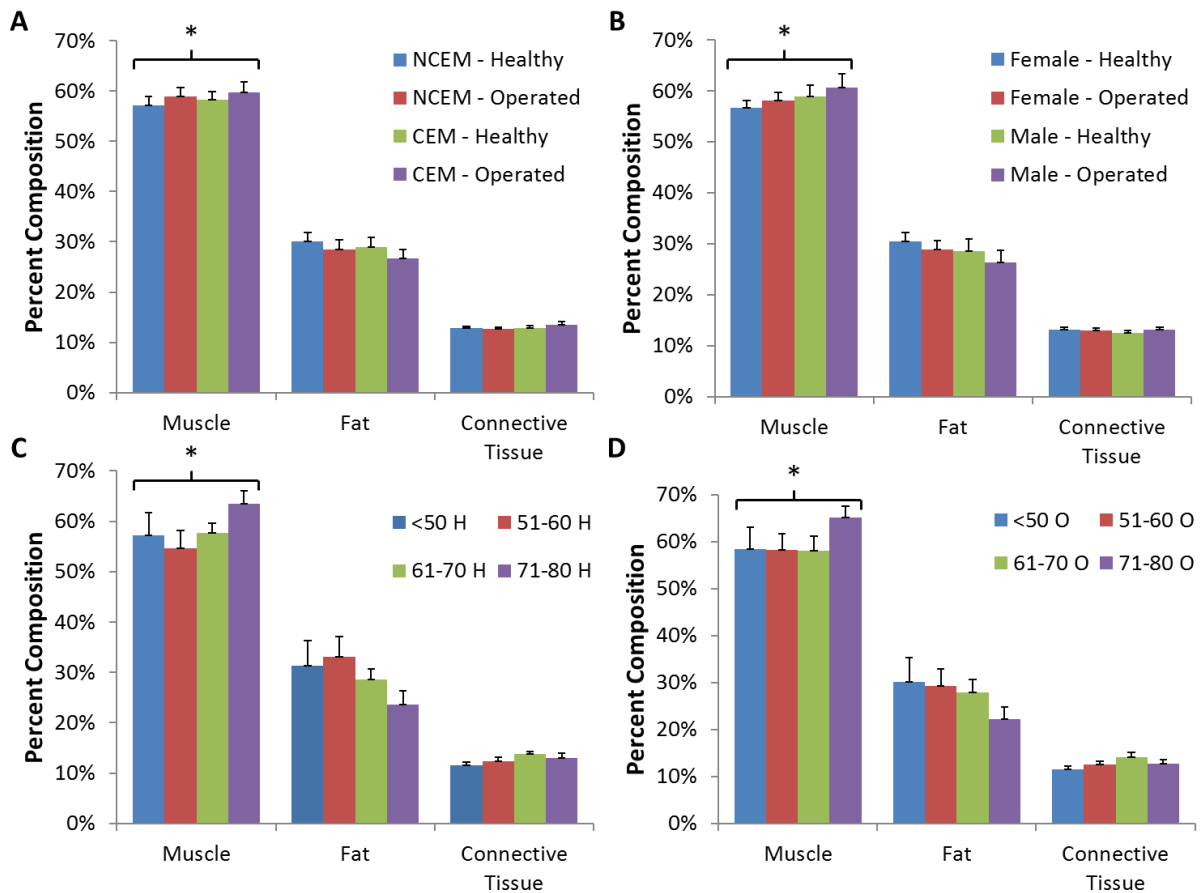


Figure 3.5: The average composition of the quadriceps muscles for each of the specific patient groups and healthy versus operative legs. A) Compositions from patients with cemented (CEM) versus non cemented (NCEM) implants. B) Compositions from female patients versus males. C) and D) Compositions from healthy and operative legs, respectively, from patients within each of the four previously-mentioned age groups. Note that in each

patient group, muscular percent composition was significantly higher than either fat or connective tissue percentages in all conditions (\*:  $p < 0.05$ ) [347].

Following the compositional analyses, each patient group's average Hounsfield unit (HU) histogram was analyzed to discern both variation within patient groups and histogram location shift. To do this, each patient's CT scan was binned into 20 groups of HU values, ranging from -200 to 135, and normalized to generate a patient-specific, normally-distributed histogram. Each of these histograms were then averaged to obtain an overall average curve for each patient group, which was then fit to a Gaussian distribution. The results from these analyses are displayed in Figures 3.6-3.8 for each respective patient group.

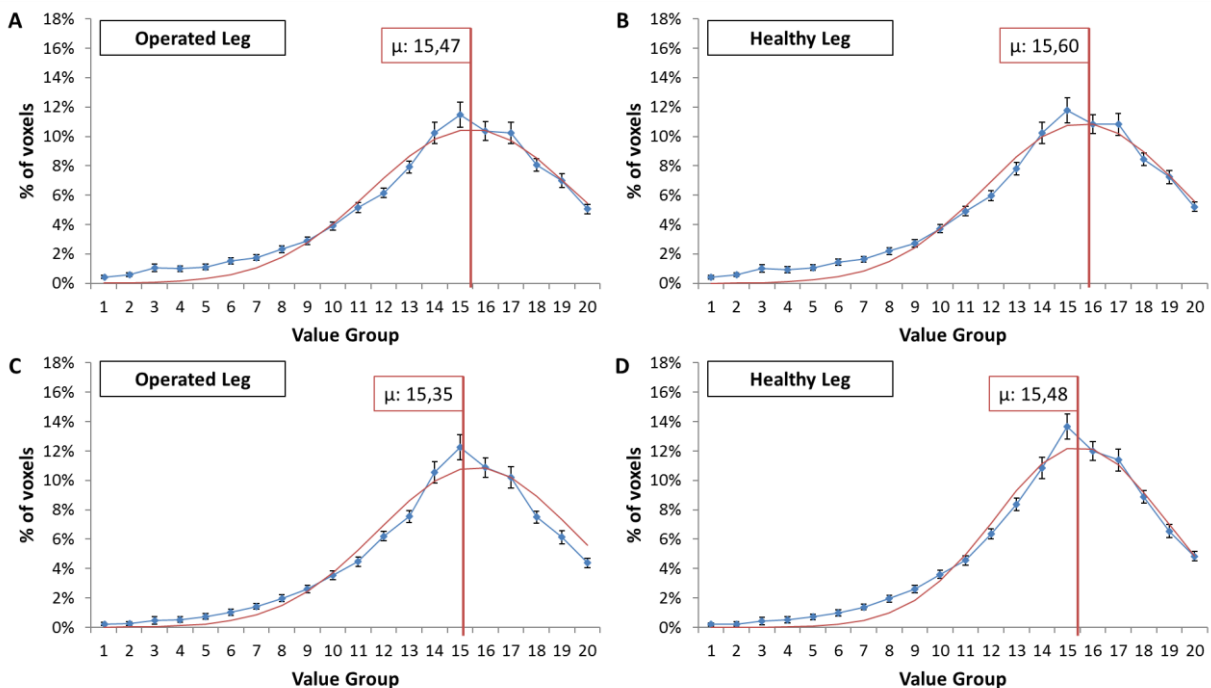


Figure 3.6: Hounsfield unit (HU) distribution from -135 to 200, divided into 20 bins. Each of the plots show mean values of each patient condition with computed standard error (blue curve). The plots on the left side show the operative leg histograms, while the plots on the right show the healthy leg. The red curve indicated the Gaussian curve fit for each HU distribution, and the vertical red line denotes the Gaussian centroid value, " $\mu$ ". A) and B) are non-cemented patients, while C) and D) are cemented patients [347].

As is apparent from Figure 3.6, when comparing the cemented and non-cemented implant groups, the healthy leg distribution elicited higher HU values, indicating the potential presence of more muscle in the healthy leg than within the operative leg. Additionally, HU values were higher in both legs in patients with the non-cemented prosthesis compared to those who were given a cemented implant. However, it is critical to note that statistical significances when comparing these values were not computed for average HU value analysis; further exploration in this regard is crucial to support physiological interpretation of these results.

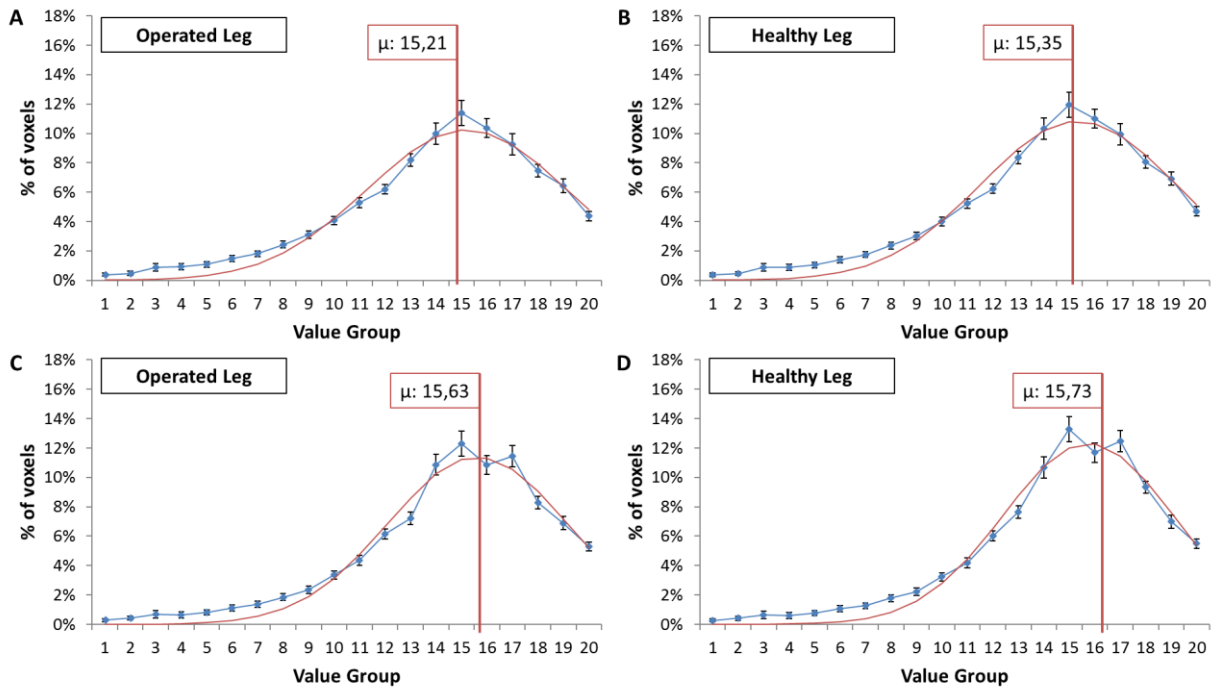


Figure 3.7: Binned Hounsfield unit (HU) distribution for patients grouped by sex. The red and blue curves were generated analogously to those shown in Figure 3.6. A) and B) are female patients, while C) and D) are male patients [347].

When comparing female to male patients, what is immediately evident is that the HU peak is shifted to the right in both legs of male patients compared to those of females, indicating somewhat expectedly that male patients had higher muscular density in both legs. Additionally, once again patients of either sex exhibited higher HU centroids in healthy legs compared to those which were fitted with an implant, confirming the results depicted in Figure 3.6.

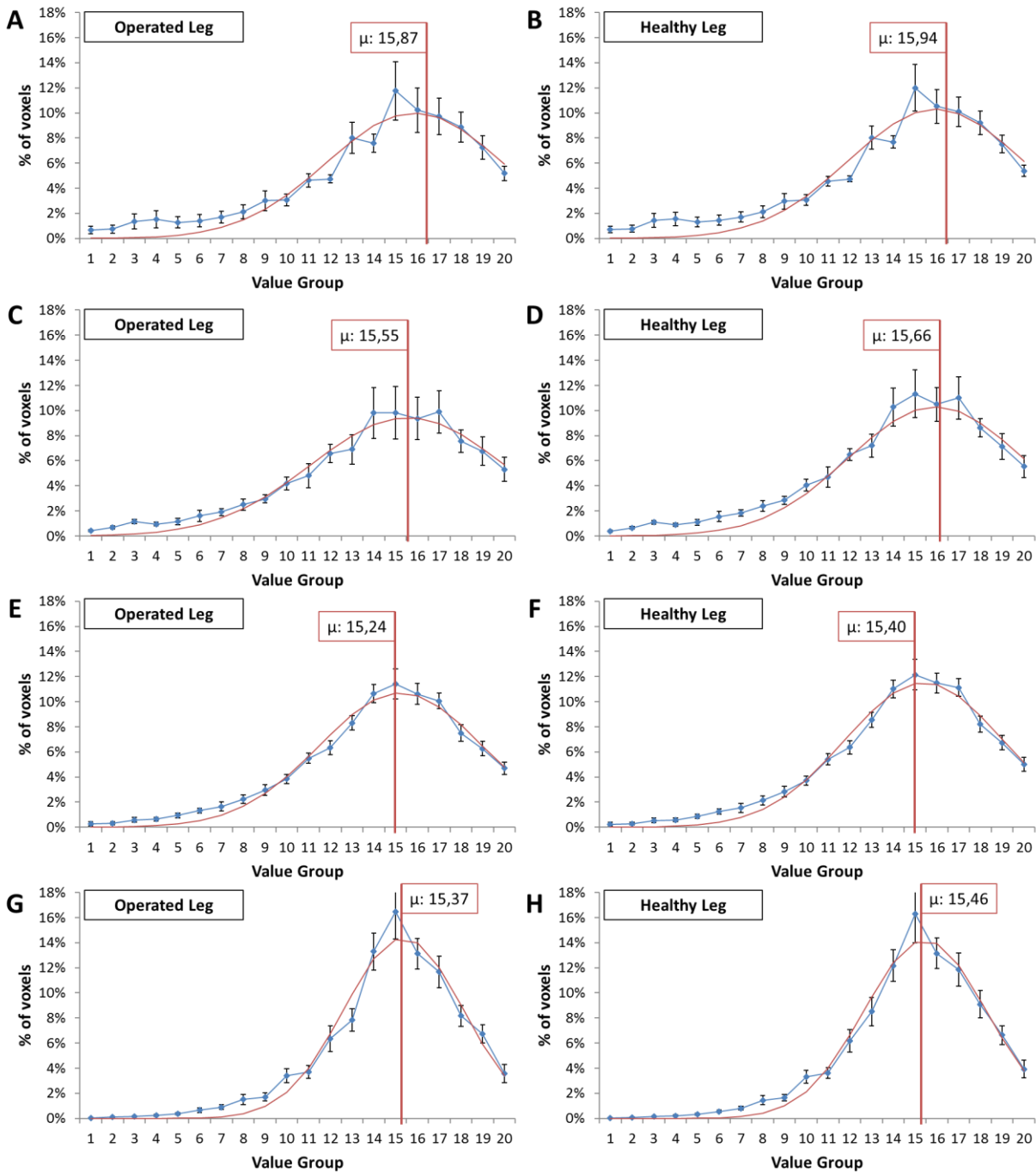


Figure 3.8: Binned Hounsfield unit (HU) distribution for patients grouped by age. The red and blue curves were generated analogously to those shown in Figures 3.6 and 3.7. A) and B) are patients less than 50 years old, C) and D) are patients between 51 and 61 years old, E) and F) are patients between 61 and 70 years old, and G) and H) are patients between 71 and 80 years old [347].

Finally, when comparing HU distributions for patients grouped according to age, youngest patients had much higher HU centroid values than those of older patients, with minimum values in both legs corresponding to the largest (n of 16) patient group, or individuals from ages 61-70. Interestingly, once again in all conditions, average HU values were higher in the healthy leg than in the operated leg. In addition to the location of each HU curve peak, it is evident that patients in the oldest age group (71-80) exhibited much narrower HU

distributions than those of other conditions, suggesting that within both legs of these patients, there was much less variation in the tissue type that was present. However, again, the computation of statistical significance in these comparisons is crucial to support physiological interpretation or relevance.

### 3.4.4 Discussion and Conclusions

What is most evident from the data presented is that although the muscular composition of operated legs was higher than healthy legs in almost every patient group, the average HU distribution centroids were higher in healthy legs than in the operated side. Shifts in average HU values has traditionally been an indicator of overall muscle quality, with higher HU values indicating a greater amount of lean muscle than fat or loose connective tissue. The presented results suggest that comparing percent composition to HU distribution does not necessarily correlate, but instead suggest that while muscular composition might be highest in the operated legs of patients, the overall muscular density, e.g. quality, may yet be lower in this leg compared to the healthy side. Further exploration into which analysis methodology best prescribes the capacity for the operated muscle to withstand both the implantation procedure and post-surgical rehabilitation is crucial to develop better decision-making in THA planning. In addition to this comparison of analysis methods, it also appears that males have higher percentages of muscle than females, but the significance of these differences must be computed to support the validity of this notion. The same notion is true when comparing patient age and implant procedure. These data together suggest that there is no clear utility in using traditional surgical metrics for governing THA prosthesis choice, such as age and sex. Finally, the distribution of HU values according to implant type indicates that the population of non-cemented patients is more similar in distribution (smaller variance), which thereby confirms the doctors' decisions to give them non cemented implants. The cemented patients' distributions show higher percentages of HU voxel values around those that correspond to muscular tissue, while these patients also exhibit larger variance in these values, indicating that some of the patients may have erroneously been prescribed a cemented implant, while a majority clearly received the optimal one. In sum, the comparison of muscular composition and HU distribution is a useful first step in developing a better understanding of the optimum THA procedure. Additionally, showing the similarities in muscle composition and quality between patients grouped by traditional planning metrics of age and sex suggests that surgical planning should incorporate additional patient conditions to identify the optimum THA planning strategy.

## Chapter 4

# Nonlinear Trimodal Regression Analysis of Radiodensitometric Distributions to Quantify Sarcopenic and Sequelae Muscle Degeneration

### 4.1 Introduction

Muscle degeneration, characterized by the progressive loss of muscle mass, strength, and function, has been consistently identified as an independent risk factor for high mortality in both aging populations and individuals suffering from neuromuscular pathology or injury. While there is much extant literature on its quantification and correlation to comorbidities, a quantitative gold standard for analyses in this regard remains undefined. Herein, we hypothesize that rigorously quantifying entire radiodensitometric Hounsfield Unit (HU) distributions can elicit much more information regarding muscle quality than extant methods that typically employ only average attenuation values. This study reports the development and utility of this method [45], wherein upper leg muscle quality was assessed with nonlinear trimodal regression analysis on radiodensitometric distributions from computed tomography (CT) scans of a healthy young adult, a healthy elderly subject, and a spinal cord injury (SCI) patient exhibiting complete lower motor neuron denervation. The method was then utilized with a total hip arthroplasty (THA) cohort to assess differences in healthy and operative legs, both presurgically and one-year following operation. Results from the initial representative models elicited high degrees of correlation to their HU distributions, and theoretical curve parameters highlighted notable, physiologically-evident differences between subjects. Likewise, results from the THA cohort echo initial physiological justification and additionally indicate significant improvement in muscle quality in both legs following surgery – a phenomenon most evident in the patients' operative legs. Altogether, these results highlight the utility of entire HU attenuation value distributions and identify novel curve-fitting parameters that could provide further insight into how muscle degeneration may be optimally quantified.

## 4.2 Materials and Methods

### 4.2.1 Subject Details and Recruitment

To first ascertain potential differences in muscle degeneration pathways, as evidenced by subtle changes in HU distributions, three subjects were utilized in the first part of this study. The first of these subjects was a healthy, 35 year old adult male subject, and the second was a healthy 68 year old elderly male. Both subjects' CT scans were obtained as part of a general volunteer dataset for research in our facility. The third subject was a 52 year old male who had suffered a right pelvic mass infiltration of the sciatic nerve, which had to be partially sacrificed during surgery. Both skin sensation and voluntary anterior-external leg movement were rescued following surgery, but despite the progressive reinnervation of the thigh and posterior leg muscles, complete denervation of the *Tibialis anterioris* and severe, partial denervation of the glutei and posterior muscles of the thigh was confirmed one year post-surgery. CT images at this time were obtained via academic collaboration with the RISE2-Italy project for the purposes of this study [42-44]. To further support the utility of the reported method, CT scans from healthy and operative legs of 15 primary THA patients were utilized. Patient data was obtained as part of our ongoing collaborative database with the Icelandic National Hospital (Landspítali, Reykjavik).

### 4.2.2 CT Acquisition and Soft Tissue Voxel Segmentation

All participants in the project were scanned with a 64 Philips Brilliance spiral-CT machine. The scanning region extended from the iliac crest to the middle of the femur (Figure 4.1). The image protocol included slice thicknesses of 1 mm, with slice increments of 0.5 mm, and the tube intensity was set to 120 keV. In order to assemble 3D models of each patient's leg for soft tissue voxel segmentation, each patient's CT scan was imported into MIMICS Software (Materialise, Leuven, Belgium). Tissue compositions within each leg volume were quantified by transforming CT numbers into HU values as previously reported [43]. These voxels were binned within the segmented volume into three HU intervals, which is evidenced in Figure 4.1 as follows: [-200 to -10], [-9 to 40], and [41 to 200] HU representing, respectively: fat (yellow), loose connective tissue and atrophic muscle (cyan), and normal muscle (red).



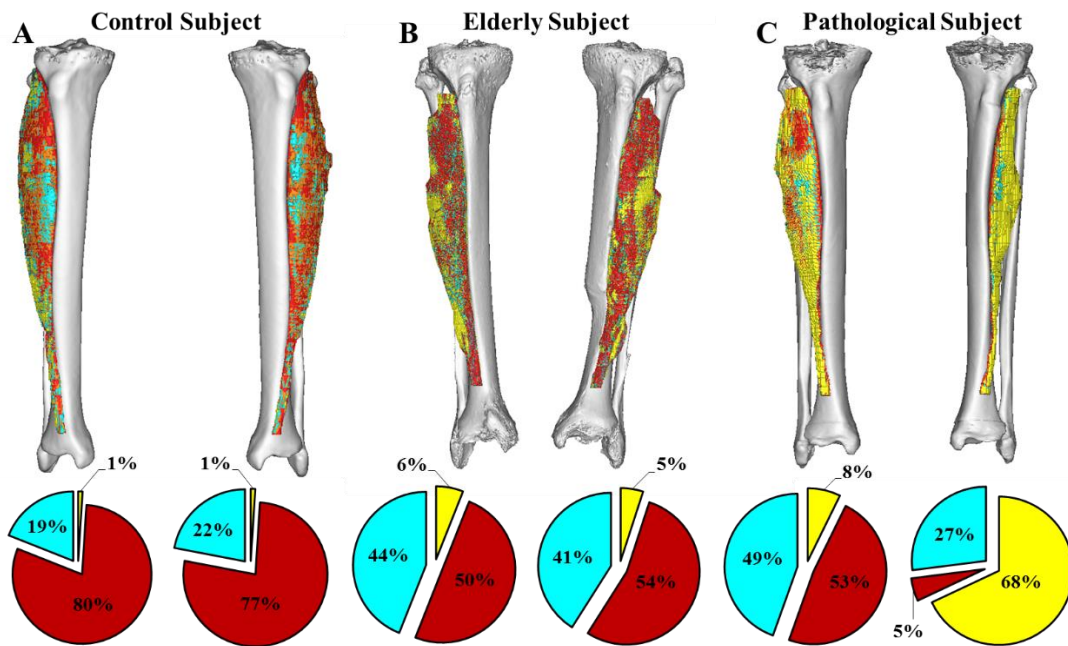


Figure 4.1: Segmented soft tissues and compositions within the *Tibialis anterioris* from A) the healthy control subject, B) the elderly subject, and C) the pathological subject. Three tissue types of distinct radiodensitometric domains were utilized for the purposes of this study as follows: [-200 to -10], [-9 to 40], and [41 to 200] HU representing, respectively: fat (yellow), loose connective tissue and atrophic muscle (cyan), and normal muscle (red). Note that the fat voxel elements of the right (healthy) muscle of this patient were almost entirely superficial (visible on the surface of the segmentation model) [45].

### 4.2.3 Voxel Distribution Binning

For each subject, HU distributions were derived from summing and transforming each voxel’s CT number value according to the following linear transformation expression, defined by discretization of distributions into 128 CT bins from the total range [-200 to 200] as performed in literature [34, 43-46]:

$$HU = CT \times 3.125 - 200 \tag{4.1}$$

Each resultant histogram was then exported for regression analyses. It should be noted that, for the purposes of comparing pathological muscle degeneration to sarcopenic degeneration, only the radiodensitometric distributions from subjects’ left legs were utilized in the first part of this study. However, both the healthy and operative legs were utilized for the analysis of THA patients.

### 4.2.4 Statistical Analyses

Results from the THA cohort analyses were assessed for statistical significance by two-tailed heteroscedastic student’s T-tests. Differences were considered statistically significant for  $p < 0.05$ .

### 4.2.5 The Method: Nonlinear Trimodal Regression Analysis

The method utilized to computationally define each HU distribution was a modified methodology for nonlinear regression analysis. First, the general equation for each distribution was defined as a quasi-probability density function by summing two skewed and one standard ( $\alpha=0$ ) Gaussian probability density functions ( $\varphi$ ):

$$\sum_{i=1}^3 \varphi(x, \mu_i, \sigma_i, \alpha_i) = \sum_{i=1}^3 \frac{N_i}{\sigma_i \sqrt{2\pi}} e^{-\frac{(x-\mu_i)^2}{2\sigma_i^2}} \operatorname{erfc}\left(\frac{\alpha_i(x-\mu_i)}{\sigma_i \sqrt{2}}\right) \quad (4.2)$$

where  $N$  is the amplitude,  $\mu$  is the location,  $\sigma$  is the width, and  $\alpha$  is the skewness of each distribution – all of which are iteratively evaluated at each CT bin, which is herein defined as the dependent variable,  $x$ . This definition is resultant from the hypothesis that each HU distribution is trimodal, in that they consist of three separate tissue types whose linear attenuation coefficients occupy distinct HU domains: namely, fat [-200 to -10 HU], loose connective tissue and atrophic muscle [-9 to 40], and normal muscle [41 to 200]. Additionally, we hypothesized that the inwardly-sloping asymmetries within the fat and muscle peaks could be described by skewnesses (defined by the error function component,  $\operatorname{erfc}$ ) of their probability density functions, whereas the central connective tissue distribution was assumed to be a normal, non-skewed Gaussian distribution. Utilizing this definition, a theoretical curve was generated by employing an iterative generalized reduced gradient algorithm via minimization of the sum of standard errors at each CT bin value,  $x$ , thereby generating an 11-parameter matrix of probability density function variables. This algorithm iterates each function variable according to the computed variance of each step, and the selection of new trial values is guided by computing the rates of change of this variance as new inputs are generated. The minimization of the sum of standard errors at each point, and thereby the maximization of the coefficient of determination,  $R^2$ , was computed according to standard definitions [45].

An illustration of the results of this concept is shown in Figure 4.2, where each of the three tissue types and their respective probability density functions have been depicted.

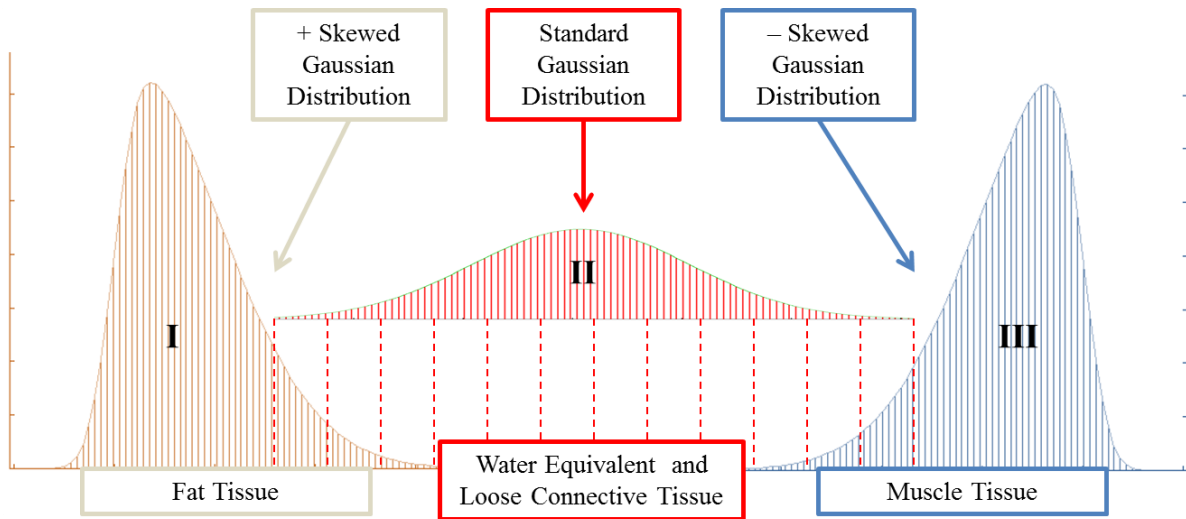


Figure 4.2: Diagram depicting the three components of the trimodal radiodensitometric distribution utilized in this study. This figure illustrates the location and skewnesses of each probability density function, with tissue types as previously defined [45].

### 4.3 Results and Discussion

#### 4.3.1 Initial Case Studies: A Comparison of Degeneration Pathways

As is evident from the results displayed in Figure 4.3, there are significant qualitative differences between the shapes of the HU distributions of the healthy, elderly, and pathological subjects. The curve of the healthy subject exhibits a definitively high-amplitude muscle peak and a comparatively blunted fat peak, whereas the fat and muscle components in the elderly subject’s curve is decidedly the opposite in appearance. Contrastingly, the pathological subject elicited a distribution with heavily skewed fat and muscle peaks which were likewise closer together and shifted towards negative HU values.

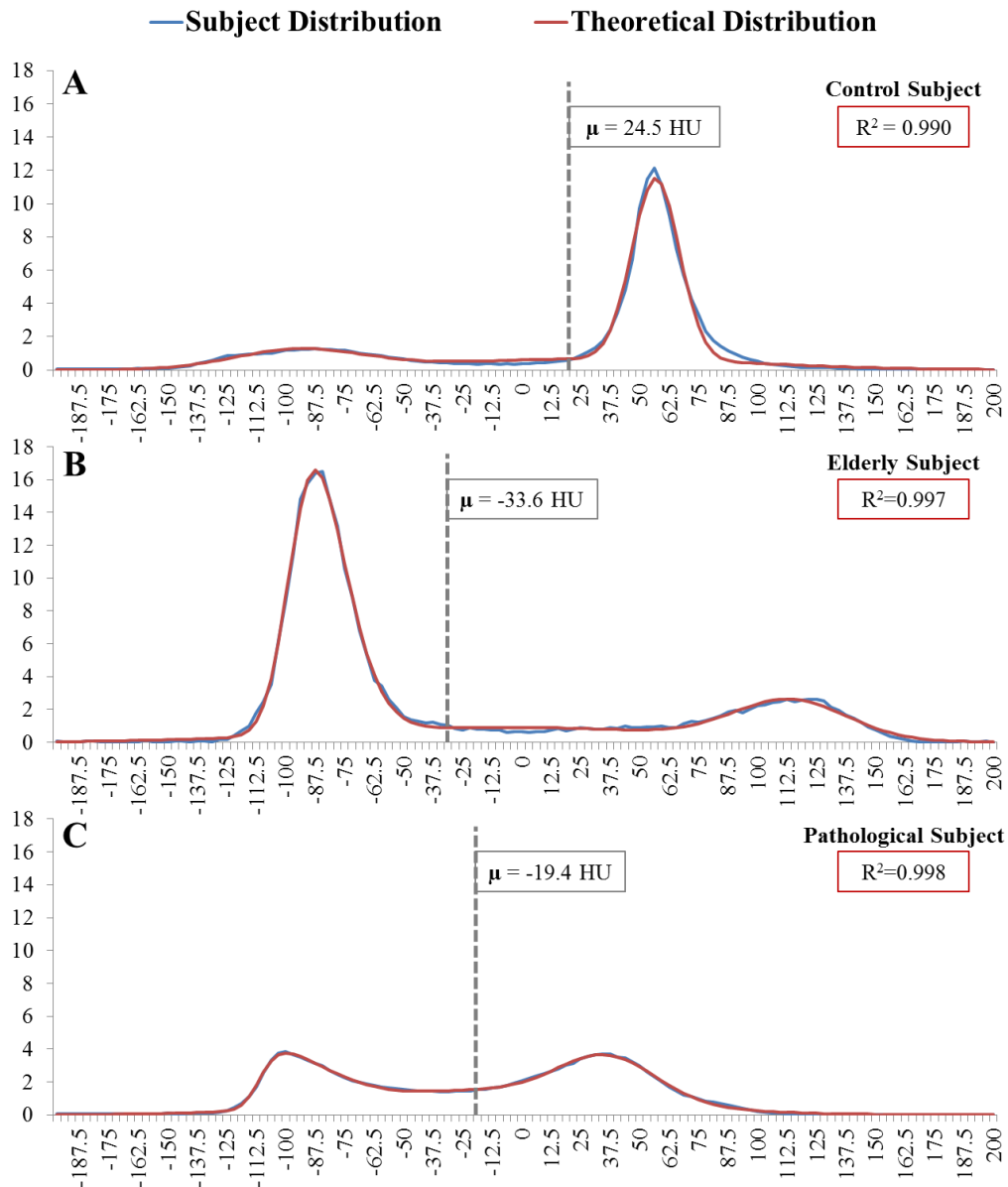


Figure 4.3: Radiodensitometric distributions showing their respective nonlinear regression curves and average HU values. A) The control subject's curve showed a large muscle peak at around 55 HU, which directly contrasted with B) the elderly subject's distribution. C) The pathological subject's distribution was much lower in total pixel count (due to lower overall mass within the leg volume) and elicited fat and muscle peaks that are similar in amplitude with a large connective tissue regime between them [45].

When compared according to the typical metric of average HU value, it is evident that the healthy subject's average HU value was significantly shifted towards the muscle peak in the distribution. However, the average HU values of the elderly and pathological subjects were nearly indistinguishable from one another. To better explore the clearly obtuse differences in their distributions, each regression analysis parameter was compiled and compared for the three subjects. The qualitatively distinguishable differences between HU distributions are further exemplified by the results from regression analyses and are compiled in Figure 4.4.

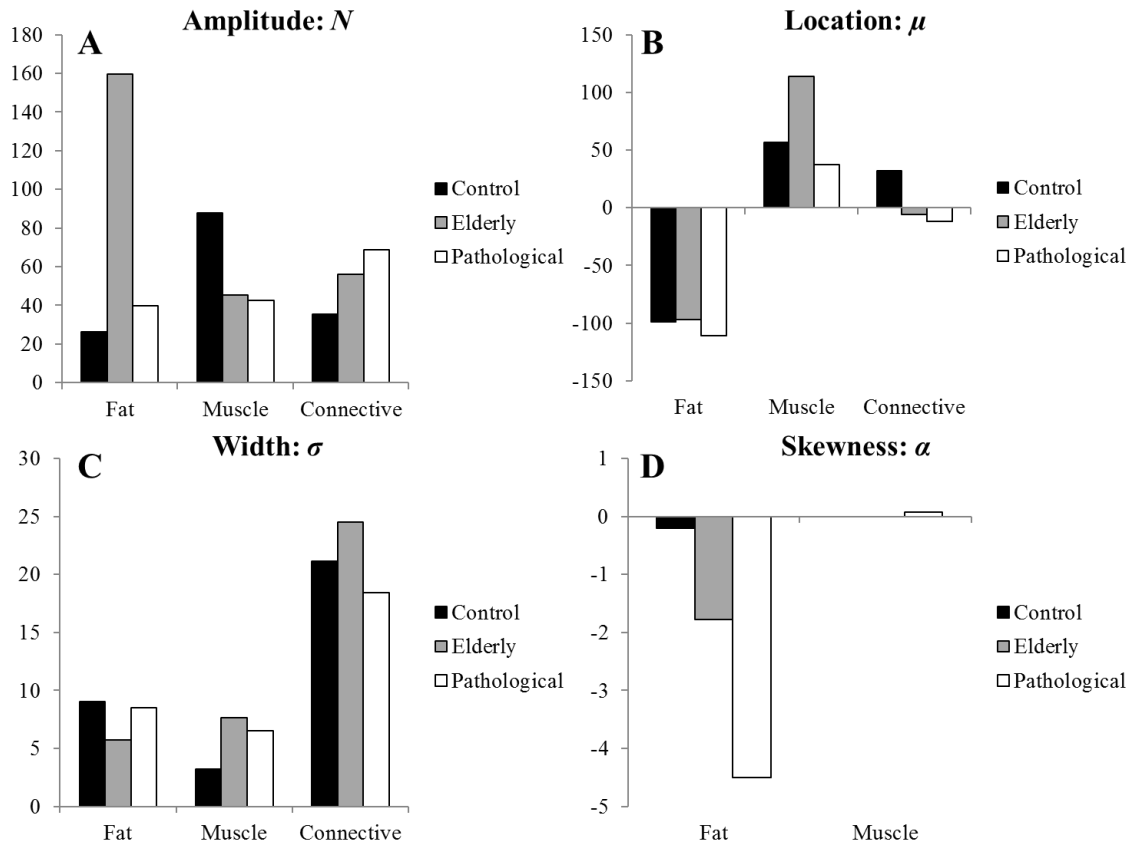


Figure 4.4: Results from the three representative subjects' nonlinear trimodal regression analyses. A) The amplitude parameter,  $N$ ; B) the location parameter,  $\mu$ ; C) the width parameter,  $\sigma$ ; D) the skewness parameter,  $\alpha$  [45].

As is evident in Figure 4.4, each of the distribution parameters confers its own distinct differences and relationships between subjects. The amplitude parameter,  $N$ , elicits particularly intriguing results when accounting singular tissue types; the elderly subject's fat amplitude is at least fourfold larger than those of the other subjects, and the control subject's muscle amplitude is largest by at least twofold. However, the connective tissue amplitude is highest in the pathological subject; intriguingly, these values increase nearly linearly between subjects, with the lowest connective tissue amplitude in the control subject. These data are qualitatively apparent in the muscle and fat tissue peaks, but somewhat less obvious in the central connective tissue peak. It is important to recall that our definition for the connective tissue distribution accounts for water-equivalent and loose-fibrous tissues that are always part of healthy leg volumes, but degraded, unhealthy muscle with aforementioned significant fatty infiltration would likewise populate this central HU attenuation region. This notion is described very well by the connective tissue amplifications progressively increasing from the control subject to the elderly and pathological subjects.

An analogous linearity is apparent when observing the fat tissue skewness, which is almost zero in the control subject and most extreme (highly negative) in the pathological subject. Interestingly, muscle skewness was zero in the elderly and control subjects, and nonzero but very small (0.07) in the pathological subject. These data suggest that the fat peak's positive asymmetry could likewise be due to the progressive infiltration of fatty tissue into the much higher HU value muscle tissue. However, as this skewness relationship is not commensurate in the muscle peak, it remains unclear whether skewness as a variable can completely

describe muscle degeneration.

The location parameter is almost identical between subjects' fat distributions, but the muscle peak location was singularly high in the elderly subject. Likewise, the control subject had a singularly positive connective tissue HU location, whereas the other subjects' values were negative. While less significant, perhaps, these results are still intriguing, as shifts in the connective tissue location parameter towards more negative HU values may physiologically implicate myosteatorsis or the general infiltration of non-contractile tissue; indeed, the present results show that the central connective tissue regime shifted towards more negative, "fatter" HU values in the elderly and pathological subjects. However, the fat peaks remained unshifted, and, unexpectedly, the muscle peak was higher in HU value in the elderly subject and nearly identical in the control and pathological subjects.

Finally, the width parameter exhibited noticeable differences between subjects. The control subject had the widest fat distribution, but the control muscle width was at least twofold lower than the other subjects. Likewise, while the elderly and pathological subjects had similar fat and muscle widths, the elderly subject elicited a comparatively much higher connective tissue distribution width. The physiological interpretation of width as a parameter is somewhat obscure, but one could argue that a sharply-defined muscle and/or fat peak might suggest a comparative reduction in muscle degeneration. This notion is supported by the control subject's muscle peak being remarkably lower in width the other subjects', but this is unsupported by the fat peak results.

#### **4.3.2 Assessing Changes in Muscle Following Total Hip Arthroplasty**

As previously mentioned, the potential utility of the reported method was further tested with a cohort of 15 THA patients to assess changes in their upper leg muscle following surgery. To do this, HU distributions from each patient were acquired from both presurgical and one-year postoperative CT scans. Each distribution parameter was analyzed for both healthy and operative legs, and differences were assessed for statistical significance.

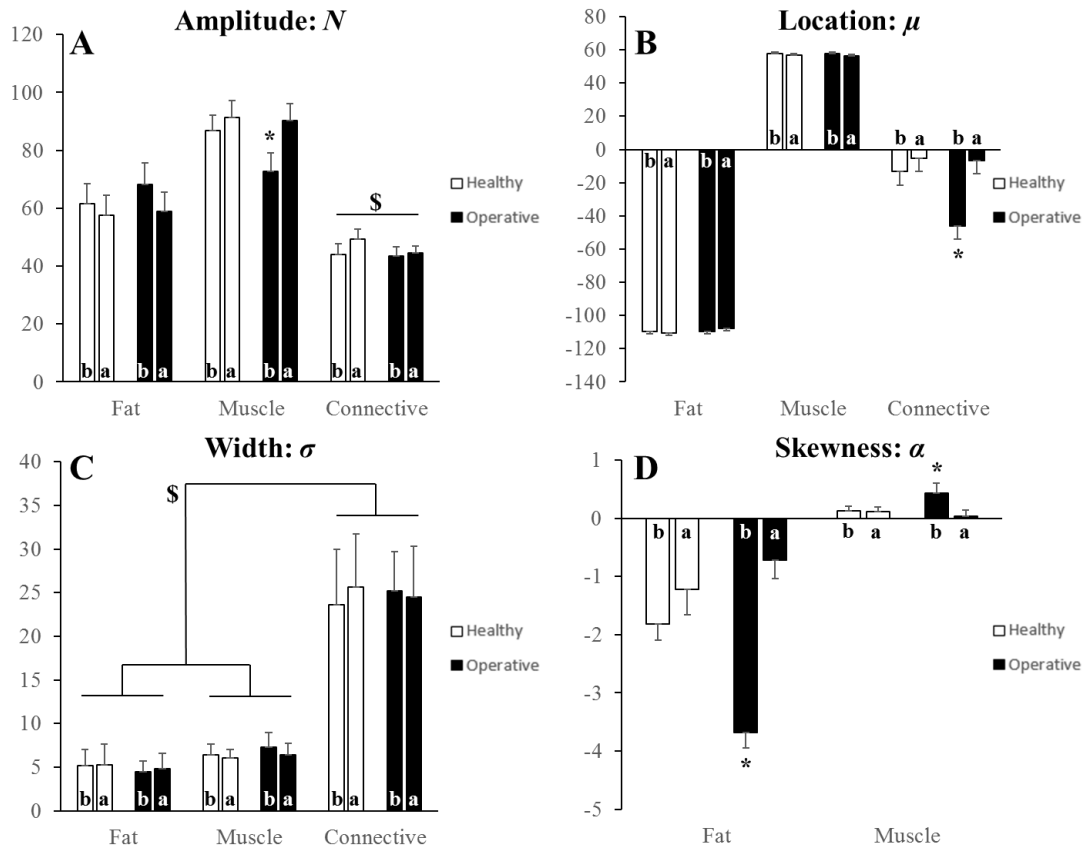


Figure 4.5: Results from the nonlinear trimodal regression analyses of the n=15 THA cohort. A) The amplitude parameter,  $N$ ; B) the location parameter,  $\mu$ ; C) the width parameter,  $\sigma$ ; D) the skewness parameter,  $\alpha$ . Note that \$ and \* denote  $p < 0.05$ , and the results are presented for before (b) and one-year after (a) surgery [45].

As is evident in Figure 4.5, the results from our THA cohort analyses further support many aforementioned relationships between regression parameters and the degree of muscle degeneration, if one operates under the physiological assumption that patient operative legs would naturally be less utilized than their healthy legs. In general, fat amplitudes decreased while muscle amplitudes increased one year after surgery. However, it was only in the operative legs that a significant increase in muscle amplitude was observed. Connective tissue amplitudes were all significantly lower than fat and muscle.

Regarding the location parameter, there were minimal shifts evident in muscle and fat peaks, but commensurate with previous observation, there were notable increases in connective tissue location values in both the healthy and operative legs one-year post surgery. This suggests the notion that connective tissue distributions may shift towards healthy muscle following one year of corrective ambulation and normative use. Indeed, once again, this was most evident and singularly significant in the operative leg.

The width parameter elicited no significant or meaningful changes in either leg, but in accordance with previous observation, the connective tissue peak widths were significantly larger than either the muscle or fat peaks, which were both nearly identical in magnitude in both legs. While not apparently useful, it still remains intriguing that each distribution parameter seems to have its own sensitivity with respect to the population.

Finally, the skewness parameter decreased in magnitude in both the healthy and operative fat peaks, but remained relatively constant and small (less than one) in the muscle peak – with one exception: the preoperative muscle peak was significantly higher than each of the others. We previously saw that the pathological subject had a much more extreme (more negative) fat skewness than the other two initial subjects – suggesting the infiltration and/or buildup of intramuscular fat in his degenerating muscle. This was once again similarly evident here, as the operative legs of the THA cohort elicited significantly more extreme, negative skewnesses than the rest of the fat peak values.

Altogether, these results indicate significant improvement in muscle quality in both legs following surgery – a notion which is most evident in patient operative legs. These data further support the notion that each HU distribution parameter may have a particular range of specificity when it comes to muscle assessment, thereby suggesting the method's utility as a straightforward indicator for muscle degeneration.

### 4.3.3 Exploring the Partial Volume Effect

One of the more commonly-discussed topics regarding tissue segmentation from medical images is that of the Partial Volume Effect (PVE). This phenomenon may be defined as the loss of fidelity in small regions or morphologies from limitations in spatial resolution of a particular imaging modality, and PVE is of particular relevance in positron emission tomography (PET) and dissemination of intracranial tissues using magnetic resonance imaging (MRI) [48]. In regards to our study here, one might argue that it may be necessary to initially correct pixels on the boundary of muscle groups and subcutaneous fat, due to the PVE being highest in these pixels. While this may indeed allow for a better fat to muscle segmentation fidelity, it may be argued that the degradation of myofibers would readily dictate the prevalence of PVE within our CT images. The correction of boundary pixels would therefore correct the very pixels we wish to consider in our distributions, as it is clear that their presence could be utilized as a supportive metric for assessing muscle degeneration.

To test this notion, we took the control subject's HU CT scan and segmented a two-pixel wide boundary layer between fat and muscle tissues. These pixels were then subtracted from the distribution at their given HU values and redistributed to either the fat or muscle mean HU value based on their respective proximities to either tissue. The results from this analysis are shown in Figure 4.6. As is evident from these results, the subtraction of these pixels resulted in a great reduction in the central connective tissue distribution and elicited minimal changes in regression analysis parameter values. However, the significant reduction in the water-equivalent and loose connective tissue peak highlights the possibility for PVE correction to remove useful data – especially considering that degenerated muscle and infiltrative adipose tissue would most likely exist in this region.



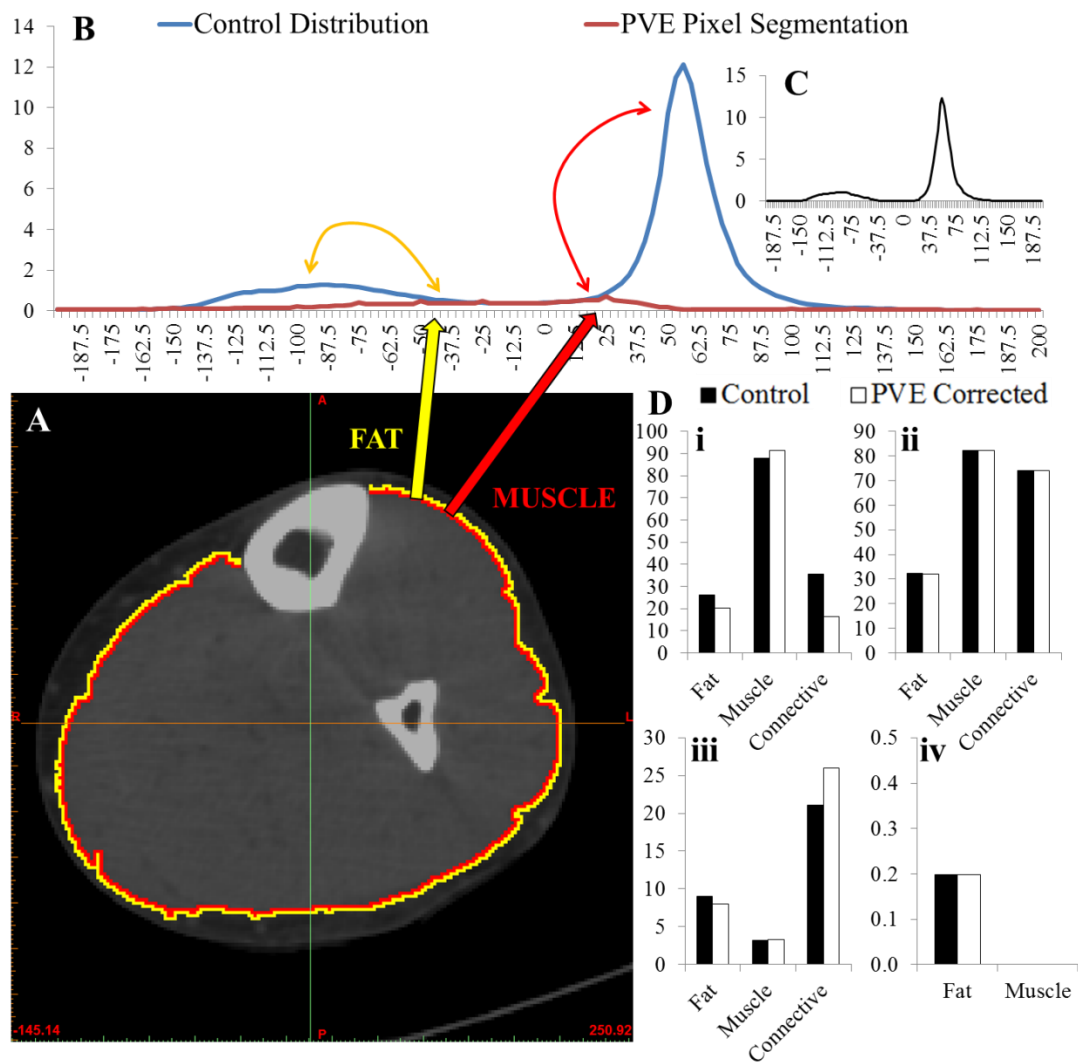


Figure 4.6: Results from Partial Volume Effect pixel removal using the healthy control subject. A) Transverse CT cross section of the control subject’s leg with two pixel boundary layers segmented and corrected. B) Distributions illustrating the control subject HU distribution and the segmented PVE pixel layer distribution. C) Resultant distribution showing an almost nonexistent connective tissue central peak. D) Results from the corrected distributions with each parameter: i: N; ii:  $\mu$ ; iii:  $\sigma$ ; iv:  $\alpha$  [45].

## 4.4 Conclusions

While there is much extant literature reporting the use of average HU values to investigate muscle quality and its utility as a comorbidity index, no studies have yet to utilize the entire radiodensitometric distribution. The increasing prevalence of sarcopenic and cachexic muscle degeneration necessitates the establishment of a robust quantitative myological assessment methodology. Herein, we hypothesize that rigorously quantifying entire HU distributions can elicit much more information regarding muscle quality than extant methods. This study reports the development and use of this method, wherein we assess upper leg muscle quality utilizing nonlinear trimodal regression analysis with radiodensitometric distributions from computed tomography (CT) scans of a healthy young

adult, a healthy elderly subject, and a spinal cord injury patient exhibiting complete lower motor neuron denervation. We show that physiological justification for these initial results is yet again evidenced by the use of a cohort of total hip arthroplasty (THA) subjects. While the use of more subjects and rigorous comparison to extant gold standard analyses will be essential to reinforcing the physiological claims reported here, these results altogether highlight the potential utility of our method and the importance of utilizing entire HU attenuation value distributions. We have likewise identified a host of novel regression parameters from these analyses that could provide further insight into how muscle degeneration can be optimally quantified. These notions support the conclusion that our method may be a pivotal first step in the development of a new gold standard for the analysis of muscle.

## Chapter 5

# Advanced Quantitative Methods in Correlating Sarcopenic Muscle Degeneration with Lower Extremity Function Biometrics and Comorbidities

### 5.1 Introduction

Sarcopenic muscular degeneration has been consistently identified as an independent risk factor for mortality in aging populations. Recent investigations have realized the quantitative potential of computed tomography (CT) image analysis to describe skeletal muscle volume and composition; however, the optimum approach to assessing these data remains debated. Indeed, most extant literature reports average Hounsfield Unit (HU) values and/or segmented soft tissue cross-sectional areas to investigate muscle quality. However, standardized methods for these gold standard analyses and their utility as a comorbidity index remain undefined, and no existing studies compare these methods to the assessment of entire radiodensitometric distributions. Herein, we investigate the combinatorial utility of extant gold standard analyses and nonlinear trimodal regression analysis (NTRA) of entire radiodensitometric distributions in correlating mid-thigh muscle quality with continuous class lower extremity function (LEF) biometrics and sarcopenic comorbidities. CT scans, LEF biometrics (normal/fast gait speed, timed up-and-go, and isometric leg strength), and sarcopenic comorbidities (total solubilized cholesterol and body mass index) were obtained from 3,162 subjects, aged 66-96 years from the population based AGES-Reykjavik Study [398]. 1-D k-means clustering was utilized to discretize each biometric and comorbidity dataset into twelve subpopulations, in accordance with Sturges' Formula for Class Selection. Dataset linear regressions were performed against eleven NTRA distribution parameters and gold standard analyses (fat/muscle cross-sectional area and average HU value). Additionally, NTRA parameters and gold standards were analogously assembled by age and sex. Results from gold standard analyses and specific NTRA parameters conferred linear correlation coefficients greater than 0.85, but multiple regression analysis of correlative

NTRA parameters yielded a correlation coefficient of 0.99 ( $P < 0.005$ ). These results highlight the specificities of each muscle quality metric to LEF biometrics and sarcopenic comorbidities and emphasize the utility of specific NTRA parameters from the analysis of entire radiodensitometric distributions. Standardizing a quantitative methodology for myological assessment in this regard would allow for the generalizability of sarcopenia research to the indication of compensatory targets for clinical intervention.

## 5.2 Materials and Methods

### 5.2.1 Subject Recruitment

The 3,162 subjects in this study were recruited as part of the AGES-Reykjavik Study in Reykjavík, Iceland. This cohort served as a five-year follow-up investigation that consisted of the remaining participants from the original AGES-Reykjavik study. The follow-up occurred from 2007-2011 and the percent of original subjects who participated was 71%. Informed consent was obtained from all participants [398].

The follow-up group initially included 3,316 subjects whereof 3,168 were with CT scans of the mid-thigh. Seven were excluded due to their non-participation in biometric or comorbidity measurements. The remaining 3,162 subjects (1,327 males, 1,835 females, mean age  $79.9 \pm 4.8$ ) participated in at least one of the investigation's data measurements, and, in total, the percentage of participants in each measurement ranged from 93.9% to 98.8% of the cohort population.

### 5.2.2 CT Acquisition and Segmentation

All participants in the project were scanned with a 4-row CT detector system at 120-kV (Sensation; Siemens Medical Systems, Erlangen, Germany) as previously described [399, 400]. The localizer scanning region extended from the iliac crest to the knee joints. For each subject, a single 10-mm thick transaxial mid-femur section was utilized in generating HU distributions and calculating fat and muscle cross-sectional areas. Prior to the transaxial imaging, the correct position for mid-femur imaging was determined by measuring the maximum length of the femur on an anterior-posterior localizer image, followed by locating the center of the femoral long axis.

Fat and muscle lean areas were segmented using the fascial plane outline between muscle and subcutaneous fat as previously described [49]. A manual contouring program to draw the contours of the total muscle bundle, and a threshold was chosen within each region to select voxels with CT densities greater than the maximal density of fat, as documented [401]. The lean area of each muscle region was then calculated as the number of voxels above this threshold, and lean tissue attenuation was defined as the mean CT density of these thresholded voxels. The average values for the left and right legs were utilized; if data for one leg were missing or invalid, then the extant thigh was singularly used; this was the case for 34 participants (approximately 0.70% of the total population).

### 5.2.3 LEF Biometrics and Sarcopenic Comorbidity Measurements

LEF biometrics were assessed as part of the aforementioned AGES-Reykjavik Study. Measurements included normal and fastest-comfortable gait speed (GSN and GSF, respectively), timed up-and-go (TUG), and isometric leg strength (STR). Gait speeds were calculated in seconds over a distance of six meters, and two trials were averaged for each subject according to published protocol [402]. The TUG test measured the time taken to stand from a seated position, walk three meters, turn around, walk back to the chair, and sit down; TUG is a well-reported screening metric for assessing balance problems and daily activity decline [403]. Finally, STR was measured via knee extension using an adjustable digital dynamometer on a fixed chair (Good Strength, Metitur, Palokka, Finland). STR was measured at a fixed knee angle of 60 degrees from full extension, and the subject's ankle was fastened to a strain-gauge transducer. STR was measured by taking the greater measured force of two knee extensions; each trial was four seconds in duration, with a 30 second rest between trials.

The AGES-Reykjavik study included many measurements pertaining to sarcopenic comorbidities, but the present study only considered those whose variables were continuous in class. The two cited sarcopenic comorbidities in particular that were available for utilization in this study were body mass index (BMI) and total solubilized cholesterol (SCHOL). BMI was calculated as the subject's weight (kilograms) divided by height (in meters) squared, as previously reported [404]. Fasting total solubilized cholesterol levels were measured via a Hitachi 912 with comparable enzymatic procedures (Roche Diagnostics, Mannheim, Germany) [405]. All body weight and lipid measurements fulfilled the criteria of the National Institute of Health and the National Cholesterol Education Program for accuracy and precision.

### 5.2.4 Pixel Distribution Binning and Smoothing

For each subject, HU distributions were derived from summing and transforming each pixel's CT number value according to the following linear transformation expression:

$$HU = CT \times 3.125 - 200 \quad (5.1)$$

Following transformation, HU values were binned into 128 bins, as typical for CT assessment protocols [333]. Resultant histograms were smoothed by a non-parametric fitting algorithm to obtain underlying empirical probability density functions (PDF) for each histogram. Each PDF was then exported for NTRA regression analyses.

### 5.2.5 Nonlinear Trimodal Regression Analysis (NTRA) Method

The method utilized to computationally define each HU distribution was a modified methodology for nonlinear regression analysis. First, the general equation for each distribution was defined as a quasi-probability density function by summing two skewed and one standard ( $\alpha=0$ ) Gaussian distributions:

$$\sum_{i=1}^3 \varphi(x, \mu_i, \sigma_i, \alpha_i) = \sum_{i=1}^3 \frac{1}{\sigma_i \sqrt{2\pi}} e^{-\frac{(x-\mu_i)^2}{2\sigma_i^2}} \operatorname{erfc}\left(\frac{\alpha_i(x-\mu_i)}{\sigma_i \sqrt{2}}\right) \quad (5.2)$$

where  $N$  is the amplitude,  $\mu$  is the location,  $\sigma$  is the width, and  $\alpha$  is the skewness of each distribution – all of which are iteratively evaluated at each CT bin,  $x$ . This definition is resultant from the hypothesis that each HU distribution is trimodal, in that they consist of three separate tissue types whose linear attenuation coefficients occupy distinct HU domains: namely, fat [-200 to -10 HU], loose connective tissue and atrophic muscle [-9 to 40], and normal muscle [41 to 200]. Additionally, we hypothesized that the inwardly-sloping asymmetries within the fat and muscle peaks could be described by skewnesses of their probability density functions, whereas the central connective tissue distribution was assumed to be a normal, non-skewed Gaussian distribution. Utilizing this definition, a theoretical curve was generated by employing an iterative generalized reduced gradient algorithm via minimization of the sum of standard errors at each CT bin value,  $x$ , thereby generating an 11-parameter matrix of PDF variables. This algorithm iterates each function variable according to the computed variance of each step, and the selection of new trial values is guided by computing the rates of change of this variance as new inputs are generated. The minimization of the sum of standard errors at each point, and thereby the maximization of  $R^2$ , was computed according to their standard definitions:

$$R^2 = 1 - \frac{RSS}{SST}, \quad SST = \sum_{i=1}^n (y_i - \bar{y})^2, \quad RSS = \sum_{i=1}^3 (y_i - f(x_i))^2 \quad (5.3)$$

$$(5.4)$$

$$(5.5)$$

An illustration of the results of this concept is shown in Figure 4.7, where each of the three tissue types and their respective PDFs have been depicted.

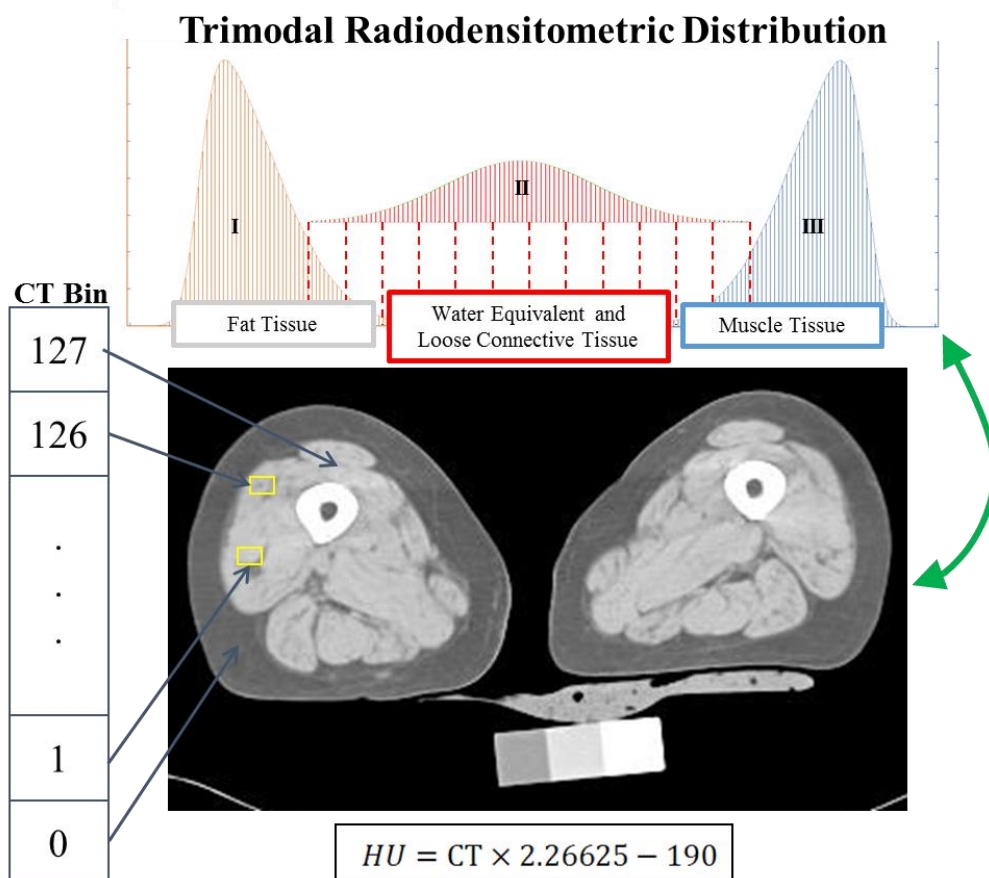


Figure 5.1: Diagram depicting the three components of the trimodal radiodensitometric distribution utilized in this study. This figure illustrates the location and skewnesses of each PDF, with tissue types as follows: I) Fat [-200 to -10 HU], II) Water Equivalent and Loose Connective Tissue [-9 to 40 HU], and III) Muscle [41 to 200 HU].

### 5.2.6 1-D K-means Clustering Discretization of LEF Biometrics and Sarcopenic Comorbidities

With the modern adoption of electronic medical records (EMRs), the availability and breadth of clinical data for use in medical research has markedly increased [406]. Commensurately, there has been a rising interest in the development of novel algorithms from the fields of data mining and machine learning for the processing of medical data [407, 408]. One of the common preprocessing steps utilized prior to the employment of many of these algorithms is the discretization of continuous variables. Discretization eliminates the necessity for presumptions regarding distribution characteristics, as the method employs the counts within the dataset to directly evaluate conditional probabilities [409].

For this reason, the present work identified the discretization of continuous class LEF biometrics and sarcopenic comorbidities as a strategic priority. Unsupervised methods for discretization were initially selected, as they eliminate the requirement for class labels and can eventually be utilized for multiple applications, unlike supervised discretization methods [410]. After investigation, the transformation of each continuous class variable was ultimately performed using one-dimensional (1-D) k-means clustering [411]. In this method,

each cluster-derived bin had observations sorted using a medoid-partitioning algorithm [412]. The number of groups ( $k$ ) was calculated using Sturges' formula for class selection, which implicitly bases bin sizes upon the range of the dataset, assuming a normal distribution of class values [409, 413]:

$$k = \lceil \log_2 n \rceil + 1 \quad (5.6)$$

where the brackets denote the ceiling function,  $n$  is the dataset population, and  $k$  is the number of bins. This yielded a  $k$  of twelve for each LEF and comorbidity parameter the study. Finally, to assess the fidelity of linear relationships between muscle quality gold standards and NATRA parameters, subjects were discretized by age and sex. Discretization was again unsupervised, but this time by equal frequency due to the truncated nature of age, which is, in concept, a continuous class variable [414]. Using Sturges' formula here resulted in 11.4 bins for men and 11.8 for women, so twelve bins were again chosen for the sake of simplicity in assessing comparative linear regressions. This yielded bin populations of 111 for men, and 153 for women.

### 5.2.7 Statistical Analyses

Simple linear regression models were utilized to statistically correlate the relationships of each independent variable (LEF biometrics and sarcopenic comorbidities) with respect to dependent variables (NTRA parameters and gold standard analyses). Multiple regression models were then utilized on assemblies of each dependent variable whose correlation coefficients described greater than 85% of the variance in each independent metric. One-way ANOVA and F-tests for overall significance were compiled from each multiple regression model to illustrate statistically meaningful correlation.

## 5.3 Results and Discussion

### 5.3.1 Gold Standard Analyses on LEF Biometrics and Sarcopenic Comorbidities

Figure 5.2 depicts the results from gold standard analyses on LEF biometrics and sarcopenic comorbidities. Each population bin is depicted with colored circles ranging from the most unhealthy comorbidity measurement or LEF value (red) to the healthiest group (green). Regression lines are likewise depicted for each data series, along with their respective coefficients of determination ( $R^2$ ).



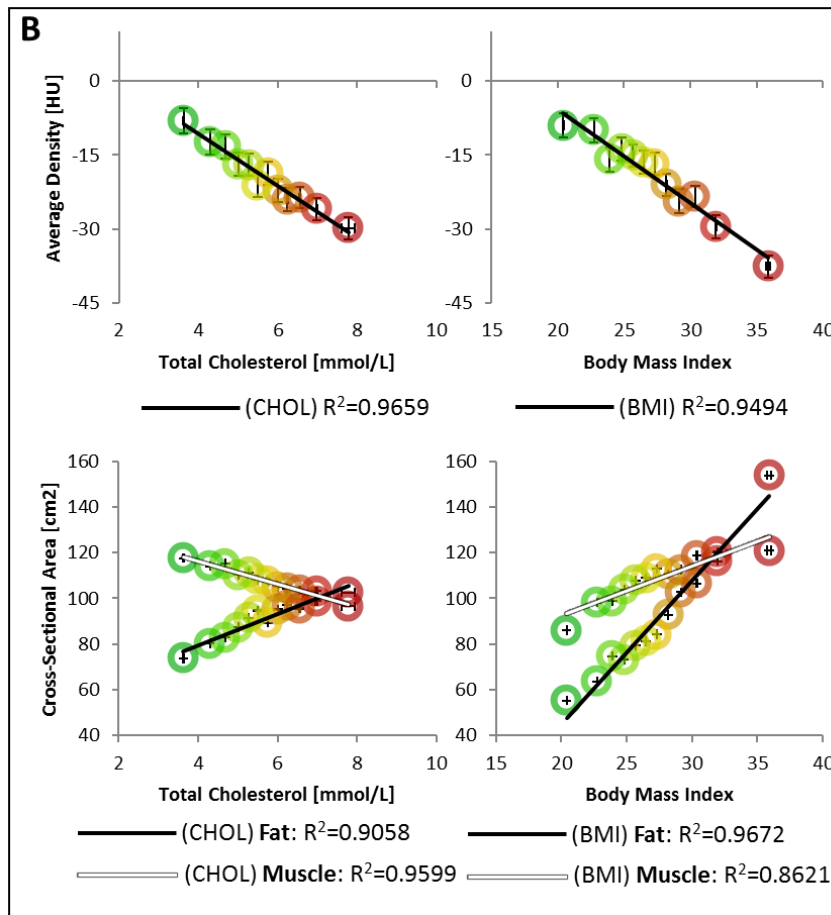
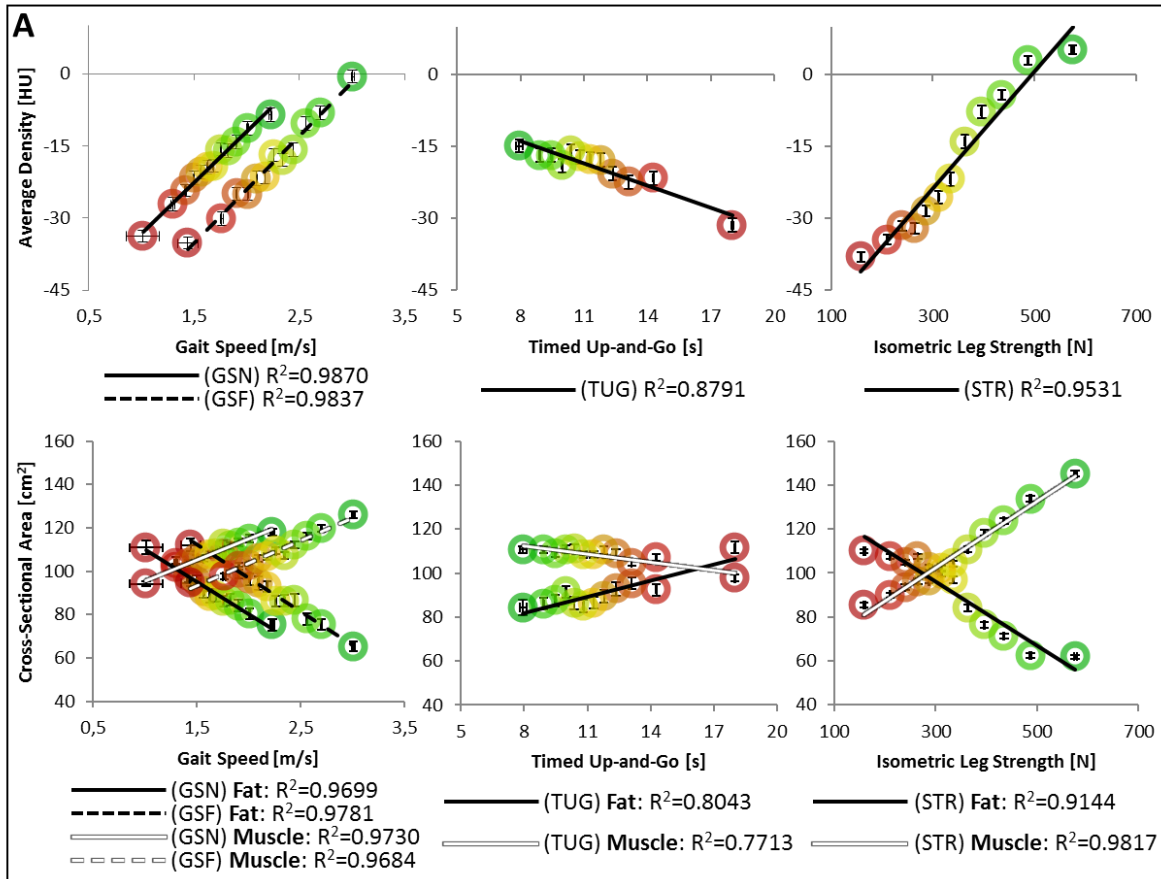


Figure 5.2: Gold standards against A) LEF biometrics and B) sarcopenic comorbidities.

As is evident in Figure 5.2, the assessment of LEF biometrics and sarcopenic comorbidities with gold standard methods elicited a host of physiologically evident results that are, to our knowledge, presented in this manner for the first time. Firstly, fat cross-sectional areas held an inverse relationship with normal gait speeds, fast gait speeds, and isometric leg strengths, while conversely showing positive correlation with timed up-and-go speeds (although while, in general, capturing considerably less of the parameter variance: 0.80 and 0.77 for fat and muscle, respectively). At the same time, muscle cross-sectional areas showed a directly antithetical relationship with LEF biometrics, compared to fat. Likewise, average HU values show commensurately expected trends: the worse the LEF performance, the greater the shift in average soft tissue density towards fat (increasingly negative HU values). While these relationships are wholly explainable by our extant understanding of muscle physiology, the apparent trends evidenced by sarcopenic comorbidities are more intriguing: indeed, one might not have expected any significant relationships without the removal of potentially-obfuscating, but entirely relevant patient details. In this regard, it is interesting to see how increasingly unhealthy BMI and Solubilized Cholesterol analogously conferred to increasing fat areas and greater shifts towards negative average HU values. However, with increasing BMI, both fat and muscle areas increased together, although the rate of increase in fat was greater than the increase in muscle area. Altogether, it is apparent that most gold standard metrics held linear regression coefficients of determination greater than 0.85, suggesting their general utility in capturing the population variance of each metric.

### **5.3.2 NTRA Analyses on LEF Biometrics and Sarcopenic Comorbidities**

As a complimentary analysis to gold standard methods, NTRA parameters were analogously assembled. Figures 5.3 and 5.4 depict linear regressions of distribution amplitudes, locations, widths, and skewnesses against LEF biometrics.

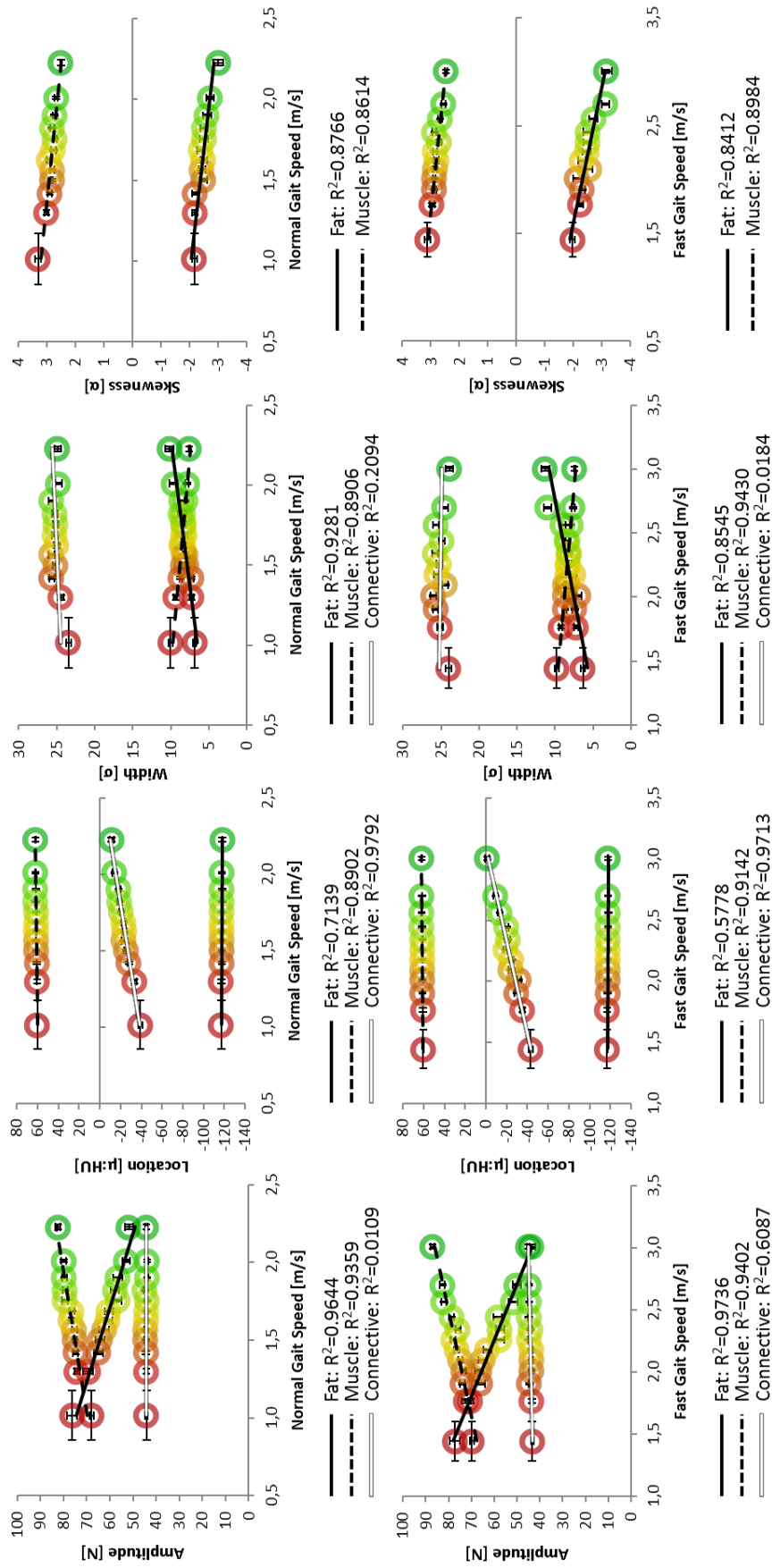


Figure 5.3: NTRA parameters against gait speed LEF biometrics.

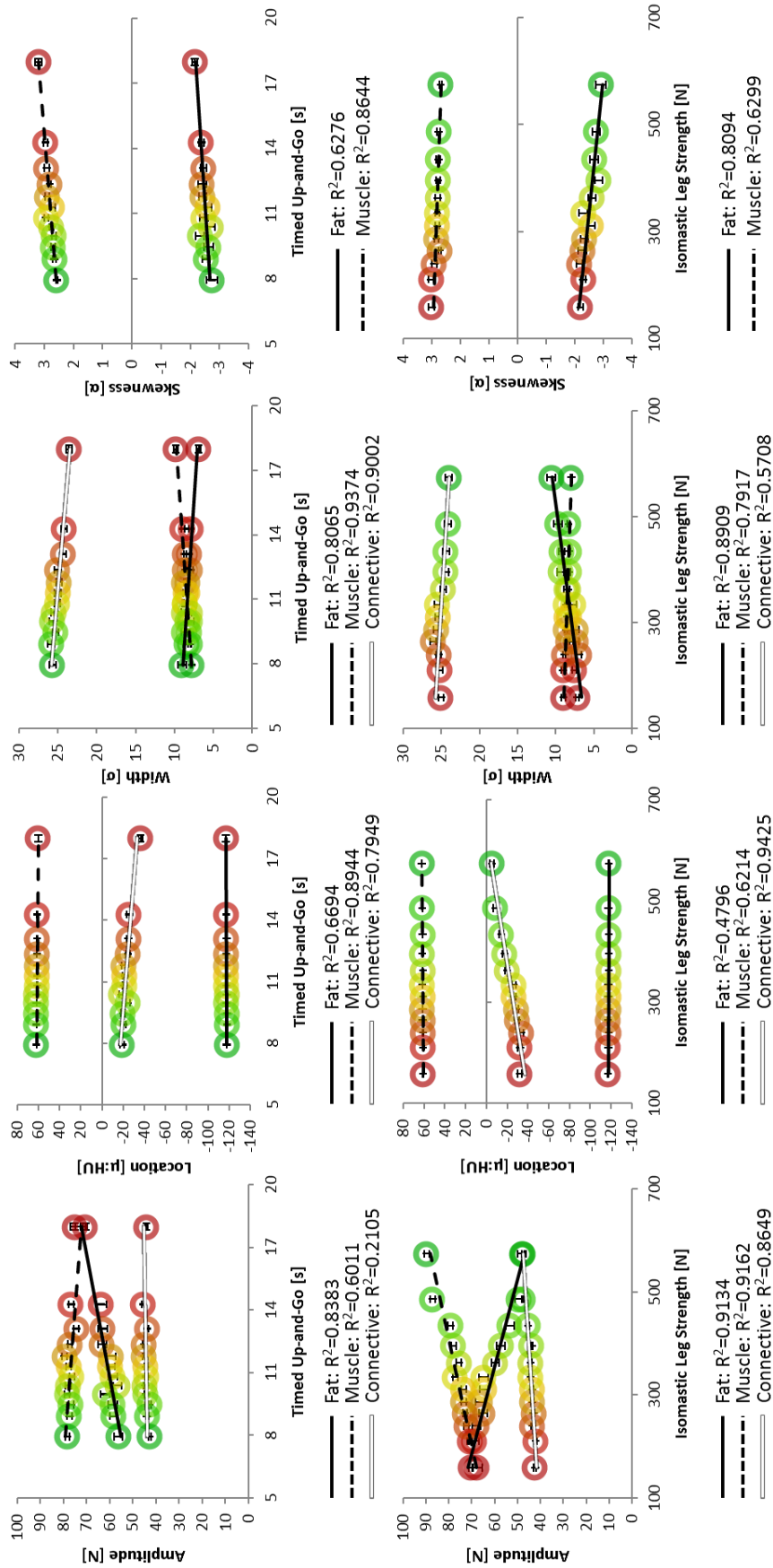


Figure 5.4: NTRA parameters against timed up-and-go and isometric strength biometrics.

What is first apparent from Figures 5.3 and 5.4 is the great variance in specificity among coefficients of determination. Many parameters yield strongly linear relationships on the order of or greater than gold standard analyses ( $R^2 > 0.85$ ), while others yield minimal or no correlation. It may be readily hypothesized that the amplitude parameter varies identically with cross-sectional area against these metrics, assumptively suggesting a direct relationship to the overall quantity of each soft tissue type. Indeed, this is readily apparent in fat and muscle amplitudes: we see increasing fat amplitudes with decreasing LEF performance, along with an antithetical muscle amplitude relationship. However, what is clearly different is the inclusion of the loose connective/water equivalent tissue regime, which according to these results seems less tied to quantity, and instead more to overall tissue quality – with the clear exception of isometric leg strength yielding a strong relationship with connective tissue amplitude. For instance, it is apparent here how connective tissue locations clearly shift towards more negative HU values with decreasing LEF performance. In the context of the aforementioned presence of myosteatosis in aging muscle, the commensurate presence of fibrosis has been observed [73, 74], but its precise measurement by gold standard metrics remains impossible. Pushing further into other medical imaging modalities such as MRI or ultrasound, to a degree, severe tissue fibrosis is detectable using traditional image processing modalities; however, as their employment methods are generally more tuned to detect and diagnose pathological hepatic fibrosis, they may not be optimized for detecting the comparatively-minute changes associated with the onset of sarcopenia. Indeed, the contribution of fibrosis to traditional metrics of muscle quality remains an essential target for further investigation; it is thereby enticing, perhaps, to observe how the inclusion of the present loose connective/water equivalent tissue regime in NTRA analysis may serve as a direct metric for fibrosis with further study.

One may likewise hypothesize that the NTRA width parameter might be directly related to the overall variation in pixel values for each tissue regime, as an increasing range of HU values would simply imply an increasing Gaussian distribution width. These data suggests that this parameter is minimally related to gait speed and isometric leg strength, but is instead almost singularly tied to timed up-and-go duration, as decreasing width clearly confers longer TUG times. In all LEF metrics, however, we see the same relationship: increasing fat width and decreasing muscle width confer decreasing LEF performance. This could likewise be more related to notions of tissue quality, as myosteatosis would confer an increase in partial volume effect from an increase in the relative proximity of inter- and intramuscular fat and lean muscle. However, why this may be singularly apparent in the fat distribution remains unclear.

In regards to the NTRA location parameter, as before, our results indicate that shifts in these values are less related to muscle and fat, but highly connected to loose connective/water equivalent tissue. The gold standard analogue in the case of location values would, of course, be the average HU value. Indeed, when comparing the linear relationships of these parameters, we see analogous shifts towards increasingly negative values in accordance with decreasing LEF performance.

Finally, the NTRA skewness parameter may again be potentially thought of as a direct descriptor for muscle quality, as intermuscular adiposity may incur the migration of lean tissue pixels towards the center of the overall distribution, resulting in an increasingly-skewed PDF shape. Intriguingly, all LEF parameters present the same trend: increasing

muscle skewness and less-negative fat skewness values inversely correlate with LEF performance. However, this dependency seems more tied to muscle than fat – an explanation for which, again, remains unclear.

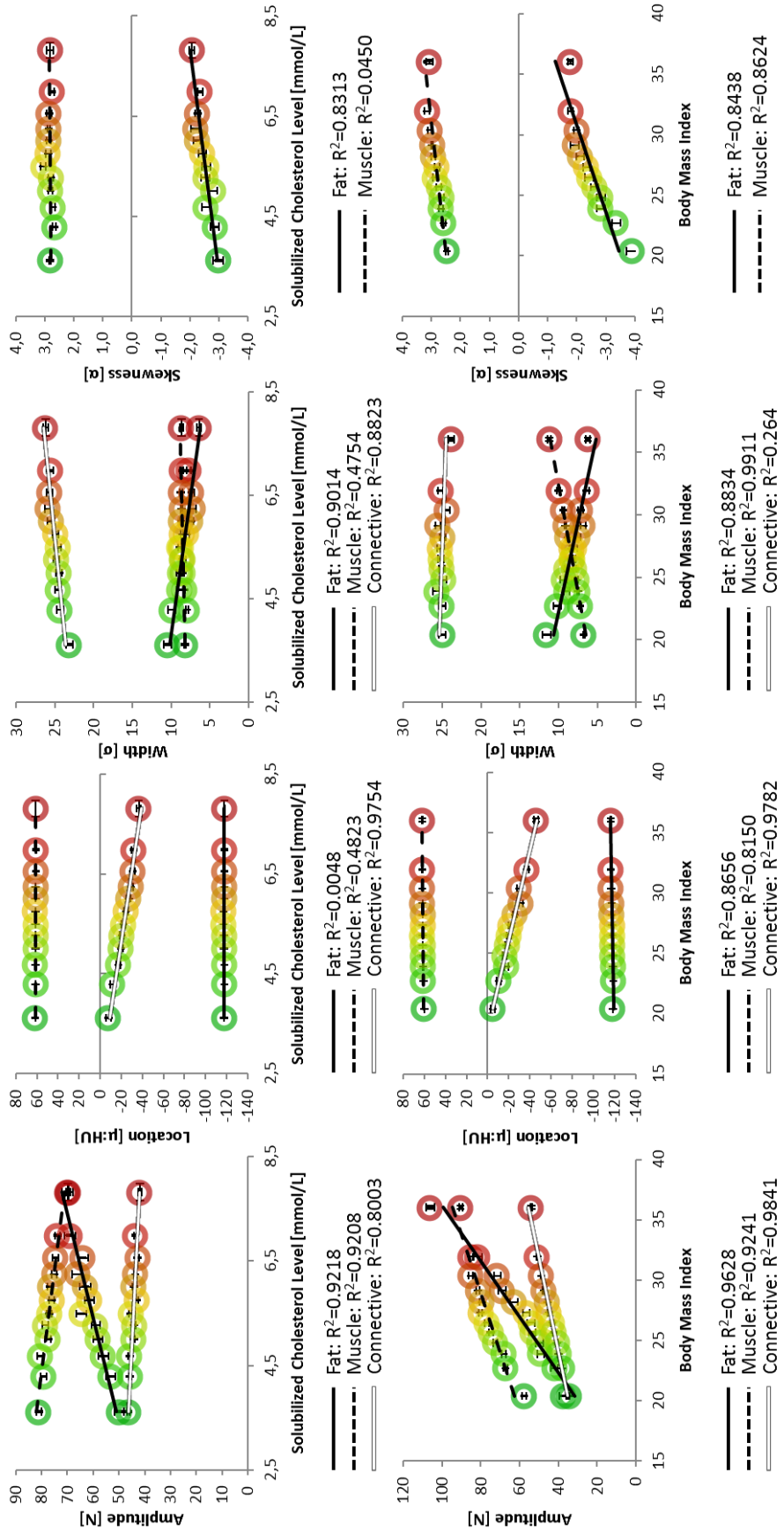


Figure 5.5: NTRA parameters against sarcopenic comorbidities.

Finally, Figure 5.5 depicts linear relationships with NTRA parameters in accordance with sarcopenic comorbidities. Here, one can immediately note analogous dependencies, as compared to LEF performance biometrics. Indeed, increasing fat amplitudes and decreasing muscle amplitudes confer healthier measurements for BMI and SCHOL levels. Likewise, shifts in connective tissue location confer increasingly negative values with greater BMI and higher SCHOL levels. Additionally, increasing fat widths and decreasing muscle widths analogously confer increasingly unhealthy comorbidity measurements; intriguingly, we also see increasing connective widths conferring higher SCHOL values. Finally, we again see increasing muscle skewnesses and less-negative fat skewnesses correlate with less healthy BMI and SCHOL values. To summarize these results, Figure 5.6 depicts the specificities of each NTRA parameter, showing associated LEF biometrics and comorbidities whose linear regressions yielded coefficients of determination of at least 0.85.

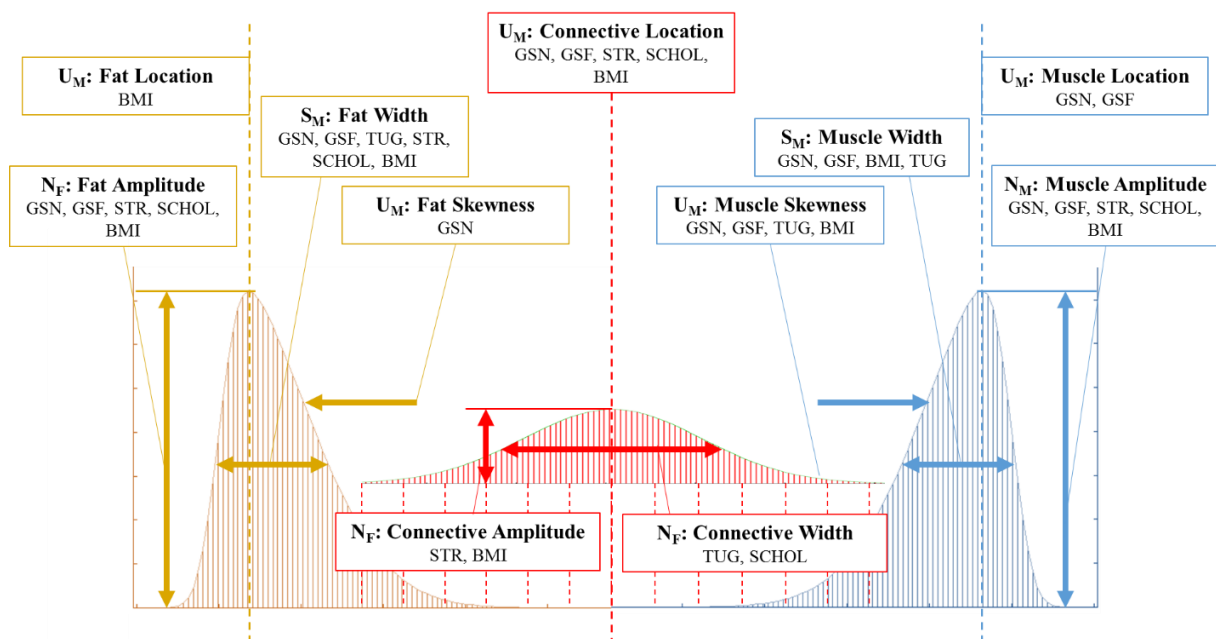


Figure 5.6: Assembly of NTRA parameters whose LEF and comorbidity parameters yielded linear correlation coefficients greater than 0.85.

Finally, multiple regression analyses were performed on all gold standards and NTRA parameters with individual linear regression coefficients of determination over 0.85 for each LEF and comorbidity metric. Results from these analyses produced multiple regression models involving each LEF and comorbidity metric, and all models yielded multiple correlation coefficients greater than 0.99 with ANOVA and F-test results with  $P < 0.005$ . These results indicate the high fidelity of multivariate correlation and robust statistical significance when all highly-linear LEF biometrics and comorbidities are included. Additionally, such strong multivariate correlation suggests, at the very least, that these NTRA parameters should be included alongside extant gold standard methods for muscle quality quantification.

### 5.3.3 NTRA and Gold Standard Analyses on Age and Sex

Figure 5.7 depicts the results from NTRA and gold standard analyses on age and sex.



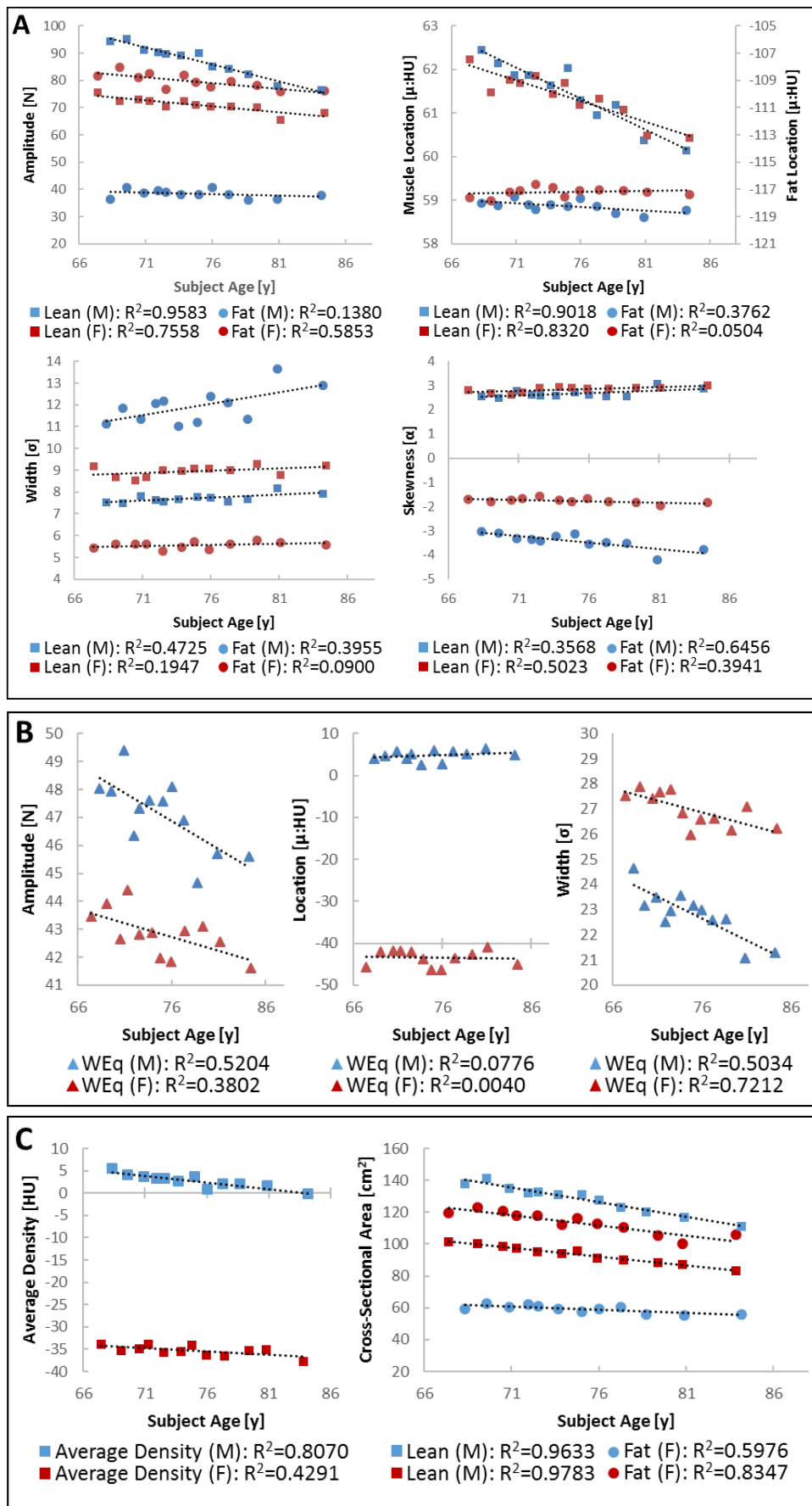


Figure 5.7: A) NTRA parameters along with B and C) gold standards against age and sex.

As an additional investigation, NTRA parameters and gold standards were assessed for linear correlation with age, stratified by subject sex. Figure 5.7 depicts these results. What is immediately evident is that, indeed, age and sex may be possible confounding factors in muscle quality analysis. However, while the linear dependencies of NTRA and gold standard metrics are clear in some cases (analogously greater than 0.85), correlation coefficients are overall much lower than those of LEF parameters and comorbidities. This altogether suggests the necessity for correcting our model for age and sex, but likewise underscores the comparative ineffectuality of classic clinical assumptions of sarcopenic muscle degeneration based on age and sex. Nonetheless, modeling muscle degeneration as depicted without such correction yet with high degrees of statistical significance is illuminating for further discussion, as being able to predict changes in LEF biometrics and comorbidities related to sarcopenia regardless of age and sex may be of considerable inherent value.

## 5.4 Conclusions

The increasing prevalence of Sarcopenic muscle degeneration necessitates the establishment of a robust quantitative myological assessment methodology. While there is much extant literature reporting the use of average HU values to investigate muscle quality as a Sarcopenic index, no studies have yet to utilize entire radiodensitometric distributions and define a generalized analytical tool for their assessment. Herein, we show that rigorous quantification of entire HU distributions can elicit many unique assessment parameters and therein provide additional information regarding muscle quality alongside extant gold standard methods. Likewise, the contribution of fibrosis to traditional metrics of muscle quality remains an essential target for further investigation, and the inclusion of the loose connective/water equivalent tissue regime in NTRA analysis may serve as a direct metric for fibrosis with further investigation. As is true in any such study, however, the use of more subjects and aging comorbidities will be essential to reinforcing any of the physiological interpretations reported here, and further discussion regarding potential applications and adjustments to the reported model will be requisite. Nonetheless, the present results highlight the importance of including the assessment of entire radiodensitometric distributions in accordance with the NTRA method and provide further insight into how muscle degeneration in Sarcopenia can be optimally diagnosed and quantified.

## Chapter 6

# Multimodal Patient-Specific Pre- and Post-Surgical Assessment in Total Hip Arthroplasty

### 6.1 Introduction

The prevalence of periprosthetic failure and discrepancies in patient outcome together necessitate the development of biometric gold standards for THA assessment. With this motivation, the objective of the research presented herein was to describe novel assemblies of biometric assessment modalities from a 100-patient THA cohort as a first step towards creating patient-specific applications that rehabilitators and orthopedic surgeons can utilize for prescribing their respective procedures. We divide the results into two separate sections: presurgical and postsurgical biometric assessment. Firstly, we report multimodal preoperative assessment via employment of 3D BMD, FEA, and interference fit modeling to simulate induced strain from cementless fixation, the use of 3D soft tissue segmentation and volumetric assessment of the *Rectus femoris*, *Vastus lateralis*, and the *Vastus medialis* muscles, and the measurement and user-friendly assembly of 11 gait parameters. Next, we report multimodal postsurgical assessment via the analysis of one-year postsurgical changes in radiodensitometric profiling amplitudes of muscle, connective, and fat tissue regimes, the measurement of changes in aforementioned gait parameters following one year of rehabilitation, and the analysis of changes in EMG activation data in segmented *Rectus femoris*, *Vastus lateralis*, and *Vastus medialis* muscles. Presurgical results are dictated with respect to three representative cementless patients with varying THA outcomes and results from each modality. Postsurgical results are depicted for one of these subjects, “Patient X”, who had a successful press fitting procedure despite disconcerting presurgical results. Within each modality, we report notable aspects of each patient’s dataset and compare these results across available subgroups of our cohort, highlighting the combinatorial utilities of both reported assemblies.

## 6.2 Methods

### 6.2.1 Cohort Recruitment and Representative Patients

The cohort for this study comprised of primary THA volunteer patients as part of a national database at the Icelandic National Hospital (Landspítali, Reykjavík Iceland). Ethical approval for patient data acquisition was obtained by the Icelandic Science and Ethics Committee (RU Code of Ethics, cf. Paragraph 3 in Article 2 of the Higher Education Institution Act no. 63/2006). All of the patients were part of the presurgical data report, but as is common in such cohorts, some patients left the study or were unavailable for various one-year postsurgical assessments. The total numbers of patients who were available for each of these investigations have been reported in their representative results and discussion sections.

As a first pass in illustrating the ultimate goal of this investigation in defining a user-friendly clinical tool for pre- and post-surgical evaluation, representative patients were chosen based primarily upon the degree to which their results elicited clear differences within the cohort, along with several other considerations. Namely, Patient X, a 64-year old female patient, was present in all pre and postsurgical assessments. Patient Y, a 48-year old female patient, exhibited very strong femoral bone strength, as evidenced by one of the highest average cortical BMD values in our cohort. Patient Z, a 46-year old female patient, was selected for her comparatively weak bones despite being the 6th youngest member of the cohort – a notion which directly contrasts common age-related orthopedic generalization. Additionally, Patient Z exhibited a periprosthetic fracture following her press-fitting procedure. In general, all representative patients were female and analogously received cementless prostheses.

### 6.2.2 CT Data Acquisition

All participants in the project were scanned with a 64 Philips Brilliance spiral-CT machine. Scanning occurred at three timepoints: immediately pre-surgery, and 24 hours and 52 weeks post-surgery. For the purpose of this study, only pre-operative and 24 hour post-operative data were used. The scanning region extended from the iliac crest to the middle of the femur (Figure 7.2). The image protocol included slice thicknesses of 1 mm, with slice increments of 0.5 mm and the tube intensity set to 120 keV. Prior to the study, the CT scanner was calibrated using a Quasar phantom to acquire the relationship between HU values and bone mineral density (BMD), and linear regression analyses of this calibration resulted in correlation coefficients of  $R^2 \sim 0.99$ .

### 6.2.3 Soft Tissue Segmentation for Volumetric and Density Assessment

Soft tissue segmentation was performed on both legs, starting 14 cm from the pubic arch of the pelvis with male patients and 11 cm for women. To achieve this, each patient's preoperative CT scan was imported into MIMICS Software (Materialise, Belgium) where contrast segmentation according to known attenuation and physiology was performed [30]. In total, volumetric segmentation and muscle densities were calculated over a 7 cm length

for the following muscles in both legs: the *Rectus femoris*, *Vastus lateralis*, and the *Vastus medialis*. An example of the results from this segmentation is depicted in Figure 6.1. Muscle density was computed via Matlab (Mathworks, Natick MA, USA) using average Hounsfield Unit (HU) values within each of the segmented muscles. Results were assessed by comparing differences in total soft tissue volumes (percent of muscle, fat, and connective tissues) within each leg, along with segmented muscle densities.

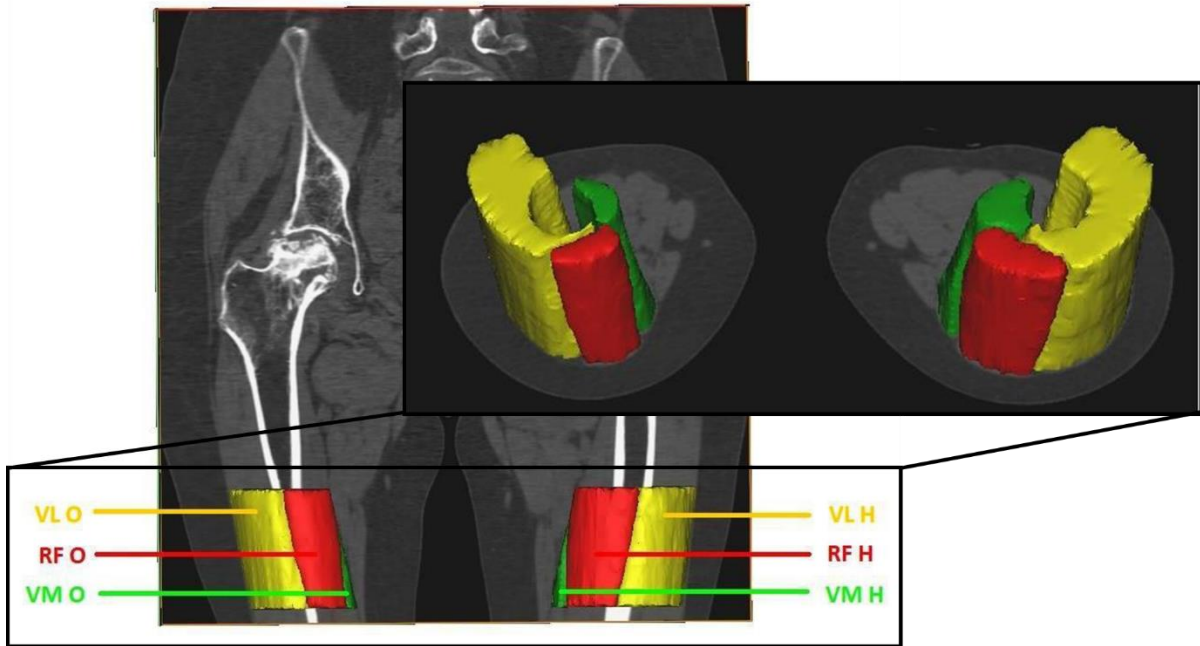


Figure 6.1: Representative 3D soft tissue segmentation of the *Rectus femoris*, *Vastus lateralis*, and the *Vastus medialis*. Images were obtained from a 64-slice spiral CT scanner and assembled using MIMCS software. [337]

### 6.2.4 3D Fracture Risk Analysis via Interference Fit Modeling

Finite element meshes were created for both the prosthesis and the femur, based on the 3D segmentation of the CT images, likewise using Mimics software. Since the femoral neck and head are removed in surgery, it was necessary to simulate this osteotomy in order to accurately predict the effects of press-fitting in cementless THA. This was achieved via manually repositioning the femur in MIMICS’ presurgical spatial reference system, followed by Boolean subtraction from the *vastus* ridge (inferior border of the greater trochanter), 45% down the femoral neck to end at the superior margin of the femoral neck [31]. The resulting mask was then exported for 3D interference fit modeling in Ansys Mechanical APDL v.14.0 (©ANSYS, Inc;). Using a linear relationship based on a phantom calibration, the following equation was used to connect bone mineral density (BMD) values with HU values:

$$BMD \left[ \frac{g}{cm^3} \right] = 0.0419 + 9.02 * 10^{-4} * HU \tag{6.1}$$

The empirical formula by Morgan et al (2003),

$$E = 6850 * \rho^{1.49} \quad (6.2)$$

was used to connect the Young's modulus of each element of the mesh to their BMD,  $\rho$ . The boundary conditions on the model for principal strain computation were defined by 0.25mm displacements of internal surface nodes, simulating interference while ensuring the hypothesis of continuum media, avoiding local effects. Calculation of principal strain values was performed in Ansys using simulated stress values and computed Young's moduli [415].

### 6.2.5 Soft Tissue Radiodensitometric Distribution Profiling

The method utilized to computationally define each HU distribution was a modified methodology for nonlinear regression analysis. First, the general equation for each distribution was defined as a trimodal sum of three separate tissue types whose linear attenuation coefficients occupy distinct HU domains: fat [-200 to -10 HU], loose connective tissue and atrophic muscle [-9 to 40 HU], and normal muscle [41 to 200 HU]. The resultant expression is a quasi-probability density function defined as the sum of two skewed and one standard ( $\alpha=0$ ) Gaussian distribution [346]:

Here, it was hypothesized that the Gaussian amplitude parameter,  $N$ , could be indicative of discrete changes in each respective tissue regime. Operating under these assumptions, a theoretical curve was generated by employing an iterative generalized reduced gradient algorithm via minimization of the sum of standard errors at each CT bin value. Amplitude values for each patient were exported for pre and post THA soft tissue assessment.

### 6.2.6 Quantitative Gait Assessment

Patients underwent gait analyses using KineView (Adaptive Optics Associates Inc., Cambridge MA, USA) and GAITrite (CIR Systems Inc., Sparta NJ, USA) at two time points: before THA and 52 weeks after surgery. Patients were instructed to walk three times along a pressure sensing carpet at a self-selected and comfortable speed. Detected footfalls of the patient were localized by the software, and 11 associated gait parameters for each walk were computed according to cited protocols [344]. Table 6.1 provides an assembly of these parameters and their definitions.

Table 6.1: Gait Parameter definitions and measurement methods [344].

Gait Parameter	Measurement	Description
Cycle Time [s]	Both Legs	Elapsed time between the first contacts of two consecutive footfalls of the same foot
Stride Length [cm]	“	Length between the heel center of two consecutive footprints on one foot

Base of Support [cm]	“	Vertical distance from heel center of one foot to the line of progression of two footprints of the opposite foot
Double Support [%GC]	“	Sum of heel strike to support footfall toe-off periods of both feet (initial/terminal footfall)
Velocity [cm/s]	“	Obtained by dividing travel distance by ambulation time
<hr/>		
Single Support [%GC]	Single Leg	Time elapsed between the last contact of the current footfall to the first of the next footfall of the same foot
Step Length [cm]	“	Distance from the heel center of the current footprint to the heel center of the previous opposite footprint
Step Time [s]	“	Time elapsed from first contact of one foot to first contact of the opposite
Stance [%GC]	“	Percent of gait cycle between two consecutive heel contacts and toe off events on the same foot
Swing [%GC]	“	Percent of gait cycle between last contact of the current footfall to the first contact of the next footfall
Toe [In/Out°]	“	Angle between the line of progression and the midline of the footprint: zero if the geometric mid-line of the footprint is parallel to the line of progression, positive if outside, and negative if inside.

---

### 6.2.7 Muscle Contraction Computation and Indexing via EMG

EMG measurements were acquired in synchrony with measure gait parameters using the wireless EMG measurement unit, KinePro (KM KINEPRO PLUS s.r.o., Olomouc, Czech Republic). This unit utilizes wireless surface electrodes, a base unit, a video camera, and specialized analysis software. Three electrodes were placed on the following muscles on each patient’s leg: the *Rectus femoris*, *Vastus lateralis*, and the *Vastus medialis*. EMG was measured thrice for each leg and further processed using Matlab (MathWorks, Natick MA, USA). First, low frequency signal demodulation was performed to obtain the linear envelope of each EMG data trace. Next, activation intervals were defined by isolating depolarization events lasting longer than 40 milliseconds, and coefficients of variation (CV) and cross-

correlation coefficients ( $R$ ) were computed to describe the intra-subject variability of each EMG signal across different trials. Additionally, peak phase indices (PP) were computed by superimposing Gaussian curve pulses under each linear envelope and assigning a temporal marker to the superimposed Gaussian distribution with the largest total area. Finally, each linear envelope was averaged across all gait cycles to assemble a Grand Ensemble Average (GEA), which was utilized to identify the period within each gait cycle with the highest overall activation, splitting each gait cycle into the stance and swing phases, as defined in literature [338].

## **6.3 Results and Discussion**

As previously mentioned, the objective of the research presented herein was to describe novel assemblies of pre and postsurgical data from a 100-patient THA cohort as a first step towards creating patient-specific applications that rehabilitators and orthopedic surgeons can utilize for determining optimal THA prosthesis fixation methods and rehabilitation procedures. We divide the results into two separate sections: presurgical and postsurgical biometric assessment. Presurgical metrics were collected for three representative patients, Patients X, Y, and Z, whose justification for selection has been previously outlined in Section 2.1. Postsurgical biometrics were assembled for Patient X, who remained present for all postsurgical measurements one year after her THA procedure.

### **6.3.1 Multimodal Biometrics for Presurgical THA Assessment**

#### **6.3.1.1 3D Fracture Risk Analysis via Interference Fit Modeling**

The voxel-based meshing technique, even if fully automated and with lower computational times, is unfit to properly represent curved surfaces by brick elements; moreover, elements insufficiently anchored to the whole model and, thus, potentially involved in partial rigid body motion, can be generated – a crucial problem in obtaining consistent FE models, hindering mechanical analyses [337]. For these reasons, the 3D FEA model for the periprosthetic proximal femur was generated by means of a geometry-based meshing technique. Strain values for nodes constituting each element of these meshes were computed, and the results from these analyses are depicted in Figure 6.2.



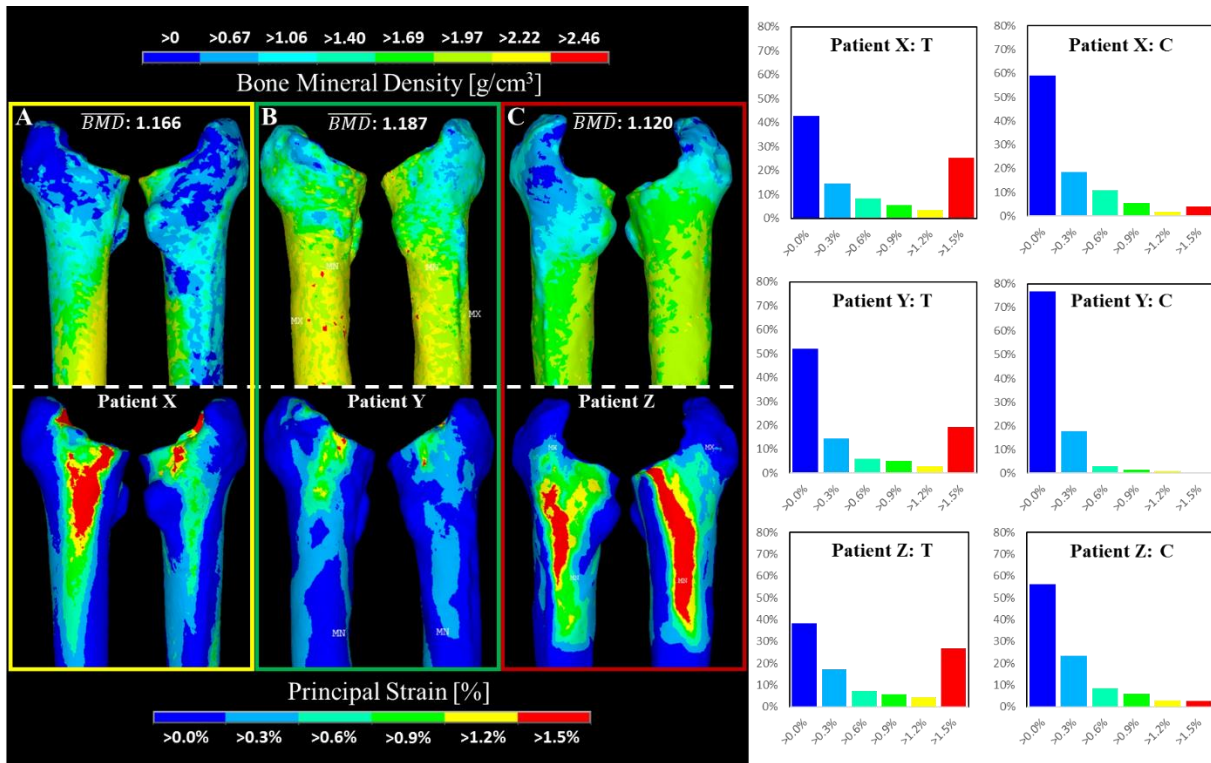


Figure 6.2: 3D Fracture Risk Analysis via Interference Fit Modeling.

The percent of elements whose strain values exceeded 1.02% in tensile strain has been suggested in literature as a minimal point at which the risk for fracturing elements may be significant [338, 339]. Nodes with strain values that exceed this threshold are clearly visible on the cortical surfaces of each patient, but to clearly different degrees. It is evident that Patient Y’s increased BMD values on her cortical surface directly led to lower numbers of critically strained cortical elements. Patients X and Z, however, clearly show distinct areas of low BMD values, which incurred large areas of critical strain on their cortical surfaces. Unfortunately, Patient Z suffered a periprosthetic fracture during her press-fitting procedure, and it is evident that such an event may have been easily predicted using our model. In general, these strain threshold values may be compared to other fracture risk indices in literature, which have otherwise involved calculating the percent of fractured elements by counting those whose Von Mises Stresses exceeded their threshold [333, 337]. Computed with this method, the threshold for critical fracture risk index was much higher – sometimes 42.67% of cortical elements. However, based on the simplicity of direct primary failure strain calculation, the interference fit modeling presented here may have a higher sensitivity to this issue of criticality. To optimally test this, many more patients with known fracture events, like Patient Z, will have to be subjected to both types of fracture risk analyses.

### 6.3.1.2 3D Segmentation and Volumetric Assessment

Pre-surgical muscle densities (average HU values) and compositions were calculated for the *Rectus femoris*, *Vastus lateralis*, and the *Vastus medialis* in both legs for each patient, along with their standard errors within the cohort. These data are compiled in Figure 6.3 for Patients X, Y, and Z. Figure 6.3A clearly illustrates the differences in overall soft tissue volume between the representative patients, with Patient Z being significantly lower in both her healthy and operative legs. Figure 6.3B shows the same trend regarding comparative muscle compositions, and the trend is reversed when observing comparative fat

compositions. Indeed, following muscle segmentation and density analysis, Patient X had greatly higher average HU values in each muscle within her healthy and operative legs, compared to the other subjects, with the exception of her operative *Vastus Medialis*.

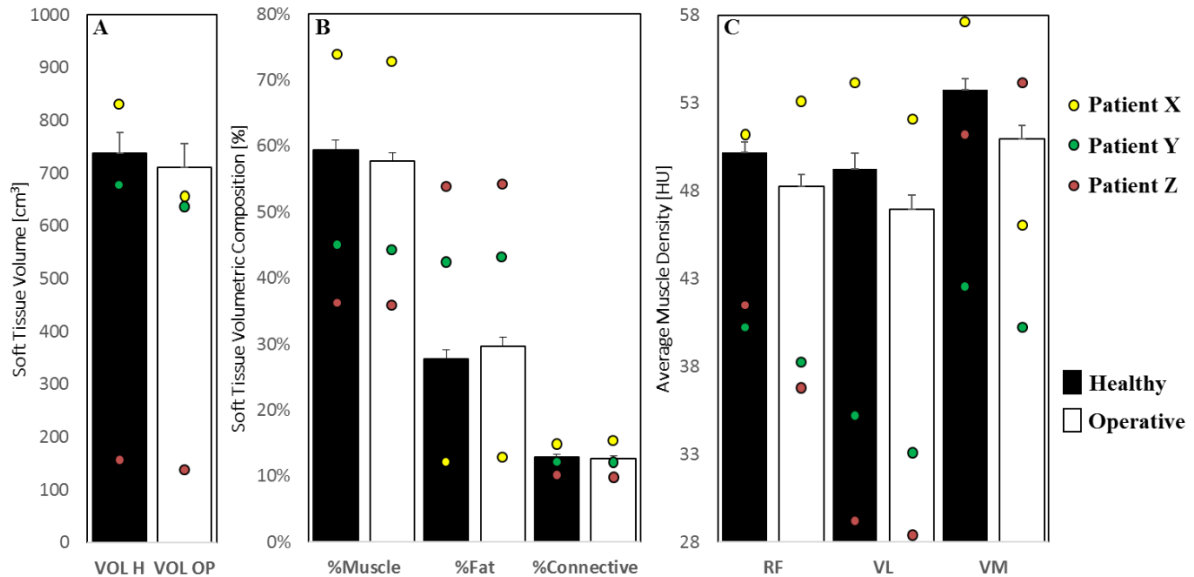


Figure 6.3: 3D Muscle Segmentation and Soft Tissue Volumetric Assessment. A) Total soft tissue volumetric comparison. B) Soft tissue compositional analyses detailing fat, lean muscle, and connective tissue. C) Segmented muscle average HU values for the *Rectus femoris*, *Vastus lateralis*, and the *Vastus medialis*. All data are reported as a comparison between healthy and operative legs.

Altogether, these data suggest the utility of muscle composition and volumetric analyses in reporting periprosthetic muscle condition prior to THA. Intriguingly, these data did not correlate with Patient Y's previously-shown higher BMD and better fracture risk assessment results than the other patients. This suggests that more patients should be assessed and sorted according to other factors or comorbidities to understand any extant relationships between the two reported metrics.

### 6.3.1.3 Presurgical Gait Parameter Assembly

Gait parameters were measured for each patient before THA in accordance with literature [334]. Patients were asked to walk on a pressure sensor carpet at a self-selected, comfortable speed. Gait values were measured for each patient within the cohort, and a normative database was defined to assess each parameter's average values and their standard deviations. The results from this assessment are depicted in Figure 6.4 as an example report for Patients X, Y, and Z.

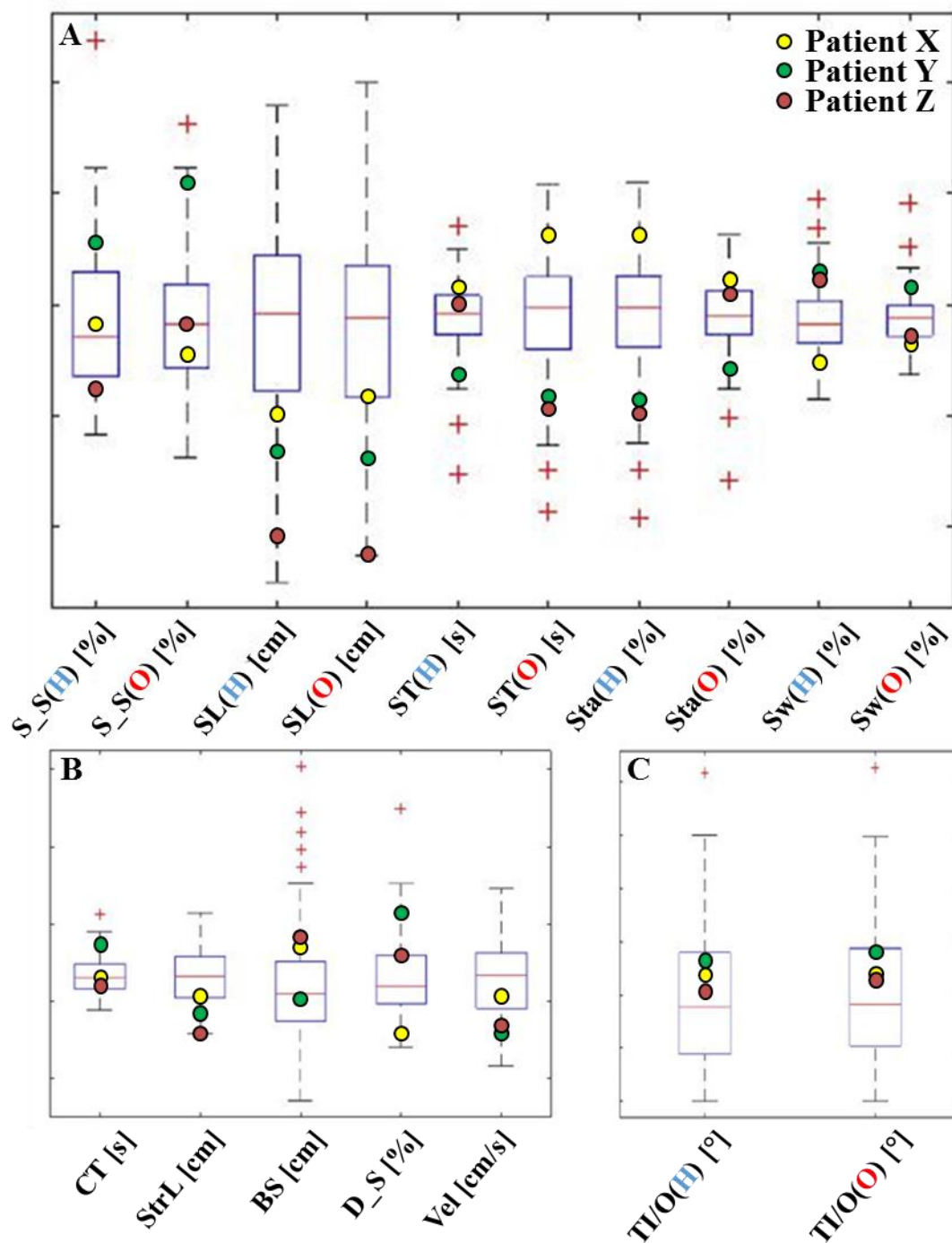


Figure 6.4: Presurgical Gait Parameter Assembly.

As is evident in Figure 6.4, Patient X had longer step lengths and step times than Patients Y and Z, altogether suggesting a more normalized, healthy ambulation. Indeed, this notion is further evidenced by Patient X's higher stance and lower swing phase gait cycle values. In accordance with clear differences in BMD values between Patients Y and Z, their ambulation parameter values were similarly disparate across many metrics – most notable with regards to step lengths. Interestingly, almost all healthy and operative leg gait parameters in all three subjects were beyond one standard deviation above or below those of the 100-patient cohort, suggesting that their ambulation was significantly different from normative values. Altogether, the ability to quickly and easily quantify these differences supports the utility of gait parameter assembly for assessing patient mobility, which thereby

suggests the metric's utility for both pre-THA prosthetic selection and post-THA rehabilitation assessment.

### 6.3.2 Multimodal Biometrics for Postsurgical THA Assessment

#### 6.3.2.1 Changes in Soft Tissue Radiodensitometric Amplitudes

As a potential postsurgical biometric, soft tissue magnitudes from radiodensitometric profiling were computed for an available subgroup of 32 cohort patients to illustrate changes in tissue composition before and one year after THA. Figure 6.5 depicts the results for this subgroup, along with the results for Patient X.

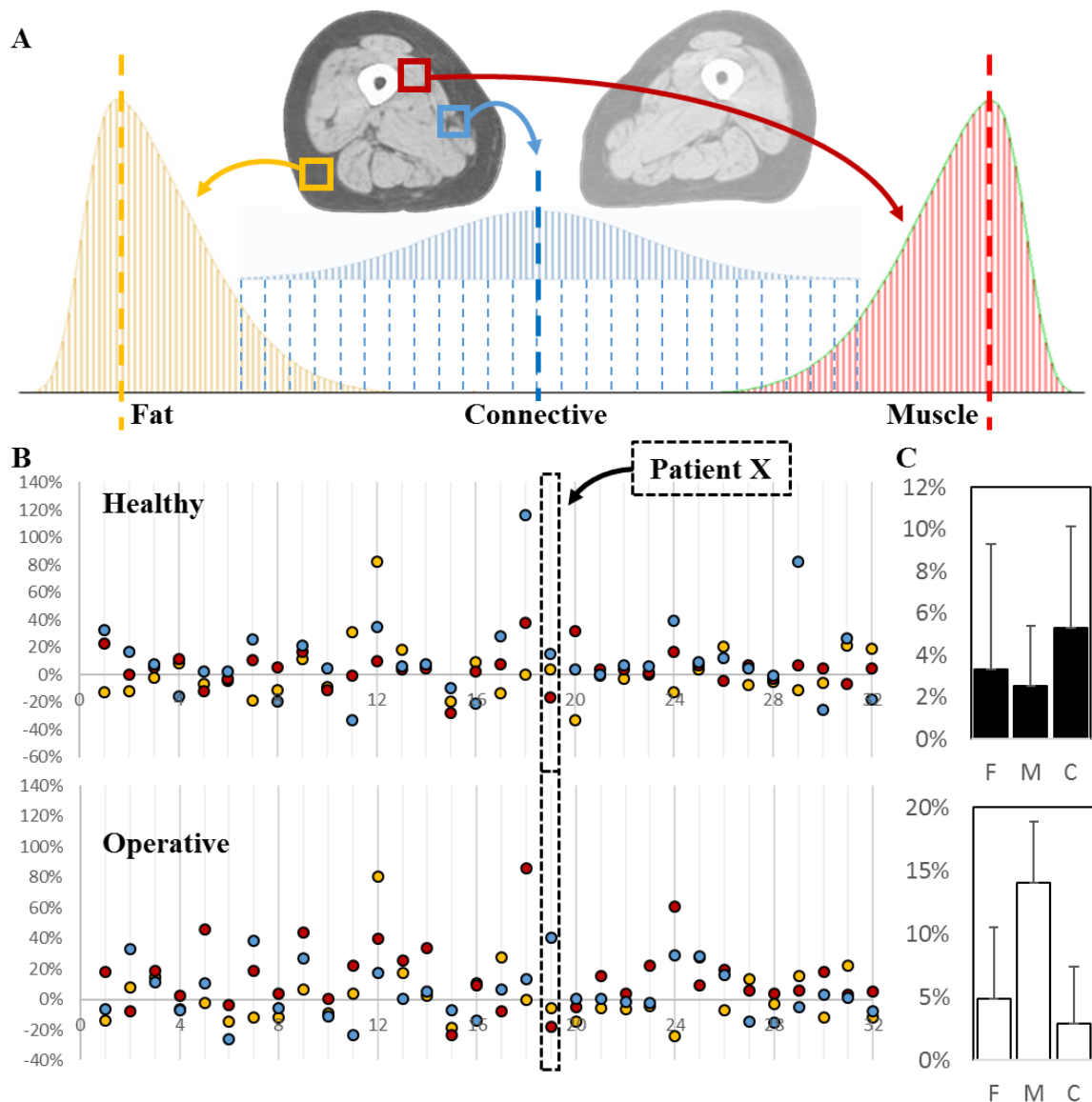


Figure 6.5: Postsurgical Changes in Soft Tissue Radiodensitometric Profile Amplitudes.

Figure 6.5B illustrates how general increases in all three soft tissue magnitudes occur when comparing presurgical values to those taken one-year post-surgery. Indeed, Figure 6.5C details the average percent changes in these tissues across all measured patients. Patient X

was one of the few patients whose muscle amplitude values actually decreased following her procedure, and it is unclear with such analyses why this may have occurred. However, one may consider some of her presurgical metrics as evidence that the degree to which her femoral quality and gait parameters yielded poor results compared to the rest of the cohort. Regardless of her particular situation, it remains suggested here that overall increases in cohort muscle amplitudes may infer an increase in lower limb utilization in this subpopulation following surgery. Utilizing additional patients and correlating any extant comorbidities could elicit further utility of this radiodensitometric profiling method. Additionally, it may be important to consider segmenting a future dataset according to precise rehabilitation methods for each patient, as these programs are often based upon many other considerations – including the type of implant procedure performed.

### 6.3.2.2 Postsurgical Gait Parameter Assembly

Gait parameters were likewise measured for each patient one year following THA. Gait values were measured for each patient analogously to presurgical assessment, and a normative database was defined to assess each parameter’s average values and their standard deviations. Likewise, average changes in these parameters were computed for the cohort to show improvements in ambulation following one year of rehabilitation. The results from these assessments are depicted in Figure 6.6 as an example report for Patient X.

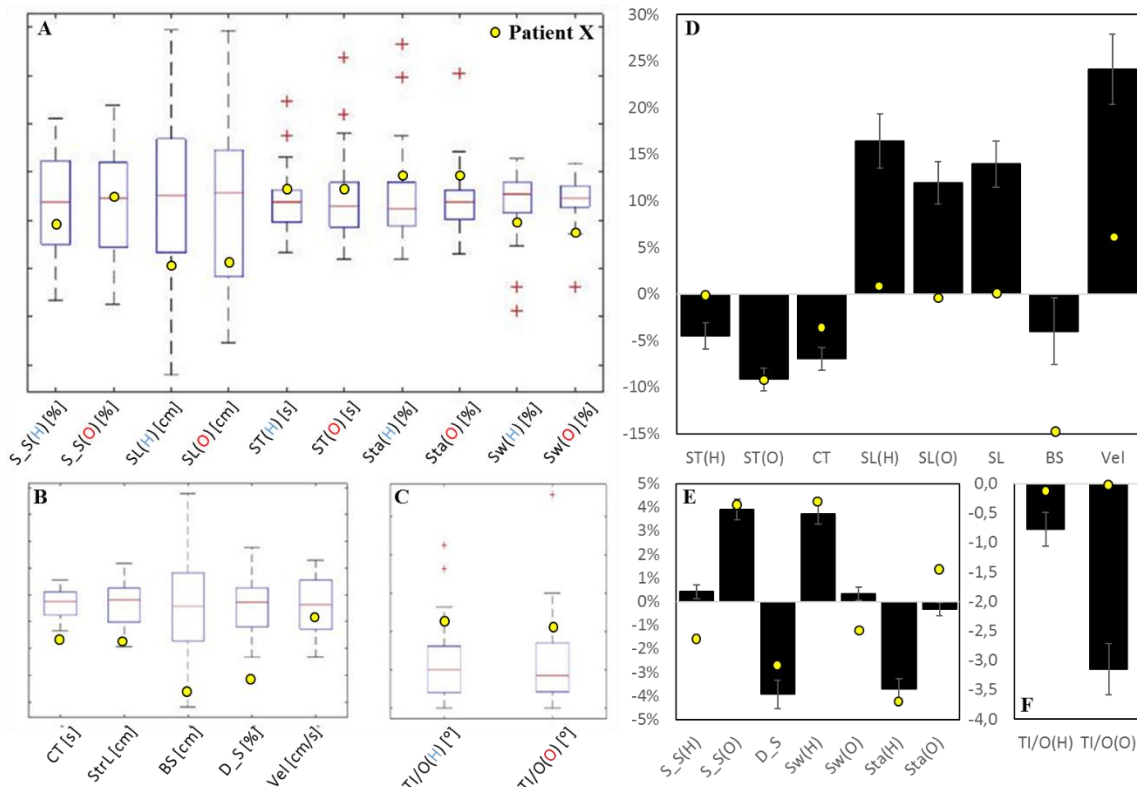


Figure 6.6: Postsurgical Changes in Patient Gait Parameters.

As is shown here, many of Patient X’s postsurgical gait values normalized to within one standard deviation of that of the patient cohort, suggesting that normative ambulation was partially rescued after one year of rehabilitation. However, the degree to which her own gait

parameters changed tells a different story – that, respective to some metrics, her progress in restoring normative gait was significantly less than those of other patients. This notion is most evident by her step lengths and velocity. Other parameter changes were very similar to those of the cohort, such as her single/double support, swing, and stance gait cycle values. These results once again confirm the utility of assembling these metrics in assessing patient mobility. However, like other reported metrics, more patients will be requisite for optimizing our understanding of these parameters’ clinical relevance.

### 6.3.2.3 Electromyographic Activity Analyses

In addition to the previous metrics, EMG activation in the *Rectus femoris*, *Vastus lateralis*, and the *Vastus medialis* was measured for an available subpopulation of 39 individuals within our cohort, both before and one year after THA. Figure 6.7 depicts these results.

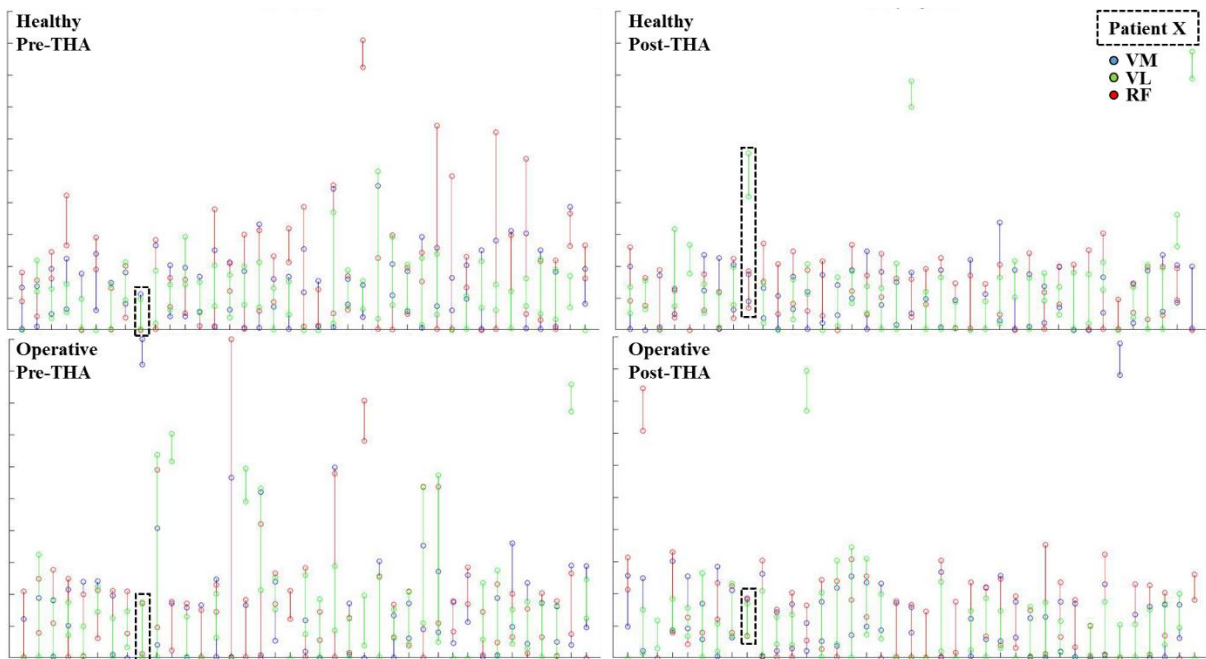


Figure 6.7: Postsurgical Changes in Periprosthetic Segmented Muscle EMG Activities.

As is illustrated here, almost every patient exhibited a post-rehabilitation shift in maximum activation intervals of all three muscles to the first 30% of the gait cycle. Prior to surgery, it is clear that these activation intervals were much more varied, sometimes encompassing over 50% of the gait cycle in some patients. Indeed, Patient X exhibited an overall change in activation intervals for each muscle type after THA, but the effects of a shortened overall gait cycle were not evident, as was the case for most other patients. Indeed, this could be due to Patient X’s presurgical gait percentage being already one of the smallest in the cohort. Understanding more about which types of implants, conditions, and rehabilitations strategies might correlate to shifts in maximum activation intervals could be another key metric in assessing THA outcome.

## 6.4 Conclusions

The objective of the research presented herein was to describe a novel assembly of data from

a 100-patient cohort as a first step towards creating patient-specific applications that rehabilitators and orthopedic surgeons can utilize for optimally determining presurgical fixation methods and postsurgical rehabilitation protocols. To our knowledge, this is the first time that such a multimodal analysis has been performed. From these data, we can generate normative databases to outline significant differences in assembled metrics and facilitate discussing patient-specific procedures in a clinical context. However, it should be noted that ideal databases for the development of these pre and postsurgical applications would involve more patients and further exploration into comorbidities and other factors that could obfuscate correlations between modalities. Moving forward, it will be critical to statistically assess the relationships between the reported metrics in order to ensure their respective clinical utilities. Likewise, the optimization of our reported assessment modalities will be key; most notably in the inclusion of segmented, hip-supporting muscle groups like the gluteal muscles and the inclusion of material anisotropy in femoral finite element models. In general, improving the outcome of THA surgery and rehabilitation would not only impact the quality of life in these patients, but would likewise have a substantial impact on reducing the propensity of revision surgery, lessening the growing impact that THA has on healthcare costs around the world.

## **Chapter 7**

# **Bone Mineral Density and Fracture Risk Assessment to Optimize Prosthesis Selection**

### **7.1 Introduction**

There is a distinct lack of pre-operative guidelines for prescribing the optimal type of prosthetic stem for total hip arthroplasty (THA): cemented or cementless. Orthopedic surgeons typically utilize patient age, gender, and bone quality via X-ray scans as generalized metrics for this decision, but the variability of post-operative complications and overall patient outcome still suggests that a more complete and quantitative approach to dictate THA prosthesis type needs to be developed. The objective of the research presented herein was to describe a novel preliminary methodology for patient evaluation before THA surgery as a first step towards creating a patient-specific, pre-surgical application for determining the optimal prosthesis procedure. The work flow for this study can be seen in Figure 7.1.



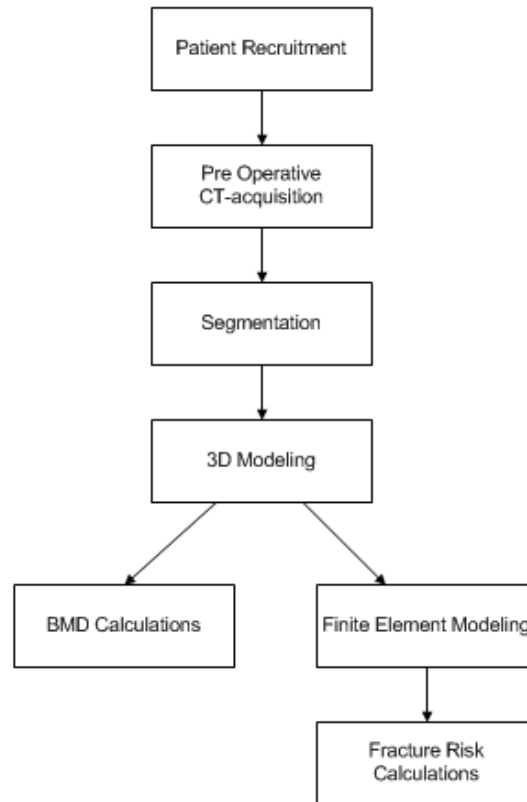


Figure 7.1: Bone Mineral Density and Fracture Risk Assessment to Optimize Prosthesis Selection: Study Workflow.

Finite element analysis (FEA) and bone mineral density (BMD) calculations were performed with ten voluntary primary THA patients to estimate the status of their operative femurs before surgery. The aim of the study was to generate a preliminary assessment from these ten patients by creating a model to simulate the press fitting procedure and its effect on the structural integrity of the femur via computation of a fracture risk index (FRI). This value was then compared to the patient's age, sex, and average proximal BMD. Results from the CT-based fracture risk simulations and BMD measurements demonstrated a high degree of variability between patients grouped according to implant procedure, reinforcing the notion that age and gender alone are poor indicators for prescribing THA procedures. Additionally, FRI results show useful correlation with patient BMD measurements, indicating that at least two of the ten patients may have received a non-ideal prosthesis. The CT-based BMD measurements and FRI calculations indicate differences between patients beyond age and sex, and the fracture risk simulation could serve as a foundation for the development of pre-surgical software applications for assisting orthopedic surgeons with selecting THA prostheses.

## 7.2 Materials and Methods

### 7.2.1 Patient Recruitment

Ten patients were voluntarily enrolled in the study (eight females and two males). Of these patients, five patients received identical cementless implants, while five received cemented implants. The implant type was decided according to the evaluation of the surgeons; qualitatively based on age, sex, and general physical condition, as typically assessed before surgery. The average age at the time of operation was  $61.4 \pm 10.1$  years old for all patients. Ages averaged  $63.5 \pm 17.7$  years for males and  $54.5 \pm 18.9$  years for females, and when grouped according to implant procedure, average ages were  $55.0 \pm 9.5$  years for cementless and  $67.8 \pm 5.8$  years for cemented. Patients with total knee implants, previous hip implants, or those who received implants during this research period were excluded from the study.

### 7.2.2 CT Data Acquisition

All participants in the project were scanned with a 64 Philips Brilliance spiral-CT machine. Scanning occurred at three timepoints: immediately pre-surgery, and 24 hours and 52 weeks post-surgery. For the purpose of this study, only pre-operative and 24 hour post-operative data were used. The scanning region extended from the iliac crest to the middle of the femur (Figure 7.2). The image protocol included slice thicknesses of 1 mm, with slice increments of 0.5 mm and the tube intensity set to 120 keV.



Figure 7.2: CT scanning protocol range on the femoral head.

Prior to the study, the CT scanner was calibrated using a Quasar phantom to acquire the relationship between HU and BMD, resulting in the relationship given by eq.1.

$$\text{BMD} \left[ \frac{\text{g}}{\text{cm}^3} \right] = (0,00036)\text{HU} + 0,56736 \quad (7.1)$$

Linear regression analysis of this calibration resulted in a correlation coefficient  $R^2 \sim 0.99$ .

### 7.2.3 Segmentation and Finite Element Modeling

In order to assemble the 3D models of each patient's femur for FEA analysis, each patient's CT scan was imported into MIMICS Software (Materialise, Belgium) where femoral contour segmentation was carried out. A solid 3D model was calculated based on these contours. Next, the femoral head was virtually cut, similarly to a typical THA surgical procedure, using Boolean operators on the 3D model. Additionally, a virtual distal cut was performed orthogonal to the femur's long axis. The final model can be seen in Figure 7.2.

Using the finite element module of MIMICS, known as 3-Matic, the model was divided into quad-node tetrahedral elements. Each model consisted of 130,000 to 170,000 of these elements, with overall element densities of around two elements per  $\text{mm}^3$ . Young's modulus and Poisson's ratio were then assigned to each element. Fifty different values of Young's modulus were assigned to the elements of each model, while the Poisson's ratio was considered a constant value of 0.33. Furthermore, these elements were considered to be isotropic. The aforementioned calibration equation was used to convert HU to BMD and eq.2 was used to convert BMD to Young's modulus [416]:

$$E = 10500 \cdot \rho_{ash}^{2.29} \quad (7.2)$$

where  $\rho_{ash}$  is the bone mineral density obtained from eq.1. This formula was used to represent both trabecular and cortical bone. In Figure 7.3, a FE model of a respective femur can be seen, following the addition of material properties.

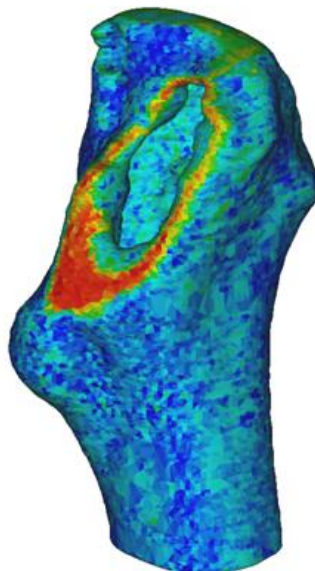


Figure 7.3. A finite element model of the femur consisting of more than 100,000 elements. The elements are given material properties: namely, Poisson's ratio and Young's modulus. Red colors indicate higher density bone.

### 7.2.4 Fracture Risk Index Computation

In order to compute the FRI of each femur, each FEA model, complete with requisite material properties, was imported into Ansys Mechanical APDL v.14.0 (©ANSYS, Inc;). There, a static structural simulation and analysis was performed on the model. The objective of this simulation was to simulate the forces introduced on the femur during the press-fitting surgery in cementless THA. In this procedure, when the stem is pushed into the medullary canal, the highest tensile stresses can be expected to arise at the medial and lateral sides of the periprosthetic end of the femur. This is due to the fact that the flare of the stem is the steepest at the top. Therefore, as boundary conditions, two equal but opposite forces were applied in these areas. In a study by Sakai et al, the average measured hammering force for uncemented prosthesis was estimated to be 9.25 kN [417]. Since the forces in cemented prosthesis are considerably lower, our model utilized this force value as a worst-case-scenario to discern whether any of the ten patients could have withstood the cementless method (Figure 7.4).

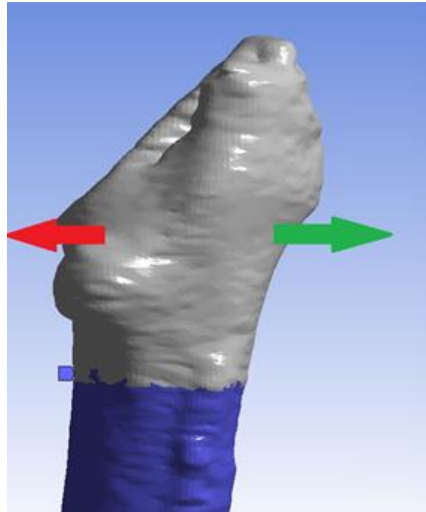


Figure 7.4: The 9.25 kN cementless prosthesis forces applied on the model where the highest stress can be expected during the press-fitting of the tapered stem.

To determine the FRI for each subject's model, the stress value of every element was compared to its calculated ultimate tensile strength (UTS). The ultimate tensile strength was calculated with a relationship given by Bessho et al (eq. 3 and eq. 4) [418].

$$UTS = 137 \cdot BMD^{1.88} \quad \text{for } BMD < 0.317 \quad (7.3)$$

$$UTS = 114 \cdot BMD^{1.72} \quad \text{for } BMD \geq 0.317 \quad (7.4)$$

The average stress experienced by each element was calculated by averaging the stress values at each node point. Then, the fracture risk index was calculated for each element using eq. 5 [419].

$$FRI(\%) = \frac{stress}{UTS} \cdot 100\% \quad (7.5)$$

### 7.2.5 Bone Mineral Density Computation

A model of the BMD region of interest was created in MIMICS, and ranging from the periprosthetic femur, without the femoral head, to the greater trochanter, with a distal axial cut through the lesser trochanter (Figure 7.5). The study focused on the structural aspects of the cortical bone, since the structural integrity of the cancellous bone is compromised post operation. The horizontal line in Figure 7.5 demonstrates the cuts made above and below the area of interest. From this region, the HU values were extracted and converted to BMD using eq.1.

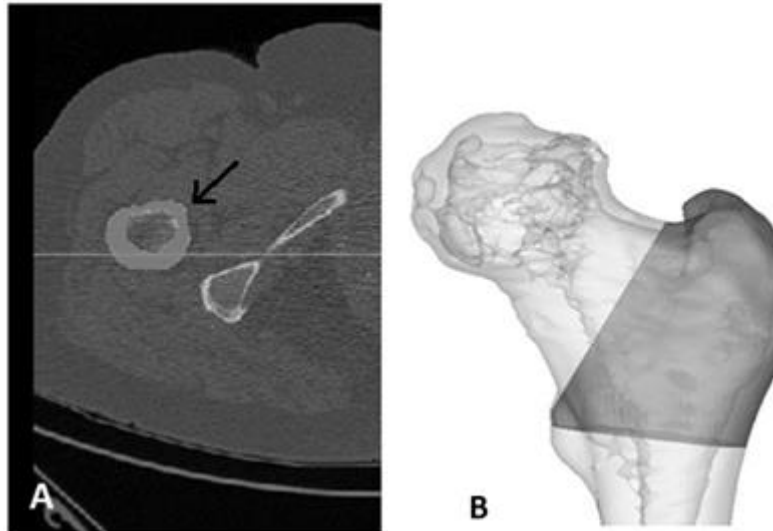


Figure 7.5: A) Axial view of one slice of the CT-data from a patient, and B) the 3D view of the region of interest for BMD calculations. The arrow in the center of image A points to the area belonging to the mask.

## 7.3 Results

Firstly, the FRI was calculated for ten patients – five of whom were previously prescribed to receive a cemented implant, and five cementless ones. The highest stresses were usually experienced in the calcar femoral on the medial side of the femur and at a similar location on the lateral side.

In Figure 7.6, the von Mises stress in every element of each model is plotted against BMD. The black-crossed line represents the ultimate stress as a function of BMD, as stated in eq.3. Should the calculated stress values exceed the UTS, then the element would be considered fractured, which can be seen as a dark color in the figure.

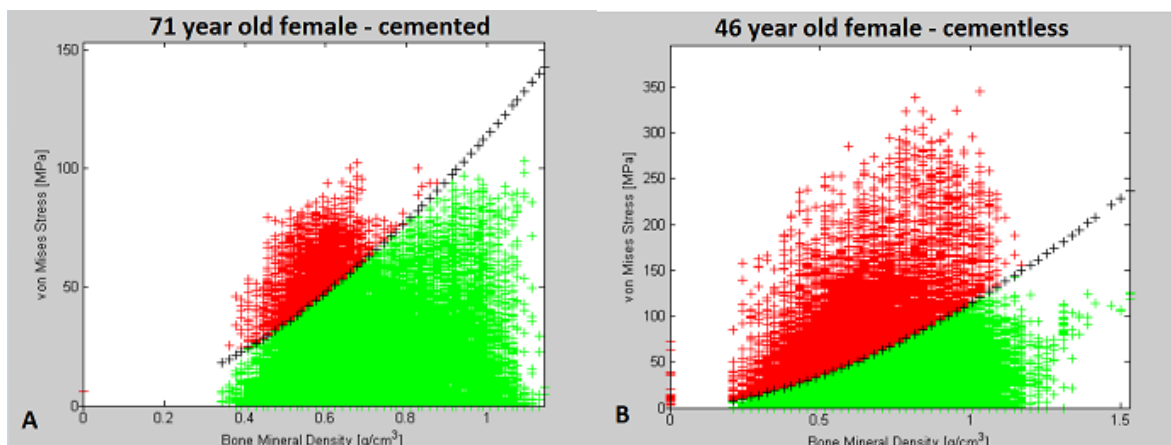


Figure 7.6: Examples of calculated FRI from A) a 71 year old female patient and B) a 46 year old female. Note that every element of the model has been plotted with von Mises stress as a function of bone mineral density. The black crossed line indicates element strength given by eq.3, and elements are considered failed if they surpass this line in stress. Subject B actually experienced femoral fracture due to the periprosthetic implant some days after the surgery.

Figure 7.6 depicts the position-independent von Mises stresses of all elements against their respective BMD values. To better visualize where the highest risk of fracture was experienced, these elements were also plotted in 3D. A typical result from the 3D plotted fracture risk index can be seen in Figure 7.7. The red-colored elements are those that exceeded their fracture threshold.

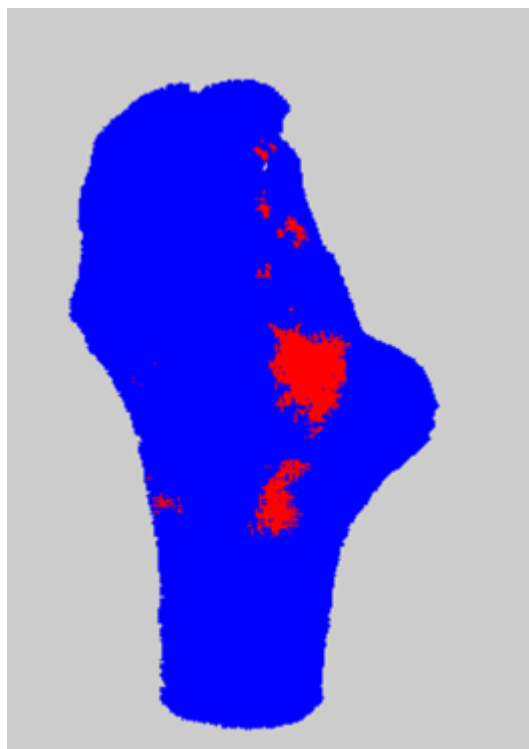


Figure 7.7: Elements plotted in their three-dimensional coordinates. Note that red elements were those that exceeded the acceptable limit for von Mises stress, indicating regions of most probable periprosthetic fracture.

In Table 7.1, the average fracture risk is calculated for the ten patients (five with cemented THA, and five with cementless), as well as the ratio of those elements that exceeded 80% of their ultimate stress value.

Table 7.1: FRI and BMD results from the ten cemented and cementless THR subjects.

Cementless THA Procedure				Cemented THA Procedure			
Age	Sex	% of elements > fracture threshold	BMD [g/cm <sup>2</sup> ]	Age	Sex	% of elements > fracture threshold	BMD [g/cm <sup>2</sup> ]
51	M	0.7%	1.127	76	M	4.0%	1.054
48	F	2.4%	1.114	70	F	3.0%	1.205
46	F	16.2%	1.114	66	F	5.1%	1.143
68	F	7.3%	1.078	60	F	8.2%	1.062
62	F	9.2%	1.069	67	F	2.4%	1.146

For the five cementless patients, the average age was  $55 \pm 9.5$  years, the average percent of fractured elements was  $7.16 \pm 6.13\%$ , and the average BMD was  $1.10 \pm 0.03 \text{g/cm}^2$ . For the five cemented patients, the average age was  $67.80 \pm 5.85$  years, the average percent of fractured elements was  $4.54 \pm 2.29\%$ , and the average BMD was  $1.122 \pm 0.06 \text{g/cm}^2$ . These values in relation to patient age and sex can be seen in Figure 7.8.

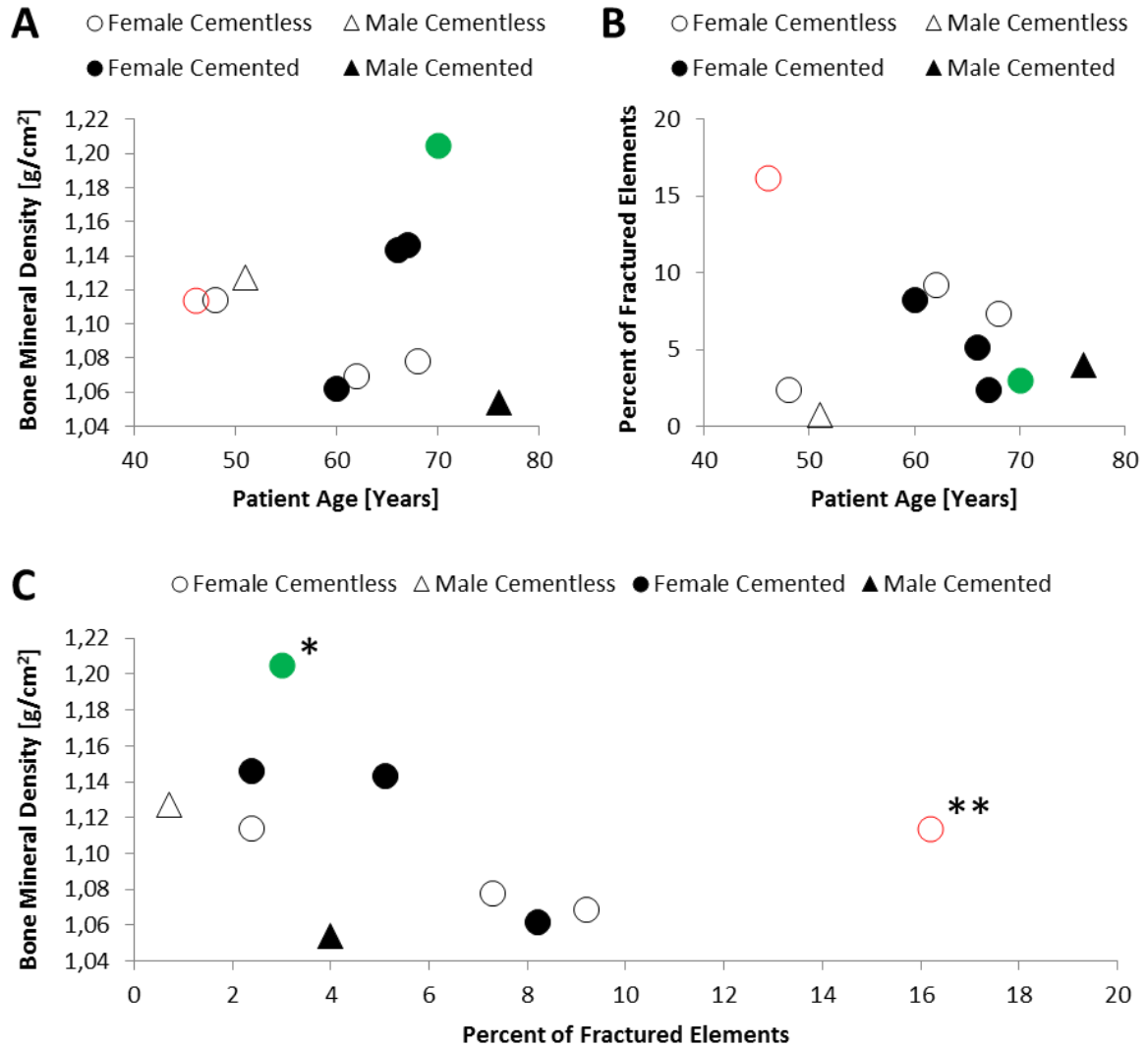


Figure 7.8: Results from FRI and BMD assessment for each patient grouped by sex and prosthesis type. A) BMD versus patient age, B) Percent fractured elements versus patient age, and C) BMD versus percent of fractured elements. Note that the female patients in green (\*) and red (\*\*) received non-optimal cemented and cementless prostheses, respectively, according to our computational assessment. Furthermore, it should be noted that the red patient suffered a periprosthetic fracture during surgery – an event that could possibly have been predicted by the above results.

## 7.4 Discussion and Conclusions

The most important criterion when choosing the type of implant for patients undergoing THA is bone quality. If the bone is of good quality, the cementless implantation method generally results in fewer patient complications and generally more delayed revision surgeries, compared to cemented THA. Since bone quality tends to decline with age and is usually lower in women than men, younger and/or male patients usually receive cementless implants, while older and/or female patients receive cemented ones. Although age and gender are somewhat reliable indicators of femoral bone quality, individual differences can be vast. The reported results highlight these differences and suggest the importance of



developing a novel, quantitative approach to assessing patients' femoral heads before THR surgery.

#### **7.4.1 Bone Mineral Density as a Potential Computational Tool in THA**

The notion that patient variation in bone quality as a function of age and sex is shown from the BMD measurements presented herein, where several patients received cemented prostheses despite having relatively higher BMD than patients who were given the cementless type. This decision was clearly based primarily on the patients' age, as the average age of cemented patients was much higher than those of cementless patients ( $67.8 \pm 5.8$  compared to  $55.0 \pm 9.5$ , respectively). Indeed, the patient with the highest BMD measurements was not only female, but also the second oldest within the assessed population. This most likely justified her receiving a cemented implant, although our model suggests that she certainly may have withstood a press fitting with a low risk of periprosthetic fracture. Additionally, our results indicate that BMD measurements may correlate inversely, to some degree, with the percent of fractured elements computed by our FEA simulation. This is evident, as higher BMD values indicate better bone quality and thereby a reduced chance of each element exceeding its fracture threshold. However, to determine if this relationship is indeed true, more patients would need to be assessed in a larger study. In general, the use of BMD as a metric in this investigation serves as an important first step in developing a quantitative method for computing bone quality at the moment of surgery, which may serve as a future tool for orthopedic surgeons to predict the ability for patient's femurs to handle the stresses in press-fitting a cementless THA prosthesis.

#### **7.4.2 Fracture Risk as a Potential Computational Tool in THA**

The calculated FRI for the 10 subjects additionally showed high degrees of variation between patients according to both their sex and age. Most importantly, our model shows that two of the five cementless patients had higher fracture risks than all of the five cemented patients – despite their being younger than four of the cemented patients. It is additionally critical to note that the 46 year old female, cementless patient experienced a periprosthetic femoral fracture immediately after the surgery, which correlated with both the considerably higher fracture risk and lower BMD discerned from our computational model (Figure 7.6B and 7.6C, respectively). However, with a larger population size for the reported assessment, it may be reasonably expected that a majority of younger patients, who typically receive cementless implants, would have lower risks of fracture and higher BMD than those of older patients. However, the reported results show again that patient age is not necessarily an adequate indicator of either fracture risk or bone quality; thus, implementing the computational technique that this paper introduces might serve as a better pre-operative tool for orthopedic surgeons to dictate the optimal THA procedure.

#### **7.4.3 Limitations and Future Directions**

As previously mentioned, the purpose of this study was to investigate whether a novel FEA simulation of press fitting could generate a potentially useful tool for assessing patient fracture risk indices, in combination with CT-based BMD measurement. Our results do

indeed highlight the potential of this methodology and furthermore suggest the inadequacy of patient age and sex in dictating the risk of periprosthetic fracture. However, a larger patient population is requisite to rigorously show the statistical dependency of FRI on measured BMD and to define limits that correlate to additional, real cases of patient periprosthetic fracture. In addition, there are some limitations of the reported FEA and FRI computations. The greatest of these is that the simulations carried out were steady-state, and did not take into consideration applied loads that are time-dependent, or the prosthetic design and surface finish. The real forces induced by a surgical hammer during the surgery are high-impact and punctate forces, or forces acting on the bone over a short period of time. This can instigate the development of microfissures in the periprosthetic region of the femur, leading to fractures in more extreme cases. Furthermore, the use of unidirectional force is an over-simplification of the distribution incurred by press-fitting: a direct strain-based method for computing fracture risk would be optimal to avoid this discrepancy. In addition, the anisotropy of femoral bone was not considered in this study and must be employed in future work to optimize periprosthetic fracture propagation prediction

Overall, this study proposes a novel approach to the predictive simulation and computation of BMD and FRI during insertion of a cementless THA prosthesis. A large part of the novelty of this work lies in the fact that the bone quality was discerned at the time of surgery rather than long after surgery, incorporating both bone mineral density averages and fracture risk indices in the periprosthetic region of the femur. This real-time surgical evaluation could serve as the basis for the development of software applications that orthopedic surgeons may use to discern which prosthesis fitting procedure may be optimal for each patient on an individual basis. Such a tool could have a profound impact on THA surgical planning and serve as a model for future surgical planning software. However, the development of a patient database with which such tools may operate would require more patient data than what was acquired for the purpose of the reported work. Additionally, a more robust model would include variations in stem designs, such as material roughness, tapering degree, cross-sectional area, and coating thickness. Incorporating materials data could provide additional details regarding shear forces applied to the bone as a result of prosthetic friction, in addition to the radial forces presented herein. Nevertheless, our results highlight the feasibility of the methodology used and can be utilized as a foundation to develop a clinical database for correlating BMD and FRI to THA patient outcomes. As an eventual software application for orthopedic surgeons, our combinatory approach of CT-based BMD measurement and FEA-based assessment of femoral fracture risk could serve as a pivotal tool in the decision making process before total hip replacement. Optimizing the pre-operative planning can increase the overall success of THA surgeries and have a profoundly beneficial impact on both patient mobility and overall surgical outcome, which could significantly aid in lessening the economic burden from revision surgeries upon many healthcare systems worldwide.

## Chapter 8

# Additional Applications of Computational Modeling of Medical Images

### 8.1 Low-Amplitude Craniofacial EMG Power Spectral Density and 3D Muscular Reconstruction from MRI

#### 8.1.1 Introduction

Improving EEG signal interpretation, specificity, and sensitivity is a primary focus of many current investigations, and the successful application of EEG signal processing methods requires a detailed knowledge of both the topography and frequency spectra of low-amplitude, high-frequency craniofacial EMG. This information remains limited in clinical research, and as such, there is no known reliable technique for the removal of these artifacts from EEG data. The results presented herein outline a preliminary investigation of craniofacial EMG high-frequency spectra and 3D MRI segmentation that offers insight into the development of an anatomically-realistic model for characterizing these effects. The data presented highlights the potential for confounding signal contribution from around 60 to 200 Hz, when observed in frequency space, from both low and high-amplitude EMG signals. This range directly overlaps that of both low  $\gamma$  (30-50 Hz) and high  $\gamma$  (50-80 Hz) waves, as defined traditionally in EEG measurement. Likewise, average EMG amplitude comparisons from each condition highlights the similarities in signal contribution of low-activity muscular movements and resting, control conditions. In addition to the FFT analysis performed, 3D segmentation and reconstruction of the craniofacial muscles whose EMG signals were measured was successful. This recapitulation of the relevant EMG morphology is a crucial first step in developing an anatomical model for the isolation and removal of confounding low-amplitude craniofacial EMG signals from EEG data. Such a model may be eventually applied in a clinical setting to ultimately help to extend the use of EEG in various clinical roles.

## 8.1.2 Materials and Methods

### 8.1.2.1 EMG Data Acquisition

EMG measurements were performed on 12 healthy volunteer subjects: 6 female and 6 male, from ages 19 to 30. The equipment used for these measurements was the Kine Measurement System with four wireless triode surface electrode pads and a simultaneous video recording system.

The subject was first asked to lay down on an inclining bench while his/her skin was cleaned with alcohol and conductive gel put on the electrodes. A video camera was placed in front of the subject, which captured the front of the subject's face. The electrodes were placed on the left and right temporal and frontal muscles of the subjects. After this setup, each subject was asked to perform a series of several facial exercises. Firstly, each subject was asked to maximally clench his/her jaw for 10 seconds, corresponding to maximum contraction of the temporal muscles. Then, EMG of the frontal muscles was recorded by having each subject both raise and furrow their eyebrows as much as possible for 10 seconds. Next, each subject was given a piece of chewing gum and left to reach a stable mastication rhythm. EMG signals were then recorded while the subject masticated with the chewing gum on the left side for 30 seconds, which was then repeated on the right side. Lastly, for control conditions, EMG was measured while each subject laid completely still with their eyes open and fixed on a spot for 30 seconds, which was then repeated with their eyes closed.

### 8.1.2.2 Frequency Analyses

The Power Spectral Density (PSD) was computed by taking the Fast Fourier Transformations (FFT) of the EMG signal. All signal analyses were performed with Matlab software (<http://www.mathworks.com>). The mean PSD with its standard deviation for each condition was computed by averaging all trials per subject first, then normalising the amplitudes to their maximum value. The next step was to average the PSD between all subjects. The mean and standard deviation values within 10 Hz frequency bins from 0 to 800 Hz were normalized in order to obtain inter-conditionally comparable results for these bandwidths.

In case of the chewing condition, the active and inactive segments had to first be defined. To accomplish this, spectral analysis was performed on these two classes separately, and signal components representing the active chewing were automatically detected by clustering analysis. First, the original signal in the time domain was segmented into 0.2 s windows with a shift of 20 ms. A variance was then computed for each window. K-means algorithm was chosen to perform the clustering analysis on an array of the previously computed variances. The number of clusters was experimentally set to three while the largest one represented the inactive chewing. The two remaining clusters were merged to obtain the active chewing class. Results from this method are exemplified in Figure 8.1.

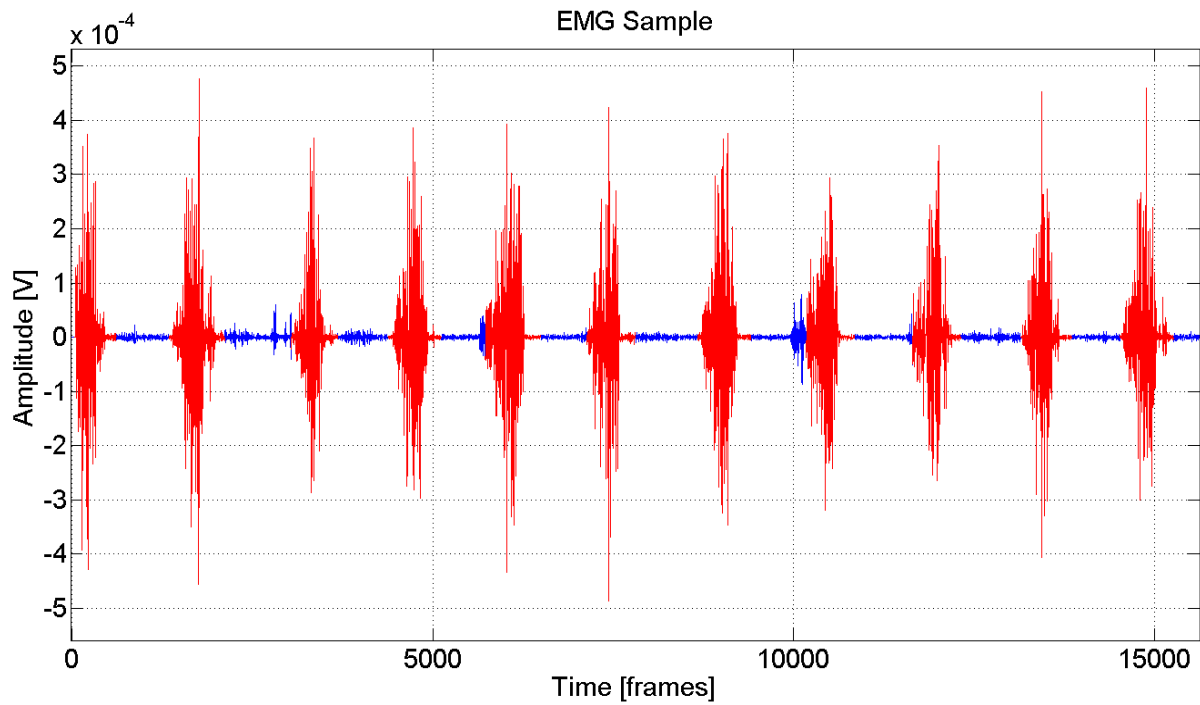


Figure 8.1: Sample raw EMG data depicting the results of the clustering methodology utilized to separate active and inactive chewing conditions (Red is active, and blue is inactive).

### 8.1.2.3 Craniofacial Muscle Modeling from MRI

The MRI segmentation and 3D reconstruction method utilized in this study can be found in [155]. The dataset used to model craniofacial muscles in the reported investigation was a T1-weighted MRI scan from a voluntary subject. The scanning protocol utilized was chosen to optimize the contrast between white and gray values with voxel sizes of 1 mm<sup>3</sup>. MIMICS image analysis software (Materialise, Leuven, Belgium) was first utilized to identify the temporalis (temporal) muscle via contrast thresholding, as its proximity to bone makes it readily visible. Next, the frontalis (frontal) muscle was identified using a combination of contrast and manual thresholding according to known anatomy and published methodologies [420]. An example image of this method is shown in Figure 8.2.

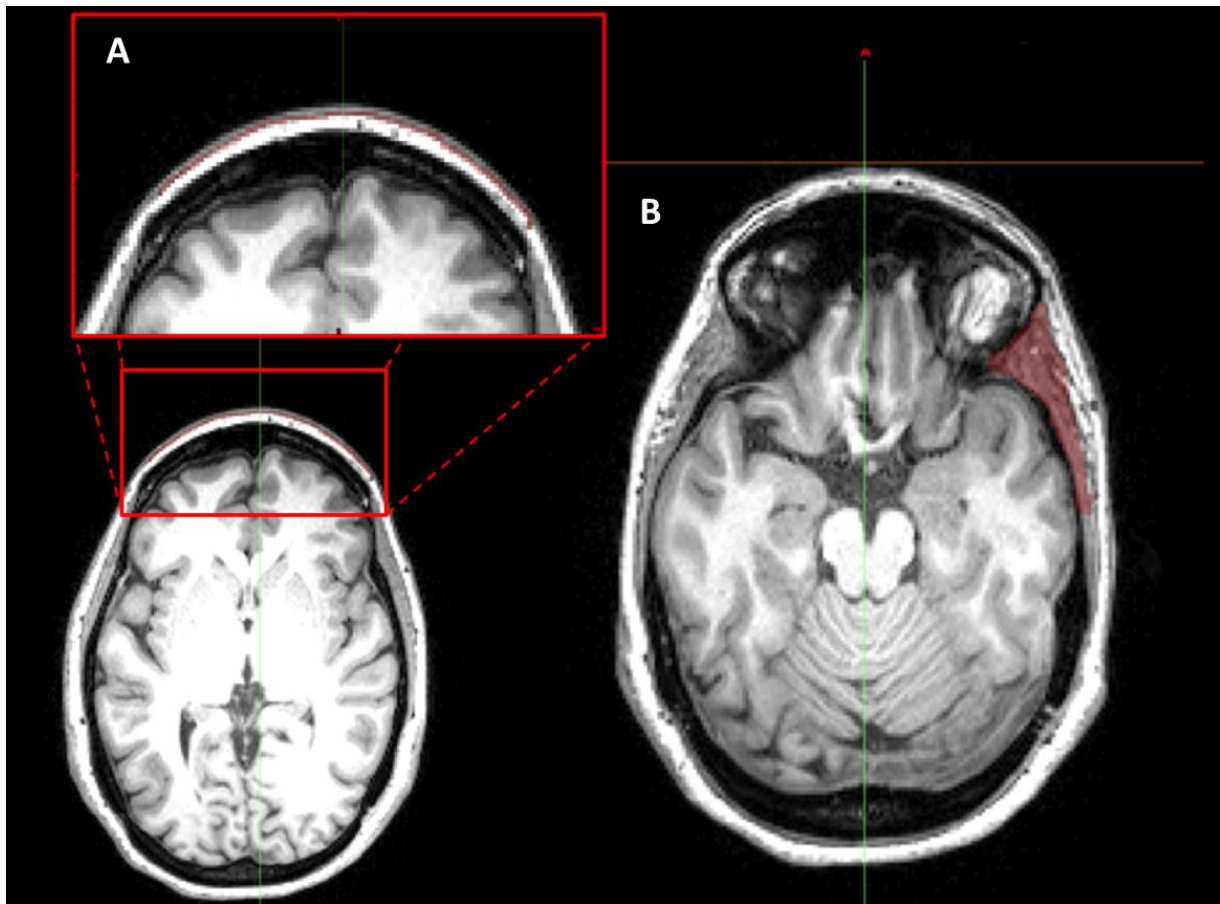


Figure 8.2: Example thresholding method using MIMICS software to identify and segment the frontal (A) and temporal (B) muscles. This technique presents its utility as a foundation for developing an anatomically-relevant model for assessing craniofacial muscle EMG artifacts and their potential to contribute to measured EEG.

#### 8.1.2.4 Statistical Analysis

Statistical analysis was performed using appropriately sized ANOVA with posthoc testing carried out using a student's T-test. Differences were considered statistically significant for  $p < 0.05$ .

### 8.1.3 Results

In order to assess the utility of comparing frequency spectra of EMG signals during each recorded facial movement, FFT analyses were completed to obtain mean PSDs and standard deviations at each 10 Hz frequency bin for each condition. Additionally, mean amplitudes for each of the subject conditions were computed by taking the absolute values of equal time frames within the recorded EMG signals. Results from these analyses are shown in Figures 8.3 and 8.4, respectively.

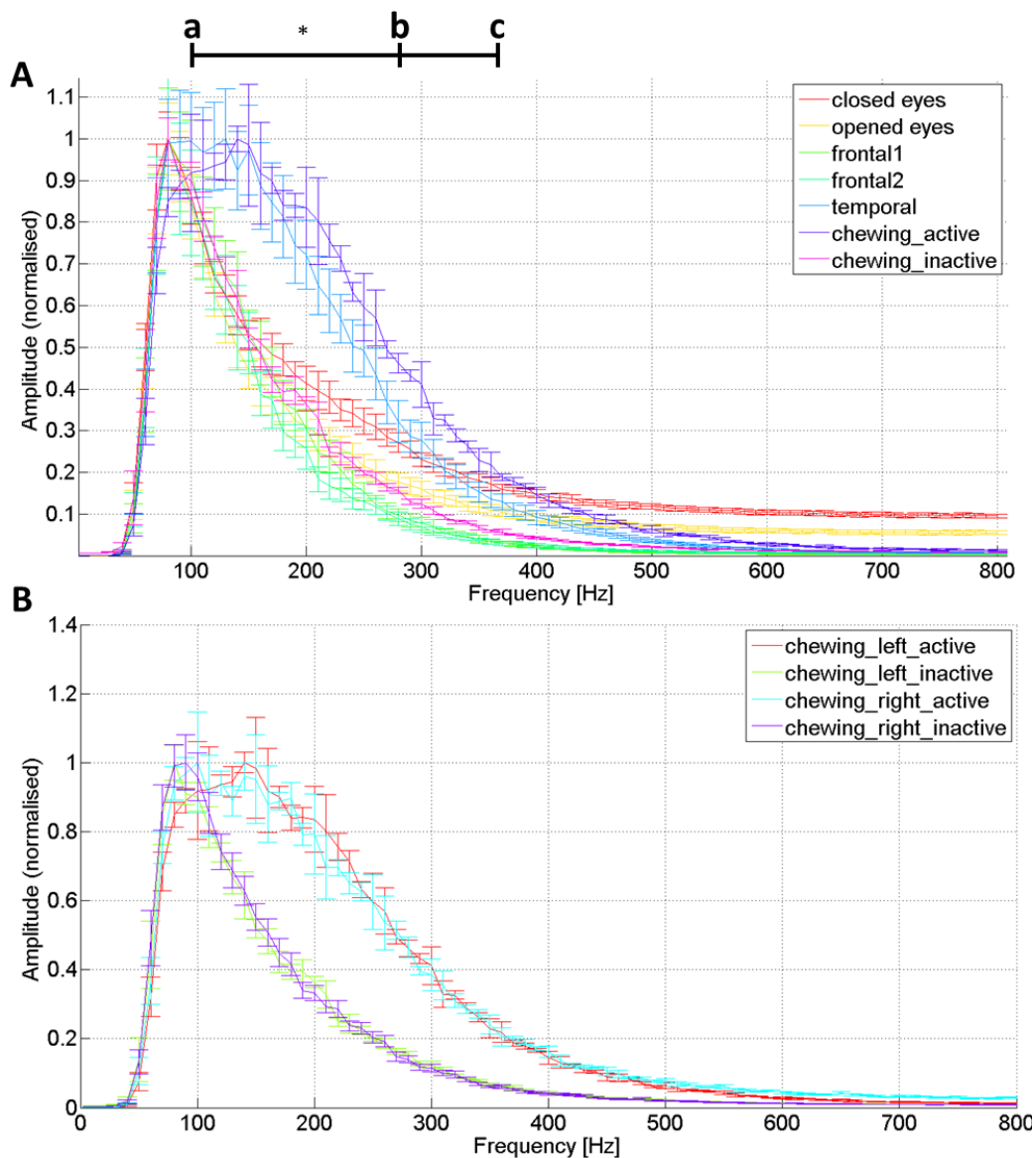


Figure 8.3: Results from EMG signal FFT analysis and mean signal amplitude assessment.

Note that the closed and open eyes conditions were both resting controls, frontal1 and frontal2 were maximum eyebrow raise and furrow conditions, respectively, temporal refers to the maximal temporal clench condition, and chewing active and inactive refer to the high-amplitude and low-amplitude portions of the chewing condition, as segmented by clustering analysis. A) Frequency spectra from each of the measured conditions (note that only the left side chewing condition was included in this plot). B) Frequency spectra for the left and right side chewing conditions. Statistical significance (\*) was determined as  $p < 0.05$  in all assessments.

Firstly, as is illustrated by comparing the frequency spectra for all of the subject conditions, frequencies from around 60 to 200 Hz comprise the majority of each curve. This frequency range corresponds to both low  $\gamma$  (30-50 Hz) and high  $\gamma$  (50-80 Hz) EEG waves. The control conditions, wherein subjects rested with eyes open or closed, contributed very similar frequency ranges to those of inactive chewing and both temporal muscle exercises (Figure 8.3A). Contrastingly, the temporal activation and active chewing conditions both contributed significantly more to the frequency ranges of 100-280 Hz and 100-370 Hz,

respectively (Figure 8.3A, a-b and a-c), than any other condition ( $p < 0.05$ ). Additionally, comparison of left and right chewing conditions showed minimal variation between conditions (Figure 8.3B), highlighting the utility of the methodology utilized in separating active and inactive signals.

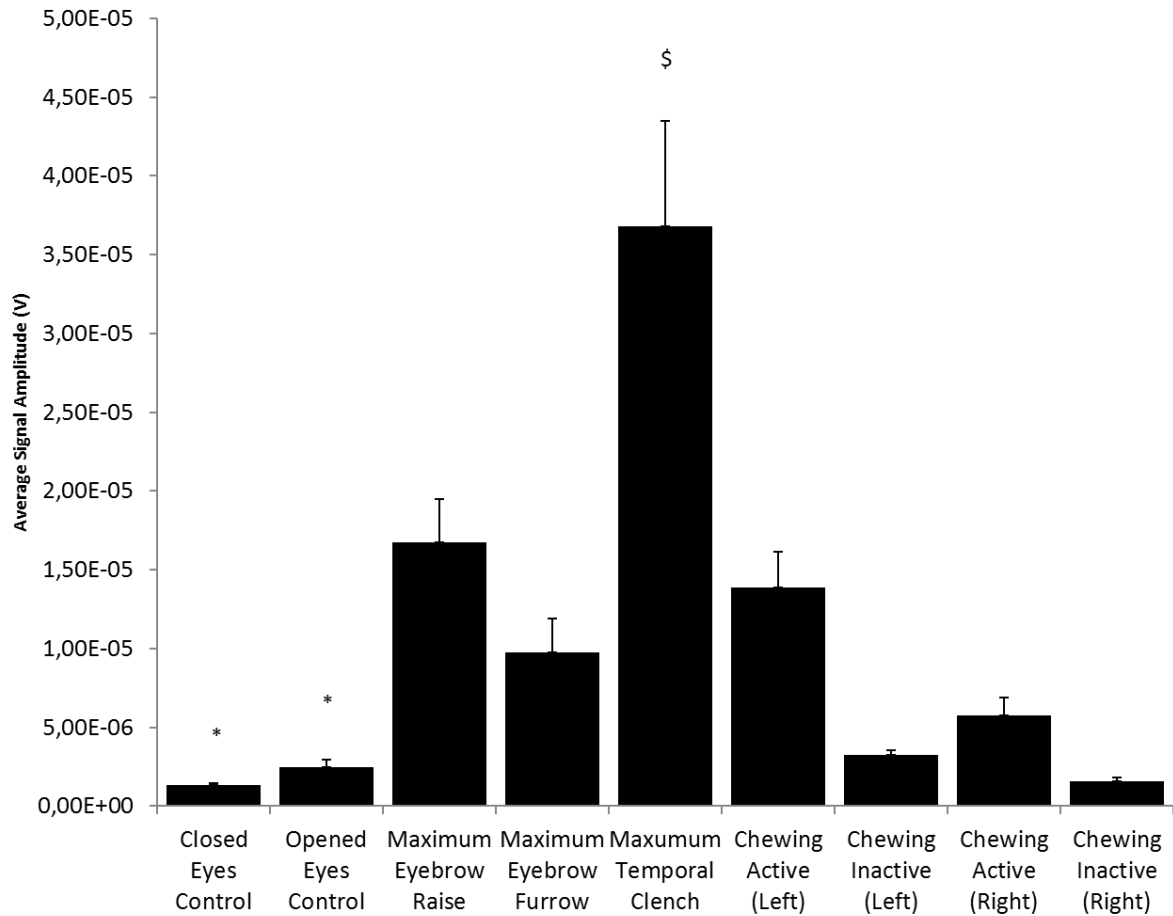


Figure 8.4: Comparison of mean signal amplitudes across all measured conditions. Note that all conditions except for both chewing inactive datasets were significantly greater in amplitude than both control conditions (\*). Likewise, the maximum temporal clench condition was significantly greater in amplitude than all other conditions (\$). Statistical significance was determined as  $p < 0.05$  in all assessments.

Finally, in comparing the relative mean EMG signal amplitudes of all conditions, all conditions except for inactive chewing exhibited significantly higher signal amplitudes than either control condition (Figure 8.4,  $p < 0.05$ ). Furthermore, the maximum temporal clench condition had significantly higher amplitudes than all other conditions ( $p < 0.05$ ).

These data are valuable because, as previously mentioned, traditional signal processing techniques perform FFT analyses to assess EEG frequency spectra, and understanding how high-frequency EMG may confound this signal is crucial to being able to optimally analyze scalp electrical activity. Our results demonstrate the presence of these confounding EMG frequencies as a normalized intensity distribution in frequency space, and understanding which frequencies optimally represent each condition's EMG signal and how they may overlap EEG frequency spectra are crucial first steps in developing a method for their removal from dense-array EEG data. However, because these frequencies are normalized, the exact contribution of each EMG in respect to its intensity at a specific frequency remains



unclear. Likewise, which frequencies are the most "important" (e.g. frequencies with the highest intensity) for each condition is additionally unclear. It is reasonable to conclude that each of the different conditions result in different intensity distributions in frequency space, which highlights the dependency of EMG frequency contribution to an EEG signal on the kind of muscle activity exhibited by the subject. This has to be taken into account during EEG data acquisition/analysis and EEG modeling and can be addressed by our analyses.

Next, to assess whether MRI segmentation and 3D reconstruction could be used to anatomically define the temporal and frontal craniofacial muscles used in EMG acquisition, a representative patient's cranial MRI was utilized. The results from the abovementioned segmentation using MIMICS are presented in Figure 8.5.

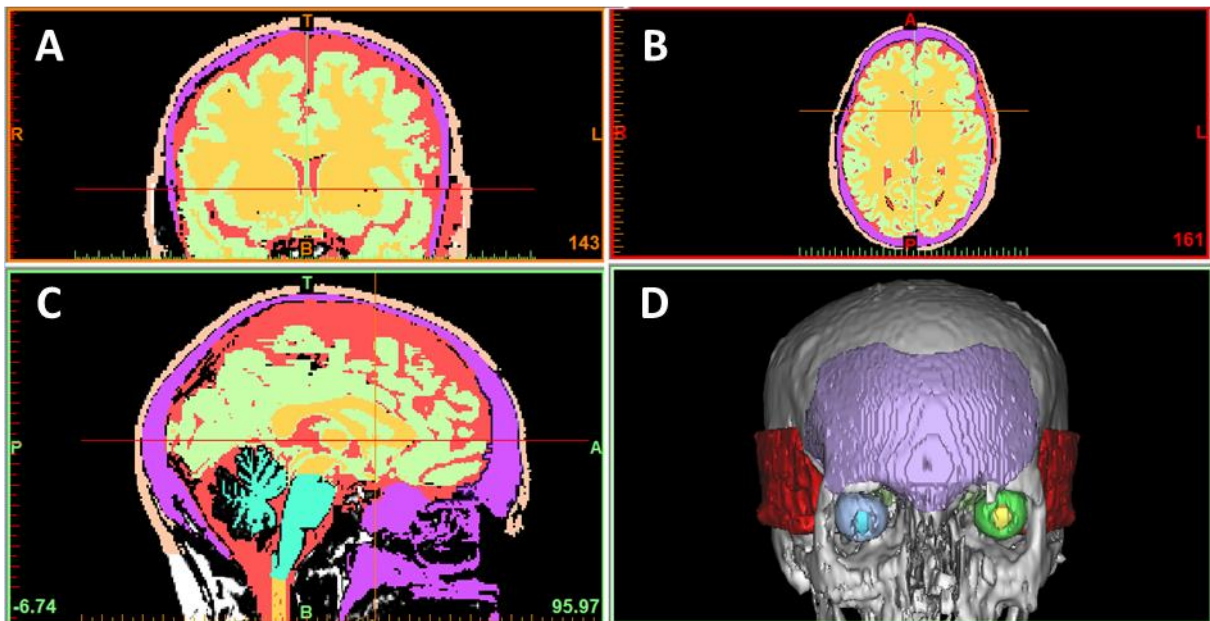


Figure 8.5: MRI segmentation and 3D reconstruction of temporal and frontal craniofacial muscles. A) Frontal, B) transverse, and C) sagittal plane cranial MRI slices. D) 3D reconstruction showing frontal (purple) and temporal (red) craniofacial muscles.

As is evident by the results from the MRI segmentation, both the left and right temporal muscles along with the frontal muscle were readily reconstructed using a combination of contrast thresholding and anatomical referencing. These results highlight the utility of this methodology in characterizing the morphology of the craniofacial muscles utilized in the EMG measurement portion of this study. Using this methodology to couple anatomical information with measured EMG signal could serve as a fundamental basis for developing an anatomical model for EMG and EEG signal measurement and processing.

#### 8.1.4 Discussion and Conclusion

The successful application of EEG signal processing methods requires a detailed knowledge of both the topography and frequency spectra of low-amplitude, high-frequency craniofacial EMG. This information remains unavailable to clinical researchers, and as such, there is no known reliable technique for the removal of these artifacts from EEG data. The results presented herein outline a preliminary investigation of craniofacial EMG high-frequency spectra and 3D MRI segmentation that offers insight into the development of an

anatomically-realistic model for characterizing these effects. The data presented highlights the potential for confounding signal contribution in EEG acquisition. However, since these data were normalized for spectral analyses, the comparative degree to which each respective craniofacial muscular movement may contribute to this signal remains unclear. Nevertheless, average EMG amplitude comparisons from each condition highlights the similarities in signal contribution of low-activity muscular movements and resting, control conditions. In addition to the FFT analysis performed, 3D segmentation and reconstruction of the craniofacial muscles whose EMG signals were measured was successful. This recapitulation of the relevant EMG morphology is a crucial first step in developing an anatomical model for the isolation and removal of confounding low-amplitude craniofacial EMG signals from EEG data. Such a model may be eventually applied in a clinical setting to ultimately help to extend the use of EEG in various clinical roles.

## **8.2 New Directions in 3D Medical Modeling: 3D Printing Anatomy and Functions in Neurosurgical Planning**

### **8.2.1 Introduction**

Three-dimensional (3D) modeling and rapid prototyping technologies have recently shown great utility in a wide variety of applications in medicine and surgery [375, 376]. In principle, the 3D recapitulation of patient-specific anatomical features provides surgeons with an immediate and intuitive understanding of even the most complex anatomical morphologies, enabling accurate planning and emulation of a host of surgical procedures [377, 421]. Indeed, the employment of these 3D anatomical models is additionally being considered for a host of implantation procedures, such as dental crowning, craniofacial reconstruction, and tissue regeneration via biological scaffolds [378-340].

Kodama et al. reported the birth of 3D rapid prototyping in 1982 [422], and the first use of the technology in support of surgical planning was reported by Anderl et al. in 1994 [423]. Since then, improvements in medical imaging modalities, such as CT and MRI, have driven both the clinical interest and academic development of 3D rapid prototyping in a medical context. Modern rapid prototyping enables the construction of anatomical models with layer thicknesses on the order of microns, and with concurrent advancements in medical image contrast segmentation, these models are able to recapitulate external and internal anatomical morphologies to high degrees of precision. The utilization of rapid prototyping models incurs a host of benefits to many surgical fields, which include improving surgical planning, enhancing diagnostic quality, decreasing patient exposure time to general anesthesia, decreasing patient blood loss, and shortening wound exposure time [424].

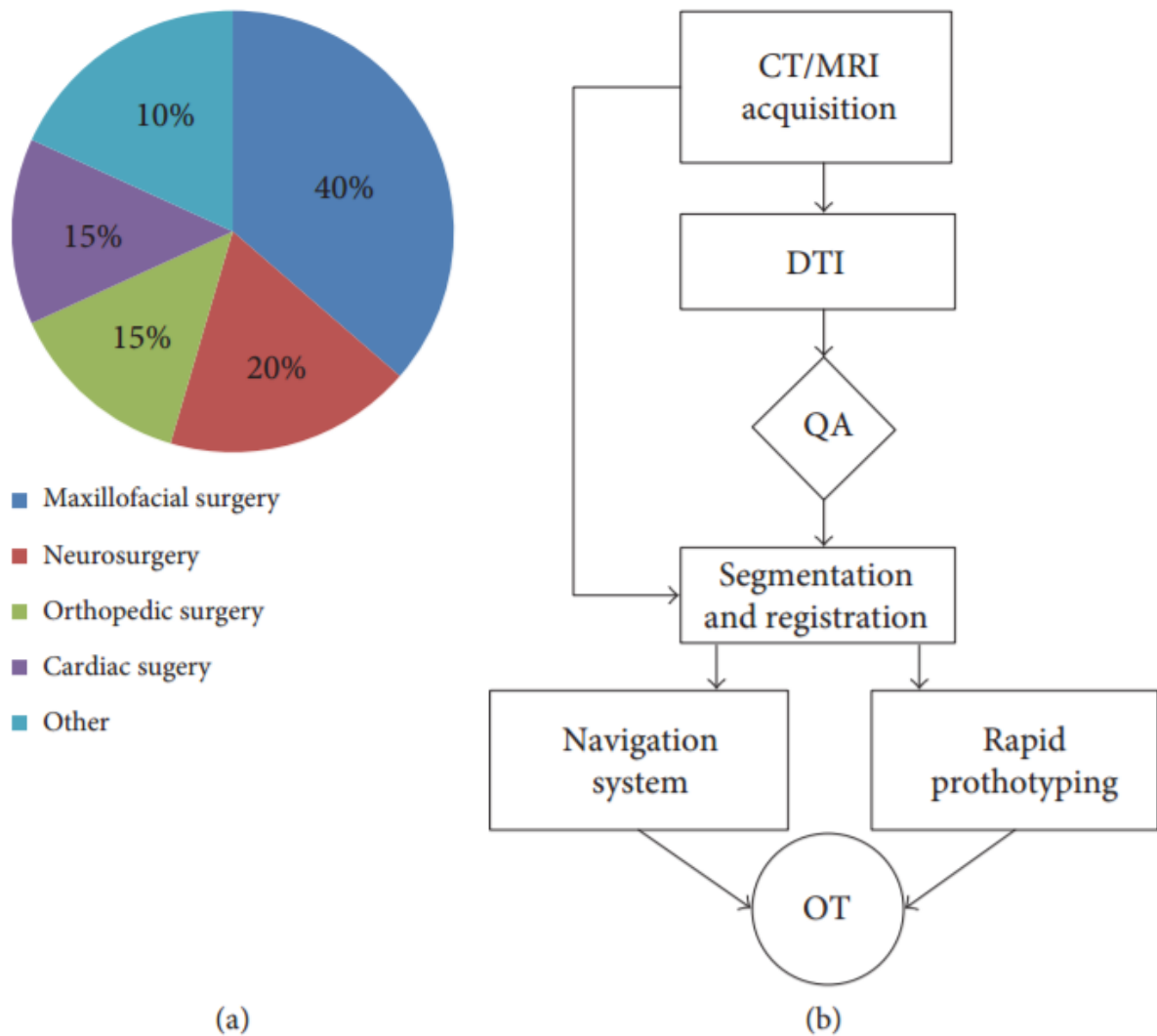


Figure 8.6: Clinical areas associated to the 200 surgeries assisted with 3D-printed models. Block diagrams showing the different steps required to create a 3D-printed model based on CT, MRI, and DTI data.

With the aims of improving surgical outcomes, reducing future costs, and developing thorough clinical guidelines for enhancing surgical planning and assessment, the National University Hospital of Iceland, Landspítali, established an in-house service for 3D rapid prototyping in 2007. Since its introduction, this service has allowed physicians and surgeons from different specialities to submit requests for a host of 3D models to be made available within 24 hours of submission. This process was simultaneously employed in research activities to study both the anthropometry of human muscles [47] and the use of rapid prototyping as preparation for complex brain surgeries in combination with neurosurgical navigation systems [425]. Since then, the National University Hospital of Iceland has fabricated over 200 surgical models for patient cases in the fields of cardiac, orthopedic, and neurosurgery (Figure 8.6(a)). The overwhelming success of this 3D rapid prototyping service has led to its solidification as an essential service within the hospital, and the rapid prototyping service continues to expand its impact on an increasing number of assisted surgical cases [421].

In neurosurgery, one technique that has likewise been increasingly used for preoperative planning is diffusion tensor imaging (DTI) tractography or fiber tracking. Tractography is a

noninvasive technique that allows for the *in vivo* localization of fiber tracts in the brain. Tractography uses DTI, which is based on magnetic resonance imaging (MRI), to map brain connectivity, which can provide neurosurgeons with the opportunity to visualize nerve fiber tracts before surgery [426]. More specifically, this technique may be applied to that of functional MRI (fMRI), which has shown great utility in the context of surgical planning. fMRI utilizes hemodynamic responses within the brain to implicate regional recruitment with a variety of cortical functions, such as motor control and language processing [427]. Unfortunately, the routine integration of surgical planning, DTI, and preoperative fMRI has been primarily limited by concerns regarding acquisition and registration reliability. Nonetheless, there is much promise in this regard—evidenced most relevantly in the reconstruction of corticospinal tracts for preoperative tumor planning [428, 429]. The purpose of this paper is to detail a novel approach to neurosurgical planning via the use of 3D printing, which combines patient-specific anatomy from traditional computer tomography (CT) and MRI images, with brain function derived from the *in vivo* localization of fiber tracts in the brain using DTI.

## 8.2.2 Materials and Methods

The procedure of creating the 3D-printed models based on CT, MRI, and DTI data can be seen in Figure 8.6(b).

### 8.2.2.1 CT and MRI Acquisition

CT data were acquired from a Philips/Brilliance 64, the Head scan protocol was set to 119 mA X-ray for the tube current and 120 KV for tube voltage, and the slice thickness is typically between 0, 6 and 1 mm. Once the image was reconstructed from the 3D data by 3 converting into a matrix of picture elements (pixels) where each pixel was assigned the attenuation value of the corresponding voxel which is the smallest distinguishable boxshaped part of a three-dimensional space, linear attenuation coefficients were rescaled to an integer range that encompasses 4096 values, ranging between  $-1000$  and  $3095$  named Hounsfield values.

MRI data were acquired from a 1.5T Siemens Avanto and the head coil used was Head Matrix Coil from Siemens. Both anatomical images and DTI were acquired for this process. The DTI protocol included a spin echoecho planar imaging- (SE-EPI-) based DTI sequence with 20 diffusion directions, two repetitions to boost the SNR and b value (b is the diffusion sensitivity) equal to  $1000 \text{ s/mm}^2$ . The anatomical image protocol included a T1-weighted 3D magnetization-prepared rapid acquisition gradient echo sequence (MP-RAGE).

### 8.2.2.2 DTI: Fiber Tract Extrapolation

Two different software (StealthViz [430] and nordicBrainEx [431]) programs were used to extrapolate the optimal fiber tracts for planning and rapid prototyping. The fiber tracts of major interest for this process are the so called eloquent fiber tracts; these tracks are easily clinically assessed and are most important for the patient outcome. In total, five fiber tracts were extrapolated from both software platforms:

- (i) Corpus callosum: the corpus callosum is located in the center of the brain and forms the largest white matter bundle. Its role is to transfer information between the left and right cerebral hemispheres [432].
- (ii) Motor tracts: it originates in the motor cortex area and descends down to the brain stem and spinal cord to control  $\alpha$ -motor neurons. It can control posture, reflexes, and muscle tone as well as conscious voluntary movements [433].
- (iii) Sensory tracts: it is responsible for the sense of touch. It receives incoming messages for touch and limb movements from the body [434].
- (iv) Optic tracts: they transfer the information from the retina to the visual cortex of the brain [435, 436].
- (v) Broca's area to Wernicke's area: arcuate Fasciculus is the prominent fiber tracts that connect these two areas that play a role in our language and speech [437].

StealthViz is a surgical planning software application. It allows import of Digital Imaging and Communications in Medicine (DICOM) datasets that can be reviewed in 2D and with 3D volume rendering, multimodality image fusion, and segmentation of structures with manual and semiautomatic tools. The software performs white matter tractography. It enables realignment of diffusion-weighted gradient, co-registration with other anatomical and functional datasets, and tensor calculations. The fiber tracking uses deterministic FACT algorithm [438]. The workflow is the following:

- (i) Import data: the MRI data are imported in DICOM format. Anatomical and diffusion tensor images are merged and the diffusion tensor positioned in the correct anatomical position.
- (ii) Segmentation: StealthViz allows segmentation with five different tools; pick region tool, brush tool, lasso tool, magic wand, and blow. A brain tumor can be segmented by using a blow tool which marks the region of interest on one cross section. The process can be iterated on several slices and those marked regions can be interpolated creating a 3D object of the tumor.
- (iii) Fiber tracking: to trace tracts in StealthViz a start box (and eventually a middle and end box) can be placed on specific regions of interest in the brain, called seeding point, for example, in our application, we start in the region of corpus callosum. Then, the software computed all the fibers that go through the designed box. Different combinations of the boxes can be used to find the tracts of interest. Tracts that are not of interest can be removed. Calculated fiber tracts are visualized within the structural images both in 2D and in 3D.
- (iv) Calculate as 3D object: when the tractography planning is completed and approved by neurosurgeon, the tracts are converted in 3D objects and saved in a DICOM format. In this phase, an error margin of 1 mm is added to each fiber tract.

- (v) **Export planning:** results can be exported as a one file or separated files (each for every track) to the surgical navigation system or to a USB flash memory.

NordicBrainEx is DICOM compatible and can analyze DTI data acquired with all major MRI scanners. DTI datasets acquired with two different b values (one  $b = 0$  and six or more DWI where  $b \neq 0$ ) can be analyzed in nordicBrainEx. The DTI analysis in nordicBrainEx generates parametric maps of various attributes of the diffusion tensor, including eigenvector color map (cDTI), fractional anisotropy index (FA), mean diffusivity (ADC), tensor eigenvalues ( $\lambda_1$ ,  $\lambda_2$ , and  $\lambda_3$ ), and trace weighted (TraceW). The fiber tracking is performed by using FACT [26]. The workflow is the following:

- (i) **Import data:** an automatic registration allows to place DTI data correctly according with the structural images.
- (ii) **Fiber tracking:** to perform tractography planning 5 different geometrical shapes can be selected for fiber tracking; ellipsoid, cube, polygon, free hand, or scatter. These geometrical shapes are used to define volume of interest (VOI) and find the tracts of interest. On a defined VOI, three logical operators are available: (1) AND which only visualize fibers passing through that VOI, (2) OR which will only visualize fibers passing through this and any other VOIs defined, or (3) NOT that will disregard all fibers passing through that VOI. When finished tracking, one fiber, for example, corpus callosum, can be saved individually.
- (iii) **Export planning:** results can be exported as separated files (each for every track) to the surgical navigation system or to a USB flash memory.

### 8.2.2.3 Quality Assessment: Anatomical Accuracy and Incorrectly Displayed Fibers

It is known that the different surgical planning software for fiber tracks may provide different results even though they are based on the same reconstruction algorithm [439]. For this reason, we performed a comparison between the software available in our institution to find the optimal one for rapid prototyping application. The assessment is based on anatomic accuracy and incorrectly displayed fibers for each fiber tract. These comparisons are done by grading the fiber-tracking results. Table 8.1 shows the grading for incorrectly displayed fibers and Table 8.2 shows the grading for anatomic accuracy. The grades vary from 1 (best) up to 4 (worst). A white matter atlas was used as a reference for the evaluation [440, 441].

Table 8.1: Grades for incorrectly displayed fibers.

Incorrectly displayed fibers	
Grade 1	None
Grade 2	<10% of all displayed fibers
Grade 3	<25% of all displayed fibers
Grade 4	>50% of all displayed fibers

Table 8.2: Grades for anatomical accuracy.

Anatomic accuracy	
Grade 1	Follow fiber tracts within anatomical boundaries
Grade 2	Follow fiber tracts outside anatomical boundaries
Grade 3	Follow poorly anatomical fiber tracts
Grade 4	Do not follow anatomical fiber tracts

#### 8.2.2.4 Segmentation and Registration

The next step is to combine the anatomical data such as the skull and other regions of interest with the tracks from the DTI software. We use for this propose the software MIMICS [442] that is a platform for medical image processing. The process can be divided in three steps:

- (i) CT data are imported in MIMICS and the skull bone is segmented. This operation is threshold based; where a range of HU (typically, from 600 to 2000) values are selected that allow to display the bone tissue. Next we apply region growing to assemble the entire connected pixel within the defined threshold in a so called mask. Now a 3D object can be created directly from the mask and further modification (such as opening the skull model to see inside) can be applied on the 3D object using CAD tools. Finally the 3D model can be saved as standard tessellation language (STL) file which is a format compatible with 3D Printing technologies.
- (ii) The next step is to import the tractography DICOM files to MIMICS. The 5 tracks of interest are superimposed on the anatomy (MRI data) but appearing brighter compared to those of the surrounding tissue (Figure 8.7(a)); therefore, the threshold-based segmentation of each tracts is easy. The five 3D objects associated to each tracks were created in the same way as described in step 1. In order to improve the quality of the 3D objects for 3D printing, we applied some morphological operations on the mask in order to smoothen details equal or below to 0.25 mm and closing distance equal to 2.5 mm (holes or gaps of 0.25 mm or less are filled). Finally, the 3D model can be saved as STL file.
- (iii) The final step is to combine Tracts, MRI, and CT data within the same 3D object. First, we imported the MRI T1-weighted images to MIMICS. Soft tissues like tumor are better visualized with MRI, and therefore, the segmentation and creation of the 3D object for this region of interest is done in this phase using the same threshold-based procedure described above. Next, we import the STL files of the skull and fiber tracts. Fiber tracts were positioned in a semiautomatic way on the 2D structural images by projecting the contours from the 3D object of the tracts. Next, we imported the STL file of the skull. Since the CT and MRI data have different coordinate system, the skull 3D object is registered manually using a 3D-positioning panel. When the skull is in the right position, then the necessary connections (bridges drawn manually) between tumor, fiber tracts, and skull are built in order to create a 3D model that can be printed. Finally, the skull, tumor, fiber tracts, and the bridges are combined in one 3D object using Boolean operations, and the

results are saved as STL (Figure 8.7(b)).

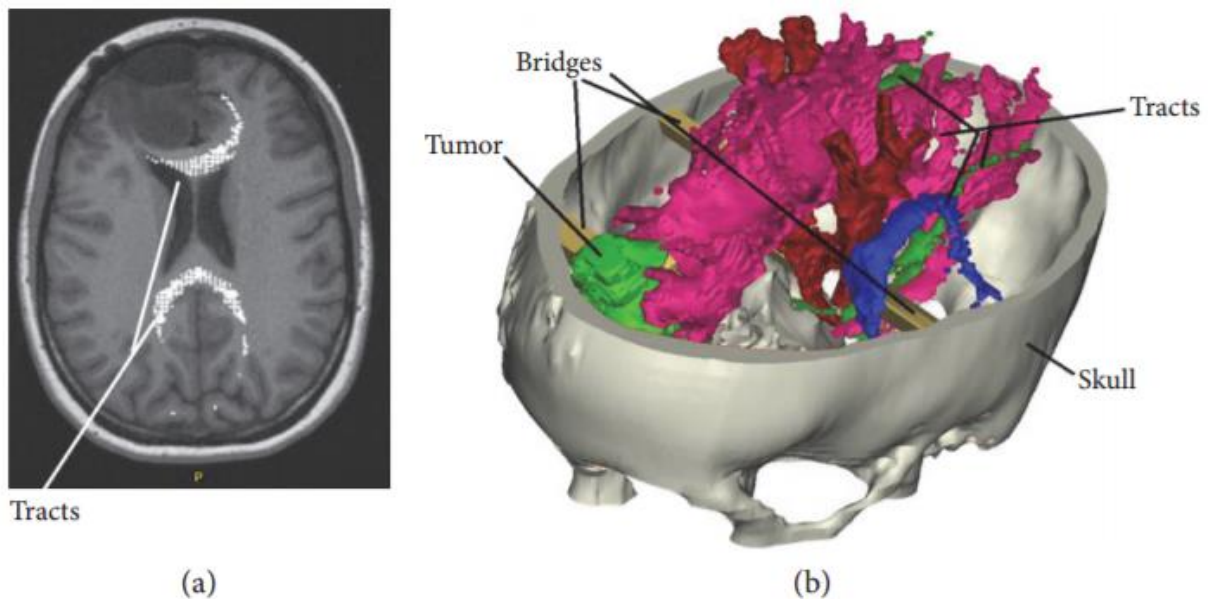


Figure 8.7: TRACTS superimposed on MRI structural data. (a) 3D model including skull from CT, tumor from MRI, fiber tracts, and connecting bridges (b).

#### 8.2.2.5 Navigation System and Rapid Prototyping

The 3D model of Figure 8.7 is finally printed using a ProJet® (3D systems, Rock Hill, USA) printer using a material called VisiJet®M3- X which is an organic colorless mixture that allow rendering of small details (mm scale). After print, the model is hardened with an infrared light. The computer model can be exported to the surgical navigation system as DICOM set, StealthStation® [443], which works as a GPS system determining the position of surgical instruments in relation to patient images by automatically fusing CT and MRI scans. Then, a registration is done with patient anatomy; so, there is a linkage between the patient and the system. In this application, we use the 3D-printed model instead of the real patient; in this way advanced preparation of the surgery can start before the patient enters the operation theatre.

### 8.2.3 Results

We validate this process collaborating to a neurosurgical planning of a 29-year-old female having a low-grade glioma located on the frontal lobe. The five fiber tracts that we focused on in this study can be seen in Figure 8.8, it shows the side views tractography planning from the two surgical planning software platforms; Figure 8.8(a) and 8.8(b) for StealthViz and Figure 8.8(c) and 8.8(d) for nordicBrainEx.



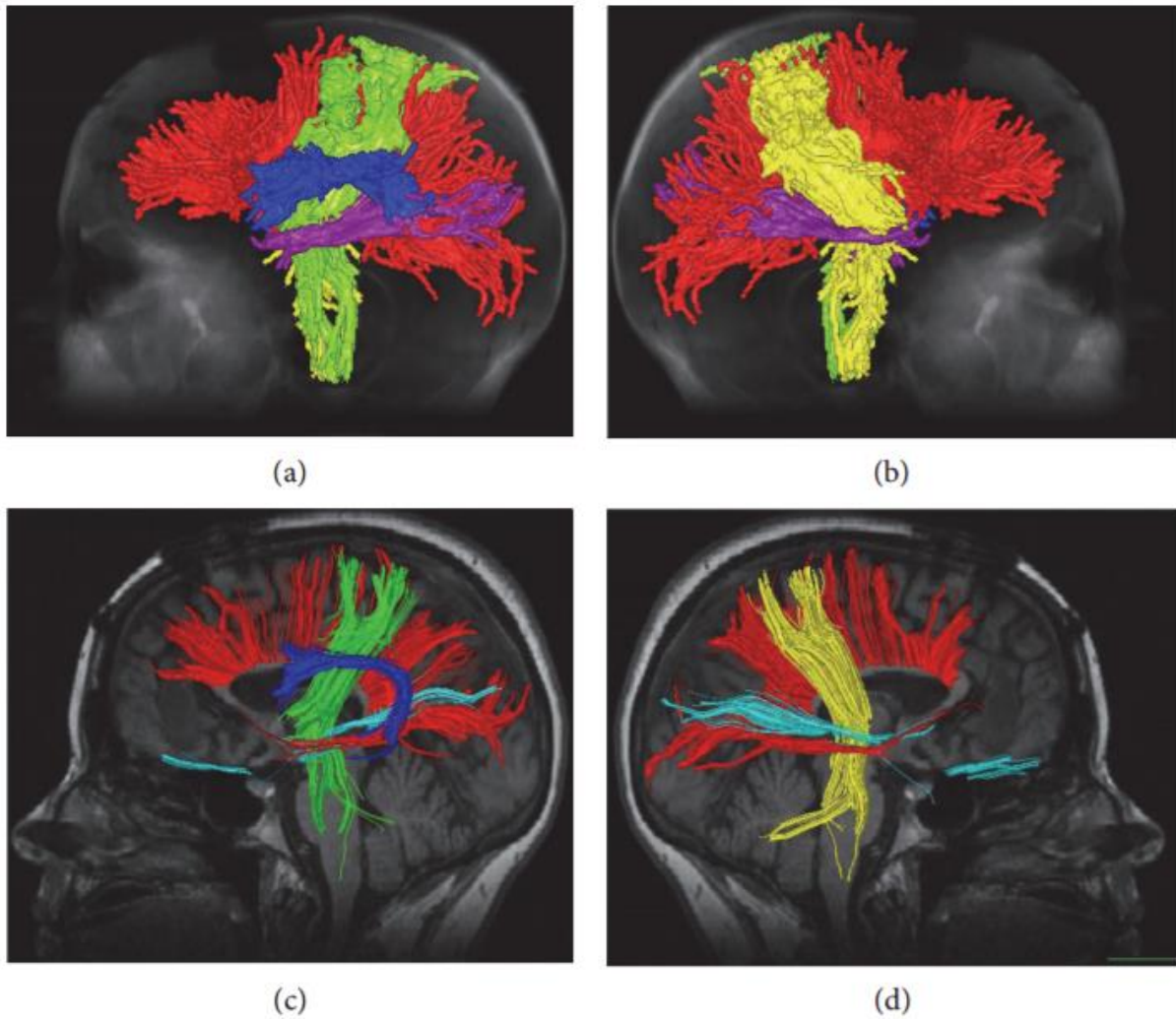


Figure 8.8: Tractography planning from StealthViz (a-b) and nordicBrainEx (c-d). Red color represents fiber tracts from corpus callosum, green color the tracts from motor and sensory area on the left side, and yellow showing the same tracts on the right side. Dark blue represents the arcuate fasciculus and purple shows the optic nerves.

It can be noticed that the pathways for the tracts are similar but not the identical; indeed, there are remarkable differences in thickness and ending morphology between the software platforms that may be important in relation to the pathological area of interest. In order to assess the results from the two fiber tracts planning, we use image comparison software called XERO viewer [444]; here, the fiber tracts, superimposed on the MRI data, were viewed simultaneously and visually assessed. Figure 8.9 shows the comparison of corpus callosum.

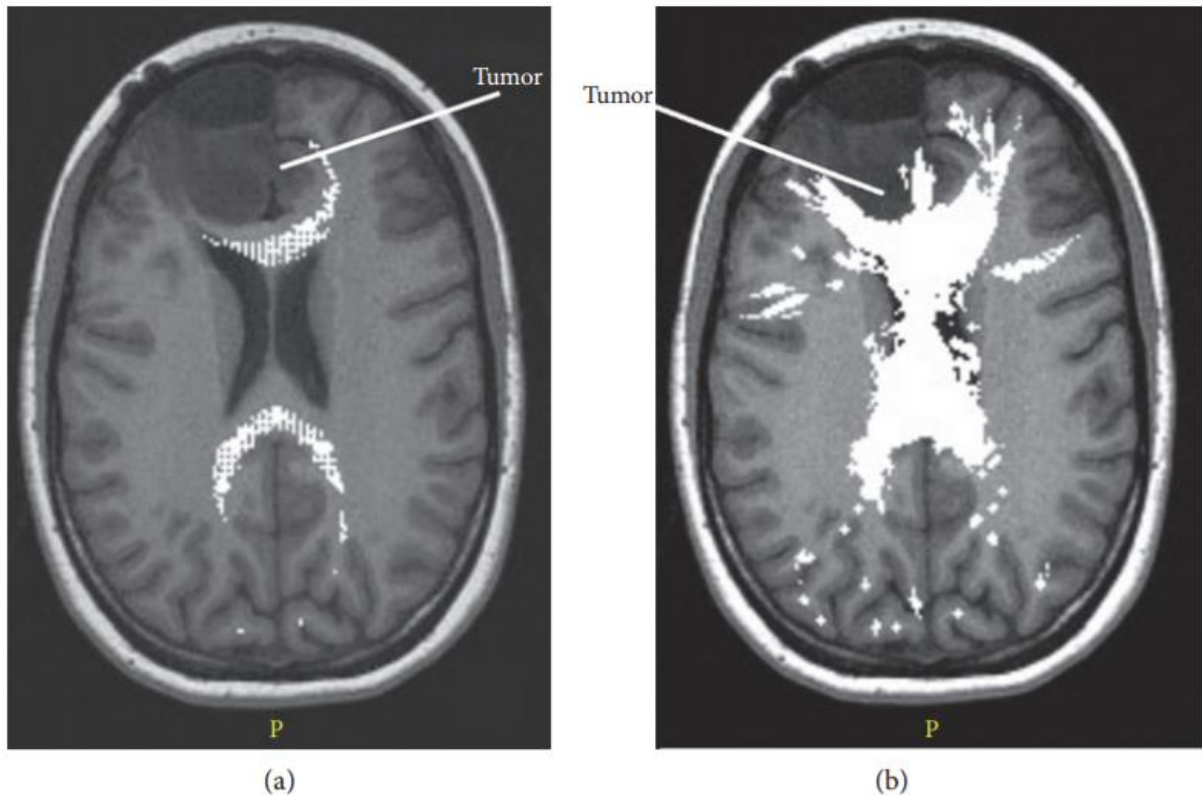


Figure 8.9: Comparison between the corpus callosum tracts obtained with different software: nordicBrainEx (a) and StealthViz (b). Both a and b show the same slice.

To be noticed, the surface of corpus callosum is shown in Figure 8.9(b) that displays a false positive. Moreover, the fiber tract from StealthViz goes out of white matter in the brain and it is difficult to assess the exact position. Based on comparison, slice by slice and tract by tract, we assess the two tractography planning based on anatomic accuracy and incorrectly displayed fibers [440, 441]. The quantitative results are displayed in Table 8.3 where for this study case, the tractography plane made with nordicBrainEx has a better score and was chosen for the next step.

Table 8.3: The grading results for anatomic accuracy and for incorrectly displayed fibers both for StealthViz (SV) and nordicBrainEx (BE).

Nerve tracts	Anatomic accuracy		Incorrectly displayed fibers	
	BE	SV	BE	SV
Arcuate fasciculus	3.5	1.0	3.5	3.0
Corpus callosum	2.0	1.0	2.0	1.5
Left motor and sensory tracts	2.0	1.5	2.0	1.5
Right motor and sensory tracts	2.0	1.5	2.0	1.5
Optic tracts	4.0	3.0	4.0	4.0
Total	13.5	8	13.5	12.5

Figure 8.10 shows the computer model (a) and 3D-printed model (b) resulting from the nordicBrainEx surgical planning. DTI planning and 3D-printed models were used with the

neurosurgical navigation system [425] to prepare the surgical operation where the tumor was removed from the frontal lobe. The operation was successful, and advanced planning provided with DTI planning and 3D models allowed the neurosurgeons to be better prepared during surgery.

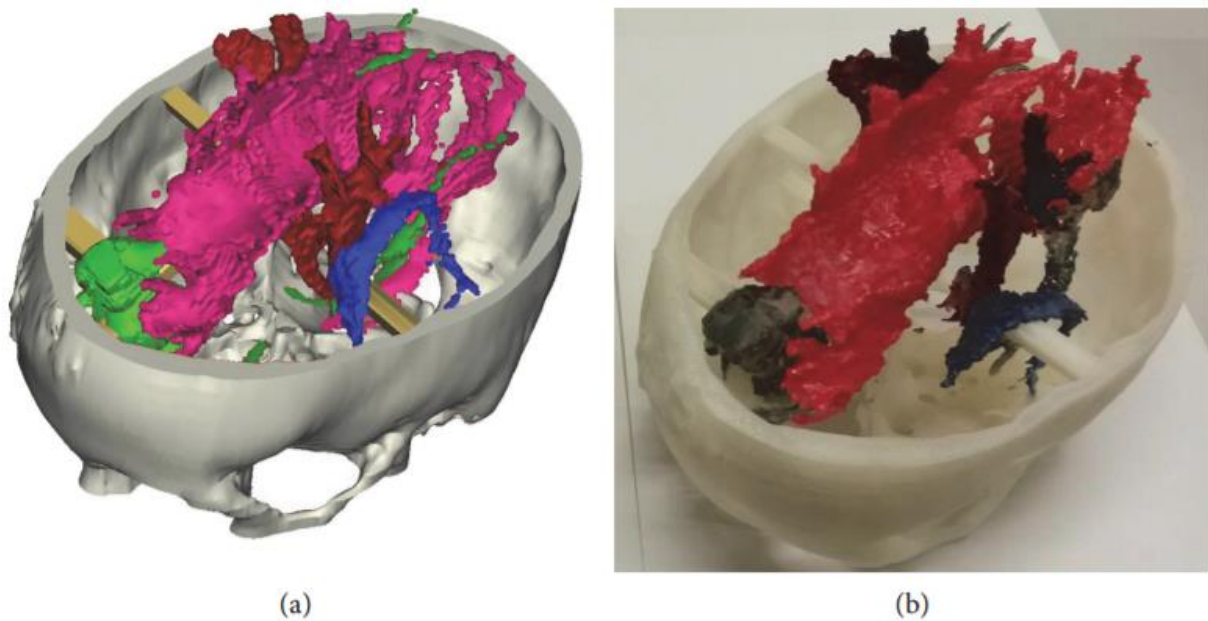


Figure 8.10: 3D computer model made in mimics with fiber tracts result from nordicBrainEx (a) and when it has been 3D printed and painted (b).

#### 8.2.4 Conclusion

Three-dimensional models and navigation systems for neurosurgery can be combined to improve surgical planning and surgeon training [425, 444]. The work reported herein demonstrates that preoperative planning using diffusion tensor imaging (DTI) tractography and 3D models is feasible and can be employed in the preparation of complex operations. Additionally, it is likely that this process can shorten operation times, contribute to better patient safety, and be used for training surgeons. Even though DTI tractography is not a fully reliable method, it can still provide the neurosurgeons with an overview of fiber tract position, and it has been shown that the use of DTI improves tumor resection results and decreases postoperative deficits [426, 445]. Altogether, this work demonstrates that the reported 3D-printing process may be integrated with DTI planning and add valuable information for neurosurgical planning—especially in association with surgical navigation systems.

## Chapter 9

# Conclusions and Future Directions

In the clinical context, medical imaging remains a vital tool for diagnostic and clinical investigations. For the purposes of mobility assessment, though both the lenses of translational myology and surgical planning, the optimization and standardization of soft tissue assessment methodology has been of particular importance. Indeed, visually simplistic medical imaging methods that can enable the noninvasive, high-resolution assessment of diseased or damaged tissues have implicated a wide variety of extant computational and mathematical modeling methods as preferential for investigation in this regard. However, the optimal employment of such methods remains debated, and reported techniques may not be sufficient for various avenues of research in translational myology or surgical planning.

This thesis focuses on the development, application, and assessment of novel methods in computational and mathematical modeling of medical images to quantify muscle degeneration and optimize our understanding of two mobility-restorative procedures: Functional Electrical Stimulation and Total Hip Arthroplasty. Additional impacts of these methods are further explored in defining multimodal metrics for mobility analysis, characterizing the utility of 3D printing for surgical planning, modeling craniofacial electromyography, and computing pre-surgical periprosthetic fracture risk. Results from these investigations altogether present the efficacies and limitations of available image processing modalities, and introduce novel methodologies, such as nonlinear trimodal regression analysis of radiodensitometric distributions and computational interference fitting for periprosthetic femoral fracture analysis. Such analyses and perspectives are herein presented in both a theoretical and practical context. Standardizing computational modeling methodologies for medical image assessment in these contexts would allow for the generalizability of such research to the indication of respective compensatory targets for clinical intervention.

- **Chapter 3:** The focus of this chapter is on the introduction of the impacts of modern methods for X-Ray Computed Tomography image analyses in the contexts of investigating muscle degeneration, functional electrical stimulation, and total hip

arthroplasty. The intent of the collection of these works is to inspire a discussion of extant assessment methods and therapeutic interventions currently investigated by the fields of translational myology and surgical planning.

- **Chapter 4:** The focus of this chapter is on the definition and utility of our novel method for quantifying muscle quality by radiodensitometric attenuation distribution analysis using a combinatorial methodology involving nonlinear trimodal regression analysis and histogram iteration via a generalized reduced gradient algorithm. This method was tested first with three subjects with varying degrees of muscle quality defined by their respective conditions as a proof-of-concept. Following this, the utility of the method was demonstrated with a cohort of total hip arthroplasty patients to investigate changes in periprosthetic muscle quality according to implant procedure and post-surgical normalization of ambulation.
- **Chapter 5:** This chapter continues the investigation on the utility of the abovementioned nonlinear trimodal regression analysis method by assembling computed tomography radiodensitometric distributions, cross-sectional areas, average Hounsfield unit values, lower extremity function biometrics, and sarcopenic comorbidities in the AGES-II database of 3,162 aging subjects. This investigation highlights the specificities of each muscle quality metric as quantitative indicators for sarcopenia.
- **Chapter 6:** This chapter describes the novel assembly of biometric assessment and computational modeling modalities from a 100-patient total hip arthroplasty cohort as a first step towards creating patient-specific applications that rehabilitators and orthopedic surgeons can utilize for prescribing their respective surgical procedures. Along with outlining further utility of the previously-described nonlinear trimodal regression analysis method for muscle quality assessment, this investigation reports notable aspects of each patient's dataset and compares these results across available subgroups of the cohort, highlighting the combinatorial utilities of each reported modality.
- **Chapter 7:** The objective of the research presented in this chapter was to continue computational modeling discussion in the context of surgical support by describing a novel finite elements analysis methodology for patient fracture risk evaluation before total hip arthroplasty surgery. The presented results highlight the feasibility of the methodology as a foundation to develop a clinical database for correlating bone mineral density obtained from computed tomography images with computational methods for assuming fracture risk and predicting patient outcomes.
- **Chapter 8:** This chapter contains two additional computation and mathematical modeling applications across the aforementioned fields of translational myology and surgical planning. The first of these studies describes the recapitulation of craniofacial morphology as a crucial first step in developing an anatomical model for the isolation and removal of confounding low-amplitude craniofacial electromyographic signals from electroencephalography datasets. The second study reports the integration of 3D-printing process with diffusion tensor imaging for neurosurgical planning, in association with surgical navigation systems.

The increasing prevalence of Sarcopenic muscle degeneration necessitates the establishment of a robust quantitative myological assessment methodology. While there is much extant literature reporting the use of average HU values to investigate muscle quality as a Sarcopenic index, no studies have yet to utilize entire radiodensitometric distributions and define a generalized analytical tool for their assessment. Herein, we have shown that rigorous quantification of entire HU distributions using our nonlinear trimodal regression analysis (NTRA) method can elicit many unique assessment parameters and therein provide additional information regarding muscle quality alongside extant gold standard methods. This is perhaps the most impactful work presented in this thesis, with a host of potential impacts across many fields of soft tissue investigation. Indeed, the contribution of fibrosis to traditional metrics of muscle quality remains an essential target for further investigation, and the inclusion of the loose connective/water equivalent tissue regime in NTRA analysis may serve as a direct metric for fibrosis with further investigation. As is true in any such study, however, the use of more subjects and aging comorbidities will be essential to reinforcing any of the physiological interpretations reported here, and further discussion regarding potential applications and adjustments to the reported model will be requisite.

Perhaps the most ambitious of our reported investigations is presented in Chapter 6, on the multimodal quantitative assessment of THA patients. It must be stressed that many of the results presented herein are quite preliminary in nature; especially with regards to subject involvement. As is the case with any multimetric study (especially those with longitudinal datasets), patient involvement across all metrics must be stressed to optimize the validity of reported results. In this regard, a larger patient population will be requisite to rigorously show the statistical significance of each parameter and to define limits that correlate to additional, real cases of patient periprosthetic fracture.

As our most investigated THA metric, the limitations of the reported FEA and FRI computations must likewise be made clear. The greatest of these is that the simulations carried out were steady-state, and did not take into consideration applied loads that are time-dependent, or the prosthetic design and surface finish. The real forces induced by a surgical hammer during the surgery are high-impact and punctate forces, or forces acting on the bone over a short period of time. This can instigate the development of microfissures in the periprosthetic region of the femur, leading to fractures in more extreme cases. Furthermore, the use of unidirectional force is an over-simplification of the distribution incurred by press-fitting. For this reason, using a direct strain-based method such as interference fitting (preliminarily reported in Chapter 6) for computing fracture risk will be optimal in future studies to avoid this discrepancy. In addition, the anisotropy of femoral bone was not considered in present studies and must be employed in future work to optimize periprosthetic fracture propagation prediction.

Aside from their aforementioned limitations, the investigations presented in this thesis altogether present the efficacies and novel employment of available image processing modalities, and results and perspectives are herein presented in both a theoretical and practical context. Standardizing computational modeling methodologies for medical image assessment in these contexts would allow for the generalizability of such research to the indication of respective compensatory targets for clinical intervention.



## Bibliography

- [1] Metter, E. J., Talbot, L. a, Schrager, M., & Conwit, R. (2002). Skeletal muscle strength as a predictor of all-cause mortality in healthy men. *J Gerontol A Biol Sci Med Sci*, 57(10), B359–65.
- [2] Rantanen, T. (2000). Muscle strength and body mass index as long-term predictors of mortality in initialle healthy men. *J Gerontol*, 55A(3), 168–173.
- [3] Newman, A. B., Kupelian, V., Visser, M., Simonsick, E. M., Goodpaster, B. H., Kritchevsky, S. B., Harris, T. B. (2006). Strength, but not muscle mass, is associated with mortality in the health, aging and body composition study cohort. *J Gerontol A Biol Sci Med Sci*, 61(1), 72–77.
- [4] Goodpaster, B. H., Carlson, C. L., Visser, M., Kelley, D. E., Scherzinger, A., Harris, T. B., Newman, a B. (2001). Attenuation of skeletal muscle and strength in the elderly: The Health ABC Study. *Journal of Applied Physiology (Bethesda, Md. : 1985)*, 90(6), 2157–2165.
- [5] Volpi, E., Nazemi, R., & Fujita, S. (2004). Muscle tissue changes with aging. *Current Opinion in Clinical Nutrition and Metabolic Care*, 7(4), 405–410.
- [6] Lynch, G. S. (2001). Therapies for improving muscle function in neuromuscular disorders. *Exercise and Sport Sciences Reviews*, 29(4), 141–8.
- [7] Kalyani, R. R., Corriere, M., & Ferrucci, L. (2014). Age-related and disease-related muscle loss: the effect of diabetes, obesity, and other diseases. *The Lancet. Diabetes & Endocrinology*, 2(10), 819–29.
- [8] Baumgartner, R. N., Koehler, K. M., Gallagher, D., Romero, L., Heymsfield, S. B., Ross, R. R., ... Lindeman, R. D. (1998). Epidemiology of sarcopenia among the elderly in New Mexico. *American Journal of Epidemiology*, 147(8), 755–763.
- [9] Janssen, I., Heymsfield, S. B., & Ross, R. (2002). Low relative skeletal muscle mass (sarcopenia) in older persons is associated with functional impairment and physical disability. *Journal of the American Geriatrics Society*, 50(5), 889–896.
- [10] Newman, A. B., Kupelian, V., Visser, M., Simonsick, E., Goodpaster, B., Nevitt, M., ... Harris, T. B. (2003). Sarcopenia: Alternative Definitions and Associations with Lower Extremity Function. *J Am Geriatr Soc*, 51, 1602–1609. doi:10.1046/j.1532-5415.2003.51534.x
- [11] Larsson, L., Sjödin, B., & Karlsson, J. (1978). Histochemical and biochemical changes in human skeletal muscle with age in sedentary males, age 22--65 years. *Acta Physiologica Scandinavica*, 103(1), 31–39.



- [12] Larsson, L., Li, X., & Frontera, W. R. (1997). Effects of aging on shortening velocity and myosin isoform composition in single human skeletal muscle cells. *The American Journal of Physiology*, 272(2 Pt 1), C638–C649.
- [13] Lang, T., Cauley, J. a, Tylavsky, F., Bauer, D., Cummings, S., & Harris, T. B. (2010). Computed tomographic measurements of thigh muscle cross-sectional area and attenuation coefficient predict hip fracture: the health, aging, and body composition study. *Journal of Bone and Mineral Research: The Official Journal of the American Society for Bone and Mineral Research*, 25(3), 513–9.
- [14] Visser, M., Goodpaster, B. H., Kritchevsky, S. B., Newman, A. B., Nevitt, M., Rubin, S. M., ... Harris, T. B. (2005). Muscle mass, muscle strength, and muscle fat infiltration as predictors of incident mobility limitations in well-functioning older persons. *The Journals of Gerontology. Series A, Biological Sciences and Medical Sciences*, 60(3), 324–333.
- [15] Kirkland, J. L., Tchkonina, T., Pirtskhalava, T., Han, J., & Karagiannides, I. (2002). Adipogenesis and aging: does aging make fat go MAD? *Experimental Gerontology*, 37(6), 757–767.
- [16] Goodpaster, B. H., Theriault, R., Watkins, S. C., & Kelley, D. E. (2000). Intramuscular lipid content is increased in obesity and decreased by weight loss. *Metabolism: Clinical and Experimental*, 49(4), 467–72.
- [17] Kelley, D. E., Mintun, M. a., Watkins, S. C., Simoneau, J. A., Jadali, F., Fredrickson, A., Thériault, R. (1996). The effect of non-insulin-dependent diabetes mellitus and obesity on glucose transport and phosphorylation in skeletal muscle. *Journal of Clinical Investigation*, 97(12), 2705–2713.
- [18] Simoneau, J. a, Colberg, S. R., Thaete, F. L., & Kelley, D. E. (1995). Skeletal muscle glycolytic and oxidative enzyme capacities are determinants of insulin sensitivity and muscle composition in obese women. *The FASEB Journal : Official Publication of the Federation of American Societies for Experimental Biology*, 9(2), 273–278.
- [19] Goodpaster, B. H., Thaete, F. L., Simoneau, J. a., & Kelley, D. E. (1997). Subcutaneous abdominal fat and thigh muscle composition predict insulin sensitivity independently of visceral fat. *Diabetes*, 46(10), 1579–1585.
- [20] Brooks, S. V, & Faulkner, J. A. (1994). Skeletal muscle weakness in old age: underlying mechanisms. *Medicine and Science in Sports and Exercise*, 26(4), 432.
- [21] Reed, R. L., Pearlmutter, L., Yochum, K., Meredith, K. E., & Mooradian, A. D. (1991). The relationship between muscle mass and muscle strength in the elderly. *Journal of the American Geriatrics Society*, 39(6), 555–561.
- [22] Jubrias, S. a, Odderson, I. R., Esselman, P. C., & Conley, K. E. (1997). Decline in isokinetic force with age: muscle cross-sectional area and specific force. *Pflügers Archiv : European Journal of Physiology*, 434(3), 246–53.
- [23] Nordal, H. J., Dietrichson, P., Eldevik, P., & Gronseth, K. (1988). Fat infiltration, atrophy and hypertrophy of skeletal muscles demonstrated by X-ray computed tomography in neurological patients. *Acta Neurol Scand*, 77(2), 115–122.
- [24] Janssen, I., Shepard, D. S., Katzmarzyk, P. T., & Roubenoff, R. (2004). The Healthcare Costs of Sarcopenia in the United States. *Journal of the American Geriatrics Society*, 52(1), 80–85.

- [25] Cooper, R., Kuh, D., & Hardy, R. (2010). Objectively measured physical capability levels and mortality: systematic review and meta-analysis. *BMJ (Clinical Research Ed.)*, 341, c4467.
- [26] Sayer, A. A., Robinson, S. M., Patel, H. P., Shavlakadze, T., Cooper, C., & Grounds, M. D. (2013). New horizons in the pathogenesis, diagnosis and management of sarcopenia. *Age and Ageing*, 42(2), 145–50.
- [27] Rantanen T, Guralnik JM, Ferrucci L, et al. Coimpairments: strength and balance as predictors of severe walking disability. *J Gerontol A Biol Sci Med Sci*. 1999 Apr;54(4):M172–176, Studenski S, Perera S, Wallace D, et al. Physical performance measures in the clinical setting. *J Am Geriatr Soc*. 2003 Mar;51(3):314–322
- [28] Chang, M., Saczynski, J. S., Snaedal, J., Bjornsson, S., Einarsson, B., Garcia, M., ... Jonsson, P. V. (2013). Mid-life physical activity preserves lower extremity function in older adults: Age Gene/Environment Susceptibility (AGES) - Reykjavik Study. *Journal of the American Geriatrics Society*, 61(2), 237–242.
- [29] Goodpaster BH, Thaete FL, Kelley DE. Thigh adipose tissue distribution is associated with insulin resistance in obesity and in type 2 diabetes mellitus. *The American journal of clinical nutrition*. 2000;71(4):885-92..
- [30] Kent-Braun J.A., Ng A.V. (1985). Skeletal muscle oxidative capacity in young and older women and men. *J Appl Physiol* (1985). 2000 Sep;89(3):1072-8.
- [31] Buford T.W., Lott D.J., Marzetti E., Wohlgemuth S.E., Vandenborne K., Pahor M., Leeuwenburgh C., Manini T.M. (2012). Age-related differences in lower extremity tissue compartments and associations with physical function in older adults. *Exp Gerontol*. 2012 Jan;47(1):38-44.
- [32] Guralnik JM, Ferrucci L, Simonsick EM, Salive ME, Wallace RB. Lower-extremity function in persons over the age of 70 years as a predictor of subsequent disability. *N Engl J Med*. 1995;332:556–561
- [33] Guralnik JM, Simonsick EM, Ferrucci L, et al. A short physical performance battery assessing lower extremity function: association with self-reported disability and prediction of mortality and nursing home admission. *J Gerontol. A Biol Sci Med Sci*. 1994;49:M85–M94
- [34] Nair KS. Aging muscle. *Am J Clin Nutr*. 2005;81:953–963.
- [35] Rosenberg IH. Sarcopenia: origins and clinical relevance. *J Nutr*. 1997;127(5 Suppl):990S–991S.
- [36] McGregor, R. A., Cameron-Smith, D., & Poppitt, S. D. (2014). It is not just muscle mass: a review of muscle quality, composition and metabolism during ageing as determinants of muscle function and mobility in later life. *Longevity & Healthspan*, 3(1), 9.
- [37] Janssen I, Heymsfield SB, Wang ZM, Ross R. Skeletal muscle mass and distribution in 468 men and women aged 18-88 yr. *J Appl Physiol*. 2000;89:81–88.
- [38] Silva AM, Shen W, Heo M, Gallagher D, Wang Z, Sardinha LB, Heymsfield SB. Ethnicity-related skeletal muscle differences across the lifespan. *Am J Hum Biol*. 2010;22:76–82.
- [39] Kostka T. Quadriceps maximal power and optimal shortening velocity in 335 men aged 23-88 years. *Eur J Appl Physiol*. 2005;95:140–145. doi: 10.1007/s00421-005-1390-8.

- [40] Mitchell WK, Williams J, Atherton P, Larvin M, Lund J, Narici M. Sarcopenia, dynapenia, and the impact of advancing age on human skeletal muscle size and strength; a quantitative review. *Front Physiol.* 2012;3:260.
- [41] Maden-Wilkinson TM, Degens H, Jones DA, McPhee JS. Comparison of MRI and DXA to measure muscle size and age-related atrophy in thigh muscles. *J Musculoskelet Neuronal Interact.* 2013;13:320–328.
- [42] Zoico E, Rossi A, Di Francesco V, Sepe A, Oliosio D, Pizzini F, Fantin F, Bosello O, Cominacini L, Harris TB, Zamboni M. Adipose tissue infiltration in skeletal muscle of healthy elderly men: relationships with body composition, insulin resistance, and inflammation at the systemic and tissue level. *J Gerontol A Biol Sci Med Sci.* 2010;65:295–299.
- [43] Goodpaster BH, Kelley DE, Thaete FL, He J, Ross R. Skeletal muscle attenuation determined by computed tomography is associated with skeletal muscle lipid content. *J Appl Physiol.* 2000;89:104–110.
- [44] Gargiulo, P., Kern, H., Carraro, U., Ingvarsson, P., Knútsdóttir, S., Gudmundsdóttir, V. Helgason, T. (2010). Quantitative color three-dimensional computer tomography imaging of human long-term denervated muscle. *Neurological Research*, 32(1), 13.
- [45] Edmunds K.J., Árnadóttir Í., Gíslason M.K., Carraro U., Gargiulo P. (2016). Nonlinear Trimodal Regression Analysis of Radiodensitometric Distributions to Quantify Sarcopenic and Sequelae Muscle Degeneration. *Comput Math Methods Med.* 2016;2016:8932950.
- [46] Mah, P., Reeves, T. E., & McDavid, W. D. (2010). Deriving Hounsfield units using grey levels in cone beam computed tomography. *Dento Maxillo Facial Radiology*, 39(6), 323–35.
- [47] Carraro, U., Edmunds, K.J., Gargiulo, P. (2015). 3D False Color Computed Tomography for Diagnosis and Follow-up of Permanently Denervated Human Femoral Muscles Submitted to Functional Electrical Stimulation. *European Journal of Translational Myology*, 25 (2): 129-140.
- [48] Kern H. Funktionelle Elektrostimulation Paraplegischer Patienten. *ÖZPM, Österreichische Zeitschrift für Physikalische Medizin* 1995;5:1-75. ISSN 1021-4348.
- [49] Kern H, Boncompagni S, Rossini K, et al. Long-term denervation in humans causes degeneration of both contractile and excitation contraction coupling apparatus, which is reversible by functional electrical stimulation (FES). A role for myofiber regeneration? *J Neuropathol Exp Neurol* 2004;63:919-31.
- [50] Kern H, Rossini K, Carraro U, et al. Muscle biopsies show that FES of denervated muscles reverses human muscle degeneration from permanent spinal motoneuron lesion. *J Rehabil Res Dev* 2005;42:43-53.
- [51] Boncompagni S, Kern H, Rossini K, et al. Structural differentiation of skeletal muscle fibers in the absence of innervation in humans. *Proc Natl Acad Sci USA* 2007;104:19339-44.
- [52] Kern H, Hofer C, Mayr W. Protocols for clinical work package of the European project RISE. *Eur J Transl Myol - Basic Appl Myol* 2008;18:39-44.
- [53] Kern H, Carraro U, Adami N, et al. One year of home-based Functional Electrical Stimulation (FES) in complete lower motor neuron paraplegia: Recovery of tetanic contractility drives the structural improvements of denervated muscle. *Neurol Res* 2010;32:5-12,doi: 10.1189/ 184313209 X385644.

- [54] Kern H, Carraro U, Adami N, et al. Home-based functional electrical stimulation rescues permanently denervated muscles in paraplegic patients with complete lower motor neuron lesion. *Neurorehabil Neural Repair* 2010;24:709-21. doi: 10.1177/1545968310366129. Epub 2010 May 11.
- [55] Rossini K, Zanin ME, Carraro U. To stage and quantify regenerative myogenesis in human long-term permanent denervated muscle. *Basic Appl Myol* 2002;12:277-87.
- [56] Carraro U, Rossini K, Mayr W, Kern H. Muscle fiber regeneration in human permanent lower motoneuron denervation: relevance to safety and effectiveness of FES-training, which induces muscle recovery in SCI subjects. *Artif Organs* 2005;29:187-91.
- [49] Reinders, I., Murphy, R. A., ... Brouwer, I. A. (2016). Muscle Quality and Myosteatosis: Novel Associations With Mortality RiskThe Age, Gene/Environment Susceptibility (AGES)-Reykjavik Study. *American Journal of Epidemiology*, 183(1), 53.
- [50] Maughan RJ, Watson JS, Weir J. Strength and cross-sectional area of human skeletal muscle. *J Physiol.* 1983;338:37-49.
- [51] Lafortuna CL, Tresoldi D, Rizzo G. Influence of body adiposity on structural characteristics of skeletal muscle in men and women. *Clin Physiol Funct Imaging.* 2014;34:47-55.
- [52] Zierath JR, Hawley JA. Skeletal muscle fiber type: influence on contractile and metabolic properties. *PLoS Biol.* 2004;2:e348. doi: 10.1371/journal.pbio.0020348.
- [53] Wilson, J. M., Loenneke, J. P., Jo, E., Wilson, G. J., Zourdos, M. C., & Kim, J.-S. (2012). The effects of endurance, strength, and power training on muscle fiber type shifting. *Journal of Strength and Conditioning Research / National Strength & Conditioning Association*, 26(49), 1724-9.
- [54] Van Wessel T, de Haan A, van der Laarse WJ, Jaspers RT. The muscle fiber type-fiber size paradox: hypertrophy or oxidative metabolism? *Eur J Appl Physiol.* 2010;110:665-694. doi: 10.1007/s00421-010-1545-0.
- [55] Verdijk LB, Snijders T, Beelen M, Savelberg HHCM, Meijer K, Kuipers H, Van Loon LJC. Characteristics of muscle fiber type are predictive of skeletal muscle mass and strength in elderly men. *J Am Geriatr Soc.* 2010;58:2069-2075.
- [56] Grimby G, Aniansson A, Zetterberg C, Saltin B. Is there a change in relative muscle fibre composition with age? *Clin Physiol.* 1984;4:189-194.
- [57] Trappe S, Gallagher P, Harber M, Carrithers J, Fluckey J, Trappe T. Single muscle fibre contractile properties in young and old men and women. *J Physiol.* 2003;552(Pt 1):47-58.
- [58] D'Antona G, Pellegrino MA, Adami R, Rossi R, Carlizzi CN, Canepari M, Saltin B, Bottinelli R. The effect of ageing and immobilization on structure and function of human skeletal muscle fibres. *J Physiol.* 2003;552(Pt 2):499-511.
- [59] Reid KF, Pasha E, Doros G, Clark DJ, Patten C, Phillips EM, Frontera WR, Fielding RA. Longitudinal decline of lower extremity muscle power in healthy and mobility-limited older adults: influence of muscle mass, strength, composition, neuromuscular activation and single fiber contractile properties. *Eur J Appl Physiol.* 2014;114:29-39.

- [60] Romanick M, Brown-Borg HM. Murine models of atrophy, cachexia, and sarcopenia in skeletal muscle. *Biochimica et biophysica acta*. 2013;1832(9):1410-1420.
- [61] D'Adda di Fagagna F, Hande MP, Tong WM, Roth D, Lansdorp PM, Wang ZQ, Jackson SP. Effects of DNA nonhomologous end-joining factors on telomere length and chromosomal stability in mammalian cells. *Curr Biol*. 2001;11:1192–1196.
- [62] Nussenzweig A, Chen C, da Costa Soares V, Sanchez M, Sokol K, Nussenzweig MC, Li GC. Requirement for Ku80 in growth and immunoglobulin V(D)J recombination. *Nature*. 1996;382:551–555.
- [63] Didier N, Hourdé C, Amthor H, Marazzi G, Sassoon D. Loss of a single allele for Ku80 leads to progenitor dysfunction and accelerated aging in skeletal muscle. *EMBO Mol Med*. 2012;4:910–923.
- [64] Pugh TD, Conklin MW, Evans TD, Polewski MA, Barbian HJ, Pass R, Anderson BD, Colman RJ, Eliceiri KW, Keely PJ, Weindruch R, Beasley TM, Anderson RM. A shift in energy metabolism anticipates the onset of sarcopenia in rhesus monkeys. *Aging Cell*. 2013;12:672–681.
- [65] Narici MV, Maffulli N. Sarcopenia: characteristics, mechanisms and functional significance. *Br Med Bull*. 2010;95:139–159.
- [66] Ohira Y, Jiang B, Roy RR, Oganov V, Ilyina-Kakueva E, Marini JF, Edgerton VR. Rat soleus muscle fiber responses to 14 days of spaceflight and hindlimb suspension. *J Appl Physiol*. 1992;73:51S–57S.
- [67] Zhang P, Chen X, Fan M. Signaling mechanisms involved in disuse muscle atrophy. *Med Hypothesis*. 2007;69:310–321.
- [68] Buford TW, Anton SD, Judge AR, et al. Models of Accelerated Sarcopenia: Critical Pieces for Solving the Puzzle of Age-Related Muscle Atrophy. *Ageing research reviews*. 2010;9(4):369-383.
- [69] Stenroth L, Peltonen J, Cronin NJ, Sipilä S, Finni T. Age-related differences in Achilles tendon properties and triceps surae muscle architecture in vivo. *J Appl Physiol*. 2012;113:1537–1544.
- [70] Kawakami Y, Akima H, Kubo K, Muraoka Y, Hasegawa H, Kouzaki M, Imai M, Suzuki Y, Gunji A, Kanehisa H, Fukunaga T. Changes in muscle size, architecture, and neural activation after 20 days of bed rest with and without resistance exercise. *Eur J Appl Physiol*. 2001;84:7–12.
- [71] Edmunds, K. J., & Gargiulo, P. (2015). Imaging Approaches in Functional Assessment of Implantable Myogenic Biomaterials and Engineered Muscle Tissue. *European Journal of Translational Myology*, 25(2), 4847.
- [72] Mann CJ, Perdiguero E, Kharraz Y, Aguilar S, Pessina P, Serrano AL, Muñoz-Cánoves P. Aberrant repair and fibrosis development in skeletal muscle. *Skelet Muscle*. 2011;1:21.
- [73] Do G-M, Oh HY, Kwon E-Y, Cho Y-Y, Shin S-K, Park H-J, Jeon S-M, Kim E, Hur C-G, Park T-S, Sung M-K, McGregor RA, Choi M-S. Long-term adaptation of global transcription and metabolism in the liver of high-fat diet-fed C57BL/6 J mice. *Mol Nutr Food Res*. 2011;55:173–185.

- [74] Kwon E-Y, Shin S-K, Cho Y-Y, Jung UJ, Kim E, Park T, Park JHY, Yun JW, McGregor RA, Park YB, Choi M-S. Time-course microarrays reveal early activation of the immune transcriptome and adipokine dysregulation leads to fibrosis in visceral adipose depots during diet-induced obesity. *BMC Genomics*. 2012;13:450.
- [75] Brack AS, Conboy MJ, Roy S, Lee M, Kuo CJ, Keller C, Rando TA. Increased Wnt signaling during aging alters muscle stem cell fate and increases fibrosis. *Science*. 2007;317:807–810.
- [76] Fleg JL, Morrell CH, Bos AG, Brant LJ, Talbot LA, Wright JG, Lakatta EG. Accelerated longitudinal decline of aerobic capacity in healthy older adults. *Circulation*. 2005;112:674–682.
- [77] Short KR, Bigelow ML, Kahl J, Singh R, Coenen-Schimke J, Raghavakaimal S, Nair KS. Decline in skeletal muscle mitochondrial function with aging in humans. *Proc Natl Acad Sci*. 2005;102:5618–5623.
- [78] Fiser WM, Hays NP, Rogers SC, Kajkenova O, Williams AE, Evans CM, Evans WJ. Energetics of walking in elderly people: factors related to gait speed. *J Gerontol A Biol Sci Med Sci*. 2010;65:1332–1337.
- [79] Coen PM, Jubrias SA, Distefano G, Amati F, Mackey DC, Glynn NW, Manini TM, Wohlgenuth SE, Leeuwenburgh C, Cummings SR, Newman AB, Ferrucci L, Toledo FGS, Shankland E, Conley KE, Goodpaster BH. Skeletal muscle mitochondrial energetics are associated with maximal aerobic capacity and walking speed in older adults. *J Gerontol A Biol Sci Med Sci*. 2013;68:447–455.
- [80] Bijlsma AY, Meskers CGM, van Heemst D, Westendorp RGJ, de Craen AJM, Maier AB. Diagnostic criteria for sarcopenia relate differently to insulin resistance. *Age*. 2013;35:2367–2375.
- [81] Abbatecola AM, Ferrucci L, Ceda G, Russo CR, Lauretani F, Bandinelli S, Barbieri M, Valenti G, Paolisso G. Insulin resistance and muscle strength in older persons. *J Gerontol A Biol Sci Med Sci*. 2005;60:1278–1282.
- [82] Kuo C-K, Lin L-Y, Yu Y-H, Wu K-H, Kuo H-K. Inverse association between insulin resistance and gait speed in nondiabetic older men: results from the U.S. National Health and Nutrition Examination Survey (NHANES) 1999-2002. *BMC Geriatr*. 2009;9:49.
- [83] Carraro, U., Kern, H., Gava, P., Hofer, C., Loeffler, S., Gargiulo, P., ... Mosole, S. (2016). Recovery from muscle weakness by exercise and FES: lessons from Masters, active or sedentary seniors and SCI patients. *Aging Clinical and Experimental Research*.
- [84] Ferrara CM, Goldberg AP, Ortmeier HK, Ryan AS. Effects of aerobic and resistive exercise training on glucose disposal and skeletal muscle metabolism in older men. *J Gerontol A Biol Sci Med Sci*. 2006;61:480–487.
- [85] Scott D., de Courten B., Ebeling P.R. (2016). Sarcopenia: a potential cause and consequence of type 2 diabetes in Australia's ageing population? *Med J Aust*. 2016 Oct 3;205(7):329-33.
- [86] Addison O., Marcus RL, Lastayo PC et al. Intermuscular fat: a review of the consequences and causes. *Int J Endocrinol* . 2014;2014:309570.
- [87] Marcus RL, Addison O, Dibble LE, Foreman KB, Morrell G, Lastayo P. Intramuscular adipose tissue, sarcopenia, and mobility function in older individuals. *J Aging Res*. 2012;2012:629637.

- [88] Kumar V, Gu Y, Basu S, Berglund A, Eschrich SA, Schabath MB, et al. Radiomics: the process and the challenges. *Magnetic resonance imaging*. 2012;30(9):1234-48.
- [89] Häkkinen K, Kraemer WJ, Kallinen M, Linnamo V, Pastinen UM, Newton RU. Bilateral and unilateral neuromuscular function and muscle cross-sectional area in middle-aged and elderly men and women. *J Gerontol A Biol Sci Med Sci*. 1996;51:B21–B29.
- [90] McNeil CJ, Doherty TJ, Stashuk DW, Rice CL. Motor unit number estimates in the tibialis anterior muscle of young, old, and very old men. *Muscle Nerve*. 2005;31:461–467.
- [91] Larsson L. Motor units: remodeling in aged animals. *J Gerontol A Biol Sci Med Sci*. 1995;50:91–95
- [92] Kung TA, Cederna PS, van der Meulen JH, Urbanchek MG, Kuzon WM, Faulkner JA. Motor Unit Changes Seen With Skeletal Muscle Sarcopenia in Oldest Old Rats. *The Journals of Gerontology Series A: Biological Sciences and Medical Sciences*. 2014;69(6):657-665
- [93] Hill AV. The physiological basis of athletic records. *The Scientific Monthly* 1925;2:409-28.
- [94] Gava P, Kern H, Carraro U. Age-associated power decline from running, jumping, and throwing male masters world records. *Exp Aging Res* 2015;41:115-35
- [95] Mosole S, Rossini K, Kern H, et al. Significant increase of vastus lateralis reinnervation in 70-year sportsmen with a lifelong history of high-level exercise. *Eur J Transl Myol - Basic Appl Myol* 2013;23:117-22.
- [96] Mosole S, Carraro U, Kern H, et al. Long-term high-level exercise promotes muscle reinnervation with age. *J Neuropathol Exp Neurol* 2014;73:284-94.
- [97] Stålberg E, Fawcett PR. Macro EMG in healthy subjects of different ages. *J Neurol Neurosurg Psychiatry* 1982;45:870–8.
- [98] Doherty TJ. Invited review: aging and sarcopenia. *J Appl Physiol* 2003;95:1717–27.
- [99] Lexell J, Downham DY. The occurrence of fibre-type grouping in healthy human muscle: a quantitative study of cross-sections of whole vastus lateralis from men between 15 and 83 years. *Acta Neuropathol* 1991;81:377–81.
- [100] Ling SM, Conwit RA, Ferrucci L, Metter EJ. Age-associated changes in motor unit physiology: observations from the Baltimore Longitudinal Study of Aging. *Arch Phys Med Rehabil* 2009;90:1237–40.
- [101] Lexell J, Taylor CC, Sjostrom M. What is the cause of ageing atrophy? Total number, size and proportion of different fiber types studied in whole vastus lateralis muscle from 15- to 83-year-old men. *J Neurol Sci* 1988;84:275–94.
- [102] Doherty TJ, Vandervoort AA, Taylor AW, Brown WF. Effects of motor unit losses on strength in older men and women. *J Appl Physiol* (1985). 1993;74:868–74.
- [103] Payne AM, Delbono O. Neurogenesis of excitation-contraction uncoupling in aging skeletal muscle. *Exerc Sport Sci Rev* 2004;32:36–40.
- [104] Delbono O. Neural control of aging skeletal muscle. *Aging Cell* 2003;2:21–9.
- [105] Zampieri S, Pietrangelo L, Loeffler S, et al. Lifelong Physical Exercise Delays Age-Associated Skeletal Muscle Decline. *J Gerontol A Biol Sci Med Sci* 2015;70:163-73.

- [106] Messi ML, Li T, Wang ZM, Marsh AP, Nicklas B, Delbono O. Resistance training enhances skeletal muscle innervation without modifying the number of satellite cells or their myofiber association in obese older adults. *J Gerontol A Biol Sci Med Sci* 2015 Oct 7. pii: glv176.
- [107] Dow DE, Dennis RG, Faulkner JA. Electrical stimulation attenuates denervation and age-related atrophy in extensor digitorum longus muscles of old rats. *J Gerontol A Biol Sci Med Sci* 2005;60:416-24.
- [108] Hennig R, Lømo T. Firing patterns of motor units in normal rats. *Nature* 1985;314:164-6.
- [109] Lomo T. The response of denervated muscle to long-term stimulation (1985, revisited here in 2014). *Eur J Transl Myol - Basic Appl Myol* 2014;24:13-9.
- [110] Crane JD, MacNeil LG, Tarnopolsky MA. Long-term aerobic exercise is associated with greater muscle strength throughout the life span. *J Gerontol A Biol Sci Med Sci*. 2013;68:631–638.
- [111] Valeria, Z., Renato, G., Luisa, C., Bruno, V., & Matteo, Z. M. and C. (2014). Interventions Against Sarcopenia in Older Persons. *Current Pharmaceutical Design*
- [112] Anton, S. D., Hida, A., Mankowski, R., Layne, A., Solberg, L., & Buford, A. G. M. and T. W. (2016). Nutrition and Exercise in Sarcopenia. *Current Protein & Peptide Science*
- [113] Cruz-Jentoft, A. J., Baeyens, J. P., Bauer, J. M., Boirie, Y., Cederholm, T., Landi, F., ... Zamboni, M. (2010). Sarcopenia: European consensus on definition and diagnosis. *Age and Ageing*, 39(4), 412–423.
- [114] Zampieri S, Mosole S, Löfler S, et al. Physical exercise in Aging: Nine weeks of leg press or electrical stimulation training in 70 years old sedentary elderly people. *Eur J Transl Myol - Basic Appl Myol* 2015;25:237-42.
- [115] Kern H, Barberi L, Löfler S. et al. Electrical stimulation counteracts muscle decline in seniors. *Front Aging Neurosci*. 2014; 6:189.
- [116] Carnio S, LoVerso F, Baraibar MA, Longa E, Khan MM, Maffei M, Reischl M, Canepari M, Loeffler S, Kern H, Blaauw B, Friguet B, Bottinelli R, Rudolf R, Sandri M. Autophagy impairment in muscle induces neuromuscular junction degeneration and precocious aging. *Cell Rep* 2014;8:1509-21.
- [117] Barberi L, Scicchitano BM, Musaro A. Molecular and cellular mechanisms of muscle aging and sarcopenia and effects of electrical stimulation in seniors. *Eur J Transl Myol - Basic Appl Myol* 2015;25:231-6.
- [118] Scicchitano BM, Rizzuto E, Musarò A. Counteracting muscle wasting in aging and neuromuscular diseases: the critical role of IGF-1. *Aging* 2009; 451-7.
- [119] Vinciguerra M, Musaro A, Rosenthal N. Regulation of muscle atrophy in aging and disease. *Adv Exp Med Biol* 2010; 694:211-33.
- [120] Carosio S, Berardinelli MG, Aucello M, Musarò A. Impact of ageing on muscle cell regeneration. *Ageing Res Rev* 2011;10:35-42.
- [121] Barberi L, Scicchitano BM, De Rossi M, et al. Age-dependent alteration in muscle regeneration: the critical role of tissue niche. *Biogerontology*. 2013; 14:273-92.
- [122] Carraro U, Franceschi C. Apoptosis of skeletal and cardiac muscles and physical exercise. *Aging (Milano)*. 1997 Feb-Apr;9(1-2):19-34. Review.



- [123] Musarò A. The Basis of Muscle Regeneration. *Advances in Biology* 2014, 2014: 1-16.
- [124] Snijders T, Verdijk LB, van Loon LJ. The impact of sarcopenia and exercise training on skeletal muscle satellite cells. *Ageing Res. Rev.* 2009; 8: 328-38.
- [125] Mikkelsen UR, Langberg H, Helmark IC. et al. Local NSAID infusion inhibits satellite cell proliferation in human skeletal muscle after eccentric exercise. *Journal of applied physiology* 2009; 107: 1600-11.
- [126] Farup J, Rahbek SK, Riis S. et al. Influence of exercise contraction mode and protein supplementation on human skeletal muscle satellite cell content and muscle fiber growth. *Journal of applied physiology (Bethesda, Md :1985)* 2014; 117: 898-909.
- [127] Farup J, Rahbek SK, Knudsen IS. et al. Whey protein supplementation accelerates satellite cell proliferation during recovery from eccentric exercise. *Amino Acids* 2014; 46: 2503-16.
- [128] McKay BR, Ogborn DI, Bellamy LM. et al. Myostatin is associated with age related human muscle stem cell dysfunction. *FASEB J.* 2012; 26: 2509-21.
- [129] McPherron AC, Lawler AM, Lee SJ. Regulation of skeletal muscle mass in mice by a new TGF-beta superfamily member. *Nature* 1997;387:83-90.
- [130] Sandri M, Barberi L, Bijlsma AY. et al. Signalling pathways regulating muscle mass in ageing skeletal muscle: the role of the IGF1-Akt- mTOR-FoxO pathway. *Biogerontology* 2013;14:303-23.
- [131] Kadi F, Schjerling P, Andersen LL. et al. The effects of heavy resistance training and detraining on satellite cells in human skeletal muscles. *Physiol J* 2004; 558:1005-12.
- [132] Mackey AL, Holm L, Reitelseder S. et al. Myogenic response of human skeletal muscle to 12 weeks of resistance training at light loading intensity. *Scand J Med Sci Sports* 2010;21:773-82.
- [133] Adamo ML, Farrar RP. Resistance training, and IGF involvement in the maintenance of muscle mass during the aging process. *Ageing Res Rev* 2006;5:310-31. Epub 2006 Sep 1.
- [134] Wallace JD, Cuneo RC, Baxter R. et al. Responses of the growth hormone (GH) and insulin-like growth factor axis to exercise, GH administration, and GH withdrawal in trained adult males: A potential test for GH abuse in sport. *J Clin Endocrinol Metab.* 1999; 84:3591-601.
- [135] Kostka T, Patricot MC, Mathian B. et al. Anabolic and catabolic hormonal responses to experimental two-set low- volume resistance exercise in sedentary and active elderly people. *Aging Clin Exp Res* 2003; 15:123-30.
- [136] Berg U, Bang P. Exercise and circulating insulin-like growth factor I. *Horm Res.* 2004; 62: 50-8.
- [137] Kern H, Pelosi L, Coletto L, et al. Atrophy/hypertrophy cell signaling in muscles of young athletes trained with vibrational-proprioceptive stimulation. *Neurol Res* 2011;33:998-1009.
- [138] Sandri M, Barberi L, Bijlsma AY. et al. Signalling pathways regulating muscle mass in ageing skeletal muscle: the role of the IGF1-Akt- mTOR-FoxO pathway. *Biogerontology* 2013;14:303-23.

- [139] Pelosi L, Berardinelli MG, De Pasquale L. Functional and Morphological Improvement of Dystrophic Muscle by Interleukin 6 Receptor Blockade. *EBioMedicine* 2015; 2: 274-5.
- [140] Prior SJ, Joseph LJ, Brandauer J, Katzel LI, Hagberg JM, Ryan AS. Reduction in midhigh low-density muscle with aerobic exercise training and weight loss impacts glucose tolerance in older men. *J Clin Endocrinol Metab.* 2007;92:880–886.
- [141] Manini TM, Clark BC, Nalls MA, Goodpaster BH, Ploutz-Snyder LL, Harris TB. Reduced physical activity increases intermuscular adipose tissue in healthy young adults. *Am J Clin Nutr.* 2007;85:377–384.
- [142] Seynnes OR, de Boer M, Narici MV. Early skeletal muscle hypertrophy and architectural changes in response to high-intensity resistance training. *J Appl Physiol.* 2007;102:368–373.
- [143] Snijders T, Nederveen JP, Joannisse S, et al. Muscle fibre capillarization is a critical factor in muscle fibre hypertrophy during resistance exercise training in older men. *Journal of Cachexia, Sarcopenia and Muscle.* 2017;8(2):267-276.
- [144] Hepple RT, Rice CL. Innervation and neuromuscular control in ageing skeletal muscle. *J Physiol* 2015 Oct 6.
- [145] Krenn M, Haller M, Bijak M, et al. Safe neuromuscular electrical stimulator designed for the elderly. *Artif. Organs* 2011; 35:253-6.
- [146] Sarabon N, Löfler S, Hosszu G, Hofer Ch. Mobility test protocols for the elderly: a methodological note. *Eur J Transl Myol - Basic Appl Myol* 2015;25:253-6.
- [147] He Y, Huang C, Lin X, Li J. MicroRNA-29 family, a crucial therapeutic target for fibrosis diseases. *Biochimie* 2013; 95:1355–1359.
- [148] Kern H, Carraro U. Home-based Functional Electrical Stimulation (h-b FES) for long-term denervated human muscle: History, basics, results and perspectives of the Vienna Rehabilitation Strategy. *Eur J Transl Myol/.*
- [149] Kern H, Hofer C, Strohhofer M, et al. Standing up with denervated muscles in humans using functional electrical stimulation. *Artif Organs* 1999; 23: 447–452
- [150] Mayr W, Bijak M, Rafolt D, et al. Basic design and construction of the Vienna FES implants: Existing solutions and prospects for new generations of implants. *Med Eng Phys* 2001; 23: 53–60
- [151] Hofer C, Mayr W, Stöhr H, Unger E, Kern H. A stimulator for functional activation of denervated muscles. *Artif Organs* 2002;26:276–9.
- [152] Kern H, Hofer C, Modlin M, et al. Denervated muscles in humans: Limitations and problems of currently used functional electrical stimulation training protocols. *Artif Organs* 2002; 26: 216–218
- [153] Kern H, Boncompagni S, Rossini K, et al. Long-term denervation in humans causes degeneration of both contractile and excitation-contraction coupling apparatus that can be reversed by functional electrical stimulation (FES). A role for myofiber regeneration? *J Neuropath Exp Neurol* 2004;63:919–931.
- [154] Kern H, Hofer C, Mayr W, et al. European Project RISE: Partners, protocols, demography. *Basic Appl Myol/ European Journal of Translational Myology* 2009;19:211-216.

- [155] Gargiulo P, Vatnsdal B, Ingvarsson P, et al. Restoration of muscle volume and shape induced by electrical stimulation of denervated degenerated muscles: qualitative and quantitative measurement of changes in rectus femoris using computer tomography and image segmentation. *Artif Organs* 2008;32:609–613.
- [156] Gargiulo P, Vatnsdal B, Ingvarsson P, et al. Computational methods to analyse tissue composition and structural changes in denervated muscle undergoing therapeutic electrical stimulation. *Basic Appl Myol/ European Journal of Translational Myology* 2009;19:157-162.
- [157] Gargiulo P, Kern H, Carraro U, et al. Quantitative colour 3D CT imaging of human long-term denervated muscle. Progression to fibrosis of perimysium and a case report of FES recovery. *Neurol Res* 2010; 32 (1) 13-19.
- [158] Kern H, Carraro U, Adami N, Biral D, Hofer C, Forstner C, Mödlin M, Vogelauer M, Boncompagni S, Paolini C, Mayr W, Protasi F, Zampieri S. Home-based Functional Electrical Stimulation (h-bFES) recovers permanently denervated muscles in paraplegic patients with complete lower motor neuron lesion. *Neurorehab Neur Rep* 2010;24:709-21.
- [159] Kern H, Carraro U, Adami N, et al. One year of home-based Functional Electrical Stimulation (FES) in complete lower motor neuron paraplegia: Recovery of tetanic contractility drives the structural improvements of denervated muscle. *Neurol Res* 2010; 32 (1) 5-12.
- [160] Kern H, Hofer C, Mayr W. Protocols for Clinical Work Package of the European Project RISE. *Basic Appl Myol/European Journal of Translational Myology* 2008;18:39–44.
- [161] Hamar D. Universal linear motor driven Leg Press Dynamometer and concept of Serial Stretch Loading. *Eur J Transl Myol - Basic Appl Myol* 2015;25:215-9.
- [162] Cvecka J, Tirpakova V, Sedliak M, Kern H, Mayr W, Hamar D. Physical activity in elderly. *Eur J Transl Myol - Basic Appl Myol* 2015;25:249-52.
- [163] Kern H, Hofer C, Mödlin M, et al. Stable muscle atrophy in long-term paraplegics with complete upper motor neuron lesion from 3- to 20-year SCI. *Spinal Cord* 2008;46:293-304.
- [164] Eberstein A1, Eberstein S. Electrical stimulation of denervated muscle: is it worthwhile? *Med Sci Sports Exerc* 1996;28:1463-9.
- [165] Salmons S, Ashley Z, Sutherland H, Russold MF, Li F, Jarvis JC. Functional electrical stimulation of denervated muscles: basic issues. *Artif Organs* 2005;29:199-202.
- [166] Carraro U, Boncompagni S, Gobbo V, et al. Persistent muscle fiber regeneration in long term denervation. Past, present, future. *Eur J Transl Myol- Basic Appl Myol* 2015;25:77-92.
- [167] Brown MC, Holland RL. A central role for denervated tissues in causing nerve sprouting. *Nature* 1979;282(5740):724-6.
- [168] Nishimune H, Stanford JA, Mori Y. Role of exercise in maintaining the integrity of the neuromuscular junction. *Muscle Nerve* 2014; 49: 315–24. Published online 2013 Dec 17.

- [169] Eberstein A, Pachter BR. The effect of electrical stimulation on reinnervation of rat muscle: contractile properties and endplate morphometry. *Brain Res* 1986;384:304-10.
- [170] Bian W, Bursac N. Tissue engineering of functional skeletal muscle: challenges and recent advances. *IEEE Eng Med Biol Mag.* 2008 Sep-Oct;27(5):109-13
- [171] Alsberg E, Hill EE, Mooney DJ. Craniofacial tissue engineering. *Crit Rev Oral Biol Med.* 2001;12:64-75
- [172] Bach AD, Beier JP, Stern-Staeter J, Horch RE. Skeletal muscle tissue engineering. *J Cell Mol Med.* 2004 Oct./Dec.8:413-422
- [173] Morgan KY, Black LD III. Investigation into the effects of varying frequency of mechanical stimulation in a cycle-by-cycle manner on engineered cardiac construct function. *J Tissue Eng Regen Med.* 2014 Jun 11
- [174] Bach AD, Beier JP, Stern-Staeter J, Horch RE. Skeletal muscle tissue engineering. *J Cell Mol Med.* 2004 Oct-Dec;8(4):413-22
- [175] DiEdwardo CA, Petrosko P, Acarturk TO, Di Milla PA, LaFramboise WA, Johnson PC. Muscle tissue engineering. *Clin Plast Surg.* 1999;26:647-656
- [176] Vilquin JT. Myoblast transplantation: Clinical trials and perspectives. A mini review. *Acta Myol.* 2005 Oct.24:119-127
- [177] Mouly V, Aamiri A, Perie S, Mamchaoui K, Barani A, Bigot A, Bouazza B, Francois V, Furling D, Jacquemin V, Negroni E, Riederer I, Vignaud A, Guily JL, Butler-Browne GS. Myoblast transfer therapy: Is there any light at the end of the tunnel? *Acta Myol.* 2005 Oct.24:128-133
- [178] Vandeburgh HH. Functional assessment and tissue design of skeletal muscle. *Ann NY Acad Sci.* 2002;961:201-202
- [179] Law PK, Goodwin TG, Fang Q, Deering MB, Duggirala V, Larkin C, et al. Cell transplantation as an experimental treatment for Duchenne muscular dystrophy. *Cell Transplant.* 1993;2:485-505
- [180] Urish K, Kanda Y, Huard J. Initial failure in myoblast transplantation therapy has led the way toward the isolation of muscle stem cells: Potential for tissue regeneration. *Curr Top Dev Biol.* 2005;68:263-280
- [181] Qu Z, Balkir L, van Deutekom JC, Robbins PD, Pruchnic R, Huard J. Development of approaches to improve cell survival in myoblast transfer therapy. *J Cell Biol.* 1998 Sept.14 2:1257-1267
- [182] Pancrazio JJ, Wang F, Kelley CA. Enabling tools for tissue engineering. *Biosens Bioelectron.* 2007 Jun 15;22(12):2803-11
- [183] Assmann A, Akhyari P, Delfs C, Flogel U, Jacoby C, Kamiya H, et al. Development of a growing rat model for the in vivo assessment of engineered aortic conduits. *J Surg Res.*2012;176:367-75
- [184] Williams C, Quinn KP, Georgakoudi I, Black LD III. Young developmental age cardiac extracellular matrix promotes the expansion of neonatal cardiomyocytes in vitro. *Acta Biomater.* 2014 Jan;10(1):194-204 3.
- [185] Van Meerloo J, et al. "Cell sensitivity assays: the MTT assay." *Methods Mol Biol* 2011. 731:237-45

- [186] Chemaly ER, Yoneyama R, Frangioni JV, Hajar RJ. Tracking stem cells in the cardiovascular system. *Trends Cardiovasc Med*. 2005 Nov;15(8):297-302
- [187] AM Morawski, GA Lanza, SA Wickline. Targeted contrast agents for magnetic resonance imaging and ultrasound. *Curr. Opin. Biotechnol.*, 16 (2005), pp. 89–92
- [188] Martin Y, Vermette P. Bioreactors for tissue mass culture: design, characterization, and recent advances. *Biomaterials*. 2005 Dec;26(35):7481-503
- [189] de Boer J, van Blitterswijk C, Löwik C. Bioluminescent imaging: emerging technology for non-invasive imaging of bone tissue engineering. *Biomaterials*. 2006 Mar;27(9):1851-8. Epub 2005 Oct 20
- [190] Stringari C, Cinquin A, Cinquin O, Digman MA, Donovan PJ, Gratton E. Phasor approach to fluorescence lifetime microscopy distinguishes different metabolic states of germ cells in a live tissue. *Proc Natl Acad Sci U S A*. 2011 Aug 16;108(33):13582-7
- [191] Kasischke KA, Vishwasrao HD, Fisher PJ, Zipfel WR, Webb WW. Neural activity triggers neuronal oxidative metabolism followed by astrocytic glycolysis. *Science*. 2004;305(5680):99–103
- [192] Skala MC, et al. In vivo multiphoton microscopy of NADH and FAD redox states, fluorescence lifetimes, and cellular morphology in precancerous epithelia. *Proc Natl Acad Sci USA*. 2007;104:19494–19499
- [193] König K, Uchugonova A, Gorjup E. Multiphoton fluorescence lifetime imaging of 3D-stem cell spheroids during differentiation. *Microsc Res Tech*. 2011;74(1):9–17
- [194] Bird DK, et al. Metabolic mapping of MCF10A human breast cells via multiphoton fluorescence lifetime imaging of the coenzyme NADH. *Cancer Res*. 2005;65:8766–8773
- [195] Uchugonova A, König K. Two-photon autofluorescence and second-harmonic imaging of adult stem cells. *J Biomed Opt*. 2008;13:054068
- [196] Guo HW, et al. Reduced nicotinamide adenine dinucleotide fluorescence lifetime separates human mesenchymal stem cells from differentiated progenies. *J Biomed Opt*. 2008;13:050505
- [197] Rice WL, Kaplan DL, Georgakoudi I. Two-photon microscopy for non-invasive, quantitative monitoring of stem cell differentiation. *PLoS ONE*. 2010;5:e10075
- [198] Kantelhardt SR, et al. Imaging of brain and brain tumor specimens by time-resolved multiphoton excitation microscopy ex vivo. *Neuro-oncol*. 2007;9(2):103–112
- [199] Multi-agency tissue engineering science: a foundation for the future. *Advancing tissue science and engineering: a multi-agency strategic plan*. Jun, 2007
- [200] Chance B, Baltscheffsky H. Respiratory enzymes in oxidative phosphorylation. VII. binding of intramitochondrial reduced pyridine nucleotide. *J Biol Chem*. 1958;233:736–739
- [201] Chance B, Oshino N, Sugano T, Mayevsky A. Basic principles of tissue oxygen determination from mitochondrial signals. *Adv Exp Med Biol*. 1973;37A:277–292
- [202] Chance B, Lieberman M. Intrinsic fluorescence emission from the cornea at low temperatures: Evidence of mitochondrial signals and their differing redox states in epithelial and endothelial sides. *Exp Eye Res*. 1978;26:111–117

- [203] Mayevsky A, Rogatsky GG. Mitochondrial function in vivo evaluated by NADH fluorescence: From animal models to human studies. *Am J Physiol Cell Physiol*. 2007;292:C615–C640
- [204] Vergen J, Hecht C, Zholudeva LV, Marquardt MM, Hallworth R, Nichols MG. Metabolic imaging using two-photon excited NADH intensity and fluorescence lifetime imaging. *Microsc Microanal*. 2012 Aug;18(4):761-70
- [205] Skala M, Ramanujam N. Multiphoton redox ratio imaging for metabolic monitoring in vivo. *Methods Mol Biol*. 2010;594:155-62
- [206] Smith J, Ladi E, Mayer-Proschel M, Noble M. Redox state is a central modulator of the balance between self-renewal and differentiation in a dividing glial precursor cell. *Proc Natl Acad Sci USA*. 2000;97:10032–10037
- [207] Skala MC, et al. In vivo multiphoton microscopy of NADH and FAD redox states, fluorescence lifetimes, and cellular morphology in precancerous epithelia. *Proc Natl Acad Sci USA*. 2007;104:19494–19499
- [208] Georgakoudi I, Quinn KP. Optical imaging using endogenous contrast to assess metabolic state. *Annu Rev Biomed Eng*. 2012;14:351-67
- [209] Quinn KP, Sridharan GV, Hayden RS, Kaplan DL, Lee K, Georgakoudi I. Quantitative metabolic imaging using endogenous fluorescence to detect stem cell differentiation. *Sci Rep*. 2013 Dec 5;3:3432
- [210] Denk W, Strickler JH, Webb WW. Two-photon laser scanning fluorescence microscopy. *Science*. 1990;248:73–6
- [211] Huang S, Heikal AA, Webb WW. Two-photon fluorescence spectroscopy and microscopy of NAD(P)H and flavoprotein. *Biophys J*. 2002;82:2811–25
- [212] Squirrell JM, Wokosin DL, White JG, Bavister BD. Long-term two-photon fluorescence imaging of mammalian embryos without compromising viability. *Nat Biotechnol*. 1999;17:763–7
- [213] Zipfel WR, Williams RM, Christie R, Nikitin AY, Hyman BT, Webb WW. Live tissue intrinsic emission microscopy using multiphoton-excited native fluorescence and second harmonic generation. *Proc Natl Acad Sci U S A*. 2003;100:7075–7080
- [214] Blinova K, Combs C, Kellman P, Balaban RS. Fluctuation analysis of mitochondrial NADH fluorescence signals in confocal and two-photon microscopy images of living cardiac myocytes. *J Microsc*. 2004;213:70–75
- [215] An J, Camara AK, Rhodes SS, Riess ML, Stowe DF. Warm ischemic preconditioning improves mitochondrial redox balance during and after mild hypothermic ischemia in guinea pig isolated hearts. *Am J Physiol Heart Circ Physiol*. 2005;288:H2620–H2627
- [216] Rocheleau JV, Head WS, Piston DW. Quantitative NAD(P)H/flavoprotein autofluorescence imaging reveals metabolic mechanisms of pancreatic islet pyruvate response. *J Biol Chem*. 2004;279:31780–31787
- [217] Romashko DN, Marban E, O'Rourke B. Subcellular metabolic transients and mitochondrial redox waves in heart cells. *Proc Natl Acad Sci U S A*. 1998;95:1618–1623
- [218] Kasischke KA, Vishwasrao HD, Fisher PJ, Zipfel WR, Webb WW. Neural activity triggers neuronal oxidative metabolism followed by astrocytic glycolysis. *Science*. 2004;305:99–103

- [219] Vishwasrao HD, Heikal AA, Kasischke KA, Webb WW. Conformational dependence of intracellular NADH on metabolic state revealed by associated fluorescence anisotropy. *J Biol Chem*. 2005;280:25119–25126
- [220] Piston DW, Masters BR, Webb WW. Three-dimensionally resolved NAD(P)H cellular metabolic redox imaging of the in situ cornea with two-photon excitation laser scanning microscopy. *J Microsc*. 1995;178 ( Pt 1):20–27
- [221] Levene MJ, Dombeck DA, Kasischke KA, Molloy RP, Webb WW. In vivo multiphoton microscopy of deep brain tissue. *J Neurophysiol*. 2004;91:1908–1912
- [222] Wang LV, Hu S. Photoacoustic tomography: in vivo imaging from organelles to organs. *Science*. 2012;335:1458–62
- [223] Su JL, Wang B, Wilson KE, Bayer CL, Chen YS, Kim S, et al. Advances in clinical and biomedical applications of photoacoustic imaging. *Expert Opin Med Diagn*. 2010;4:497–510
- [224] Gamelin J, Maurudis A, Aguirre A, Huang F, Guo P, Wang LV, et al. A real-time photoacoustic tomography system for small animals. *Opt Express*. 2009;17:10489–98
- [225] Cai X, Zhang Y, Li L, Choi SW, MacEwan MR, Yao J, et al. Investigation of neovascularization in three-dimensional porous scaffolds in vivo by a combination of multiscale photoacoustic microscopy and optical coherence tomography. *Tissue Eng Part C Methods*. 2013;19:196–204
- [226] Cai X, Li L, Krumholz A, Guo Z, Erpelding TN, Zhang C, et al. Multi-scale molecular photoacoustic tomography of gene expression. *PloS ONE*. 2012;7:e43999
- [227] Jose J, Manohar S, Kolkman RG, Steenbergen W, van Leeuwen TG. Imaging of tumor vasculature using Twente photoacoustic systems. *J Biophotonics*. 2009;2:701–17
- [228] Siphanto RI, Thumma KK, Kolkman RG, van Leeuwen TG, de Mul FFM, van Neck JW, et al. Serial noninvasive photoacoustic imaging of neovascularization in tumor angiogenesis. *Opt Express*. 2005;13:89–95
- [229] Zhang Y, Cai X, Choi SW, Kim C, Wang LV, Xia Y. Chronic label-free volumetric photoacoustic microscopy of melanoma cells in three-dimensional porous scaffolds. *Biomaterials*. 2010;31:8651–8
- [230] Nam SY, Mallidi S, Zhang G, Suggs L, Emelianov S. Ultrasound and photoacoustic imaging to monitor vascular growth in tissue engineered constructs. *Proc SPIE*. 2009;7179
- [231] Pan D, Pramanik M, Senpan A, Allen JS, Zhang H, Wickline SA, et al. Molecular photoacoustic imaging of angiogenesis with integrin-targeted gold nano-beacons. *FASEB J*. 2011;25:875–82
- [232] Kim S, Chen YS, Luke GP, Emelianov SY. In vivo three-dimensional spectroscopic photoacoustic imaging for monitoring nanoparticle delivery. *Biomed Opt Express*. 2011;2:2540–50
- [233] Chung E, Nam SY, Ricles LM, Emelianov S, Suggs L. Evaluation of gold nanotracers to track adipose-derived stem cells in a pegylated fibrin gel for dermal tissue engineering applications. *Int J Nanomed*. 2013;8:325–36
- [234] Nam SY, Ricles LM, Suggs L, Emelianov SY. In vivo ultrasound and photo-acoustic monitoring of mesenchymal stem cells labeled with gold nanotracers. *PloS ONE*. 2012;7:e37267

- [235] Helmchen F, Denk W. Deep tissue two-photon microscopy. *Nat Methods*. 2005;2:932–940
- [236] Stringari, C., Sierra, R., Donovan, P. J. & Gratton, E. Label-free separation of human embryonic stem cells and their differentiating progenies by phasor fluorescence lifetime microscopy. *J Biomed Opt* 17 (4), 046012 (2012)
- [237] Konig, K., Uchugonova, A. & Gorjup, E. Multiphoton fluorescence lifetime imaging of 3D-stem cell spheroids during differentiation. *Microsc Res Tech* 74 (1), 9 (2011)
- [238] Yu, Q. & Heikal, A. A. Two-photon autofluorescence dynamics imaging reveals sensitivity of intracellular NADH concentration and conformation to cell physiology at the single-cell level. *J. Photochem. Photobiol. B* 95, 46–57 (2009).
- [239] Blacker TS, Mann ZF, Gale JE, Ziegler M, Bain AJ, Szabadkai G, Duchen MR. Separating NADH and NADPH fluorescence in live cells and tissues using FLIM. *Nat Commun*. 2014;May 29;5:3936
- [240] Zheng K, Rupnick MA, Liu B, Brezinski ME. Three dimensional OCT in the engineering of tissue constructs: a potentially powerful tool for assessing optimal scaffold structure. *Open Tissue Eng. Regen*. 2009;Med. 2, 8–13
- [241] Brezinski ME. Optical coherence tomography for identifying unstable coronary plaque. 2006; *Int. J. Cardiol.* 107, 154–165
- [242] Huang D et al. Optical coherence tomography. *Science* 1991;254, 1178–1180
- [243] Boppart S, Oldenburg A, Xu C, Marks D. Optical probes and techniques for molecular contrast enhancement in coherence imaging. *J. Biomed. Opt.* 2005;10, 41208
- [244] Liang X, Graf BW, Boppart SA. Imaging engineered tissues using structural and functional optical coherence tomography. *J Biophotonics*. 2009;2:643–55
- [245] Zheng K, Rupnick MA, Liu B, Brezinski ME. Three dimensional OCT in the engineering of tissue constructs: a potentially powerful tool for assessing optimal scaffold structure. *Open Tissue Eng Regen Med J*. 2009;2:8–13
- [246] Saidha S, Eckstein C, Ratchford J. Optical coherence tomography for the detection of axonal damage in multiple sclerosis. *Ophthalmology* 2010;20,77–88
- [247] Chen W-L, Huang C-H, Chiou L-L, Chen T-H, Huang Y-Y, Jiang C-C, Lee HS, Dong CY. Multiphoton imaging and quantitative analysis of collagen production by chondrogenic human mesenchymal stem cells cultured in chitosan scaffold. *Tissue Eng. C, Methods* 2010;16, 913–920
- [248] Smith LE, Smallwood R, Macneil S. A comparison of imaging methodologies for 3D tissue engineering. *Microsc. Res. Tech.* 2010;73, 1123–1133
- [249] Tan W, Oldenburg AL, Norman JJ, Desai TA, Boppart SA. Optical coherence tomography of cell dynamics in three-dimensional tissue models. *Opt Express*. 2006;14:7159–71
- [250] Xu X, Wang RK, El Haj A. Investigation of changes in optical attenuation of bone and neuronal cells in organ culture or three-dimensional constructs in vitro with optical coherence tomography: relevance to cytochrome oxidase monitoring. *Eur Biophys J*. 2003;32:355–62



- [251] Woiciechowsky C, Abbushi A, Zenclussen ML, Casalis P, Krüger JP, Freymann U, Endres M, Kaps C. Regeneration of nucleus pulposus tissue in an ovine intervertebral disc degeneration model by cell-free resorbable polymer scaffolds. *J. Tissue Eng. Regen. Med.* 2012;10:1002
- [252] Yang Y, Bagnaninchi PO, Ahearne M, Wang RK, Liu K-K. A novel optical coherence tomography based micro-indentation technique for mechanical characterization of hydrogels. *J. R. Soc. Interface* 4 2007;1169–1173
- [253] Ishii K, Ma Z, Ninomiya T, Takegoshi M, Kushibiki T, Yamamoto M, Hinds M, Tabata T, Wang RK, Awazu K. Control of guided hard tissue regeneration using phosphorylated gelatin and OCT imaging of calcification. *Prog. Biomed. Opt. Imaging Proc.* 2007;SPIE 6439: 64390D
- [254] Smith LE, Bonesi M, Smallwood R, Matcher SJ, Macneil S. Using swept-source optical coherence tomography to monitor the formation of neo-epidermis in tissue-engineered skin. *J. Tissue Eng. Regen. Med.* 2010;4, 652–658
- [255] Yang Y, Dubois A, Qin XP, Li J, El Haj A, Wang RK. Investigation of optical coherence tomography as an imaging modality in tissue engineering. *Phys Med Biol.* 2006;51:1649–59
- [256] Chen C-W, Betz MW, Fisher JP, Paek A, Chen Y. Macroporous hydrogel scaffolds and their characterization by optical coherence tomography. *Tissue Eng Part C Methods.* 2011;17:101–12
- [257] Villa C, Erratico S, Razini P, Farini A, Meregalli M, Belicchi M, et al. In vivo tracking of stem cell by nanotechnologies: future prospects for mouse to human translation. *Tissue Eng Part B Rev.* 2011;17:1–11
- [258] Hendee WR, Cleary K, Ehman RL, Fullerton GD, Grundfest WS, Haller J, et al. Bioengineering and imaging research opportunities workshop V: a summary on imaging and characterizing structure and function in native and engineered tissues. *Cytometry A.* 2008;73:779–84
- [259] Nieuwoudt M, Wiggert S, Malfeld S, van der Merwe SW. Imaging glucose metabolism in perfluorocarbon-perfused hepatocyte bioreactors using positron emission tomography. *J Artif Organs.* 2009;12:247
- [260] Chouinard JA, Rousseau JA, Beaudoin JF, Vermette P, Lecomte R. Positron emission tomography detection of human endothelial cell and fibroblast monolayers: effect of pretreatment and cell density on <sup>18</sup>F-FDG uptake. *Vasc Cell.* 2012;4:5
- [261] Radiological Society of North America. "Target Pathophysiologies of Radiopharmaceuticals." 2012. Issue 5
- [262] Mackewn, Jane E., et al. "Design and development of an MR-compatible PET scanner for imaging small animals." *Nuclear Science, IEEE Transactions on* 52.5 (2005): 1376-1380.
- [263] Zaidi, Habib, and Marie-Louise Montandon. "The new challenges of brain PET imaging technology." *Current Medical Imaging Reviews* 2.1 (2006): 3-13.
- [264] Daniela Schulz et al. simultaneous assessment of rodent behavior and neurochemistry using a miniature positron emission tomograph. *Nature Methods* April 2011;vol. 8, no. 4

- [265] Zaidi, Habib, Osama Mawlawi, and Colin G. Orton. "Simultaneous PET/MR will replace PET/CT as the molecular multimodality imaging platform of choice." *Medical Physics-New York-Institute of Physics* 34.5 (2007): 1525-1528.
- [266] H. Iida, S. Kanno, S. Miuri, M. Murakami, K. Takahashi, and K. Uemura. A simulation study of a method to reduce positron annihilation spread distributions using a strong magnetic field in positron emission tomography. *IEEE Trans. Nucl. Sci.* 1986;vol. 33, pp. 597-600
- [267] McElroy, David P., et al. Evaluation of silicon photomultipliers: a promising new detector for MR compatible PET. *Nuclear Instruments and Methods in Physics Research Section A: Accelerators, Spectrometers, Detectors and Associated Equipment* 571.1 (2007): 106-109.
- [268] Roncali, Emilie, and Simon R. Cherry. Application of silicon photomultipliers to positron emission tomography. *Annals of biomedical engineering* 39.4 (2011): 1358-1377.
- [269] Yoon, Hyun Suk, et al. Initial results of simultaneous PET/MRI experiments with an MRI-compatible silicon photomultiplier PET scanner. *Journal of Nuclear Medicine* 53.4 (2012): 608-614.
- [270] A. Honigman, E. Zeira, P. Ohana, R. Abramovitz, E. Tavor, I. Bar, et al. Imaging transgene expression in live animals. *Mol Ther*, 4 (2001), pp. 239–249
- [271] Zhao, H., et al., Emission spectra of bioluminescent reporters and interaction with mammalian tissue determine the sensitivity of detection in vivo. *J. Biomed. Opt.*, 2005. 10(4): p. 0412101-9
- [272] Hastings, J.W., *Chemistries and colors of bioluminescent reactions: a review.* *Gene*, 1996. 173: p. 5-11
- [273] Roda, A., et al., Bioluminescence in analytical chemistry and in vivo imaging. *Trends Anal. Chem.*, 2009. 28(3): p. 307-322
- [274] S. Levenberg, J. Rouwkema, M. Macdonald, E.S. Garfein, D.S. Kohane, D.C. Darland, et al. Engineering vascularized skeletal muscle tissue. *Nat Biotechnol*, 23 (2005), pp. 879–884
- [275] De Boer J, van Blitterswijk C, Lowik C. Bioluminescent imaging: emerging technology for non-invasive imaging of bone tissue engineering. *Biomaterials*. 2006;27:1851–8
- [276] Bago JR, Aguilar E, Alieva M, Soler-Botija C, Vila OF, Claros S, et al. In vivo bioluminescence imaging of cell differentiation in biomaterials: a platform for scaffold development. *Tissue Eng Part A*. 2013;19:593–603
- [277] Hwang do W, Jang SJ, Kim YH, Kim HJ, Shim IK, Jeong JM, et al. Real-time in vivo monitoring of viable stem cells implanted on biocompatible scaffolds. *Eur J Nucl Med Mol Imaging*. 2008;35:1887–98
- [278] Logeart-Avramoglou D, Oudina K, Bourguignon M, Delpierre L, Nicola M-A, Bensidhoum M, et al. In vitro and in vivo bioluminescent quantification of viable stem cells in engineered constructs. *Tissue Eng Part C Methods*. 2010;16:447–58
- [279] Roman I, Vilalta M, Rodriguez J, Matthies AM, Srouji S, Livne E, et al. Analysis of progenitor cell-scaffold combinations by in vivo non-invasive photonic imaging. *Biomaterials*. 2007;28:2718–28

- [280] Rice, B.W., M.D. Cable, and M.B. Nelson, In vivo imaging of light-emitting probes. *J. Biomed. Opt.*, 2001. 6(4): p. 432-440
- [281] Geuze RE, Prins H-J, Oner FC, van der Helm YJM, Schuijff LS, Martens AC, et al. Luciferase labeling for multipotent stromal cell tracking in spinal fusion versus ectopic bone tissue engineering in mice and rats. *Tissue Eng Part A*. 2010;16:3343–51
- [282] Prins H-J, Fernandes H, Rozemuller H, Van Blitterswijk C, De Boer J, Martens AC. Spatial distribution and survival of human and goat mesenchymal stromal cells on hydroxyapatite and b-tricalcium phosphate. *J Tissue Eng Regen Med*. 2012
- [283] Geuze RE, Prins H-J, Oner FC, van der Helm YJM, Schuijff LS, Martens AC, et al. Luciferase labeling for multipotent stromal cell tracking in spinal fusion versus ectopic bone tissue engineering in mice and rats. *Tissue Eng Part A*. 2010;16:3343–51
- [284] Alberich-Bayarri A, Moratal D, Escobar Ivirico JL, Rodríguez Hernández JC, Valles-Lluch A, Marti-Bonmati L, et al. Microcomputed tomography and microfinite element modeling for evaluating polymer scaffolds architecture and their mechanical properties. *J Biomed Mater Res B Appl Biomater*. 2009;91:191–202
- [285] Chimenti I, Rizzitelli G, Gaetani R, Angelini F, Ionta V, Forte E, et al. Human cardiosphere-seeded gelatin and collagen scaffolds as cardiogenic engineered bioconstructs. *Biomaterials*. 2011;32:9271–81
- [286] Ho ST, Hutmacher DW. A comparison of micro CT with other techniques used in the characterization of scaffolds. *Biomaterials*. 2006;27:1362–76
- [287] Landis FA, Stephens JS, Cooper JA, Cicerone MT, Lin-Gibson S. Tissue engineering scaffolds based on photocured dimethacrylate polymers for in vitro optical imaging. *Biomacromolecules*. 2006;7:1751–7
- [288] Muller B, Beckmann F, Huser M, Maspero F, Szekely G, Ruffieux K, et al. Nondestructive three-dimensional evaluation of a polymer sponge by microtomography using synchrotron radiation. *Biomol Eng*. 2002;19:73–8
- [289] Yang Y, Dorsey SM, Becker ML, Lin-Gibson S, Schumacher GE, Flaim GM, et al. X-ray imaging optimization of 3D tissue engineering scaffolds via combinatorial fabrication methods. *Biomaterials*. 2008;29:1901–11
- [290] Patel ZS, Ueda H, Yamamoto M, Tabata Y, Mikos AG. In vitro and in vivo release of vascular endothelial growth factor from gelatin microparticles and biodegradable composite scaffolds. *Pharm Res*. 2008;25:2370–8
- [291] Gargiulo, Paolo, et al. "CT and MRI assessment and characterization using segmentation and 3D modeling techniques: applications to muscle, bone and brain." *European Journal of Translational Myology* 24.1 (2014).
- [292] Behravesh E, Timmer MD, Lemoine JJ, Liebschner MA, Mikos AG. Evaluation of the in vitro degradation of macroporous hydrogels using gravimetry, confined compression testing, and microcomputed tomography. *Biomacromolecules*. 2002;3:1263–70
- [293] Hedberg EL, Shih CK, Lemoine JJ, Timmer MD, Liebschner MA, Jansen JA, et al. In vitro degradation of porous poly(propylene fumarate)/poly(dl-lactic-co-glycolic acid) composite scaffolds. *Biomaterials*. 2005;26:3215–25

- [294] Cartmell S, Huynh K, Lin A, Nagaraja S, Guldborg R. Quantitative micro-computed tomography analysis of mineralization within three-dimensional scaffolds in vitro. *J Biomed Mater Res A*. 2004;69:97–104
- [295] Chatterjee K, Lin-Gibson S, Wallace WE, Parekh SH, Lee YJ, Cicerone MT, et al. The effect of 3D hydrogel scaffold modulus on osteoblast differentiation and mineralization revealed by combinatorial screening. *Biomaterials*. 2010;31:5051–62
- [296] van Lenthe, G.H., et al. Nondestructive micro-computed tomography for biological imaging and quantification of scaffold-bone interactions in vivo. *Biomaterials*, 2007. 28: p. 2479-2490
- [297] Porter, B.D., et al. Noninvasive image analysis of 3D construct mineralization in a perfusion bioreactor. *Biomaterials*, 2007. 28: p. 2525-2533
- [298] Faraj KA, Cuijpers V, Wismans RG, Walboomers F, Jansen JA, van Kuppevelt T, et al. Micro-computed tomographical imaging of soft biological materials using contrast techniques. *Tissue Eng Part C Methods*. 2009;15:493–9
- [299] Arkudas A, Beier J, Prymachuk G, Hoereth T, Bleiziffer O, Polykandriotis E, et al. Automatic quantitative micro-computed tomography evaluation of angiogenesis in an axially vascularized tissue-engineered bone construct. *Tissue Eng Part C Methods*. 2010;16:1503–14
- [300] Ji C, Khademhosseini A, Dehghani F. Enhancing cell penetration and proliferation in chitosan hydrogels for tissue engineering applications. *Biomaterials*. 2011;32:9719–29
- [301] Zou D, Zhang Z, He J, Zhang K, Ye D, Han W, et al. Blood vessel formation in the tissue-engineered bone with the constitutively active form of HIF-1a mediated BMSCs. *Biomaterials*. 2012;33:2097–108
- [302] Young S, Kretlow JD, Nguyen C, Bashoura AG, Baggett LS, Jansen JA, et al. Microcomputed tomography characterization of neovascularization in bone tissue engineering applications. *Tissue Eng Part B Rev*. 2008;14:295–306
- [303] Watling CP, Lago N, Benmerah S, FitzGerald JJ, Tarte E, McMahon S, et al. Novel use of X-ray micro computed tomography to image rat sciatic nerve and integration into scaffold. *J Neurosci Methods*. 2010;188:39–44
- [304] Belicchi M, Cancedda R, Cedola A, Fiori F, Gavina M, Giuliani A, et al. Some applications of nanotechnologies in stem cells research. *Mater Sci Eng B*. 2009;165:139–47
- [305] A. Mol, R.G.M. Breuls, R. Petterson, C.V.C. Bouten. Quantification of cell viability in engineered tissues. Eindhoven University of Technology, Department of Biomedical Engineering. Accessed from: <http://repository.tue.nl/posters/738771.pdf>
- [306] Juhas M, Engelmayer GC Jr, Fontanella AN, Palmer GM, Bursac N. Biomimetic engineered muscle with capacity for vascular integration and functional maturation in vivo. *Proc Natl Acad Sci U S A*. 2014 Apr 15;111(15):5508-13
- [307] A. A. Salem. Protocol of Rapid Immunostaining of Lymph Node Touch Imprints. The Royal College of Surgeons in Edinburgh. Accessed from: [http://www.rcsed.ac.uk/fellows/aaasalem/Rapid\\_imprint\\_immunostaining.htm](http://www.rcsed.ac.uk/fellows/aaasalem/Rapid_imprint_immunostaining.htm)

- [308] P. Brescia, P. Banks. Quantifying Cytotoxicity of Thiostrepton on Mesothelioma Cells using MTT Assay and the Epoch™ Microplate Spectrophotometer. BioTek Instruments, Inc., Winooski, VT. Accessed from: <http://www.biotek.com/resources/articles/quantification-cell-viability-epoch.html>
- [309] J. C. Jennette. Renal Pathology Tutorial. UNC Nephropathology. Accessed from: <http://www.uncnephropathology.org/jennette/ch1.htm>
- [310] Li X, Gianoulis TA, Yip KY, Gerstein M, Snyder M. Extensive in vivo metabolite-protein interactions revealed by large-scale systematic analyses. *Cell*. 2010 Nov 12;143(4):639-50
- [311] H. Zaidi. SPECT Quantification. PIN lab: Geneva University Hospital, Division of Nuclear Medicine. Accessed from: <http://pinlab.hcuge.ch/research.html>
- [312] Mäkelä KT et al. Countrywise results of total hip replacement. An analysis of 438,733 hips based on the Nordic Arthroplasty Register Association database. *Acta Orthop*. 2014;85(2), pp:107-16.
- [313] Kurtz S, Ong K, Lau E, Mowat F, Halpern M. Projections of primary and revision hip and knee arthroplasty in the United States from 2005 . *J Bone Joint Surg (Am)*, 2007, 89, pp:780–5.
- [314] Nemes S et al. Projections of total hip replacement in Sweden from 2013 to 2030. *ActaOrthop*, 2014, 85(3), pp:238-43.
- [315] Singh JA. Epidemiology of Knee and Hip Arthroplasty: A Systematic Review. *The Open Orthopaedics Journal*. 2011 Mar 16;5(1):80–5.
- [316] Havelin LI et al. The Nordic Arthroplasty Register Association: A unique collaboration between 3 national hip arthroplasty registries with 280,201 THRs. *Acta Orthop*. 2009, 80(4), pp: 393–401.
- [317] Wolf BR et al. Adverse outcomes in hip arthroplasty: long-term trends. *J Bone Joint Surg Am*. 2012, 18, 94(14):e103.
- [318] Thien TM et al. Periprosthetic Femoral Fracture within Two Years After Total Hip Replacement: Analysis of 437,629 Operations in the Nordic Arthroplasty Register Association Database. *J Bone Joint Surg Am*. 2014, 96(19):e167.
- [319] van Loon CJ et al. Femoral bone loss in total knee arTHAoplasty. *ActaOrthop Belg* 1999;65, pp:154–63.
- [320] Radl, R., et al. Proximal femoral bone loss and increased rate of fracture with a proximally hydroxyapatite-coated femoral component. *Journal of Bone & Joint Surgery (Br)*, 82(8), 2000, pp: 1151-1155.
- [321] Banaszkiwicz, P.A., 2014. Porous-coated hip replacement. The factors governing bone ingrowth, stress shielding, and clinical results, in: *Classic Papers in Orthopaedics*. pp. 51–55.
- [322] Radl, R., et al. Proximal femoral bone loss and increased rate of fracture with a proximally hydroxyapatite-coated femoral component. *Journal of Bone & Joint Surgery (Br)*, 2000, 82(8), pp: 1151-1155.
- [323] Magnússon et al. Gait Analysis, bone and muscle density in THA patients, *European Journal Translational Myology-Basic Applied Myology*, 2012, 22(3), pp: 135-140.

- [324] Taaffe DR et al. Race and sex effects on the association between muscle strength, soft tissue, and bone mineral density in healthy elders: the health, aging, and body composition study. *Journal of Bone and Mineral Research*, 2001, 16(7), pp: 1343–1352.
- [325] Gargiulo P et al. Assessment of total hip arthroplasty by means of computed tomography 3D models and fracture risk evaluation. *Artificial organs*, 2013, 37(6), pp: 567-573.
- [326] Ewen AM et al. Post-operative gait analysis in total hip replacement patients – A review of current literature and meta-analysis. *Gait and posture*, 2012, 36(1), pp:1-6.
- [327] Petersen MK et al. Gait analysis after total hip replacement with hip resurfacing implant or Mallory-head Eveterprotheris:a randomised vontrolled trial. *International Orthopedics*, 2011, 35(5), pp:667-674.
- [328] Hodt-Billington C et al. Changes in gait Symmetry, gait velocity and self-reported function followings total hip replacement. *Journal of Rehabilitation Medicine*, 2011, 43(9), pp: 787-793.
- [329] Olsson E et al. Total hip replacement, A comparison between Cemented (Charnley) and Non-cemented (HP Garches) Fixation by clinical Assessment and objective Gait Analysis. *Scandinavian J Rehab Med*, 1985, 18, pp:107-116.
- [330] PéturssonTh et al. Bone and muscle assessment in patients undergoing total hip arthroplasty using HU based analysis. *European Journal of Translational Myology*, 2012, 22(3), pp: 147-152.
- [331] Lindner et Al. Postoperative Development of Bone Mineral Density and Muscle Strength in the Lower Limb After Cemented and Uncemented Total Hip Replacement. *The Open Orthopaedics Journal*, 2014, 8, pp:272-280.
- [332] Gasbarra, E., Iundusi, R., Perrone, F.L., Saturnino, L., Tarantino, U., 2015. Densitometric evaluation of bone remodelling around Trabecular Metal Primary stem: a 24-month follow-up. *Aging Clin. Exp. Res.* 27 Suppl 1, S69–75.
- [333] Pétursson, P., Edmunds, K.J., Gíslason, M.K., Magnússon, B., Magnúsdóttir, G., Halldórsson, G., Jónsson, H., Gargiulo, P., 2015. Bone Mineral Density and Fracture Risk Assessment to Optimize Prosthesis Selection in Total Hip Replacement. *Comput. Math. Methods Med.* 2015, 1–7.
- [334] Zhang, Y.Z., Chen, B., Lu, S., Yang, Y., Zhao, J.M., Liu, R., Li, Y.B., Pei, G.X., 2011. Preliminary application of computer-assisted patient-specific acetabular navigational template for total hip arthroplasty in adult single development dysplasia of the hip. *Int. J. Med. Robot. Comput. Assist. Surg.* 7, 469–474.
- [335] Arachchi, S., Pitto, R.P., Anderson, I.A., Shim, V.B., 2015. Analyzing bone remodeling patterns after total hip arthroplasty using quantitative computed tomography and patient-specific 3D computational models. *Quant. Imaging Med. Surg.* 5, 575–582.
- [336] Esposito, L., Bifulco, P., Gargiulo, P., Fraldi, M., 2015. Singularity-free finite element model of bone through automated voxel-based reconstruction. *Comput. Methods Biomech. Biomed. Engin.* 1–6.

- [337] Edmunds KJ, Hermannsson Þ, Barbato M, Árnadóttir I, Gíslason MK, Jónsson H, et al. Multimodal Quantitative Assessment for Pre-operative Prosthesis Selection in Total Hip Arthroplasty. In: Kyriacou E, Christofides S, Pattichis CS, editors. XIV Mediterr. Conf. Med. Biol. Eng. Comput. 2016 MEDICON 2016, March 31st-April 2nd 2016, Paphos, Cyprus, Cham: Springer International Publishing; 2016, p. 709–14.
- [338] Falcinelli C, Schileo E, Balistreri L, Baruffaldi F, Bordini B, Viceconti M, et al. Multiple loading conditions analysis can improve the association between finite element bone strength estimates and proximal femur fractures: A preliminary study in elderly women. *Bone* 2014;67:71–80.
- [339] Bayraktar HH, Morgan EF, Niebur GL, Morris GE, Wong EK, Keaveny TM. Comparison of the elastic and yield properties of human femoral trabecular and cortical bone tissue. *J Biomech* 2004;37:27–35.
- [340] Horstmann T, Listringhaus R, Haase G-B, Grau S, Mündermann A. Changes in gait patterns and muscle activity following total hip arthroplasty: A six-month follow-up. *Clin Biomech* 2013;28:762–9.
- [341] Weber ER, Daube JR, Coventry MB. Peripheral neuropathies associated with total hip arthroplasty. *J Bone Joint Surg Am* 1976;58:66–9.
- [342] Fokter, S.K., Repše-Fokter, A., Takač, I., 2009. Case report: Femoral neuropathy secondary to total hip arthroplasty wear debris. *Clin. Orthop. Relat. Res.* 467, 3032–3035.
- [343] Rapp, W., Brauner, T., Weber, L., Grau, S., Mündermann, A., Horstmann, T., 2015. Improvement of walking speed and gait symmetry in older patients after hip arthroplasty: a prospective cohort study. *BMC Musculoskelet. Disord.* 16, 291.
- [344] McDonough, A.L., Batavia, M., Chen, F.C., Kwon, S., Ziai, J., 2001. The validity and reliability of the GAITRite system's measurements: A preliminary evaluation. *Arch. Phys. Med. Rehabil.* 82, 419–425.
- [345] Vincent KR, Vincent HK, Lee LW, Weng J, Alfano AP. Outcomes After Inpatient Rehabilitation of Primary and Revision Total Hip Arthroplasty. *Arch Phys Med Rehabil* 2006;87:1026–32.
- [346] Edmunds KJ, Gíslason MK, Arnadóttir ID, Marcante A, Piccione F, Gargiulo P. Quantitative Computed Tomography and Image Analysis for Advanced Muscle Assessment. *European Journal of Translational Myology.* 2016;26(2):6015. doi:10.4081/ejtm.2016.6015.
- [347] Magnússon B, Pétursson Þ, Edmunds K, et al. Improving Planning and Post-Operative Assessment for Total Hip Arthroplasty. *European Journal of Translational Myology.* 2015;25(2):4913. doi:10.4081/ejtm.2015.4913.
- [348] Gavaskar AS, Tummala NC, Subramanian M. Cemented or cementless THA in patients over 80??years with fracture neck of femur: a prospective comparative trial. *Musculoskelet Surg* 2014;98:205–8. doi:10.1007/s12306-013-0296-6.
- [349] Muthukumaraswamy, SD. High-frequency brain activity and muscle artifacts in MEG/EEG: a review and recommendations. *Front Hum Neurosci.* 2013 Apr 15;7:138.

- [350] Whitham EM, Pope KJ, Fitzgibbon SP, Lewis T, Clark CR, Loveless S, Broberg M, Wallace A, DeLosAngeles D, Lillie P, Hardy A, Fronsco R, Pulbrook A, Willoughby JO. Scalp electrical recording during paralysis: quantitative evidence that EEG frequencies above 20 Hz are contaminated by EMG. *Clin Neurophysiol*. 2007 Aug;118(8):1877-88.
- [351] Kennett R. Modern electroencephalography. *J Neurol*. 2012 Apr;259(4):783-9.
- [352] Whitham EM, Lewis T, Pope KJ, Fitzgibbon SP, Clark CR, Loveless S, DeLosAngeles D, Wallace AK, Broberg M, Willoughby JO. Thinking activates EMG in scalp electrical recordings. *Clin Neurophysiol*. 2008 May;119(5):1166-75.
- [353] Whitham EM, Fitzgibbon SP, Lewis TW, Pope KJ, Delosangeles D, Clark CR, Lillie P, Hardy A, Gandevia SC, Willoughby JO. Visual Experiences during Paralysis. *Front Hum Neurosci*. 2011 Dec 7;5:160.
- [354] Pope KJ, Fitzgibbon SP, Lewis TW, Whitham EM, Willoughby JO. Relation of gamma oscillations in scalp recordings to muscular activity. *Brain Topogr*. 2009 Jun;22(1):13-7.
- [355] Shackman AJ, McMenamin BW, Slagter HA, Maxwell JS, Greischar LL, Davidson RJ. Electromyogenic artifacts and electroencephalographic inferences. *Brain Topogr*. 2009 Jun;22(1):7-12.
- [356] McMenamin BW, Shackman AJ, Greischar LL, Davidson RJ. Electromyogenic Artifacts and Electroencephalographic Inferences Revisited. *Neuroimage*. 2011 Jan 1;54(1):4-9.
- [357] Barlow JS. Artifact processing (rejection and minimization) in EEG data processing. *Handbook of electroencephalography and clinical neurophysiology*. Revised series, vol. 2 Elsevier, Amsterdam (1986), pp. 15–62.
- [358] Ives JR, Schomer DL. A 6-pole filter for improving the readability of muscle contaminated EEGs. *Electroenceph clin Neurophysiol*, 69 (1988), pp. 486–490.
- [359] Panych LP, Wada JA, Beddoes MP. Practical digital filters for reducing EMG artefact in EEG seizure recordings. *Electroencephalogr Clin Neurophysiol*. 1989 Mar;72(3):268-76.
- [360] Klass, Donald W. "The continuing challenge of artifacts in the EEG." *American Journal of EEG Technology* 35 (1995): 239-269.
- [361] Pradhan, N., P. K. Sadasivan, S. Chatterji, and D. Narayana Dutt. "Patterns of attractor dimensions of sleep EEG." *Computers in biology and medicine* 25, no. 5 (1995): 455-462.
- [362] BRUNNER, DANIEL, RAYMOND VASKO, CHRISTOPHER DETKA, JAMES MONAHAN, C. H. A. R. L. E. S. REYNOLDS III, and DAVID KUPFER. "Muscle artifacts in the sleep EEG: Automated detection and effect on all-night EEG power spectra." *Journal of sleep research* 5, no. 3 (1996): 155-164.
- [363] Anderer, Peter, Stephen Roberts, A. Schlögl, Georg Gruber, G. Klösch, Werner Herrmann, Peter Rappelsberger et al. "Artifact processing in computerized analysis of sleep EEG—a review." *Neuropsychobiology* 40, no. 3 (1999): 150-157.
- [364] Lagerlund, Terrence D., Frank W. Sharbrough, and Neil E. Busacker. "Spatial filtering of multichannel electroencephalographic recordings through principal component analysis by singular value decomposition." *Journal of Clinical Neurophysiology* 14, no. 1 (1997): 73-82.



- [365] Jung, Tzyy-Ping, Scott Makeig, Colin Humphries, Te-Won Lee, Martin J. Mckeown, Vicente Iragui, and Terrence J. Sejnowski. "Removing electroencephalographic artifacts by blind source separation." *Psychophysiology* 37, no. 02 (2000): 163-178.
- [366] Junghöfer, Markus, Thomas Elbert, Don M. Tucker, and Brigitte Rockstroh. "Statistical control of artifacts in dense array EEG/MEG studies." *Psychophysiology* 37, no. 4 (2000): 523-532.
- [367] Boxtel, A., P. Goudswaard, and L. R. B. Schomaker. "Amplitude and bandwidth of the frontalis surface EMG: effects of electrode parameters." *Psychophysiology* 21, no. 6 (1984): 699-707.
- [368] Van Boxtel, Anton. "Optimal signal bandwidth for the recording of surface EMG activity of facial, jaw, oral, and neck muscles." *Psychophysiology* 38, no. 01 (2001): 22-34.
- [369] Van Boxtel, A., P. Goudswaard, G. M. Van der Molen, and W. E. Van Den Bosch. "Changes in electromyogram power spectra of facial and jaw-elevator muscles during fatigue." *J Appl Physiol* 54, no. 1 (1983): 51-8.
- [370] Abraham, K., and Cs Ajmone Marsan. "Patterns of cortical discharges and their relation to routine scalp electroencephalography." *Electroencephalography and clinical neurophysiology* 10, no. 3 (1958): 447-461.
- [371] Ramon, Ceon, Paolo Garguilo, Egill A. Fridgeirsson, and Jens Haueisen. "Changes in scalp potentials and spatial smoothing effects of inclusion of dura layer in human head models for EEG simulations." *Frontiers in neuroengineering* 7 (2014).
- [372] Ramon, Ceon, and Mark D. Holmes. "Noninvasive epileptic seizure localization from stochastic behavior of short duration interictal high density scalp EEG data." *Brain topography* 25, no. 1 (2012): 106-115.
- [373] Agatston AS, Janowitz WR, Hildner FJ, Zusmer NR, Viamonte M Jr, Detrano R. Quantification of coronary artery calcium using ultrafast computed tomography. *J Am Coll Cardiol*. 1990;15:827-32.
- [374] Ameli-Renani S, Rahman F, Nair A, Ramsay L, Bacon JL, Weller A, Sokhi HK, Devaraj A, Madden B, Vlahos I. Dual-energy CT for imaging of pulmonary hypertension: challenges and opportunities. *Radiographics*. 2014;34:1769-90.
- [375] Akiba T, Morikawa T, Ohki T. Simulation of thoracoscopic surgery using 3-dimensional tailor-made virtual lung. *J Thorac Cardiovasc Surg* 2012;143:1232-4.
- [376] Akiba T, Morikawa T, Ohki T. Thoracoscopic lung segmentectomy simulated by a tailor-made virtual lung: computed bronchography and angiography. *Thorac Cardiovasc Surg* 2013;61:151-3.
- [377] Leshnower BG, Miller DL, Fernandez FG, et al. Video-assisted thoracoscopic surgery segmentectomy: a safe and effective procedure. *Ann Thorac Surg* 2010;89:1571-6.
- [378] Watabnabe K, Uese K, Higuchi O, et al. Three-dimensional computed tomographic findings of bilateral tracheal bronchus. *Pediatr Cardiol* 2009;30:87-8.
- [379] Zhong YM, Jaffe RB, Zhu M, et al. CT assessment of tracheobronchial anomaly in left pulmonary artery sling. *Pediatr Radiol* 2010;40:1755-62.
- [380] Read R, St Cyr J, Marek J, et al. Bronchial anomaly of the right upper lobe. *Ann Thorac Surg* 1990;50:980-1.

- [381] Yildiz H, Ugurel S, Soyly K, et al. Accessory cardiac bronchus and tracheal bronchus anomalies: CT-bronchoscopy and CT-bronchography findings. *Surg Radiol Anat* 2006;28:646-9.
- [382] Suzuki M, Matsui O, Kawashima H, et al. Radio anatomical study of a true tracheal bronchus using multidetector computed tomography. *Jpn J Radiol* 2010;28:188-92.
- [383] Ohta S, Saito Y, Usuda K, et al. Tracheobronchial anomalies: report of 71 cases. *J Jpn Society Bronchology* 1985;8:122-30.
- [384] Akiba T, Marushima H, Takagi M, et al. Preoperative evaluation of a tracheal bronchus by three-dimensional 64-row multidetector-row computed tomography (MDCT) bronchography and angiography: report of a case. *Surg Today* 2008;38:841-3.
- [385] Yan, X., & Gu, P. (1996). A review of rapid prototyping technologies and systems. *CAD Computer Aided Design*.
- [386] Sen S, Sentürk E, Pabus çu E, et al. Upper lobectomy for lung cancer with true tracheal bronchus: a unique presentation. *Arch Bronconeumol* 2010;46:332-4.
- [387] Sodian R, Schmauss D, Markert M, et al. Three-dimensional printing creates models for surgical planning of aortic valve replacement after previous coronary bypass grafting. *Ann Thorac Surg* 2008;85:2105-8.
- [388] Swash M, Brown MM, Thakkar C. CT muscle imaging and the clinical assessment of neuromuscular disease. *Muscle & nerve*. 1995;18(7):708-14.
- [389] Fischer D, Kley R, Strach K, Meyer C, Sommer T, Eger K, et al. Distinct muscle imaging patterns in myofibrillar myopathies. *Neurology*. 2008;71(10):758-65.
- [390] Mercuri E, Talim B, Moghadaszadeh B, Petit N, Brockington M, Counsell S, et al. Clinical and imaging findings in six cases of congenital muscular dystrophy with rigid spine syndrome linked to chromosome 1p (RSMD1). *Neuromuscular Disorders*. 2002;12(7):631-8.
- [391] Helgason, T., Gargiulo, P., Jóhannesdóttir, F., Ingvarsson, P., Knútsdóttir, S., Gudmundsdóttir, V., & Yngvason, S. (2005). Monitoring muscle growth and tissue changes induced by electrical stimulation of denervated degenerated muscles with CT and stereolithographic 3D modeling. *Artificial Organs*, 29(6), 440–443.
- [392] Snijder M, Visser M, Dekker J, Goodpaster B, Harris T, Kritchevsky S, et al. Low subcutaneous thigh fat is a risk factor for unfavourable glucose and lipid levels, independently of high abdominal fat. *The Health ABC Study. Diabetologia*. 2005;48(2):301-8.
- [393] Goodpaster, B. H., Park, S. W., Harris, T. B., Kritchevsky, S. B., Nevitt, M., Schwartz, A. V., ... Newman, A. B. (2006). The Loss of Skeletal Muscle Strength, Mass, and Quality in Older Adults: The Health, Aging and Body Composition Study. *The Journals of Gerontology Series A: Biological Sciences and Medical Sciences*, 61(10), 1059–1064.
- [394] Hicks, G. E., Simonsick, E. M., Harris, T. B., Newman, A. B., Weiner, D. K., Nevitt, M. a, & Tyllavsky, F. a. (2005). Cross-sectional associations between trunk muscle composition, back pain, and physical function in the health, aging and body composition study. *The Journals of Gerontology. Series A, Biological Sciences and Medical Sciences*, 60(7), 882–887.

- [395] Sur M.D., Namm J.P., Hemmerich J.A., Buschmann M.M., Roggin K.K., Dale W3. Radiographic Sarcopenia and Self-reported Exhaustion Independently Predict NSQIP Serious Complications After Pancreaticoduodenectomy in Older Adults. *Ann Surg Oncol*. 2015 Nov;22(12):3897-904.
- [396] Gargiulo P, Helgason T, Ingvarsson P, et al. Morphological changes in denervated muscle treated with FES. *Basic Appl Myol* 2007;17:133-6.
- [397] Evans, W. J. (2010). Skeletal muscle loss: Cachexia, sarcopenia, and inactivity. *American Journal of Clinical Nutrition*, 91(4), 1123–1127.
- [398] Sigurdsson E., Thorgeirsson G., Sigvaldason H., et al. Prevalence of coronary heart disease in Icelandic men 1968-1986. The Reykjavik Study. *Eur Heart J*. 1993 May;14(5):584–591.
- [399] Sigurdsson G, Aspelund T, Chang M et al. Increasing sex difference in bone strength in old age: the Age, Gene/Environment Susceptibility-Reykjavik study (AGES-Reykjavik). *Bone*. 2006;393:644–651.
- [400] Johannesdottir F, Aspelund T, Siggeirsdottir K et al. Mid-thigh cortical bone structural parameters, muscle mass and strength, and association with lower limb fractures in older men and women (AGES-Reykjavik Study). *Calcif Tissue Int*. 2012;905:354–364.
- [401] Lang T., Koyama A., Li C. et al. (2008). Pelvic body composition measurements by quantitative computed tomography: association with recent hip fracture. *Bone*;424:798–805.
- [402] Cesari M, Kritchevsky SB, Penninx BW, et al. Prognostic value of usual gait speed in well-functioning older people--results from the Health, Aging and Body Composition Study. *J Am Geriatr Soc*. 2005 Oct;53(10):1675–1680.
- [403] Podsiadlo D, Richardson S. The timed "Up & Go": a test of basic functional mobility for frail elderly persons. *J Am Geriatr Soc*. 1991 Feb;39(2):142–148
- [404] Von Bonsdorff, M. B., Muller, M., Aspelund, T., Garcia, M., Eiriksdottir, G., Rantanen, T., ... for the Age, Gene/Environment Susceptibility-Reykjavik Study Investigators. (2013). Persistence of the effect of birth size on dysglycaemia and type 2 diabetes in old age: AGES-Reykjavik Study. *Age*, 35(4), 1401–1409.
- [405] Ding, J., Sigurdsson, S., Garcia, M., Phillips, C. L., Eiriksdottir, G., Gudnason, V., ... Launer, L. J. (2015). Risk Factors Associated With Incident Cerebral Microbleeds According to Location in Older People: The Age, Gene/Environment Susceptibility (AGES)-Reykjavik Study. *JAMA Neurology*, 72(6), 682–688.
- [406] Safran C, Bloomrosen M, Hammond WE, et al. Expert Panel. Toward a national framework for the secondary use of health data: an American Medical Informatics Association White Paper. *J Am Med Inform Assoc* 2007;14:1–9.
- [407] Logistic regression and artificial neural network classification models: a methodology review. *J Biomed Inform* 2002;35:352–9.
- [408] Bellazzi R, Zupan B. Predictive data mining in clinical medicine: Current issues and guidelines. *Int J Med Inform* 2008;77:81–97.
- [409] Maslove D.M., Podchiyska T., Lowe H.J. (2013) Discretization of continuous features in clinical datasets. *J Am Med Inform Assoc*. 2013 May 1;20(3):544-53.

- [410] Fayyad, U.M.; Irani, K.B. (1993). Multi-Interval Discretization of Continuous-Valued Attributes for Classification Learning. hdl:2014/35171., Proceedings of the International Joint Conference on Uncertainty in AI (Q334 .I571 1993), pp. 1022-1027.
- [411] Wang H., Song M. (2011). Ckmeans.1d.dp: Optimal k-means Clustering in One Dimension by Dynamic Programming. R J. 2011 Dec;3(2):29-33.
- [412] Manning CD, Raghavan P, Schütze H. Flat clustering. Introduction to information retrieval. New York: Cambridge University Press, 2008;365.
- [413] Sturges, H. A. (1926). The Choice of a Class Interval. Journal of the American Statistical Association, 21(153), 65–66.
- [414] De Roos, A. M. (2008). Demographic analysis of continuous-time life-history models. Ecology Letters, 11(1), 1–15.
- [415] Helgason, B., Viceconti, M., Rúnarsson, T.P., Brynjólfsson, S., 2008. On the mechanical stability of porous coated press fit titanium implants: A finite element study of a pushout test. J. Biomech. 41(8), 1675-1681
- [416] Keller TS. Predicting the compressive mechanical behavior of bone. J Biomech 1994; 27(9): 1159-1168.
- [417] Sakai R, Takahashi A, Takahira N, Uchiyama K, Yamamoto T, Uchida K, et al. Hammering force during cementless total hip arthroplasty and risk of microfracture. Hip Int. 2011 Jun 13;21(3):330–5.
- [418] Bessho M, Ohnishi I, Matsuyama J, Matsumoto T, Imai K, Nakamura K. Prediction of Strength and Strain of the Proximal Femur by a CT based Finite Element Method. J Biomech 2007; 40(8): 1745-1753.
- [419] Gislason M.K., Coupaud S., Sasagawa K., Tanabe Y., Purcell M., Allan D.B., Tanner K.E.: Prediction of risk of fracture in the tibia bone due to altered mineral density distribution resulting from disuse: a finite element study, Journal of Engineering in Medicine: Proceedings of the IMechE Part H, 2014, Vol. 228(2), pp:165-174.
- [420] Gargiulo, Paolo, Ugo Carraro, Thomas Mandl, Helmut Kern, Sandra Zampieri, Winfried Mayr, and Thordur Helgason. "Anthropometry of human muscle using segmentation techniques and 3D modelling: applications to lower motor neuron denervated muscle in Spinal Cord Injury." In Handbook of Anthropometry, pp. 323-354. Springer New York, 2012.
- [421] P. Gargiulo and G. Á. Björnsson, "Integrated medical modeling service to optimize planning for mandibular distraction osteogenesis and maxillofacial surgeries: 5 years' experience," Anaplastology, vol. 2, no. 121, pp. 2161–1173, 2013.
- [422] H. Kodama, "Automatic method for fabricating a threedimensional plastic model with photo-hardening polymer," Review of Scientific Instruments, vol. 52, no. 11, pp. 1770– 1773, 1981.
- [423] H. Anderl, D. Zur Nedden, W. Mu et al., "CT-guided stereolithography as a new tool in craniofacial surgery," British Journal of Plastic Surgery, vol. 47, no. 1no. 1, pp. 60–64, 1994.
- [424] P. A. Webb, "A review of rapid prototyping (RP) techniques in the medical and biomedical sector," Journal of Medical Engineering & Technology, vol. 24, no. 4, pp. 149–153, 2000.

- [425] P. Gargiulo, S. B. Sævarsdóttir, B. Baldvinsdóttir, and I. H. 5 Ólafsson, "Use of 3 dimensional models and navigation system in preparation for brain surgery," *Biomedizinische Technik*, vol. 58, p. 1, 2013.
- [426] D. Leclercq, C. Delmaire, N. Menjot de Champfleury, J. Chiras, 6 and S. Lehericy, "Diffusion tractography: methods, validation and applications in patients with neurosurgical lesions," *Neurosurgery Clinics of North America*, vol. 22, no. 2, pp. 253–268, 2011.
- [427] K. Kośła, B. Bryszewski, D. Jaskólski, N. Błasiak-Kołacińska, L. Stefańczyk, and A. Majos, "Reorganization of language areas in patient with a frontal lobe low grade glioma—fMRI case study," *Polish Journal of Radiology*, vol. 80, p. 290, 2015.
- [428] D. Frey, V. Strack, E. Wiener, D. Jussen, P. Vajkoczy, and T. Picht, "A new approach for corticospinal tract reconstruction based on navigated transcranial stimulation and standardized fractional anisotropy values," *NeuroImage*, vol. 62, no. 3, pp. 1600–1609, 2012.
- [429] V. A. Coenen, T. Krings, L. Mayfrank et al., "Three-dimensional visualization of the pyramidal tract in a neuronavigation system during brain tumor surgery: first experiences and technical note," *Neurosurgery*, vol. 49, no. 1, pp. 86–93, 2001.
- [430] Medtronic, "StealthViz with StealthDTI application reference guide," Medtronic, 2011-2008.
- [431] NordicNeuroLab AS, "nordicBrainEx Tutorial - DTI Module," NordicNeuroLab AS, 15-Jan-2015.
- [432] A. Fittsiori, D. Nguyen, A. Karentzos, J. Delavelle, and M. I. Vargas, "The corpus callosum: white matter or terra incognita," *The British Journal of Radiology*, vol. 84, no. 997, pp. 5–18, 2011.
- [433] Bioon.com, "Basic motor pathway," February 2017, <http://www.bioon.com/bioline/neurosci/course/basmot.html>.
- [434] Study.com, "Sensory cortex: definition & function - video & lesson transcript," February 2017 <http://study.com/academy/lesson/sensory-cortex-definition-function.html>.
- [435] Healthline.com, "Optic nerve function, anatomy & definition | 7 body maps," February 2017 <http://www.healthline.com/human-body-maps/optic-nerve>.
- [436] A. D. Friederici, "Pathways to language: fiber tracts in the human brain," *Trends in Cognitive Sciences*, vol. 13, no. 4, pp. 175–181, 2009
- [437] F.-C. Yeh, T. D. Verstynen, Y. Wang, J. C. FernándezMiranda, and W.-Y. I. Tseng, "Deterministic diffusion fiber Journal of Healthcare Engineering 7 tracking improved by quantitative anisotropy," *PloS One*, vol. 8, no. 11, article e80713, 2013.
- [438] G. C. Feigl, W. Hiergeist, C. Fellner et al., "Magnetic resonance imaging diffusion tensor tractography: evaluation of anatomic accuracy of different fiber tracking software packages," *World Neurosurgery*, vol. 81, no. 1, pp. 144–150, 2014.
- [439] M. Catani and M. Thiebaut de Schotten, "A diffusion tensor imaging tractography atlas for virtual in vivo dissections," *Cortex*, vol. 44, no. 8, pp. 1105–1132, 2008.
- [440] K. Oishi, A. V. Faria, P. C. M. van Zijl, and S. Mori, *MRI Atlas of Human White Matter*, Academic Press, 2010.

- [441] MIMICS software,” February 2017, [http://biomedical .materialise.com/mimics](http://biomedical.materialise.com/mimics).
- [442] Xero viewer software,” February 2017, [http://agfahealthcare.com/he/usa/en/binaries/XERO%20sheet%202013\\_tcm561-113934.pdf](http://agfahealthcare.com/he/usa/en/binaries/XERO%20sheet%202013_tcm561-113934.pdf).
- [443] Medtronic,” <http://www.medtronic.com/for-healthcare-professionals/products-therapies/spinalorthopedics/surgicalnavigation-imaging/surgicalnavigation-systems/index.htm>.
- [444] P. Gargiulo, “3D modelling and monitoring of denervated muscle under functional electrical stimulation treatment and associated bone structural change,” *European Journal of Translational Myology/Basic Applied Myology*, vol. 21, pp. 31–94, 2011.
- [445] O. Ciccarelli, M. Catani, H. Johansen-Berg, C. Clark, and A. Thompson, “Diffusion-based tractography in neurological disorders: concepts, applications, and future developments,” *Lancet Neurology*, vol. 7, no. 8, pp. 715–727, 2008.
- [446] Parker, J. Anthony. "DICOM Rescale (DICOM\_RescaleTP)." *DICOM Rescale*. Harvard Medical School, 10 Dec. 2007. Web. 17 May 2017.
- [447] Mosekilde, L., Bentzen, S. M., Ortoft, G., & Jorgensen, J. (1989). The predictive value of quantitative computed tomography for vertebral body compressive strength and ash density. *Bone*, 10(6), 465–470.
- [448] Haba Y, Lindner T, Fritsche A, et al. Relationship Between Mechanical Properties and Bone Mineral Density of Human Femoral Bone Retrieved from Patients with Osteoarthritis. *The Open Orthopaedics Journal*. 2012;6:458-463.
- [449] Haba Y, Skripitz R, Lindner T, et al. Bone Mineral Densities and Mechanical Properties of Retrieved Femoral Bone Samples in relation to Bone Mineral Densities Measured in the Respective Patients. *The Scientific World Journal*. 2012;2012:242403.
- [450] Imai K. Computed tomography-based finite element analysis to assess fracture risk and osteoporosis treatment. *World Journal of Experimental Medicine*. 2015;5(3):182-187.
- [451] Nicolella DP, Bredbenner TL. Development of a Parametric Finite Element Model of the Proximal Femur using Statistical Shape and Density Modeling. *Computer Methods in Biomechanics and Biomedical Engineering*. 2012;15(2):101-110
- [452] Danielson ME, Beck TJ, Karlamangla AS, et al. A comparison of DXA and CT based methods for estimating the strength of the femoral neck in post-menopausal women. *Osteoporosis international : a journal established as result of cooperation between the European Foundation for Osteoporosis and the National Osteoporosis Foundation of the USA*. 2013;24(4):1379-1388.
- [453] Kheirollahi H, Luo Y. Assessment of Hip Fracture Risk Using Cross-Section Strain Energy Determined by QCT-Based Finite Element Modeling. *BioMed Research International*. 2015;2015:413839.
- [454] Fraldi, M., Esposito, L., Perrella, G., Cutolo, A., & Cowin, S. C. (2010). Topological optimization in hip prosthesis design. *Biomechanics and Modeling in Mechanobiology*, 9(4), 389–402.
- [455] Manda K, Xie S, Wallace RJ, Levrero-Florencio F, Pankaj P. Linear viscoelasticity - bone volume fraction relationships of bovine trabecular bone. *Biomechanics and Modeling in Mechanobiology*. 2016;15(6):1631-1640.







# Appendix A

## Code: NTRA

The following codes are extracted from the following matlab scripts for the nonlinear trimodal regression analysis (NTRA) method: *hjarta\_spline.m*, *createFit.m*, and *gauss\_fitting.m*, respectively.

### *hjarta\_spline.m*

```
close all
clear all
clc

%Load the data
load heart.mat
%Create the CT bin vector
index=1:128;
%Define the high indexes
index_high=[1 4 8 12 16 19 23 27 31 34 38 42 46 49 53 57 61 65 68 72 76 80 83 87 91 95 98 102
106 110 113 117 121 125];
ct_high=index_high;
%convert to Hounsfield units
index_high=index_high*2.265625-190;
%Define the low indexes
index_low=setdiff(index,ct_high);
ct_low=index_low;
%convert to Hounsfield units
index_low=index_low*2.265625-190;

%HU=CT*2.265625-190;
%Average curve from all subjects

%N=3167;
N=10;
C_upper=zeros(N,11);
C_lower=zeros(N,11);
S=zeros(N,12);
R=zeros(N,1);
j=0;
x=-190:0.01:100;
N_high=length(x);
N_low=length(x);
```

```

YY_high=zeros(N_high);
YY_low=zeros(N_low);

% figure
for i=19008:19008+N;
    tic
    j=j+1;
    V=A(i,7:end);
    V_high=V(ct_high);
    V_low=V(ct_low);
    %High
    y_high=spline(index_high,V_high,x);
    [S_temp,R_temp,Cl,Cu, y_fit]=gauss_fitting(x,y_high);
    S_high(j,:)=S_temp;
    R(j,1)=R_temp;

    YY_high(:,j)=y_fit;

    %Low
    y_low=spline(index_low,V_low,x);
    [S_temp,R_temp,Cl,Cu, y_fit]=gauss_fitting(x,y_low);
    S_low(j,:)=S_temp;
    R(j,2)=R_temp;
    YY_low(:,j)=y_fit;
    plot(x,YY_high(:,j),'r-',index_high,V_high,'k+',x,YY_low(:,j),'b-',index_low,V_low,'ko')
    axis([-190 100 0 20])
    disp(['Subject number: ' num2str(j) ' out of ' num2str(N)])
    toc
    pause
end

break

save('muscles_spline_fit.mat','A', 'index_high','index_low','R', 'S_low', 'S_high')

figure
plot(S_low(:,1),'b-')
hold
plot(S_low(:,2),'r-')
plot(S_low(:,3),'g-')
plot(S_low(:,4),'k-')
legend('Amplitude', 'Stdev', 'Mean', 'ERF')
%axis([0 10 0 150])
title('Fat tissue')

figure
plot(S_low(:,5),'b-')
hold
plot(S_low(:,6),'r-')
plot(S_low(:,7),'g-')
plot(S_low(:,8),'k-')
legend('Amplitude', 'Stdev', 'Mean', 'ERF')
title('Muscle tissue')
%axis([0 10 0 150])

```

```

figure
plot(S_low(:,9),'b-')
hold
plot(S_low(:,10),'r-')
plot(S_low(:,11),'g-')
legend('Amplitude', 'Stdev', 'Mean')
%axis([0 10 0 150])

figure
plot(C_lower(:,1),'b-')
hold
plot(C_lower(:,2),'r-')
plot(C_lower(:,3),'g-')
plot(C_lower(:,4),'k-')
legend('Amplitude', 'Stdev', 'Mean', 'ERF')
%axis([0 10 0 150])

%[fitresult, gof] = gauss_fit(index_high, v_high)

```

### ***createFit.m***

```

function [fitresult, gof] = createFit(index_high, V_high)
%CREATEFIT(INDEX_HIGH,V_HIGH)
% Create a fit.
%
% Data for 'untitled fit 1' fit:
%   X Input : index_high
%   Y Output: V_high
% Output:
%   fitresult : a fit object representing the fit.
%   gof : structure with goodness-of fit info.
%
% See also FIT, CFIT, SFIT.

% Auto-generated by MATLAB on 30-Jan-2015 14:06:29

%% Fit: 'untitled fit 1'.
[xData, yData] = prepareCurveData( index_high, V_high );

% Set up fitype and options.
ft = fitype( 'a*1/(b*sqrt(2*pi))*(exp(-(x-c).^2/(sqrt(2)*b)^2)).*(erfc(d*(x-
c)/(b*sqrt(2))))+e*1/(f*sqrt(2*pi))*(exp(-(x-g).^2/(sqrt(2)*f)^2)).*(erfc(h*(x-
g)/(f*sqrt(2))))+k*1/(m*sqrt(2*pi))*(exp(-(x-n).^2/(sqrt(2)*m)^2))', 'independent', 'x', 'dependent',
'y');
opts = fitoptions( 'Method', 'NonlinearLeastSquares' );
opts.Display = 'Off';
opts.Robust = 'Bisquare';
opts.StartPoint = [200 10 30 1 200 10 110 1 10 1 50];
opts.Lower=[1 0 20 0 1 0 90 0 1 0 30];
opts.Upper=[1e3 50 50 4 1e3 50 130 4 1e3 50 80];
% Fit model to data.
[fitresult, gof] = fit( xData, yData, ft, opts );

```

```

% Plot fit with data.
% figure( 'Name', 'untitled fit 1' );
% h = plot( fitresult, xData, yData, 'predobs', 0.99 );
% legend( h, 'V_high vs. index_high', 'untitled fit 1', 'Lower bounds (untitled fit 1)', 'Upper bounds
(untitled fit 1)', 'Location', 'NorthEast' );
% % Label axes
% xlabel( 'index_high' );
% ylabel( 'V_high' );
% grid on

R(j,2)=R_temp;
YY_low(:,j)=y_fit;
plot(x,YY_high(:,j),'r-',index_high,V_high,'k+',x,YY_low(:,j),'b-',index_low,V_low,'ko')
axis([-190 100 0 20])
disp(['Subject number: ' num2str(j) ' out of ' num2str(N)])
toc
pause
end

break

```

### ***gauss\_fitting.m***

```

function [S,R,C_lower,C_upper, y_fit]=gauss_fitting(x,y)

[xData, yData] = prepareCurveData( x, y );
% Set up fitype and options.
ft = fitype( 'a*1/(b*sqrt(2*pi))*(exp(-((x-
c).^2/(sqrt(2)*b)^2)))*d*normcdf(x,c,b)+e*1/(f*sqrt(2*pi))*(exp(-((x-
g).^2/(sqrt(2)*f)^2)))*h*normcdf(-x,-g,f)+k*1/(m*sqrt(2*pi))*(exp(-((x-n).^2/(sqrt(2)*m)^2))));',
'independent', 'x', 'dependent', 'y' );
opts = fitoptions( 'Method', 'NonlinearLeastSquares' );
opts.Display = 'Off';
opts.Robust = 'Bisquare';
%opts.StartPoint = [200 10 30 1 200 10 110 1 10 1 50];
opts.StartPoint = [200 10 -110 1 200 10 50 1 10 1 -50];
opts.Lower=[1 0 -150 0 1 0 20 -4 1 0 -80];
opts.Upper=[1e3 50 -50 4 1e3 50 100 1 1e3 50 10];

% Fit model to data.
[fitresult, gof] = fit( xData, yData, ft, opts );
% plot( fitresult, xData, yData)
% axis([0 140 0 20])
% text(20,18, strcat('measurement number: ', num2str(j)));
%Read in coefficients
S(1)=fitresult.a;
S(2)=fitresult.b;
S(3)=fitresult.c;
S(4)=fitresult.d;
S(5)=fitresult.e;
S(6)=fitresult.f;
S(7)=fitresult.g;
S(8)=fitresult.h;
S(9)=fitresult.k;

```

```

S(10)=fitresult.m;
S(11)=fitresult.n;
R(1)=gof.rsquare;
cc=confint(fitresult);
C_lower=cc(1,:);
C_upper=cc(2,:);

y_fit=feval(fitresult,x);

save('muscles_spline_fit.mat','A', 'index_high','index_low','R', 'S_low', 'S_high')

figure
plot(S_low(:,1),'b-')
hold
plot(S_low(:,2),'r-')
plot(S_low(:,3),'g-')
plot(S_low(:,4),'k-')
legend('Amplitude', 'Stdev', 'Mean', 'ERF')
%axis([0 10 0 150])
title('Fat tissue')

figure
plot(S_low(:,5),'b-')
hold
plot(S_low(:,6),'r-')
plot(S_low(:,7),'g-')
plot(S_low(:,8),'k-')
legend('Amplitude', 'Stdev', 'Mean', 'ERF')
title('Muscle tissue')
%axis([0 10 0 150])

figure
plot(S_low(:,9),'b-')
hold
plot(S_low(:,10),'r-')
plot(S_low(:,11),'g-')
legend('Amplitude', 'Stdev', 'Mean')
%axis([0 10 0 150])

figure
plot(C_lower(:,1),'b-')
hold
plot(C_lower(:,2),'r-')
plot(C_lower(:,3),'g-')
plot(C_lower(:,4),'k-')
legend('Amplitude', 'Stdev', 'Mean', 'ERF')
%axis([0 10 0 150])

% [fitresult, gof] = gauss_fit(index_high, v_high)

```











School of Science and Engineering  
Reykjavík University  
Menntavegur 1  
101 Reykjavík, Iceland  
Tel. +354 599 6200  
Fax +354 599 6201  
[www.ru.is](http://www.ru.is)